Genes to Cells

Derivation of human differential photoreceptor cells from adult human dermal fibroblasts by defined combinations of CRX, RAX, OTX2 and NEUROD

Yuko Seko[1,2]*, Noriyuki Azuma[3], Toshiyuki Ishii[4], Yukari Komuta[1], Kiyoko Miyamoto[1], Yoshitaka Miyagawa[2], Makoto Kaneda[4] and Akihiro Umezawa[2]

[1]Visual Functions Section, Department of Rehabilitation for Sensory Functions, Research Institute, National Rehabilitation Center for Persons with Disabilities, Tokorozawa, Saitama 359-8555, Japan
[2]Department of Reproductive Biology, Center for Regenerative Medicine, National Institute for Child Health and Development, Okura, Setagaya, Tokyo, 157-8535, Japan
[3]Department of Ophthalmology, National Center for Child Health and Development, Setagaya, Tokyo 157-8535, Japan
[4]Department of Physiology, Nippon Medical School, Sendagi, Bunkyo, Tokyo 113-8602, Japan

Redirecting differentiation of somatic cells by over-expression of transcription factors is a promising approach for regenerative medicine, elucidation of pathogenesis and development of new therapies. We have previously defined a transcription factor combination, that is, CRX, RAX and NEUROD, that can generate photosensitive photoreceptor cells from human iris cells. Here, we show that human dermal fibroblasts are differentiated to photoreceptor cells by the same transcription factor combination as human iris cells. Transduction of a combination of the CRX, RAX and NEUROD genes up-regulated expression of the photoreceptor-specific genes, recoverin, blue opsin and PDE6C, in all three strains of human dermal fibroblasts that were tested. Additional OTX2 gene transduction increased up-regulation of the photoreceptor-specific genes blue opsin, recoverin, S-antigen, CNGB3 and PDE6C. Global gene expression data by microarray analysis further showed that photoreceptor-related functional genes were significantly increased in induced photoreceptor cells. Functional analysis, that is, patch-clamp recordings, clearly revealed that induced photoreceptor cells from fibroblasts responded to light. Both the NRL gene and the NR2E3 gene were endogenously up-regulated in induced photoreceptor cells, implying that exogenous CRX, RAX, OTX2 and NEUROD, but not NRL, are sufficient to generate rod photoreceptor cells.

Introduction

Redirecting differentiation of somatic cells by over-expression of transcription factors is a promising approach for regenerative medicine, elucidation of pathogenesis and development of new therapies. The process is called ‘direct reprogramming’ or ‘direct conversion’ and has been shown in b cells, cardiomyocytes, neurons, platelets and photoreceptors. A specific combination of three transcription factors (Ngn3, Pdx1 and MafA) reprogram differentiated pancreatic exocrine cells in adult mice into cells that closely resemble beta cells (Zhou et al. 2008) and a combination of three factors (Gata4, Tbx5 and Baf60c) induce noncardiac mesoderm to differentiate directly into contractile cardiomyocytes (Takeuchi & Bruneau 2009). We recently employed the strategy of ‘direct reprogramming’ to generate retinal photoreceptor cells from human somatic cells, defining a combination of transcription factors, CRX, RAX and NEUROD, that induce light responsive photoreceptor cells (Seko et al. 2012). In that study, we induced ‘iris cells’ into photoreceptor cells. During vertebrate eye development, the inner layer of the optic cup differentiates into the

Communicated by: Takashi Tada
*Correspondence: seko-yuko@rehab.go.jp

DOI: 10.1111/gtc.12127

neural retina and iris-pigmented epithelium (IPE). Therefore, the common developmental origin of the iris and the retina may make photoreceptor-induction from iris cells easier than from other types of somatic cells.

The induced pluripotent stem cells (iPS) developed by Takahashi and Yamanaka were the first model for ‘direct reprogramming’, in which mouse adult fibroblasts were reprogrammed by transduction of four transcription factor genes, Oct3/4, Sox2, c-Myc and Klf4 (Takahashi & Yamanaka 2006). Additionally, functional neurons were generated from mouse fibroblasts by a combination of three factors (Ascl1, Brn2 and Myt1 l) (Vierbuchen et al. 2010), and functional platelets were generated from mouse and human fibroblasts by a combination of three factors (p45NF-E2, MafG and MafK) (Ono et al. 2012). Because human dermal fibroblasts are less specialized than iris cells, we tested whether human dermal fibroblasts could be converted into photoreceptors by the same defined combination of genes used successfully for human iris cells, CRX, RAX and NEUROD, to generalize and establish our technology for ‘generating photoreceptors’.

In this study, we also investigated an effect of additional transcription factor, OTX2, on transdifferentiation of somatic cells into retinal cells. Otx2 is essential for the cell fate determination of retinal photoreceptor cells (Nishida et al. 2003), and conditional disruption of the Otx2 gene decreases photoreceptor-associated genes (Omori et al. 2011).

Here, we show that the same combination of genes used for human iris cells, that is, CRX, RAX and NEUROD, generate human photoreceptor cells from human dermal fibroblasts, and that additional OTX2 gene transduction further amplifies the expression of retina-specific genes. Our data therefore indicate that human dermal fibroblasts are a superior cell source for reprogramming into photoreceptor cells.

Results

Human dermal fibroblasts are induced into a rod- or cone-specific phenotype by defined transcription factors

We selected seven genes, POU1F1, SOX2, PAX6, RAX, CRX, OTX2 and NEUROD, as candidate factors that may contribute to induce photoreceptor-specific phenotypes in human dermal fibroblasts, on the basis that such factors play a role in the development of photoreceptors. CRX, RAX and NEUROD are essential factors that induce photoreceptor cells from human iris cells (Seko et al. 2012) and POU1f1, Sox2 and Otx2 bind to the Rx promoter (Martinez-de Luna et al. 2010). Human dermal fibroblasts were infected with these genes and were examined for inducible expression of photoreceptor-specific genes. RT-PCR results showed that transduction of CRX, RAX and NEUROD (CRN) genes up-regulated the expression of the photoreceptor-specific genes recoverin, blue opsin and PDE6C, in all strains of fibroblasts tested (Fig. 1, panel A, B, C). Additionally, CRN-infected fibroblasts became positive for rhodopsin and blue opsin by immunohistochemistry (Fig. 1D). These results suggest that photoreceptor-specific phenotypes are induced by the same combination of transcription factors in human dermal fibroblasts as in human iris cells. However, it appeared that the combination of CRX, RAX, NEUROD and OTX2 (CRNO) up-regulated the photoreceptor-specific blue opsin gene more strongly than the combination of CRN.

Additional OTX2 gene transduction increases up-regulation levels of photoreceptor-specific genes

Expression levels of opsin- and phototransduction-related genes in induced- and noninduced fibroblasts were quantitated. Expression levels of S-antigen and recoverin, which are specifically expressed in rod photoreceptors, were much higher in CRNO-infected cells than in CRN-infected cells (S-antigen, $P < 0.01$, recoverin, $P < 0.05$; Welch’s t-test, Fig. 2). In contrast, expression levels of rhodopsin, blue opsin, green opsin, recoverin, S-antigen, CNGB3 and PDE6C were not increased by additional PAX6 gene infection (CRNP vs. CRN, in Fig. 2).

OTX2 is not an essential factor but an amplifier for induction of photoreceptor cells from human dermal fibroblasts

To investigate whether OTX2 could be used as an alternative to the essential three genes, that is, CRX, RAX and NEUROD, we tested the effect of withdrawal of each individual factor from the four genes, that is, CRX, RAX, NEUROD and OTX2, on expression levels of the opsin- and phototransduction-related genes in induced photoreceptor cells (Fig. 3). Removal of either CRX, RAX or NEUROD resulted in a marked decrease in blue opsin, S-antigen, PDE6C

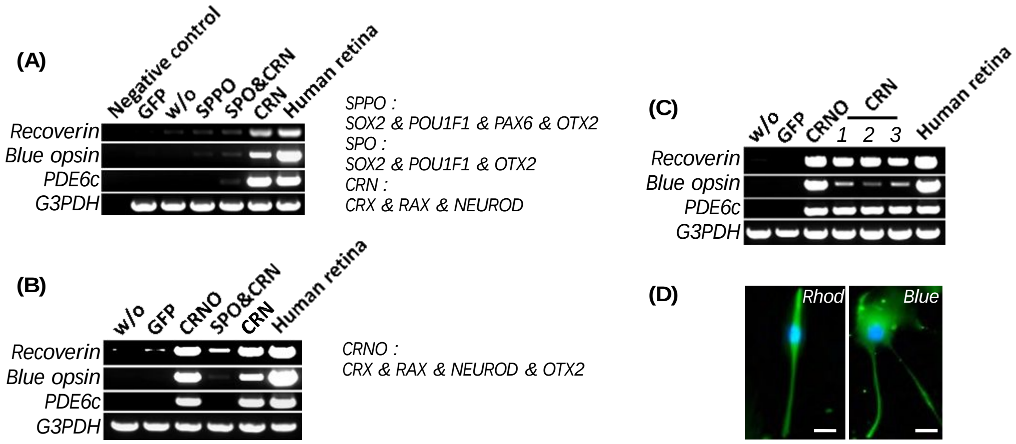

Figure 1 Induction of retina-specific genes in human dermal fibroblasts by the retroviral infection of genes for defined transcription factors. (A) RT-PCR analysis for photoreceptor-specific genes in cultured human dermal fibroblasts (NHDF) obtained from Lonza after gene transfer of several kinds of transcription factors. Recoverin, blue opsin and PDE6c genes were up-regulated by CRN transduction. 'Negative control': amplified water as a negative control. 'GFP': cultured fibroblasts after retroviral gene transfer of the GFP gene as another negative control. 'w/o': cultured fibroblasts without gene transfer as the other negative control. 'SPPO': SOX2, POU1F1, PAX6 and OTX2. 'SPO': SOX2, POU1F1 and OTX2. 'CRN': CRX, RAX and NEUROD. 'Human retina': human retinal tissue as a positive control. The amount of cDNA as a template was a half in the positive control. (B) RT-PCR analysis for photoreceptor-specific genes in cultured human dermal fibroblasts (NHDF) obtained from Promo Cell after gene transfer of several transcription factors. Recoverin, blue opsin and PDE6c genes were up-regulated by CRN or CRNO transduction. 'w/o': cultured fibroblasts without gene transfer as a negative control. 'GFP': cultured fibroblasts after retroviral gene transfer of the GFP gene as another negative control. 'CRNO': CRX, RAX, NEUROD and OTX2. (C) RT-PCR analysis for photoreceptor-specific genes in cultured human dermal fibroblasts (HDF-a) obtained from ScienCell after gene transfer of several transcription factors. Recoverin, blue opsin and PDE6C genes were up-regulated by CRN or CRNO transduction. Expression levels of blue opsin were increased by additional OTX2 gene transduction. 'w/o': cultured fibroblasts without gene transfer as a negative control. 'GFP': cultured fibroblasts after retroviral gene transfer of the GFP gene as another negative control. 'CRNO': CRX, RAX, NEUROD and OTX2. '1', '2' and '3' mean independently cultured, transfected and harvested cells by the same combination of CRN genes. (D) Immunocytochemistry using antibodies to rhodopsin and blue opsin (green). Nuclei were stained with DAPI (blue). Experiments were carried out at 2 weeks after infection. The cells in the left panel and the right panel are CRN-infected Fib#2 and Fib#1, respectively. Scale bars represent 10 μm.

and CNGB3 levels; withdrawal of RAX resulted in a marked decrease in expression of blue opsin, and withdrawal of NEUROD resulted in a striking decrease in expression of PDE6C. Alternatively, withdrawal of OTX2 alone did not affect the up-regulation of any of the tested photoreceptor-specific genes. These results indicate that OTX2 is not an essential factor but an amplifier for induction of photoreceptor cells from human dermal fibroblasts, suggesting that additional OTX2 plays a role in improving the balance and stability of photoreceptor-related gene expression in induced photoreceptor cells. Removal of either CRX, RAX or NEUROD resulted in a marked decrease in blue opsin, S-antigen, PDE6C and CNGB3 levels, suggesting that each transcription factor plays a role for specific molecular functions along with a role as a constituent of a combination for transdifferentiation to photoreceptor cells.

Photoreceptor-related functional genes are clearly up-regulated in induced photoreceptor cells from human dermal fibroblasts

To clarify the specific gene expression profile in induced photoreceptor cells, we compared the expression profiles of 50 599 probes in the induced photoreceptor cells (CRN-infected fibroblasts (CRN-Fib), CRNO-infected fibroblasts (CRNO-Fib) and parental cells [fibroblast (Fib)] by microarray analysis (uploaded to GEO accession #GPL16699 at http://www.ncbi.nlm.nih.gov/geo/index.cgi). We first extracted the intersection of the two groups of genes, that is, up-regulated genes by CRN-infection ([CRN-Fib] vs. [Fib]) and those by CRNO-infection ([CRNO-Fib] vs. [Fib]) (signal ratio ≥ +1.5 for 'up'). According to gene ontology (GO) term annotation, the differentially expressed genes (4124 probes), which were

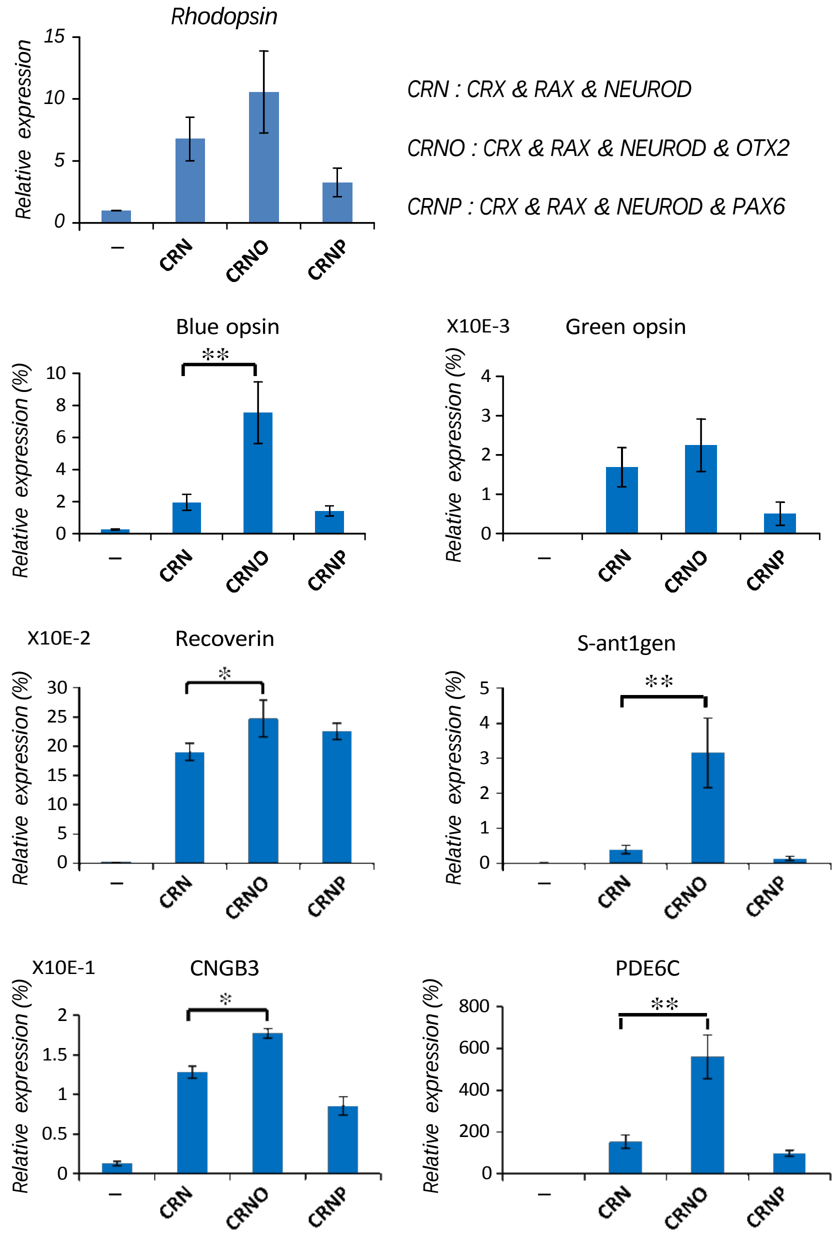

Figure 2 Effect of additional OTX2 gene infection. Quantitative RT-PCR results for expression levels of rod- or cone-specific genes in induced photoreceptor cells from human dermal fibroblasts by the defined transcription factors. Quantitative expression levels of rhodopsin, blue opsin, green opsin, recoverin, S-antigen, CNGB3 and PDE6c genes were investigated. The data of green opsin, recoverin and CNGB3 were the results in experiments using Fib#2, and the data of rhodopsin, blue opsin and S-antigen were the results in experiments using Fib#3. The vertical axis indicates expression levels of each gene (%) in the indicated cells, relative to human retinal tissues. For rhodopsin, expression in cultured fibroblasts is regarded as 1.0. Results of statistical analyses for comparison of expression levels between CRNO-infected cells and CRN-infected cells are shown [*$P < 0.05$ and **$P < 0.01$ (Welch's t-test)]. '–': cultured fibroblasts without gene transfer as a negative control. 'CRN': CRX, RAX and NEUROD. 'CRNO': CRX, RAX, NEUROD and OTX2. 'CRNP': CRX, RAX, NEUROD and PAX6.

included in the intersection, were categorized into functional groups. Interestingly, when phototransduction-related genes were extracted, they accounted for up to 0.2% of the total (Fig. 4A; Table S1 in Supporting Information). In fact, signals of 16 probes were increased among the 30 phototransduction-related probes.

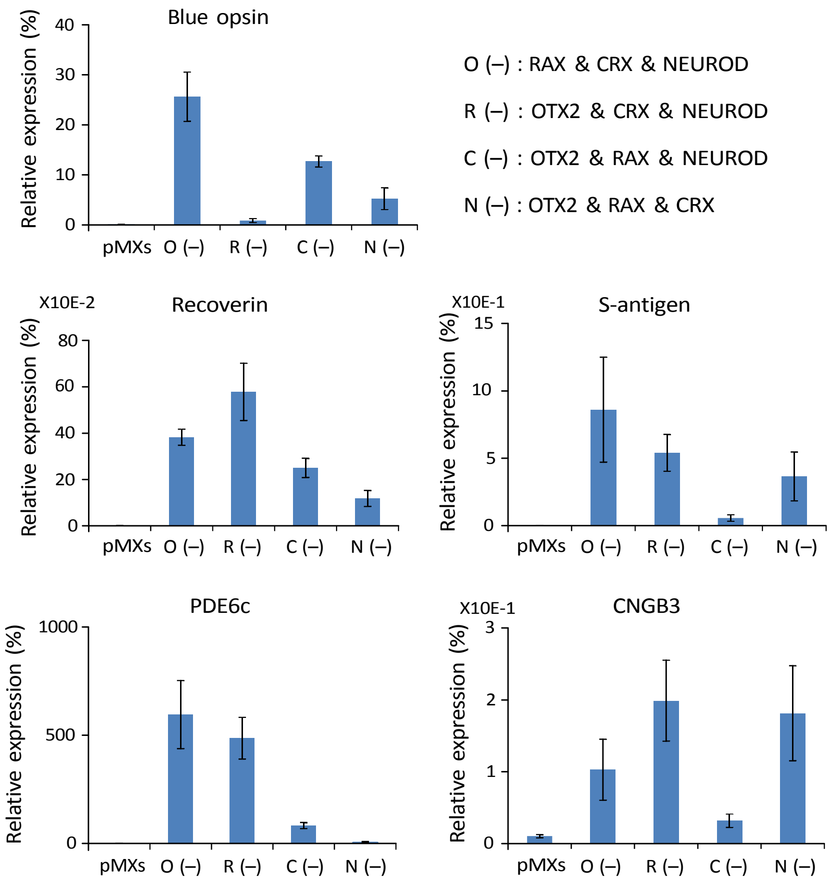

Figure 3 Effect of individual withdrawal of each gene from the combination of CRX, RAX, NEUROD and OTX2. Quantitative RT-PCR results for expression levels of rod- or cone-specific genes in induced photoreceptor cells from human dermal fibroblasts by the defined transcription factors. To determine which of the four genes, that is, CRX, RAX, NEUROD and OTX2, are critical, we examined the effect of withdrawal of individual factors from the pool of the candidate genes on expression of the opsin genes. In this experiment, Fib#3 was used. Quantitative expression levels of blue opsin, recoverin, S-antigen, CNGB3 and PDE6C genes were investigated. Vertical axis indicates expression levels of each gene (%) in the indicated cells, relative to human retinal tissues. Individual withdrawal of RAX resulted in a significant decrease in expression of blue opsin and withdrawal of CRX resulted in a significant decrease in S-antigen PDE6C and CNGB3. Individual withdrawal of NEUROD resulted in a significant decrease in PDE6C. However, withdrawal OTX2 could up-regulate all of the retina-specific genes tested. 'O(-)': CRX, RAX and NEUROD. 'R(-)': CRX, OTX2 and NEUROD. 'C(–)': OTX2, RAX and NEUROD. 'N(-)': CRX, RAX and OTX2. 'pMXs': cultured fibroblasts after retroviral gene transfer of the pMXs gene as a negative control.

To clarify the difference in gene expression profiles between fibroblast-derived and iris-derived photoreceptor cells, we investigated the expression profiles of default cells (iris cells) and induced cells (CRN-infected iris cells). We carried out GO analysis based on the differentially expressed genes (2585 probes), which were included in the commonly up-regulated genes, that is, ([CRNO-Fib] vs. [Fib]) and ([CRN-Iris] vs. [Iris]) (signal ratio ≥ +1.5 for 'up'). The phototransduction-related genes were extracted and accounted for up to 4.4% (Fig. 4B; Table S2 in Supporting Information). Although detection/perception, which includes detection of external stimulus, detection of abiotic stimulus and detection of light stimulus, accounted for up to 0.6% of the total in Fig. 4A, the detection/perception accounted for up to 21.1% in Fig. 4B.

A dermal fibroblast could be a cell source as well as an iris cell

We searched up-regulated genes both in the CRNO-infected fibroblasts and in CRN-infected iris cells (signal ratio ≥ 2.0 for 'up') and named as 'intersection

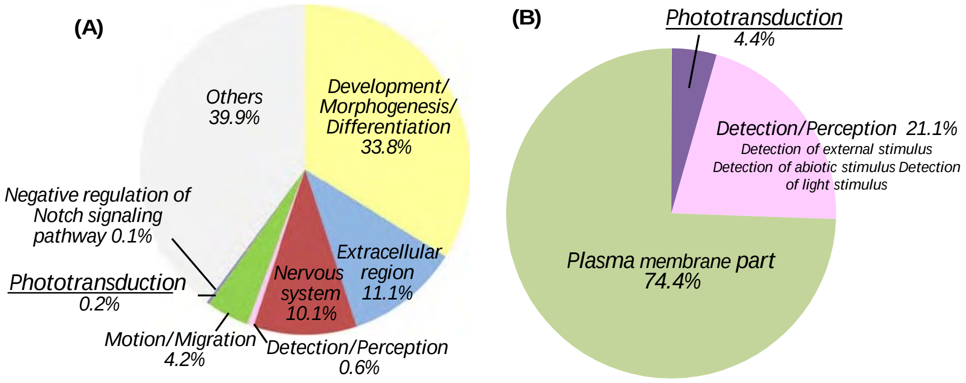

Figure 4 Categorization of the genes differentially expressed in induced photoreceptor cells from human dermal fibroblasts by the defined transcription factors. (A) Categorization of commonly up-regulated genes in induced photoreceptor cells from human dermal fibroblasts by genes transduction of CRN and CRNO. To clarify the specific gene expression profile in induced photoreceptor cells, we compared the expression levels of 50 599 probes in the induced photoreceptor cells (CRN-infected fibroblasts (CRN-Fib), CRNO-infected fibroblasts (CRNO-Fib) and parental cells [fibroblast (Fib)] by microarray analysis. We searched up-regulated genes in the induced photoreceptor cells by CRN- and CRNO-infection compared with parental cells (signal ratio ≥ +1.5 for 'up'), respectively. We then extracted the intersection of the two groups of genes, that is, up-regulated genes by CRN-infection and those by CRNO-infection. According to gene ontology (GO) term annotation, the genes differentially expressed in the induced photoreceptor cells by CRN- and CRNO-infection (4124 probes) were categorized into functional group, figuring out the relative importance or significance of the GO-term [corrected *P*-value < 0.01)]. After that, we carried out additional categorization into eight groups. Interestingly, phototransduction-related genes were extracted and account for up to 0.15% of the total. (B) Categorization of commonly up-regulated genes (2585 probes) in the CRNO-transfected dermal fibroblasts and CRN-transfected iris cells (signal ratio ≥ 1.5 for 'up'). According to gene ontology (GO) term annotation, the genes differentially expressed in the induced photoreceptor cells (2585 probes) were categorized into functional groups to figure out the relative importance or significance of the GO term (corrected *P*-value < 0.01).

of Fib and Iris'. Then, we extracted retina-related genes from them according to Gene Ontology and a previous paper (Omori *et al.* 2011). We focused on remarkably up-regulated genes ([CRNO-Fib]/[Fib] > 9.0) and extracted them (Fig. 5A). We then compared signal ratios between [CRNO-Fib]/[Fib] (DFib) and [CRN-Iris]/[Iris] (DIris). The signal ratios of 18 probes were higher in [CRNO-Fib] (DFib/DIris ≥ 2.0); however, the signal ratios of 47 signals were higher in [CRN- Iris] (DIris/DFib ≥ 2.0). As for other 78 probes, the signal ratios were regarded not to be significantly different (Fig. 5B; Table S3 in Supporting Information). To analyze the gene expression data in an unsupervised manner, we carried out principal component analysis (PCA). The gene expression patterns in the CRN-Fib, CRNO-Fib and CRN-Iris were close based on component 2 (PC2) but were apart from the parent cells (Fib and Iris) (Fig. 5C). We investigated the difference in endogenous expression of *CRX*, *RAX* and *NEUROD* between CRN-Fib and CRN-iris by RT-PCR (Fig. 5D). The endogenous *CRX* genes started to be expressed in CRN-Fib, but the expression levels of *RAX* and *NEUROD* were higher in CRN-Iris than in CRN-Fib. Both the *NRL* gene and the *NR2E3* gene were endogenously up-regulated in the induced photoreceptor cells, that is, CRN-Fib, CRNO-Fib and CRN-Iris (Fig. 5E).

Induced photoreceptor cells from fibroblasts are photoresponsive *in vitro*

Light stimulation was applied to infected or noninfected human fibroblasts because CRN- or CRNO-infected cells showed the photoreceptor-like phenotypes by RT-PCR and global gene expression analyses. Among cells tested, significant light responses were detected in a portion of infected cells (Fig. 5F; Fig. S2 in Supporting Information). An infected cell presented a large outward current when exposed to light (Fig. 5F, upper panel). However, no detectable outward current was evoked when light stimulation was given to a noninfected cell (Fig. 5F, lower panel).

Discussion

This is the first report that human dermal fibroblasts can differentiate into photoreceptor cells by the same combination of transcription factors, *CRX*, *RAX* and

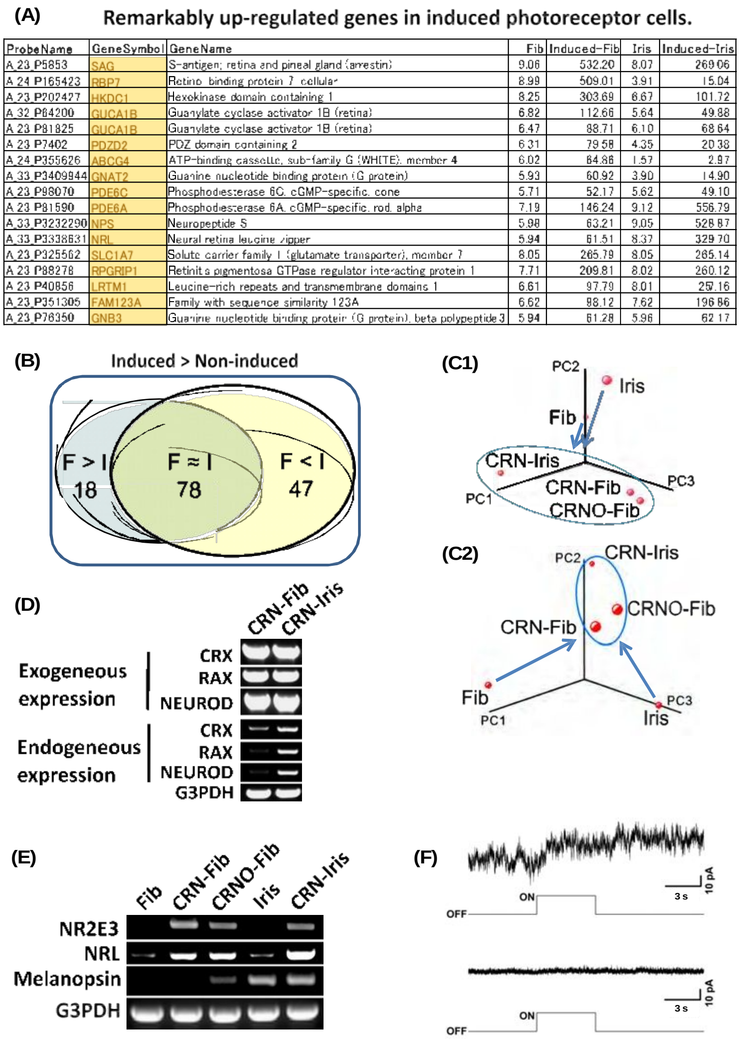

(A) Remarkably up-regulated genes in induced photoreceptor cells.

ProbeName	GeneSymbol	GeneName	Fib	Induced-Fib	Iris	Induced-Iris
A_23_P5853	SAG	S-antigen; retina and pineal gland (arrestin)	9.06	532.20	8.07	269.06
A_24_P165423	RBP7	Retinol binding protein 7, cellular	8.99	509.01	3.91	15.04
A_23_P207427	HKDC1	Hexokinase domain containing 1	8.25	303.69	6.67	101.72
A_32_P64200	GUCA1B	Guanylate cyclase activator 1B (retina)	6.82	112.66	5.64	49.88
A_23_P81825	GUCA1B	Guanylate cyclase activator 1B (retina)	6.47	88.71	6.10	68.64
A_23_P7402	PDZD2	PDZ domain containing 2	6.31	79.58	4.35	20.38
A_24_P355626	ABCG4	ATP-binding cassette, sub-family G (WHITE), member 4	6.02	64.86	1.57	2.97
A_33_P3409944	GNAT2	Guanine nucleotide binding protein (G protein)	5.93	60.92	3.90	14.90
A_23_P98070	PDE6C	Phosphodiesterase 6C, cGMP-specific, cone	5.71	52.17	5.62	49.10
A_23_P81590	PDE6A	Phosphodiesterase 6A, cGMP-specific, rod, alpha	7.19	146.24	9.12	556.79
A_33_P3232290	NPS	Neuropeptide S	5.98	63.21	9.05	528.87
A_33_P3338631	NRL	Neural retina leucine zipper	5.94	61.51	8.37	329.70
A_23_P325562	SLC1A7	Solute carrier family 1 (glutamate transporter), member 7	8.05	265.79	8.05	265.14
A_23_P88278	RPGRIP1	Retinitis pigmentosa GTPase regulator interacting protein 1	7.71	209.81	8.02	260.12
A_23_P40856	LRTM1	Leucine-rich repeats and transmembrane domains 1	6.61	97.79	8.01	257.16
A_23_P351305	FAM123A	Family with sequence similarity 123A	6.62	98.12	7.62	196.86
A_23_P76350	GNB3	Guanine nucleotide binding protein (G protein), beta polypeptide 3	5.94	61.28	5.96	62.17

Figure 5 Comparison of gene expression profiles of up-regulated genes in induced photoreceptor cells from dermal fibroblasts and from iris cells. (A) Remarkably up-regulated genes in induced photoreceptor cells ([CRNO-Fib]/[Fib] > 9.0). (B) Microarray analysis data sets from up-regulated genes in induced photoreceptor cells from dermal fibroblasts and from iris cells. F > I: Signal ratio of F/signal ratio of I ≥ 2.0. F < I: Signal ratio of I/signal ratio of F ≥ 2.0. The numbers of probes in each category are indicated. (C) Three-dimensional representation of PCA of gene expression levels (C-1: PCA based on the expression of all genes. C-2: PCA based on the expression of retina-related genes). It was shown that CRN-Fib, CRNO-Fib and CRN-Iris were grouped into the same group (shown in circle), suggesting that genes expression patterns in the CRN-Fib, CRNO-Fib and CRN-Iris were similar based on component 2 (PC2) and were apart from parent cells (Fib and Iris). (D) RT-PCR analysis of the exogenous and endogenous genes in induced retinal cells. Expression of the CRX, RAX and NEUROD and genes in the transgene-induced cells was analyzed by RT-PCR, using the exogenous and endogenous gene-specific primers (Seko *et al.* 2012). Equal amounts of RNAs were examined as determined by normalization by expression of the G3PDH gene. The levels of endogenous genes expression of CRX, RAX and NEUROD were clearly higher in CRN-Iris than in CRN-Fib. (E) RT-PCR analysis of genes expression of the transcription factor, NRL and NR2E3, and melanopsin. Expression of NRL and NR2E3 was clearly up-regulated in the transgene-induced cells. The combination of CRN may be sufficient to up-regulate those transcription factors genes. As for melanopsin, expression was detected in CRNO-fib, but not in Fib or CRN-Fib. By microarray analysis, any expression of melanopsin was not detected (uploaded to GEO accession #GPL16699 at http://www.ncbi.nlm.nih.gov/geo/index.cgi). (F) Responses to light in infected cells and noninfected cells. Responses to light in infected cells (upper panel) and noninfected cells (lower panel). In a CRNO-infected cell (Fib #2), there was a large outward current when cell was exposed to light (upper panel). However, no detectable outward current was evoked when light stimulation was given to a noninfected cell (lower panel). A timing and duration of light stimulation is shown under the current trace. Holding potential was 0 mV.

NEUROD (Seko et al. 2012), that were used successfully for iris cells (Fig. 1). An additional gene added to the combination, OTX2, further increases expression levels of photoreceptor-specific genes (Fig. 2). Global gene expression data by microarray analysis further shows that photoreceptor-related functional genes are significantly increased in induced photoreceptor cells (Fig. 4). Our data suggest that OTX2 plays a role as an amplifier of photoreceptor-related functions (Figs 2 and 3; Fig. S1 in Supporting Information). Functional analysis also revealed that induced photoreceptor cells from fibroblasts by CRX, RAX, NEUROD and OTX2 are photoresponsive in vitro (Figs 5F; Fig. S2 in Supporting Information).

Dermal fibroblasts are of mesodermal origin and immunogenic, whereas iris-pigmented epithelial cells (IPE cells) are of neural ectoderm-origin and show immune tolerance. Iris cells studied here include not only IPE cells but also iris stromal cells, which are of neural crest origin. We have previously shown that iris cells, IPE cells and iris stromal cells are differentiated into photoreceptor cells in the same way (Seko et al. 2012). However, dermal fibroblasts are harvested easily and safely, and iris cells are obtained surgically. To find a more suitable cell source than the iris cells for reprogramming into photoreceptor cells, we compared signal ratios between CRNO-Fib and CRN-Iris by a microarray analysis. The results show that there is an increase in both the expression levels and the variety of up-regulated photoreceptor-specific genes in induced cells from iris when compared with dermal fibroblasts (Fig. 5B; Table S3 in Supporting Information). From the standpoint of regenerative medicine, iris cells may be more suitable than dermal fibroblasts based on their characteristics of immune tolerance and higher expression of retina-specific genes in differentiated cells. The difference in induced endogenous expression of transcription factors CRX, RAX and NEUROD between CRN-Fib and CRN-Iris as well as the difference in up-regulated photoreceptor-specific genes may suggest a difference in reprogramming potential between the human dermal fibroblasts and the human iris cells (Fig. 5C). It may be possible to improve dermal fibroblasts as a source by use of other transcription factors or manipulating the histone methylation signature (Bramswig et al. 2013). However, dermal fibroblasts have an important advantage in that these cells are obtained safely and easily from patients. Because the direct reprogramming method may be suitable to provide the small numbers of cells required for individualized drug screening and disease modeling, dermal fibroblasts may be useful for such purposes despite their limitations.

We have previously shown that the combination of CRX and NEUROD, but not NRL, is sufficient for rod-specific gene expression (Seko et al. 2012), but Mears et al. (2001) reported that Nrl is necessary for rod-photoreceptor development. The present study indicates that both the NRL gene and the NR2E3 gene are endogenously up-regulated in induced photoreceptor cells (CRNO-Fib and CRN-Iris) by microarray analyses and RT-PCR (Fig. 5D; Table S3 in Supporting Information). Endogenous NRL expression by the three factors, CRX, RAX and NEUROD, may promote retinal differentiation in the absence of the exogenous NRL gene. This fact clearly shows that exogenous gene transduction of the combination, CRX, RAX and NEUROD, is sufficient but NRL is not essential to induce rod photoreceptor-specific gene expression.

Several retinal diseases, including retinitis pigmentosa (RP), age-related macular degeneration and cone dystrophy, lead to loss of vision, due to loss of photoreceptors and retinal pigment epithelium (RPE), especially, RP leads to visual impairment due to irreversible retinal degeneration, which is determined genetically in most cases. Gene therapy has been implicated for Leber's congenital amaurosis (Bainbridge et al. 2008). Another promising therapeutic strategy is to transplant functional photoreceptor cells and retinal pigment epithelial cells. Sheets of human fetal neural retina with retinal pigment epithelium (Radtke et al. 2004) and ES cell-derived photoreceptors (Osakada et al. 2008) have been implicated for use as sources for the photoreceptor cells. The technology for producing retinal sheets from ES cell/iPSCs by self-organogenesis (Eiraku et al. 2011) is promising for retinal transplantation. Recently, Tanaka et al. (2013) reported that inducible expression of myogenic differentiation 1 (MYOD1) in immature human iPSCs drives cells along the myogenic lineage, with efficiencies reaching 70–90%. Although induction of human neural retina takes a long time (Nakano et al. 2012), there is a possibility that the induction period could be shortened by the aid of the defined factors that we determined. We have previously reported the defined combination of transcription factors, that is, CRX, RAX and NEUROD, induce light-responsive photoreceptor cells in humans using iris cells (Seko et al. 2012). We show here the function of the OTX2 gene as an amplifier of retinal transdifferentiation of human dermal fibroblasts (Figs 2 and 3; Fig. S1 in Supporting Information). In conclusion, OTX2 and the three transcription factors, CRX, RAX and NEUROD, are promising as tools for effective retinal induction.

Experimental procedures

Cell culture

Three strains of cultured human dermal fibroblasts were used: one was obtained from Lonza (NHDF), another was from Promo Cell (NHDF) and the other was from ScienCell (HDF-a). These three kinds of fibroblasts were designated as Fib#1, Fib#2 and Fib#3, respectively. The cells were cultured in the recommended medium by the manufactures (FGM-2 Bullet kit, Fibroblast Growth Medium Kit, and Fibroblast Medium, respectively). Iris cells were obtained as previously reported (Seko et al. 2012) with the approval (approval number, #156) of the Ethics Committee of the National Institute for Child and Health Development (NCCHD), Tokyo. The ethics committees of the NCCHD and National Rehabilitation Center for Persons with Disabilities specifically approved this study. Signed informed consent was obtained from donors, and the surgical specimens were irreversibly de-identified. All experiments handling human cells and tissues were carried out in line with the Tenets of the Declaration of Helsinki. The iris cells were cultured in the growth medium [Dulbecco's modified Eagle's medium (DMEM)/Nutrient mixture F12 (1:1) supplemented with 10% fetal bovine serum, insulin–transferrin–selenium, and MEM-NEAA (GIBCO)].

Preparation and infection of recombinant retrovirus

Full-length transcription factors, SOX2 (Martinez-de Luna et al. 2010), POU1F1 (Martinez-de Luna et al. 2010), OTX2 (Nishida et al. 2003), PAX6 (Glaser et al. 1992), RAX (Mathers et al. 1997), CRX (Furukawa et al. 1997) and NEUROD (Morrow et al. 1999), were amplified from cDNAs prepared from total RNA of adult human retina (Clontech, CA, USA) by PCR and cloned into the XmnI-EcoRV sites of pENTR11 (Invitrogen). Each vector contained one transcription factor, and a mixture of vectors was used.

Preparation and infection of recombinant retrovirus were carried out as previously reported (Seko et al. 2012). In brief, the resulting pENTR11-transcription factors were recombined with pMXs-DEST by use of LR recombination reaction as instructed by the manufacturer (Invitrogen). The retroviral DNAs were then transfected into 293FT cells, and 3 days later, the media were collected and concentrated. The human dermal fibroblasts and the iris cells were infected with this media containing retroviral vector particles. After the retroviral infection, the media were replaced with the DMEM/F12/B27 medium supplemented with 40 ng/ml bFGF, 20 ng/ml EGF, fibronectin and 1% FBS. The retrovirus-infected cells were cultured for up to 14 days. We transfected retroviral eGFP under the same condition to measure efficiency of infection. The frequency of eGFP-positive cells was 90–94% of all cells at 48 h after infection.

Reverse transcriptase-PCR

Total RNA was isolated with an RNeasy Plus mini-kit@ (Qiagen, Maryland, USA) or PicoPure™ RNA Isolation Kit (Arcturus Bioscience, CA, USA) according to the manufacturer's instruction. An aliquot of total RNA was reverse transcribed using an oligo (dT) primer. The design of PCR primer sets is shown in our previous paper (Seko et al. 2012).

Quantitative RT-PCR

cDNA template was amplified (ABI7900HT Sequence Detection System) using the Platinum Quantitative PCR SuperMix-UDG with ROX (11743-100, Invitrogen). Fluorescence was monitored during every PCR cycle at the annealing step. The authenticity and size of the PCR products were confirmed using a melting curve analysis (using software provided by Applied Biosystems) and a gel analysis. A mRNA level was normalized using G3PDH as a housekeeping gene. The design of PCR primer sets is shown in our previous paper (Seko et al. 2012).

Immunocytochemistry

Immunocytochemical analysis was carried out as previously described (Kohyama et al. 2001). As a methodological control, the primary antibody was omitted. The primary antibodies used were as follows: rhodopsin (goat polyclonal, I-17, Santa Cruz) and blue opsin (goat polyclonal, P-13, Santa Cruz).

Global gene expression analysis

To clarify the specific gene expression profile in induced photoreceptor cells, we compared the expression levels of 50 599 probes in the induced photoreceptor cells and parental cells using the SurePrint G3 Human Gene Expression Microarray 8 9 60 K, ver.2.0 (Agilent) using total RNA extracted from those cells. To average experimental variations, extracted total RNA samples were pooled into one tube from three independent induction experiments of human dermal fibroblasts (Fib#2) and 12 independent induction experiments of human iris cells, respectively, and pooled samples were served to microarray analyses. To normalize the variations in staining intensity among chips, the 75th percentile of intensity distributions was aligned across arrays using GeneSpring software, version 12.5 (Agilent Technologies, Palo Alto). We then carried out GO analysis based on the normalized expression data of induced and noninduced cells. Commonly up-regulated genes in CRN- and CRNO-transfected fibroblasts (4124 probes) and those in CRNO-transfected fibroblasts and CRN-transfected iris cells (2585 probes) were extracted and were categorized into functional groups, respectively, to figure out the relative importance or significance of the gene ontology (GO) term (corrected P-value < 0.01). To analyze and compare the gene expression data of the induced cells and parent cells in an unsupervised manner, we used principal component analysis (PCA).

Light stimulation and electrophysiological recordings

We followed the method in our previous paper (Seko *et al.* 2012). Briefly, a high pressure UV lamp (USH-102D, Ushio) was used as a light source. Diffuse, unpolarized blue light was generated through bandpass filters attached with the fluorescent emission system (BX-FLA, Olympus, Tokyo, Japan). Wavelength of light for stimulation was 460–490 nm. Duration and timing of light stimulation was controlled by an electrically controlled shutter attached to the UV lamp box. The trigger signals to the electrically controlled shutter were given by commercially available software (pClamp 9) through AD/DA. Light intensity used for stimulation was 390 W/m^2. To activate the phototransduction cascade, 11-*cis* retinal (a gift from the vision research community, the National Eye Institute, National Institutes of Health) was added to the culture medium of human fibroblasts to a concentration of 37.5 μM with 0.15% ethanol as a vehicle, approximately 45 min before the electrical recording. Electrical recordings were made in the whole-cell patch-clamp configuration. The composition of the intrapipette solution was (in mM) KCl, 135; CaCl$_2$, 0.5; HEPES, 5; EGTA, 5; ATP-2Na, 5; GTP-3Na, 1; and pH was adjusted to 7.3 with KOH. The resistance of patch pipettes was 12–15 MΩ when filled with an intrapipette solution. The membrane current was recorded with a patch-clamp amplifier (Axopatch-200B; Axon Instruments, Foster City, CA, USA), low-pass filtered with a cutoff frequency of 1 kHz and digitized at 2 kHz through a DigiData 1322A Interface using pCLAMP software (version 8.0, Axon Instruments). We recorded light responses from noninfected cells, CRN-infected cells and CRNO-infected cells. Recorded data were pooled for further analysis (for details, see Fig. S2 in Supporting Information).

Acknowledgements

We are grateful for the National Eye Institute, National Institutes of Health for gift of 11-*cis* retinal, S. Kato, K. Mori, S. Toyama and Y. Takahashi for the support throughout the work and for H. Miyauchi for the technical assistance. This research was supported by grants from the Ministry of Education, Culture, Sports, Science, and Technology (MEXT) of Japan, by Ministry of Health, Labour and Welfare Sciences (MHLW) research grants, by a Research Grant on Health Science focusing on Drug Innovation from the Japan Health Science Foundation, by the program for the promotion of Fundamental Studies in Health Science of the Pharmaceuticals and Medical Devices Agency, by the Grant of National Center for Child Health and Development to AU, by the Nippon Medical School Grant-in-Aid for Medical Research to MK and by grants of National Rehabilitation Center for Persons with Disabilities.

Author contributions

YS carried out all of the experiments; MK, TI, YS, YK carried out electrophysiological analyses; YS, YM and KM prepared viral vectors; YS, NA, AU made experimental designs; and YS and AU wrote the manuscript.

References

Bainbridge, J.W., Smith, A.J., Barker, S.S. *et al.* (2008) Effect of gene therapy on visual function in Leber's congenital amaurosis. *N. Engl. J. Med.* 358, 2231–2239.

Bramswig, N.C., Everett, L.J., Schug, J., Dorrell, C., Liu, C., Luo, Y., Streeter, P.R., Naji, A., Grompe, M. & Kaestner, K.H. (2013) Epigenomic plasticity enables human pancreatic alpha to beta cell reprogramming. *J. Clin. Invest.* 123, 1275–1284.

Eiraku, M., Takata, N., Ishibashi, H., Kawada, M., Sakakura, E., Okuda, S., Sekiguchi, K., Adachi, T. & Sasai, Y. (2011) Self-organizing optic-cup morphogenesis in three-dimensional culture. *Nature* 472, 51–56.

Furukawa, T., Morrow, E.M. & Cepko, C.L. (1997) Crx, a novel otx-like homeobox gene, shows photoreceptor-specific expression and regulates photoreceptor differentiation. *Cell* 91, 531–541.

Glaser, T., Walton, D.S. & Maas, R.L. (1992) Genomic structure, evolutionary conservation and aniridia mutations in the human PAX6 gene. *Nat. Genet.* 2, 232–239.

Kohyama, J., Abe, H., Shimazaki, T., Koizumi, A., Nakashima, K., Gojo, S., Taga, T., Okano, H., Hata, J. & Umezawa, A. (2001) Brain from bone: efficient "meta-differentiation" of marrow stroma-derived mature osteoblasts to neurons with Noggin or a demethylating agent. *Differentiation* 68, 235–244.

Martinez-de Luna, R.I., Moose, H.E., Kelly, L.E., Nekkalapudi, S. & El-Hodiri, H.M. (2010) Regulation of retinal homeobox gene transcription by cooperative activity among cis-elements. *Gene* 467, 13–24.

Mathers, P.H., Grinberg, A., Mahon, K.A. & Jamrich, M. (1997) The Rx homeobox gene is essential for vertebrate eye development. *Nature* 387, 603–607.

Mears, A.J., Kondo, M., Swain, P.K., Takada, Y., Bush, R.A., Saunders, T.L., Sieving, P.A. & Swaroop, A. (2001) Nrl is required for rod photoreceptor development. *Nat. Genet.* 29, 447–452.

Morrow, E.M., Furukawa, T., Lee, J.E. & Cepko, C.L. (1999) NeuroD regulates multiple functions in the developing neural retina in rodent. *Development* 126, 23–36.

Nakano, T., Ando, S., Takata, N., Kawada, M., Muguruma, K., Sekiguchi, K., Saito, K., Yonemura, S., Eiraku, M. & Sasai, Y. (2012) Self-formation of optic cups and storable stratified neural retina from human ESCs. *Cell Stem Cell* 10, 771–785.

Nishida, A., Furukawa, A., Koike, C., Tano, Y., Aizawa, S., Matsuo, I. & Furukawa, T. (2003) Otx2 homeobox gene controls retinal photoreceptor cell fate and pineal gland development. Nat. Neurosci. 6, 1255–1263.

Omori, Y., Katoh, K., Sato, S., Muranishi, Y., Chaya, T., Onishi, A., Minami, T., Fujikado, T. & Furukawa, T. (2011) Analysis of transcriptional regulatory pathways of photoreceptor genes by expression profiling of the Otx2-deficient retina. PLoS ONE 6, e19685.

Ono, Y., Wang, Y., Suzuki, H., Okamoto, S., Ikeda, Y., Murata, M., Poncz, M. & Matsubara, Y. (2012) Induction of functional platelets from mouse and human fibroblasts by p45NF-E2/Maf. Blood 120, 3812–3821.

Osakada, F., Ikeda, H., Mandai, M., Wataya, T., Watanabe, K., Yoshimura, N., Akaike, A., Sasai, Y. & Takahashi, M. (2008) Toward the generation of rod and cone photoreceptors from mouse, monkey and human embryonic stem cells. Nat. Biotechnol. 26, 215–224.

Radtke, N.D., Aramant, R.B., Seiler, M.J., Petry, H.M. & Pidwell, D. (2004) Vision change after sheet transplant of fetal retina with retinal pigment epithelium to a patient with retinitis pigmentosa. Arch. Ophthalmol. 122, 1159–1165.

Seko, Y., Azuma, N., Kaneda, M., Nakatani, K., Miyagawa, Y., Noshiro, Y., Kurokawa, R., Okano, H. & Umezawa, A. (2012) Derivation of human differential photoreceptor-like cells from the iris by defined combinations of CRX, RX and NEUROD. PLoS ONE 7, e35611.

Takahashi, K. & Yamanaka, S. (2006) Induction of pluripotent stem cells from mouse embryonic and adult fibroblast cultures by defined factors. Cell 126, 663–676.

Takeuchi, J.K. & Bruneau, B.G. (2009) Directed transdifferentiation of mouse mesoderm to heart tissue by defined factors. Nature 459, 708–711.

Tanaka, A., Woltjen, K., Miyake, K. et al. (2013) Efficient and reproducible myogenic differentiation from human iPS cells: prospects for modeling miyoshi myopathy in vitro. PLoS ONE 8, e61540.

Vierbuchen, T., Ostermeier, A., Pang, Z.P., Kokubu, Y., Sudhof, T.C. & Wernig, M. (2010) Direct conversion of fibroblasts to functional neurons by defined factors. Nature 463, 1035–1041.

Zhou, Q., Brown, J., Kanarek, A., Rajagopal, J. & Melton, D.A. (2008) In vivo reprogramming of adult pancreatic exocrine cells to beta-cells. Nature 455, 627–632.

Received: 17 July 2013
Accepted: 26 November 2013

Supporting Information

Additional Supporting Information may be found in the online version of this article at the publisher's web site:

Figure S1 Categorization of the genes differentially expressed in induced photoreceptor cells from human dermal fibroblasts (CRNO-Fib versus CRN-Fib).

Figure S2 Method for analysis of light responses.

Table S1 List of the enriched GO term (corrected P-value < 0.01) for Fig. 4A

Table S2 Up-regulated retina-related genes both in the CRNO-infected fibroblasts and in CRN-infected iris-derived cells (signal ratio ≥ 2.0 for 'up')

SCIENTIFIC
REPORTS

OPEN

Generation of retinal ganglion cells with functional axons from human induced pluripotent stem cells

Taku Tanaka[1]*, Tadashi Yokoi[1]*, Fuminobu Tamalu[2], Shu-Ichi Watanabe[2], Sachiko Nishina[1]
& Noriyuki Azuma[1]

[1]Department of Ophthalmology and Laboratory of Cell Biology, National Centre for Child Health and Development, Tokyo, Japan,
[2]Department of Physiology, Faculty of Medicine, Saitama Medical University, Saitama, Japan.

SUBJECT AREAS:
RETINA
DIFFERENTIATION
STEM-CELL DIFFERENTIATION

Received
22 September 2014

Accepted
15 January 2015

Published
10 February 2015

Correspondence and requests for materials should be addressed to N.A. (azuma-n@ncchd.go.jp)

* These authors contributed equally to this work.

We generated self-induced retinal ganglion cells (RGCs) with functional axons from human induced pluripotent stem cells. After development of the optic vesicle from the induced stem cell embryoid body in three-dimensional culture, conversion to two-dimensional culture, achieved by supplementation with BDNF, resulted in differentiation of RGCs at a rate of nearly 90% as indicated by a marginal subregion of an extruded clump of cells, suggesting the formation of an optic vesicle. Axons extended radially from the margin of the clump. Induced RGCs expressed specific markers, such as Brn3b and Math5, as assessed using by quantitative PCR and immunohistochemistry. The long, prominent axons contained neurofilaments and tau and exhibited anterograde axonal transport and sodium-dependent action potentials. The ability to generate RGCs with functional axons uniformly and at a high rate may contribute to both basic and clinical science, including embryology, neurology, pathognomy, and treatment of various optic nerve diseases that threaten vision.

Retinal disorders are an important cause of blindness throughout the world[1,2]. Of the various types of retinal cells, photoreceptors and ganglion cells are primarily affected by retinal disorders; photoreceptors are generally affected by retinitis pigmentosa and retinal dystrophy[3,4], while ganglion cells are generally affected by optic neuropathy and glaucoma[5]. Research aimed at achieving regeneration of the diseased retina has identified several candidate structures that contain precursors of key retinal cells, including the iris[6,7], ciliary epithelium[8], and Muller glial cells[9,10]. Two dimensional (2D) cell culture methods have been employed in this work; however, efficient regeneration of photoreceptors and the other retinal cells has not been achieved without application of exogenous factors that relate to retinal morphogenesis[11–13], whereas self-induction by endogenous factors would have been ideal. The establishment of embryonic stem cell (ESC) and induced pluripotent stem cell (iPSC) technologies has recently allowed further advances in the generation of retinal cells.

The development of three-dimensional (3D) culture systems has led to more advanced work on differentiation of neural tissues from ESs and iPSCs, facilitating self-organisation of brain cortical tissue[14], the pituitary gland[15], and the retina starting from mouse and human ESCs[16,17]. First, the optic vesicle and continuous optic cup, which are two early developmental stages of the eyeball, were generated from ESC embryoid bodies. These tissues were then cut with scissors and continuously incubated in a floating culture system under a high-oxygen atmosphere, resulting in self-induction of almost all retinal layers[15,16], including the ganglion cell and photoreceptor cell layers. In further advancements to this method, all layers of the murine retina were generated from ESCs and iPSCs, and retinal sheets were successfully transplanted into the subretinal space of mice with advanced retinal degeneration (rd1), which lacked the outer nuclear layer of the retina[18].

Another series of 3D culture systems has been developed, enabling generation of the 3D retinal structure, including retinal ganglion cell and photoreceptor cell layers. In the primary experiment, adherent human embryonic stem cells and iPS cells were picked up mechanically and transferred to floating culture to be induced into an optic vesicle (OV)-like structure with retinal precursor characteristics. This structure was then reattached to a 2D culture dish, where it differentiated into the retinal cell lineage[19,20]. In subsequent experiments in 3D culture systems, the entire retinal layer, including the retinal ganglion cell layer and functional photoreceptors, was established from human iPSCs mainly using intrinsic cues[21] and addition of small amounts of exogenous factors, as reported in previous studies[22–26]. In this experiment, an OV-like structure was directly differentiated into a retina without the process of optic cup formation. There is a critical difference between these two major methods; in the former, the OV-like structures were extruded from the embryoid body, while in the latter, aggregates of human iPSCs or ESCs were directly induced into OV-like structures. In both methods[17,21], the entire retinal layer is regenerated, containing thick outer layers with well-differentiated photoreceptors and thin, immature inner layers comprised of RGCs. Moreover, the formation of RGC axons has not been realised using either 3D retinogenesis method.

The RGCs located in the ganglion cell layer of the retina typically have long axons, enabling them to connect the retina to various visual centres in the central nervous system, represented by the lateral geniculate body[27]. RGCs play roles in transmitting image-forming and non-image-forming visual information[28], processed by photoreceptors, horizontal cells, amacrine cells, and bipolar cells, to higher visual centres via converging non-myelinated nerve fibres in the retina that continue into the myelinated optic nerve. Thus, the long axons of RGCs are crucial to transmitting visual images from the retina to the brain.

However, although culture of isolated RGCs with tiny axons from animal and human retinas has been achieved by immunopanning methods[29–31], no study has reported the generation of RGCs exhibiting characteristic long, prominent axons in an in vitro culture system, with the exception of one report in which RGCs were developed from mouse iPSCs that carried an Atoh/Math5 lineage reporter[32] and another report in which almost 30% of attached aggregates of RGCs derived from human iPSCs exhibited elongated axons with action potentials[33].

Here, we describe a novel in vitro method that generated RGCs with long, functioning axons exhibiting action potentials and axonal transport, by combining cultivation of 3D floating aggregates with a subsequent 2D adhesion culture. This advance may facilitate both basic research on RGCs and translational research aimed at finding treatments for retinal diseases.

Results

Protocol for self-induction of RGCs from human iPSCs. For purposes of generating RGCs, we modified a previously established[17] 3D retinal regeneration protocol (Fig. 1). This method called for addition of both foetal bovine serum (FBS) and Matrigel to the culture medium; these components were not required by other protocols[20,21], which also produced retinal cells efficiently. Therefore, we investigated the effects of FBS concentrations (1%–10%) on D12–18 and Matrigel concentrations (0.5%–2.0%) on D1–18. At all concentrations, embryoid bodies (EBs) were well organised, and OVs, which were maintained over the duration of the study, extruded from nearly 90% of the EBs (Table S1 and Fig. S1). In order to establish RGCs with long axons in a relatively short period, we changed the OV culture conditions from floating (3D) to dish (2D) to obtain cell attachment because the incipient ganglion cell layer was located on the surface of the OV. Initially, we severed the OVs from the EBs, which is predicted to lead to differentiation into neural retinal cells, as demonstrated previously[17]. However, maintenance of the cut OVs did not succeed, as documented in another report[34]. Therefore, we directly attached the OVs to the dish while still connected to the EBs, and the attached OVs were further differentiated into an extruded clump of cells on the dishes. Around 2 days after attachment, massive axonal growth from the margin of the clump was realised. The optimal timing of attachment was also evaluated. Attachment on D26–29 was ideal for elongation of axons from the marginal portion of the clump, which was thought to representthe RGC region (RGCR), while attachment prior to D24 or after D30 seemed suboptimal for efficient development of axons (Fig. S2). When retinoic acid was added 3 days prior to the attachment, axonal growth was promoted (Fig. S3); in contrast, if retinoic acid was continuously supplemented after adhesion, axons grew by around D32, but died back by around D40 (Fig. S4). Finally, following addition of BDNF (100 ng/mL) to promote neuronal survival beyond 3 days of retinoic acid administration, RGCs and their axons were stabilised until around D50 (Fig. S5).

The time course of expression of transcription factors and protein markers associated with retinal development. The OV is derived from the eye field in the forebrain, a process in which several transcription factors, called eye-field transcription factors, play principal roles[35]. The retinal homeobox gene, Rx, and the paired box gene 6, Pax6, which belong to this group of eye-field transcription factors, are crucial in early retinogenesis[36]. During the period of attachment of the cultured EB with its extruded OV to a dish, temporal gene expression analysis clearly revealed that upregulation of Rx began on D6, when the EB had maturely formed, and peaked on D18, when the OVs began to develop. This was followed by upregulation of its downstream target Pax6. Math5, the bHLH transcription factor, is expressed in post-mitotic retinal precursor cells under direct control by Pax6[37]. Math5 crucially regulates RGC formation, and Math5 mutant mice lack RGCs[38,39]. In humans, Math5 mutation results in optic nerve aplasia[40]. Brn3b, known as the most reliable RGC marker, is a member of the POU-domain family of transcription factors, and its expression is controlled by Math5[41]. Brn3b is believed to determine RGC fate by

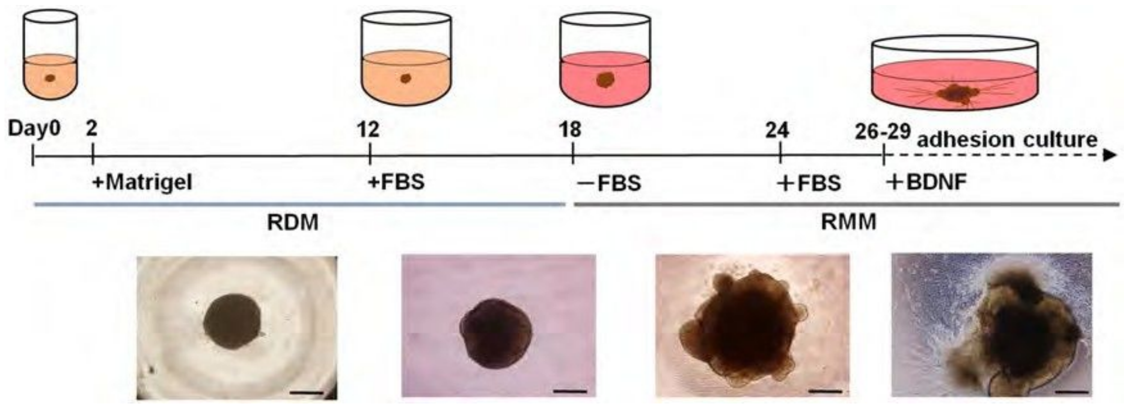

Figure 1 | Schematic diagram of the protocol for self-induction of retinal ganglion cells. This protocol consisted of a period of suspension culture (3D) followed by a period of adhesive culture (2D) and resulted in observation of axonal elongation from retinal ganglion cells (RGCs) from human iPSCs starting within 30 days. Two basal media, retinal differentiation medium (RDM) and retinal maturation medium (RDM) were used. Significant morphological changes occurred after a medium change from RDM to serum-free RMM on D18, at which point optic vesicles (OVs) appeared to extrude from the cultured cell aggregates. Beginning with the start of adhesive culture on D26–29, axons grew out radially from the mass of new RGC bodies. Phase contrast micrographs were taken on D6, D18, D24, and D30 and are shown in sequence from left to right. Scale bar, 500 mm.

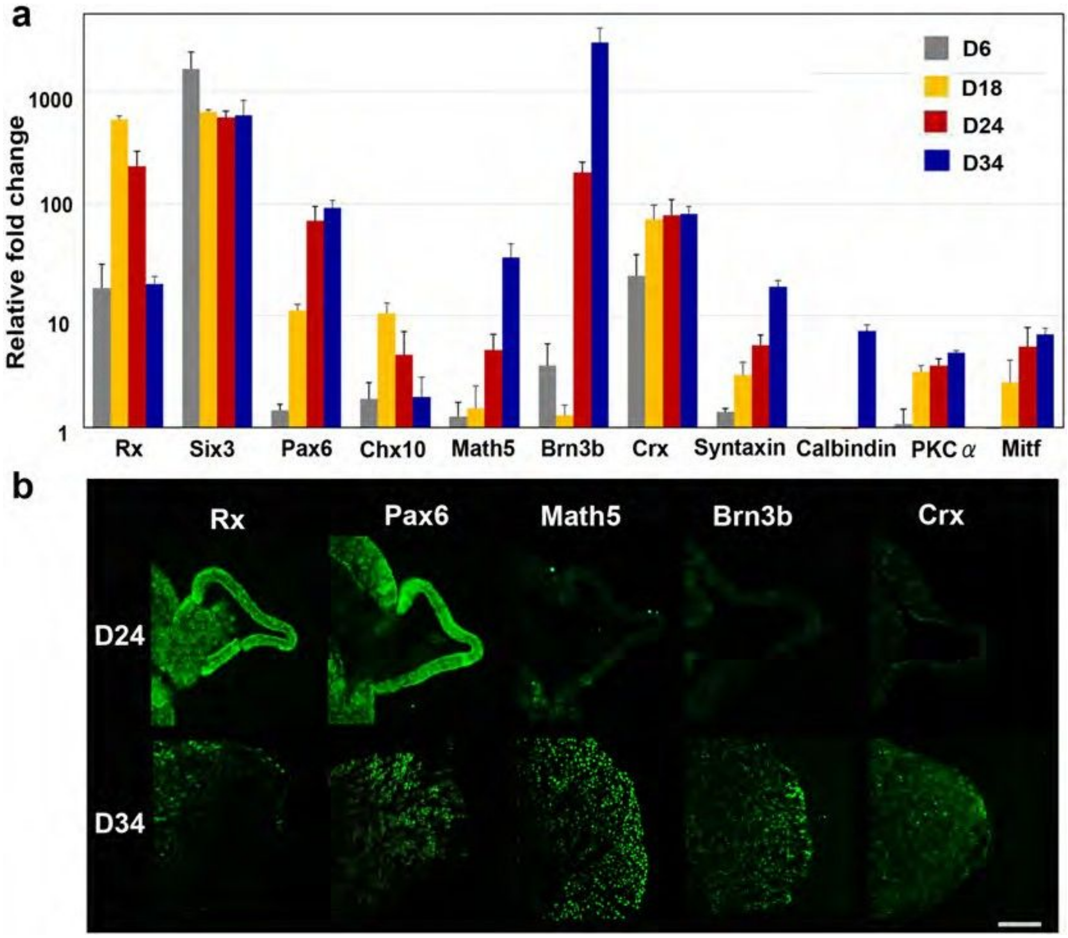

Figure 2 | Commitment of human iPSCs toward a retinal lineage and generation of retinal ganglion cells (RGCs). (a) The time-dependent expression of transcription factors involved in retinogenesis was examined. Expression changes during differentiation of iPSCs to RGCs as revealed by quantitative PCR. Total RNA was extracted on D6, D18, D24, and D34. Retinal progenitor markers, including Rx, Six3, and Pax6, were apparently expressed until D18. Brn3b, the RGC-specific marker, was upregulated in a sporadic manner, following an increase in the expression of Math5, the upstream regulator of Brn3b. Crx, the marker of the cone-rod photoreceptor precursor, could also be identified starting at D18. Syntaxin, the amacrine cell marker, gradually increased following increased Brn3b expression. Expression levels of calbindin, a marker of horizontal cells, and PKCa, a marker of bipolar cells, were quite low. The expression of Mitf, a master controller of retinal pigment epithelium differentiation, was suppressed, indicating that these cells were in the neural retinal lineage. Expression levels of mRNAs were first normalised to the expression of HPRT1 and then to the expression on D0 (the start day of suspension culture), which was set at 1.0. Error bars represent means 6 SDs of the samples from three independent experiments. The vertical axis is a base-two logarithmic scale. (b) Immunohistochemistry for Rx, Pax6, Brn3b, Math5, and Crx in the optic vesicle (OV) on the floating EB on D24 and in extrusions of cell clumps that differentiated from the OVs after attachment of the EBs on D34, using each serial section. Rx and Pax6 were expressed in the OV and the extruded clump of cells. Positive immunostaining for Brn3b and Math5, the most specific markers for RGCs, was observed not in the OV, but was observed in the clump and was localised to the outer margin of the clump. Crx, a marker for primitive photoreceptors, was not expressed in the OV but was faintly expressed in the clump. Scale bar, 100 mm.

acting as a repressor of differentiation to non-RGC cell types[42], a process in which Islet1, an LIM-homeodomain factor, acts as a coregulator[43]. In our experiments, expression of Brn3b was relatively low until D18 and then dramatically increased until D24, when the OVs were well developed from the floating EBs following an increase in Math5 expression. Chx10 is associated with the proliferation of retinal progenitor cells. It is initially expressed in all retinal progenitors, but later is restricted to bipolar cells[44]. In our experiments, expression of Chx10 became apparent at D18 and was maintaineduntil at least D34, when RGCs and axons developed after attachment of the EB. Crx, a cone-rod-containing gene, shows restricted expression in premature and mature cells of photoreceptor lineage[45,46]. Crx expression was also first observed at D18, following Chx10 expression. Amacrine cells start to differentiate immediately after RGC differentiation[47]. In our experiments, syntaxin, an amacrine cell marker[48,49], showed delayed expression following Brn3b expression. The markers associated with horizontal and bipolar cells, both of which develop at later stages of retinogenesis, showed little expression until D34. The time course of gene expression was quite consistent with that in human retinogenesis. Mitf, a microphthalmia-associated transcription factor and the master regulator of melanocyte and retinal pigment epithelium (RPE) development[50], was not highly expressed in the present study, suggesting that our induction protocol induced human iPSCs into the neural retinal lineage but not into the RPE lineage (Fig. 2a).

Immunohistochemistry also showed expression of Rx and Pax6 in both OVs and the clump, while expression of Brn3b and Math5 was observed only in the clump, localised within the margins of the clump. In contrast, low expression ofCrx was observed withinthe clump (Fig. 2b). Calbindin and PKCa were not detected in either the OV or the clump (Fig. S6).

Structure of human iPSC-derived RGCs by light and electron microscopy. We investigated the structure of the RGCs by light

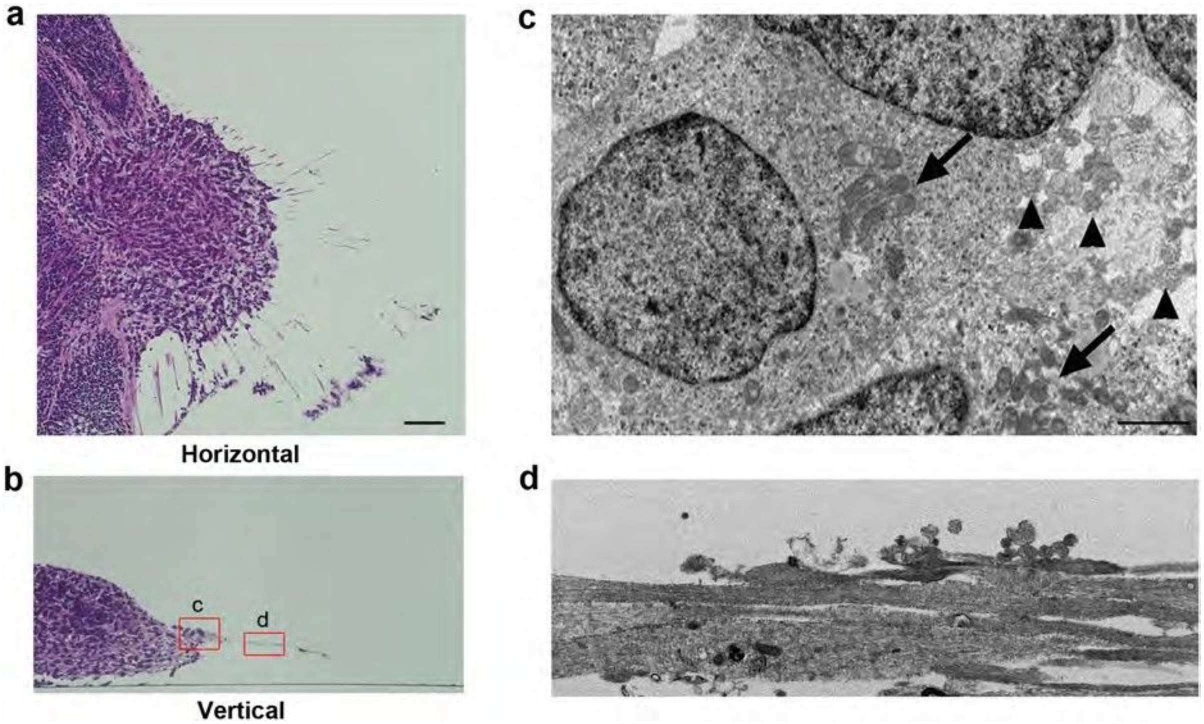

Figure 3 | Light and electron microscopy of induced retinal ganglion cells and their axons. Horizontal (a) and vertical (b) sections stained with haematoxylin and eosin showed that axons radiated from the outer margin of the clump of cells corresponding to the optic vesicle (OV), which extruded from the embryoid body late in 3D culture. Somata of new retinal ganglion cells (RGCs) were present in the marginal portion of the extruded clump and showed variations in size and relatively large nuclei, some of which has Nissl's body characteristics of RGCs, while the main part of the embryoid body (MBEB) contained many irregular rosettes. (c) Electron microscopy analysis of the square portion (c) in panel (b) revealed that cell bodies of RGCs contained prominent rough endoplasmic reticulum (arrows) and that axons (arrowheads) developed from a portion of the axon hillock. (d) Electron microscopy analysis of the square portion (d) in panel (b) revealed straight axons of varied calibre, ranging in diameter from 0.5 to 2 mm and lacking myelination. The axons contained numerous neurotubules. Scale bars, 80 mm in panels (a) and (b); 5 mm in panels (c) and (d).

and electron microscopy. After the OV became attached around D26–29, it became complanate, filled with cells, and showed radiation of numerous axons from the outer margin at the dish surface. The cells in the clump were apparently different from those in the main body of the EB, which was filled with small round cells. The cells in the clump showed relatively large cell bodies (range: 16.1–23.6 mm; average: 21.6 mm, n 5 10) with clear cytoplasms and nuclei and spindle-shaped or round cell bodies, sometimes accompanied by a prominent axon. These findings were identical to those of RGCs in vivo, whose cell body sizes ranged from 12 to 25 mm[51]. Notably, several cells located peripheral to the structure had Nissl bodies (Fig. S7), which is considered characteristic of RGCs[52]. However, Nissl bodies were not detected in other types of cells, including those in rosettes. The axons were eosinophilic, had few branches, and grew radially from the clump (Fig. 3a, b).

Electron microscopy of D35 specimens demonstrated that the RGCs, which had axons, seemed to be relatively large (range: 16.0–24.1 mm; average: 20.6 mm, n 5 10) and were stratified at the margin of the clump. These RGCs contained prominent rough endoplasmic reticulum, which represented the Nissl bodies that were observed by light microscopy. The axons developed from the axon hillock, which exhibited a characteristic conical cell body with neurotubules but no rough endoplasmic reticulum (Fig. 3c), which have also been detected in RGCs in vivo[53,54] and define the end of the soma of neurons. The axons contained numerous neurotubules. The diameters of the axons varied (range: 1.7–2.2 mm; average: 1.8 mm, n 5 10), and the axons were not myelinated (Fig. 3d). These findings were identical to those of axons in the retinal nerve fibre layer and in the optic nerve anterior to the lamina cribrosa, whose diameters range from 0.6 to 2.0 mm[51].

Determination of RGC lineages. To confirm that the cells with axons in the margin of the clump differentiated from the OV were RGCs, we examined the expression and distribution of typical markers associated with RGCs. Real-time PCR revealed a more than 30-fold increase in the expression of Brn3b, Math5, Islet1, c-synuclein (Sncg), and Tuj1. Brn3b, the most specific marker in this group, showed a nearly 3,000-fold increase in expression at D34 compared with D1 (Fig. 4a). Immunohistochemistry showed positive staining for all markers except Tuj1 in the marginal portion of the clump, which was therefore thought to be the incipient RGC layer. Math5, an upstream transcription factor for Brn3b, and Sncg, another RGC marker and contributor to neurofilament integration[55], showed similar distributions in the marginal portion of the clump. Islet1, a marker of RGCs and amacrine cells, was positive both in the margin and further toward the interior of the clump, suggesting that amacrine cells also developed there. Notably, Brn3b-positive cells apparently localised to the outermost margin of the clump at the surface of the dish, which strongly indicated that the margin was the RGCR and that the long radial axons originated from the RGCR. The costaining of Brn3b and Tuj1 demonstrated that the axons originated from the Brn3b-positive cells (Fig. 4b).

Sectional gene expression associated with RGCs and other retinal cells. For further confirmation of the presence of localised RGCs in the supposed RGCR, we mechanically divided the adherent structural complex into three parts: the RGCR, OVR, and MBEB (Fig. 5a). Notably, Brn3b showed nearly four-fold higher expression in the RGCR than that in the MBEB. In addition, Crx expression was strongly suppressed in the RGCR. These results obviously demonstrated that the RGCR was highly specified into

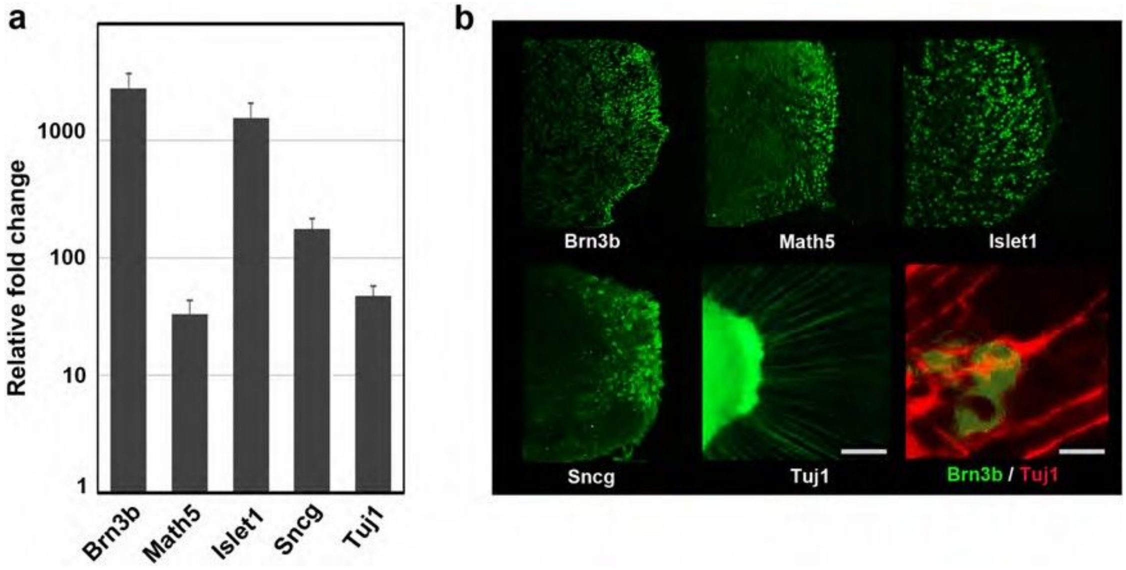

Figure 4 | Expression of characteristic markers related to retinal ganglion cells. The expression levels of representative retinal ganglion cell (RGC) markers, Brn3b, Math5, Islet1, c-synuclein (Sncg), and b3-tubulin (Tuj1), were examined. (a) Quantitative PCR analysis of total RNA extracted on D34 was used. All markers associated with the RGC lineage were obviously upregulated more than 30-fold. In particular, the mRNA levels of Brn3b and Islet1 were increased dramatically. The mRNA expression levels were first normalised to HPRT1 expression and then to mRNA expression on D0. Error bars represent means 6 SDs of three samples. The vertical axis was a base-two logarithmic scale. (b) Immunohistochemistry for Brn3b, Math5, Islet1, Sncg, and Tuj1 on D34. Whole mount staining for Tuj1 and serial section staining for the other targets were analysed. Positive immunostaining for Brn3b and Math5, the most specific markers for RGCs, was localised to the outer margin of the extrusion that differentiated from the optic vesicle. Sncg, a marker for RGCs, and Islet1, a marker for RGCs and amacrine cells, were expressed in the inner part of the clump. Axons were strongly positive for Tuj1, and the axons were confirmed to grow from Brn3b-positive cells. Scale bar, 100 mm. Scale bar for the double staining of Brn3b and Tuj1, 10 mm.

the ganglion cell lineage. Islet1 (a marker for ganglion and amacrine cells) was also up regulated in both the RGCR and OVR, which was consistent with the distribution of Islet1 expression confirmed by immunostaining (Fig. 5b). We also noticed that the isolated RGCR survived for approximately 10 days after separation from the OVR, which suggests that mechanical purification of RGCs is possible after growth of abundant axons.

RGC axon-related protein expression and determination of types of neurofilament proteins in early retinal gangliogenesis. To confirm that the apparent axons emanating from the RGCR resembled typical axons, we used tau and neurofilament (NF) immunostaining (Fig. 6b). The time-series expression of all NF components—neurofilament-light (NFL), neurofilament-medium (NFM), and neurofilament-heavy (NFH)—was studied in parallel

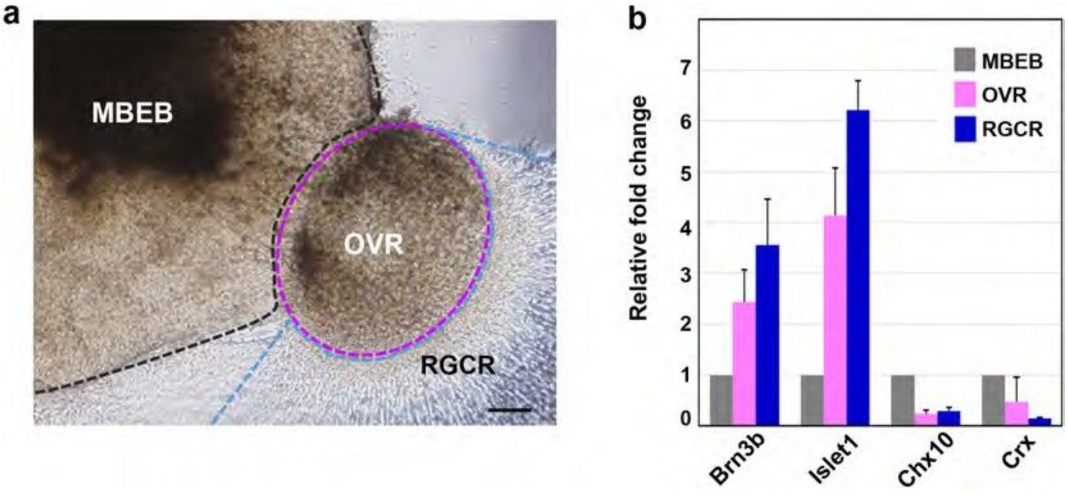

Figure 5 | Regional differentiation of retinal ganglion cells detected by RT-PCR. (a) Each colony on D34 was mechanically divided into three regions, namely the main body of the embryoid body (MBEB), the extruded clump of cells differentiated from the optic vesicle except for its marginal part (OVR; optic vesicle region), and the retinal ganglion cell region (RGCR). The latter was comprised of the marginal layer of the extrusion and the axons. (b) The gene expression of neural retinal markers in each region was investigated by quantitative PCR analysis. Analysed markers included Brn3b (RGCs), Islet1 (RGCs, amacrine cells), Crx (photoreceptors), and Chx10 (neural retina progenitor and bipolar cells). The RGCR showed high expression of Brn3b compared with the other two regions, but lacked Crx expression, suggesting that the RGCR was specifically differentiated into the RGC lineage. The mRNA expression levels were first normalised to HPRT1 expression and then to mRNA expression levels on D0. Error bars represent means 6 SDs of three samples from three independent experiments. Scale bar, 100 mm.

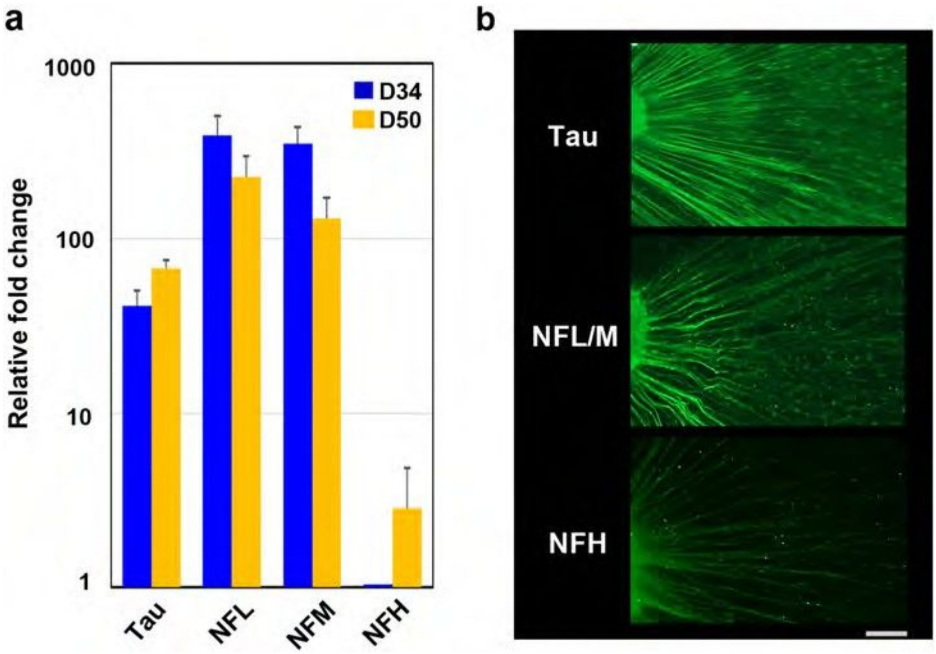

Figure 6 | Cytoskeleton in axons elongated from retinal ganglion cells. (a) Quantitative PCR analysis was applied to investigate nerve fibre markers, including neurofilament (NF) light (NFL), NF middle (NFM), NF heavy (NFH), and tau, using total RNA extracted on D34 and D50. The expression of each marker, including NFL, NFM, and tau, was already high at D34, while that for NFH was increased on D50 compared with D34, probably a reflection of axonal maturation. (b) Immunohistochemistry clearly showed positive staining in all axons for NFL, NFM, and tau at D34 and D50 and for NFH at D50. The mRNA expression levels were first normalised to HPRT1 expression and then to the mRNA expression levels of NFH on D34. Scale bar, 100 mm.

(Fig. 6a). Microtubules, NFs, microtubule-associated proteins (MAPs), and actin play crucial roles in axonal development[56]. Tau, which is a MAP, contributes to polymerisation, stabilisation, and organisation of microtubules and promotes axonal growth and effective axonal transport[57]. Once tau is hyperphosphorylated, the axonal transport process and cell survival of RGCs are compromised[58]. The axons detected in our study were clearly stained for tau and associated with evidence of axonal transport. NFs are the intermediate filaments of neurons and are especially abundant in CNS axons, where they occur as heteropolymers made up of four subunits, namely NFL, NFM, NFH, and a-internexin[59]. NFs have essential roles in radial axonal growth and maintenance of axon calibre, therefore mediating the ability to transmit action potentials[60]. Both NFL and NFM appear early in retinogenesis, while synthesis of NFH is delayed[61]. In our experiments, NFL and NFM were already highly expressed at D34 and expression continued until D50, while expression of NFH was quite low at D34 and gradually increased until D50. Specimens from D34 showed positive staining for NFL/M but weak staining for NFH, in agreement with the expression time series study. We observed temporally varying gene expression not only of transcription factors but also of genes associated with structural components of RGCs.

Axonal transport in human iPSC-derived RGCs. To establish axonal function, we tested for axonal transport in the apparent axons that radiated from the RGCR. Axonal transport showed two characteristic flows, slow and fast, both of which had anterograde and retrograde components. RGCs and their axons are known to be rich in mitochondria and to maintain homeostasis by axonal transport, as in other neurons. Neurotrophic tyrosine kinase receptor 1 (NTRK1), a member of the neurotrophic tyrosine kinase receptor family, is the receptor for nerve growth factor and is expressed in RGCs, especially when the cells are damaged[62–64]. Using NTRK1 and mitochondria as tracers, we directly introduced plasmid vectors composed of GFP-NTRK1 with a CMV promoter and mCherry-mitochondria with a CMV promoter into the cell body of RGCs around D34 by electroporation to analyse anterograde rapid axonal transport. Several axons demonstrated anterograde axonal transport after approximately 7–10 h post-introduction. The cell bodies corresponding to these axons expressed these factors as well (Fig. 7a).

To detect a time series of axonal transport, Alexa-Fluo-555 conjugated cholera toxin B, which is also known as a tracer of axonal transport[58], was administrated. Slow and fast anterograde axonal flow were clearly observed by injection of the toxin into RGCR (Fig. 7b, Fig. S8, Supplemental Video 1). The transport was blocked by an addition of 1 mM colchicine (Fig. S9, Supplemental Video S2 and S3).

Human iPS cell-derived RGCs showed neuronal excitability. To determine whether iPSC-derived RGCs could generate action potentials, we examined the RGCs in the RGCR (Fig. 8a). The RGCs each had a long axon process extending to the filter paper side and possessed some dendritic processes (Fig. 8b). Electrophysiological analysis of cells with an axon process revealed repetitive action potentials in response to current injection through the recording pipette in current clamp mode (4 of 5 cells; Fig. 8c). The resting membrane potential and the amplitude of the first action potential were 281.8 6 26.8 mV and 56.8 6 24.6 mV, respectively (n 5 4). The cells that generated action potentials exhibited tetrodotoxin (TTX)-sensitive sodium-dependent currents with a maximum amplitude of 1,248 6 573 pA (n 5 4), followed by outward currents (Fig. 8d).

Discussion

In this study, we generated RGCs with functioning axons from human iPSCs. The present quantitative PCR and immunohistochemistry results showed a gene expression profile and protein markers characteristic of RGCs, including Brn3b, Math5, Islet1, Sncg, and Tuj1. RGCs induced from ESCs and iPSCs in previous studies carried markers characteristic of RGCs[17,21,65], but were not accompanied by long axons. RGCs have also been generated in 3D culture

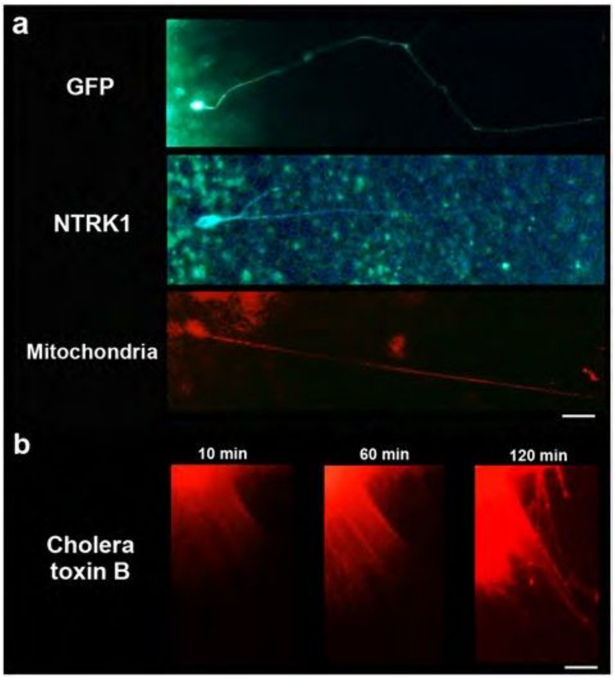

Figure 7 | Axonal transport in retinal ganglion cells. (a) Axonal transport was investigated for investigation of anterograde rapid flow employing NTRK1 and mitochondrial expression vectors. GFP was also used as a control. Plasmid vectors that carried each of these substances as well as the CMV promoter were directly introduced into the cell body using electroporation around D34. At approximately 7–10 h post-introduction, GFP expression was observed, which indicated that effective introduction of vectors by electroporation had been obtained. NTRK1 and mitochondria were identified in the cell body and in the axon, the latter location indicating anterograde rapid axonal transport. Scale bar, 80 mm. (b) A time series of axonal transport was also confirmed by the injection of Alexa-Fluo-555 conjugated cholera toxin B into retinal ganglion cell region. Cholera toxin was transported from the cell body to the peripheral area of axons by anterograde flow within approximately 2 h after injection. Scale bar, 100 mm.

systems, but without observation of the axons that would be expected with formation of the nerve fibre layers of the retina and the nerve fibre bundle of the optic nerve. In contrast, RGCs observed in the present study had long, prominent axons expressing NFs, Tuj1, and tau and growing in straight lines on the culture plate. The functionality of the axons was demonstrated by observation of axonal flow and action potentials. Anterograde axonal transport was identified by induction of both NTRK1- and mitochondria-specific vital stains and cholera toxin B into cell bodies. Sodium-dependent action potentials were demonstrated by patch clamp techniques.

RGCs were generated mostly in an OV-like clump of cells extruded from an EB where the layers of neural retina were supposed to differentiate. Most RGCs were localised to the marginal portion of the clump that adhered to the bottom of the culture dish. Because RGCs in vertebrates are located in the most anterior layer of the retina, which coincides with the marginal portion of the OV and optic cup in both embryogenesis and in previously established 3D culture systems, it is not surprising that our RGCs differentiated specifically at the surface of the clump, the inner portion of which may be an agglomerate of other retinal cell types. Relatively large cells with prominent nuclei, consistent with RGC morphology, were stratified at the marginal portion of the clump and were positive for Brn3b, the most specific marker for RGCs. Sectional analysis of RNA expression also confirmed that Brn3b expression was highest at the marginal portion of the clump without accompanying Crx expression, implying that the marginal portion of the clump had been specified purely into RGCs. This marginal portion, the RGCR, was able to survive for several weeks separated from the parent clump of cells (Fig. S3), suggesting the possibility of mechanically purifying RGCs for use in further investigations. Retinal cell determination progresses via a well-organised spatio-temporal pattern, in which RGCs appear initially and are followed by amacrine cells, photoreceptors, horizontal cells, bipolar cells, and Muller cells, a process that is highly conserved among species[47,66]In monkeys, RGC development begins around D25[67], and Brn3b, a characteristic transcriptional factor, is expressed in the retina of the human foetus at least by 8 weeks of gestation[68]. Thus, the timing of the marker expression and development of RGCs in our experiment resembles the process of the genesis of RGCs in vivo.

The axonal growth pattern differs significantly between 2D (on-dish) and 3D cultures. Two-dimensional culture methods for CNS neurons, including hippocampal[69], cortical[70,71], and hypothalamic cells[72,73], have been well established. These primary cultures can be augmented by coating the bottom of the culture dish with extracellular matrix components, including laminin, fibronectin, cadherin, and collagen, through which axons can extend[74]. In addition, neuroprotective agents, including BDNF[75,76], nerve growth factor[77], and CTNF[78,79], can easily be provided to the cells uniformly by adding them to the culture medium to further support neuron and axonal growth.

In contrast, the 3D culture approach has recently achieved in vitro organogenesis of CNS structures[80,81], including the retina[16,17,34], the pituitary gland[15] and heterogeneous neural tissue[82], in which axons generally extend into an extracellular matrix gel that contains collagen, fibronectin, or cadherin. Although 3D-cultured neurons seem more suitable for investigating stratified structures, branching, and synaptogenesis, the formation of long axons has not been obtained by previous 3D culture methods for retinogenesis. Achieving differentiation to normal RGCs by these methods may be too challenging because the surface of the self-induced retina directly contacts homogeneous culture fluid, which contains no extracellular matrix geometries capable of providing a foothold for horizontal extension of axons from RGCs. Expecting to achieve targeted horizontal extension of axons along the surface of the retina towards the optic nerve head, probably guided by extracellular signals such as Shh, BMP, and BDNF[83], would be even more difficult because self-induced retinas lack both the optic stalk and the nerve head.

Even in the environment of 2D culture where concentrations of multiple growth factors can be reliably controlled, neither self-induction of retinal layers nor prominent outgrowth of axons from RGCs have been achieved thus far. In the present study, axons extended from RGC bodies in response to a switch of the culture method from 3D to 2D at an optimal time, when the polarity and location of the new RGCs had just been determined. Supplementation with BDNF, a protective agent for RGCs, further supported axon growth. These spatio-temporal steps may be requirements for axon growth from RGCs. However, development of axons by a purely 3D culture method merits further research. RGC axons grown by the 3D to 2D culture method we established were formed uniformly, at a high rate, and in a short time and may contribute to various endeavours in basic and clinical science on human RGCs. For example, embryogenesis, nerve path finding, synaptogenesis, and interactions between nerve and glial cells in coculture may be easily investigated in vitro.

Our RGCs, which possessed long axons, also provided an excellent tool for investigating the pathogenesis and pathophysiology of optic nerve diseases. The optic nerve is composed of some 800,000–1,000,000 RGC axons[51] and can be anterogradely or retrogradely damaged by various crises, including ischemia, infection, trauma, inflammation, tumours, and genetic disorders. These can result in cell death and clinically severe visual impairment or blindness, such

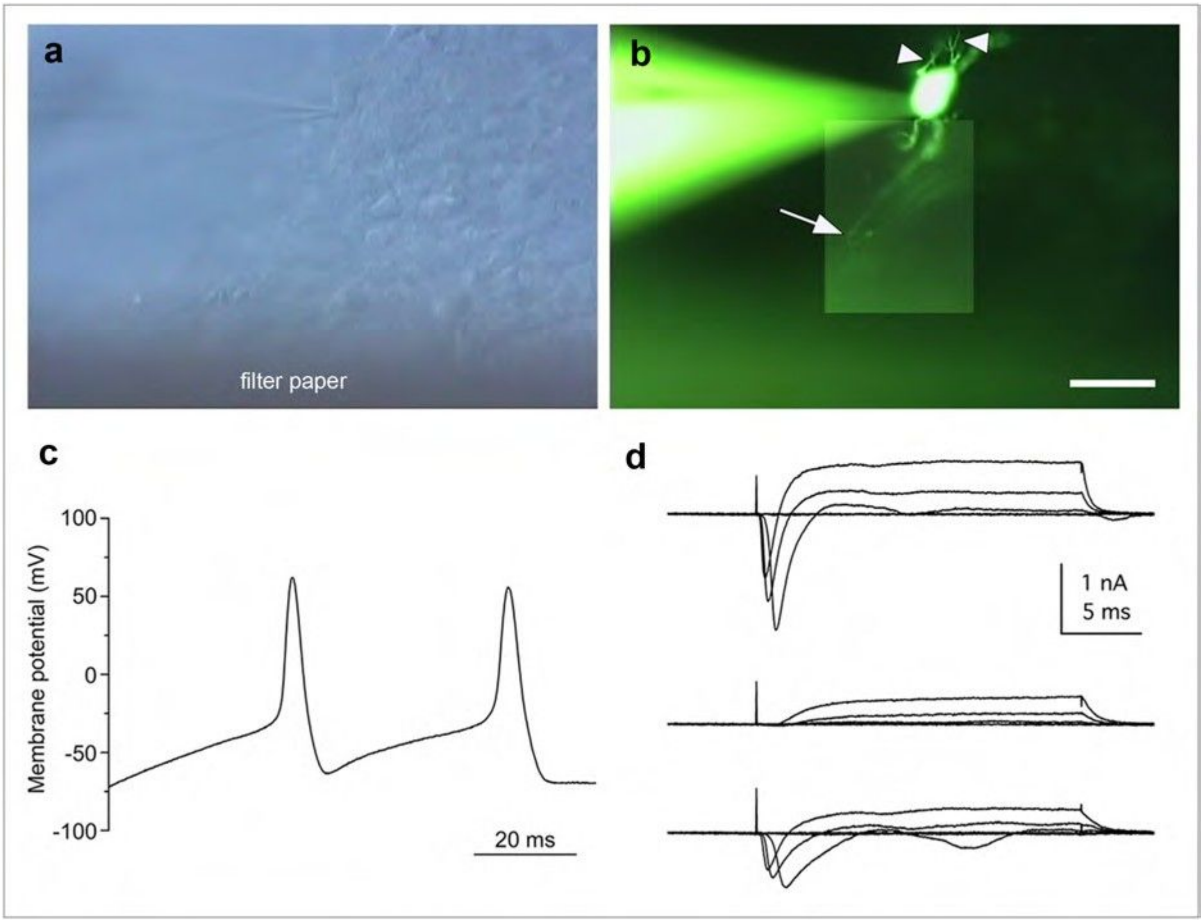

Figure 8 | Action potentials of the retinal ganglion cells. (a) Slice preparation of the cultured colony with recording electrode under DIC optics. (b) Composite photograph of an iPS cell-derived retinal ganglion cell filled with LY under fluorescence illumination. This cell exhibited some dendritic processes (arrowheads) and an axonal process (arrow). The same field is shown in (a) and (b). (c) Whole-cell recording of the retinal ganglion cells revealed action potentials in current-clamp mode (current injection of 60 pA). (d) A family of currents was recorded in voltage clamp mode in response to depolarising steps from a holding potential of 271 mV to target voltages increasing from 241 to 119 mV in 20-mV increments (upper traces). The fast inward currents were blocked by TTX (middle traces) and were recovered by washing (lower traces). Action potentials and inward currents were recorded from the LY-labelled cell shown in panel (b). Scale bar in panel (b), 30 mm.

as glaucoma. Glaucoma, a disease caused by high intraocular pressure, is an important cause of blindness globally. The pathogenesis and pathophysiology of many diseases associated with RGCs remain to be elucidated because of the difficulty of clinical examination of the deepest portions of the eyeball. RGCs induced by iPSCs derived from patients with RGC-associated diseases, especially genetic diseases, may further our understanding of the underlying molecular mechanisms of pathogenesis and pathophysiology. Precedents for this are already documented for other neurodegenerative diseases, including Parkinson' disease and Alzheimer's disease[84,85]. Moreover, the efficacy and toxicity of drugs for neuroprotection and support of axonal outgrowth and regeneration relevant to human RGC-associated diseases could be examined in vitro with our system with far more ease, accuracy, and safety than in the era of animal models. Indeed, an in vitro clinical study relevant to cardiac disease has already started[86,87]. In addition, future therapies involving isolation of human RGCs for transplantation to repair damaged optic nerves may benefit from our method, though several issues remain to be elucidated, including how to induce complex axonal projection patterns and synaptogenesis in the CNS target areas.

Methods

Ethical statement. The Ethics Committee of the National Institute for Child and Health Development (NCCHD) approved all experimental protocols (approval number #686, July 3, 2013). All experiments handling human cells and tissues were carried out in accordance with the Tenets of the Declaration of Helsinki.

Human iPSC culture. Human iPSCs (HPS0007_409B2 cell passage 29) were obtained from RIKEN BRC (Japan) and were maintained on a feeder layer of mouse embryonic fibroblasts (MEFs) inactivated by irradiation in Primate ES medium (ReproCELL) supplemented with 10 ng/mL recombinant human basic fibroblast growth factor (bFGF; Invitrogen, Carlsbad, CA, USA). For passaging, hiPSC colonies were detached and recovered from the feeder layer by treatment with dissociation solution (ReproCELL) at 37uC for 8 min. The detached hiPSC clumps were broken into smaller pieces consisting of several tens of cells by gentle pipetting. Cell passaging was performed at a 153 to 154 split ratio.

Induction of differentiation to RGCs. The induction of hiPSC differentiation employed a procedure based on SFEB methods[17]. hiPSCs were dissociated to single cells in TrypLE Express (Invitrogen) containing DNase I (0.05 mg/mL; Roche) and Y-27632 (10 mM; Wako) and were resuspended in retinal differentiation medium (RDM; G-MEM supplemented with 20% KSR, 0.1 mM nonessential amino acids, 1 mM pyruvate, 0.1 mM 2-mercaptoethanol, 100 U/mL penicillin, and 100 mg/mL streptomycin) containing Y-27636 and IWR-1e (20 and 3 mM, respectively; Merck Millipore). After separation from the feeder cells by decantation (the feeder cells adhered to the gelatine-coated bottom of the dish), the floating hiPSCs collected from the medium were seeded into V-bottomed low-cell-adhesion 96-well plates (Sumitomo Bakelite) at 9,000 cells per well. Matrigel (growth factor-reduced; BD Bioscience) was added to a final concentration of 0.5%–2% in the medium on day 2 (the day the suspension culture was initiated was defined as D0). On D12, the aggregates were transferred to low-cell-adhesion 24-well plates, and the medium was replaced with RDM containing Matrigel (0.5%–2%) and FBS (1%–10%). On D15, CHIR99021 (3 mM; Wako) and SAG (100 nM; Enzo Life Science) were added to the medium, and the suspension culture was continued for another 3 days. On D18, the aggregates were transferred to retinal maturation medium (RMM; DMEM/F12-Glutamax medium containing the N2 supplement, 100 U/mL penicillin, and 100 mg/mL streptomycin) and were then cultured in the absence of FBS. The adhesion culture started when the aggregates were transferred to poly-D-lysine/laminin-coated 24-well plates (BD Bioscience) in RMN medium containing FBS and 100 ng/mL BDNF (R&D Systems). The start day varied from D26 to D29, and the addition of retinoic acid (0.5 mM; Sigma) 3 days prior to the start of adhesion culture was preferred. The concentration of FBS was increased stepwise from 1% up to 10% over the course of the adhesion culture.

Real-time reverse transcription polymerase chain reaction (RT-PCR). Total RNA was extracted from cells using an RNeasy Mini Kit (QIAGEN, Valencia, CA, USA). The expression levels of the mRNAs in each RNA sample were determined using the StepONE Sequence Detection System (Applied Biosystems). RT-PCR was performed using a One Step SYBR PrimeScript PLUS RT-PCR Kit (TaKaRa Bio, Shiga, Japan). The primers used in this study are listed in Supplementary Table 1. The thermocycler conditions were as follows: an initial hold at 42uC for 5 min; incubation at 95uC for 10 s; and then 40 cycles at 95uC for 5 s and 60uC for 31 s. The expression of mRNA was assessed by evaluating threshold cycle (C_T) values. The C_T values were normalised to the expression level of hypoxanthine phosphoribosyltransferase 1 (HPRT1), and the relative amount of mRNA specific to each of the target genes was calculated using the $2^{2\mathrm{DDCT}}$ method.

To perform sectional gene expression analysis, adherent tissues of EBs and extruding OVs were defined as three parts: the RGCR, which was located at the outermost 2–3 layers of cells in the clump of cells; the OVR, which was an adherent structure of OVs excluding the RGCR; and the MBEB, which was an adherent structure of the EB. The regions were obviously identified under a SZ61 stereomicroscope (Olympus), and mechanical separation using a 25-G needle was performed under the same microscope.

Frozen section preparation. Specimens were fixed in 4% paraformaldehyde in 100 mM phosphate buffer for 3 h at 4uC, then rinsed in phosphate buffer, osmotic pressure-conditioned in a graded series of sucrose solutions in phosphate buffer up to 30%, and embedded in OCT compound (Tissue-Tek; Sakura Finetek). Each block was serially sectioned at 5-mm thickness using a CryoStar NX70 (Thermo Fisher Scientific).

Immunohistochemistry. Immunostaining was performed using frozen sections or whole cells fixed on the dish. Whole cells specimens were fixed with 4% paraformaldehyde (pH 7.0) for 20 min at room temperature. After two rinses with PBS, specimens were incubated with 0.1% Triton X-100 for 15 min at room temperature and then washed three times with PBS for 5 min each. Specimens of frozen sections or whole cells were then incubated with 3% bovine serum albumin (BSA) for 30 min at room temperature followed by primary antibody incubation for 16 h at 4uC. The primary antibodies used in this study and their dilutions are listed in Supplementary Table 2. Secondary antibody reactions were carried out by incubation with the corresponding species-specific Alexa Fluor-488-conjugated antibodies (15500, Invitrogen) for 1 h at room temperature in the dark. After four washes with PBS for 5 min each, specimens were mounted with ProLong Gold Antifade Reagent with DAPI (Invitrogen) and viewed with an IX71 inverted research microscope (Olympus) or BZ-9000E (KEYENCE).

Haematoxylin and eosin staining. Specimens were fixed in 4% paraformaldehyde in 100 mM phosphate buffer for 3 h at 4uC, rinsed in water, dehydrated in a graded series of alcohols/xylene, and embedded in paraffin. Each block was serially sectioned at a 3-mm thickness. Deparaffinized sections were then stained with haematoxylin and eosin.

Transmission electron microscopy. Specimens were fixed in 2% glutaraldehyde in 100 mM cacodylate buffer for 2 h, followed by 1% osmium tetroxide in 100 mM cacodylate buffer for 1 h. Specimens were then dehydrated in a graded series of alcohols/xylene, permeated with propylene oxide, and embedded in epoxy resin. Ultrathin sections of representative areas were stained with uranyl acetate and lead citrate and viewed with a JEM-1200EX electron microscope (Japan Electron Optics Laboratory).

Axonal flow observation. The NTRK1 expression vector (RG213091; ORIGENE), the pPAmCherry-Mito Vector (TaKaRa Bio), and the pcDNA^{TM}6.2/C-EmGFP Vector (Invitrogen) were electroporated into cultured cells. For electroporation, NEPA21 (NEPAGENE) with platinum electrodes was used. The cultured colony was injected with fast green-dyed DNA solution using a sharp glass pipette, placed between the electrodes, and electroporated with voltage pulses (poring pulse: voltage 100 V, width 2.5 ms, interval 50 ms, two times; transfer pulse: voltage 20 V, width 50 ms, interval 50 ms, five times). The cultured cells were then allowed to develop in humidified incubators. Observations were made with an IX71 inverted research microscope (Olympus).

The time series of anterograde axonal flow was conducted by injection of Alexa Fluo-555 conjugated cholera toxin subunit B (Life Technologies) into the RGCR. Time-lapse analysis was performed immediately after the injection of cholera toxin B with a DeltaVision ELITE (CORNES Technologies).

Electrophysiological recordings. Colonies were cultured on mixed cellulose ester filter papers (0.2-mm pore size; ADVANTEC) for 1 week. After removal of filter paper bearing colonies from the medium, suction was applied to the bottom of the filter to cause the colonies to attach firmly. Slices 200 mm thick were then cut vertically with a custom-made tissue chopper and fixed to the glass bottom of a recording chamber having a volume of 1.5 mL with a small amount of silicone grease (Dow Corning). All experiments were performed at physiological temperatures (35–37uC) using a ThermoClamp-1 (Automate Scientific). The chamber was continuously perfused at 1.5 mL/min with extracellular solution containing 120 mM NaCl, 3 mM KCl, 2.5 mM $CaCl_2$, 1 mM $MgCl_2$, 10 mM glucose, and 25 mM $NaHCO_3$ equilibrated with 95%/5% O_2/CO_2 (pH 7.4). Chemicals were purchased from Sigma unless otherwise noted. Whole-cell patch-clamp recordings were made from the retinal ganglion cells located on the outer perimeter of the cultured colony. Recordings were performed with an Axopatch 200B amplifier (Molecular Devices) using pCLAMP 9.2 software (Molecular Devices). The slice preparations were visualised using an upright microscope (BX50WI; Olympus) equipped with DIC optics and a 603 water-immersion objective. The voltage or current trace was low-pass filtered (Bessel filter, corner frequency 10 kHz) and sampled at 20–50 kHz with a Digidata 1322A interface (Molecular Devices). Voltage-dependent Na^1 currents were measured with leakage and capacitive current subtraction (P/-5 protocol) and were averaged over three trials. In some experiments, we added 1 mM tetrodotoxin (TTX) to the extracellular solution to block voltage-dependent Na^1 channels. The recording pipettes (6–8 MV) were filled with an intracellular solution containing 120 mM K gluconate, 6 mM KCl, 2 mM NaCl, 1 mM $CaCl_2$, 1 mM $MgCl_2$, 5 mM EGTA, 10 mM HEPES, 4 mM Na_2ATP, and 0.5 mM GTP (pH 7.2). In all experiments, Lucifer Yellow CH dilithium salt (LY; 0.05%) was added to the intracellular solutions to visualise the morphology of the recorded cells. Liquid junction potentials (211 mV) were corrected. The average series resistance (Rs) was 29.4 6 4.77 MV (n 5 5). Rs was compensated by 40%. Data with Rs values of more than 35 MV were excluded from the analyses. The average membrane capacitance during the recordings was 7.20 6 2.84 pF (n 5 5). Current and voltage data were acquired using pCLAMP 9.2 software and saved on a custom-built personal computer (Physio-Tech). Analyses were performed with Clampfit 9.2 (Molecular Devices) and OriginPro 8J (OriginLab). Images of LY-filled cells were captured using a high-gain colour camera (HCC-600; Flovel) and saved using INFO.TV Plus software (Infocity). The images were adjusted for brightness and contrast and complemented by pasting in a part of another image obtained from a different depth of the slice preparation using Photoshop CS6 software (Adobe Systems). All data are presented as means 6 SDs.

1. Pascolini, D. & Mariotti, S. P. Global estimates of visual impairment: 2010. Br. J. Ophthalmol. 96, 614–618 (2012).
2. Resnikoff, S. et al. Global data on visual impairment in the year 2002. Bull. World Health Organ. 82, 844–851 (2004).
3. Rattner, A. & Nathans, J. Macular degeneration: recent advances and therapeutic opportunities. Nat. Rev. Neurosci. 7, 860–872 (2006).
4. Hartong, D. T., Berson, E. L. & Dryja, T. P. Retinitis pigmentosa. Lancet 368, 1795–1809 (2006).
5. Quigley, H. A. & Broman, A. T. The number of people with glaucoma worldwide in 2010 and 2020. Br. J. Ophthalmol. 90, 262–267 (2006).
6. Sun, G., Asami, M., Ohta, H., Kosaka, J. & Kosaka, M. Retinal stem/progenitor properties of iris pigment epithelial cells. Dev. Biol. 289, 243–252 (2006).
7. Haruta, M. et al. Induction of photoreceptor-specific phenotypes in adult mammalian iris tissue. Nat. Neurosci. 4, 1163–1164 (2001).
8. Tropepe, V. et al. Retinal stem cells in the adult mammalian eye. Science 287, 2032–2036 (2000).
9. Osakada, F. et al. Wnt signaling promotes regeneration in the retina of adult mammals. J. Neurosci. 27, 4210–4219 (2007).
10. Lawrence, J. M. et al. MIO-M1 cells and similar muller glial cell lines derived from adult human retina exhibit neural stem cell characteristics. Stem Cells 25, 2033–2043 (2007).
11. Seko, Y. et al. Derivation of human differential photoreceptor-like cells from the iris by defined combinations of CRX, RX and NEUROD. PLoS One 7, e35611 (2012).
12. Lamba, D. A. et al. Generation, purification and transplantation of photoreceptors derived from human induced pluripotent stem cells. PLoS One 5, e8763 (2010).
13. Jayaram, H. et al. Transplantation of photoreceptors derived from human Muller glia restore rod function in the P23H rat. Stem Cells Transl. Med. 3, 323–333 (2014).
14. Eiraku, M. et al. Self-organized formation of polarized cortical tissues from ESCs and its active manipulation by extrinsic signals. Cell Stem Cell 3, 519–532 (2008).
15. Suga, H. et al. Self-formation of functional adenohypophysis in three-dimensional culture. Nature 480, 57–62 (2011).
16. Eiraku, M. et al. Self-organizing optic-cup morphogenesis in three-dimensional culture. Nature 472, 51–56 (2011).
17. Nakano, T. et al. Self-formation of optic cups and storable stratified neural retina from human ESCs. Cell Stem Cell 10, 771–785 (2012).
18. Assawachananont, J. et al. Transplantation of embryonic and induced pluripotent stem cell-derived 3D retinal sheets into retinal degenerative mice. Stem Cell Rep. 2, 662–674 (2014).

19. Meyer, J. S. et al. Modeling early retinal development with human embryonic and induced pluripotent stem cells. Proc. Natl. Acad. Sci. U. S. A. 106, 16698–16703 (2009).
20. Meyer, J. S. et al. Optic vesicle-like structures derived from human pluripotent stem cells facilitate a customized approach to retinal disease treatment. Stem Cells 29, 1206–1218 (2011).
21. Zhong, X. et al. Generation of three-dimensional retinal tissue with functional photoreceptors from human iPSCs. Nat. Commun. 5, 4047 (2014).
22. Ikeda, H. et al. Generation of Rx**1**/Pax6**1** neural retinal precursors from embryonic stem cells. Proc. Natl. Acad. Sci. U. S. A. 102, 11331–11336 (2005).
23. Osakada, F. et al. Toward the generation of rod and cone photoreceptors from mouse, monkey and human embryonic stem cells. Nat. Biotechnol. 26, 215–224 (2008).
24. Lamba, D. A., Karl, M. O., Ware, C. B. & Reh, T. A. Efficient generation of retinal progenitor cells from human embryonic stem cells. Proc. Natl. Acad. Sci. U. S. A. 103, 12769–12774 (2006).
25. Hirami, Y. et al. Generation of retinal cells from mouse and human induced pluripotent stem cells. Neurosci. Lett. 458, 126–131 (2009).
26. Mellough, C. B., Sernagor, E., Moreno-Gimeno, I., Steel, D. H. & Lako, M. Efficient stage-specific differentiation of human pluripotent stem cells toward retinal photoreceptor cells. Stem Cells 30, 673–686 (2012).
27. Yu, D. Y. et al. Retinal ganglion cells: Energetics, compartmentation, axonal transport, cytoskeletons and vulnerability. Prog. Retin. Eye Res. 36, 217–246 (2013).
28. Kaplan, E. & Benardete, E. The dynamics of primate retinal ganglion cells. Prog. Brain Res. 134, 17–34 (2001).
29. Hong, S., Iizuka, Y., Kim, C. Y. & Seong, G. J. Isolation of primary mouse retinal ganglion cells using immunopanning-magnetic separation. Mol. Vis. 18, 2922–2930 (2012).
30. Zhang, X. M. et al. Immunopanning purification and long-term culture of human retinal ganglion cells. Mol. Vis. 16, 2867–2872 (2010).
31. Takihara, Y. et al. Dynamic imaging of axonal transport in living retinal ganglion cells in vitro. Invest. Ophthalmol. Vis. Sci. 52, 3039–3045 (2011).
32. Xie, B. B. et al. Differentiation of retinal ganglion cells and photoreceptor precursors from mouse induced pluripotent stem cells carrying an atoh7/math5 lineage reporter. PLoS One 9, e112175 (2014).
33. Riazifar, H., Jia, Y., Chen, J., Lynch, G. & Huang, T. Chemically induced specification of retinal ganglion cells from human embryonic and induced pluripotent stem cells. Stem Cells Transl. Med. 3, 424–432 (2014).
34. Gonzalez-Cordero, A. et al. Photoreceptor precursors derived from three-dimensional embryonic stem cell cultures integrate and mature within adult degenerate retina. Nat. Biotechnol. 31, 741–747 (2013).
35. Zuber, M. E., Gestri, G., Viczian, A. S., Barsacchi, G. & Harris, W. A. Specification of the vertebrate eye by a network of eye field transcription factors. Development 130, 5155–5167 (2003).
36. Bailey, T. J. et al. Regulation of vertebrate eye development by Rx genes. Int. J. Dev. Biol. 48, 761–770 (2004).
37. Riesenberg, A. N. et al. Pax6 regulation of Math5 during mouse retinal neurogenesis. Genesis 47, 175–187 (2009).
38. Brown, N. L., Patel, S., Brzezinski, J. & Glaser, T. Math5 is required for retinal ganglion cell and optic nerve formation. Development 128, 2497–2508 (2001).
39. Wang, S. W. et al. Requirement for math5 in the development of retinal ganglion cells. Genes Dev. 15, 24–29 (2001).
40. Ghiasvand, N. M. et al. Deletion of a remote enhancer near ATOH7 disrupts retinal neurogenesis, causing NCRNA disease. Nat. Neurosci. 14, 578–586 (2011).
41. Hutcheson, D. A. & Vetter, M. L. The bHLH factors Xath5 and XNeuroD can upregulate the expression of XBrn3d, a POU-homeodomain transcription factor. Dev. Biol. 232, 327–338 (2001).
42. Qiu, F., Jiang, H. & Xiang, M. A comprehensive negative regulatory program controlled by Brn3b to ensure ganglion cell specification from multipotential retinal precursors. J. Neurosci. 28, 3392–3403 (2008).
43. Pan, L., Deng, M., Xie, X. & Gan, L. ISL1 and BRN3B co-regulate the differentiation of murine retinal ganglion cells. Development 135, 1981–1990 (2008).
44. Green, E. S., Stubbs, J. L. & Levine, E. M. Genetic rescue of cell number in a mouse model of microphthalmia: interactions between Chx10 and G1-phase cell cycle regulators. Development 130, 539–552 (2003).
45. Furukawa, T., Morrow, E. M. & Cepko, C. L. Crx, a novel otx-like homeobox gene, shows photoreceptor-specific expression and regulates photoreceptor differentiation. Cell 91, 531–541 (1997).
46. Chen, S. et al. Crx, a novel Otx-like paired-homeodomain protein, binds to and transactivates photoreceptor cell-specific genes. Neuron 19, 1017–1030 (1997).
47. Cepko, C. L., Austin, C. P., Yang, X., Alexiades, M. & Ezzeddine, D. Cell fate determination in the vertebrate retina. Proc. Natl. Acad. Sci. U. S. A. 93, 589–595 (1996).
48. Tagaya, M. et al. Syntaxin 1 (HPC-1) is associated with chromaffin granules. J. Biol. Chem. 270, 15930–15933 (1995).
49. Bennett, M. K., Calakos, N. & Scheller, R. H. Syntaxin: a synaptic protein implicated in docking of synaptic vesicles at presynaptic active zones. Science 257, 255–259 (1992).
50. Tsukiji, N. et al. Mitf functions as an in ovo regulator for cell differentiation and proliferation during development of the chick RPE. Dev Biol 326, 335–346 (2009).
51. Hogan, M. J., Alvarado, J. A. & Weddel, J. E. Histology of the Human Eye: An Atlas and Textbook. 537 (1971).
52. Drager, U. C. & Olsen, J. F. Ganglion cell distribution in the retina of the mouse. Invest. Ophthalmol. Vis. Sci. 20, 285–293 (1981).
53. Stone, J., Makarov, F. & Hollander, H. The glial ensheathment of the soma and axon hillock of retinal ganglion cells. Vis. Neurosci. 12, 273–279 (1995).
54. Wollner, D. A. & Catterall, W. A. Localization of sodium channels in axon hillocks and initial segments of retinal ganglion cells. Proc. Natl. Acad. Sci. U. S. A. 83, 8424–8428 (1986).
55. Ninkina, N. et al. Gamma-synucleinopathy: neurodegeneration associated with overexpression of the mouse protein. Hum. Mol. Genet. 18, 1779–1794 (2009).
56. Balaratnasingam, C., Morgan, W. H., Johnstone, V., Cringle, S. J. & Yu, D. Y. Heterogeneous distribution of axonal cytoskeleton proteins in the human optic nerve. Invest. Ophthalmol. Vis. Sci. 50, 2824–2838 (2009).
57. Goedert, M. & Spillantini, M. G. A century of Alzheimer's disease. Science 314, 777–781 (2006).
58. Bull, N. D., Guidi, A., Goedert, M., Martin, K. R. & Spillantini, M. G. Reduced axonal transport and increased excitotoxic retinal ganglion cell degeneration in mice transgenic for human mutant P301S tau. PLoS One 7, e34724 (2012).
59. Yuan, A. et al. Alpha-internexin is structurally and functionally associated with the neurofilament triplet proteins in the mature CNS. J. Neurosci. 26, 10006–10019 (2006).
60. Yuan, A., Rao, M. V., Veeranna & Nixon, R. A. Neurofilaments at a glance. J. Cell Sci. 125, 3257–3263 (2012).
61. Bates, C. A. & Meyer, R. L. The heavy neurofilament protein is expressed in regenerating adult but not embryonic mammalian optic fibers in vitro. Exp. Neurol. 119, 249–257 (1993).
62. Cui, Q., Tang, L. S., Hu, B., So, K. F. & Yip, H. K. Expression of trkA, trkB, and trkC in injured and regenerating retinal ganglion cells of adult rats. Invest. Ophthalmol. Vis. Sci. 43, 1954–1964 (2002).
63. Klein, R., Jing, S. Q., Nanduri, V., O'Rourke, E. & Barbacid, M. The trk proto-oncogene encodes a receptor for nerve growth factor. Cell 65, 189–197 (1991).
64. Vossel, K. A. et al. Tau reduction prevents Abeta-induced defects in axonal transport. Science 330, 198 (2010).
65. Phillips, M. J. et al. Blood-derived human iPS cells generate optic vesicle-like structures with the capacity to form retinal laminae and develop synapses. Invest. Ophthalmol. Vis. Sci. 53, 2007–2019 (2012).
66. Livesey, F. J. & Cepko, C. L. Vertebrate neural cell-fate determination: lessons from the retina. Nat. Rev. Neurosci. 2, 109–118 (2001).
67. Rapaport, D. H., Rakic, P. & LaVail, M. M. Spatiotemporal gradients of cell genesis in the primate retina. Perspect. Dev. Neurobiol. 3, 147–159 (1996).
68. Pacal, M. & Bremner, R. Induction of the ganglion cell differentiation program in human retinal progenitors before cell cycle exit. Dev. Dyn. 243, 712–729 (2014).
69. Ray, J., Peterson, D. A., Schinstine, M. & Gage, F. H. Proliferation, differentiation, and long-term culture of primary hippocampal neurons. Proc. Natl. Acad. Sci. U. S. A. 90, 3602–3606 (1993).
70. Lesuisse, C. & Martin, L. J. Long-term culture of mouse cortical neurons as a model for neuronal development, aging, and death. J. Neurobiol. 51, 9–23 (2002).
71. Sciarretta, C. & Minichiello, L. The preparation of primary cortical neuron cultures and a practical application using immunofluorescent cytochemistry. Methods Mol. Biol. 633, 221–231 (2010).
72. Guerra-Crespo, M., Ubieta, R., Joseph-Bravo, P., Charli, J. L. & Perez-Martinez, L. BDNF increases the early expression of TRH mRNA in fetal TrkB**1** hypothalamic neurons in primary culture. Eur. J. Neurosci. 14, 483–494 (2001).
73. Joseph-Bravo, P., Perez-Martinez, L., Lezama, L., Morales-Chapa, C. & Charli, J. L. An improved method for the expression of TRH in serum-supplemented primary cultures of fetal hypothalamic cells. Brain Res. Brain Res. Protoc. 9, 93–104 (2002).
74. Barros, C. S., Franco, S. J. & Muller, U. Extracellular matrix: functions in the nervous system. Cold Spring Harb. Perspect. Biol. 3, a005108 (2011).
75. Almeida, R. D. et al. Neuroprotection by BDNF against glutamate-induced apoptotic cell death is mediated by ERK and PI3-kinase pathways. Cell Death Differ. 12, 1329–1343 (2005).
76. Melo, C. V. et al. Spatiotemporal resolution of BDNF neuroprotection against glutamate excitotoxicity in cultured hippocampal neurons. Neuroscience 237, 66–86 (2013).
77. Sofroniew, M. V., Howe, C. L. & Mobley, W. C. Nerve growth factor signaling, neuroprotection, and neural repair. Annu. Rev. Neurosci. 24, 1217–1281 (2001).
78. Sendtner, M., Kreutzberg, G. W. & Thoenen, H. Ciliary neurotrophic factor prevents the degeneration of motor neurons after axotomy. Nature 345, 440–441 (1990).
79. Peterson, W. M., Wang, Q., Tzekova, R. & Wiegand, S. J. Ciliary neurotrophic factor and stress stimuli activate the Jak-STAT pathway in retinal neurons and glia. J. Neurosci. 20, 4081–4090 (2000).
80. Kadoshima, T. et al. Self-organization of axial polarity, inside-out layer pattern, and species-specific progenitor dynamics in human ES cell-derived neocortex. Proc. Natl. Acad. Sci. U. S. A. 110, 20284–20289 (2013).
81. Lancaster, M. A. et al. Cerebral organoids model human brain development and microcephaly. Nature 501, 373–379 (2013).
82. Kato-Negishi, M., Morimoto, Y., Onoe, H. & Takeuchi, S. Millimeter-sized neural building blocks for 3D heterogeneous neural network assembly. Adv. Healthc. Mater. 2, 1564–1570 (2013).

83. Lowery, L. A. & Van Vactor, D. The trip of the tip: understanding the growth cone machinery. Nat. Rev. Mol. Cell Biol. 10, 332–343 (2009).
84. Chung, C. Y. et al. Identification and rescue of alpha-synuclein toxicity in Parkinson patient-derived neurons. Science 342, 983–987 (2013).
85. Kondo, T. et al. Modeling Alzheimer's disease with iPSCs reveals stress phenotypes associated with intracellular Abeta and differential drug responsiveness. Cell Stem Cell 12, 487–496 (2013).
86. Dimos, J. T. et al. Induced pluripotent stem cells generated from patients with ALS can be differentiated into motor neurons. Science 321, 1218–1221 (2008).
87. Yazawa, M. et al. Using induced pluripotent stem cells to investigate cardiac phenotypes in Timothy syndrome. Nature 471, 230–234 (2011).

Acknowledgments

We thank Dr H. Akutsu for technical instruction on primary culture of iPSCs. This work was supported by a Grant from the Ministry of Health, Labour, and Welfare (H24-Nanchi-Ippan-031), JSPS KAKENHI (grant numbers 22390327 and 24659770) and a grant from the National Centre for Child Health and Development 25-7.

Author contributions

T.T. and T.Y. performed experiments, analysed and interpreted data, and wrote the manuscript. F.T. and S.W. designed and performed the electrophysiological recordings and contributed to the writing of the manuscripts. S.N. interpreted data. N.A. designed experiments and supervised the project.

Additional information

Supplementary information accompanies this paper at http://www.nature.com/scientificreports

Competing financial interests: The authors declare no competing financial interests.

How to cite this article: Tanaka, T. et al. Generation of retinal ganglion cells with functional axons from human induced pluripotent stem cells. Sci. Rep. 5, 8344; DOI:10.1038/srep08344 (2015).

RESEARCH ARTICLE

Morphological Features and Important Parameters of Large Optic Discs for Diagnosing Glaucoma

Satoshi Okimoto[1]*, Keiko Yamashita[2], Tetsuo Shibata[2], Yoshiaki Kiuchi[1]

1 Department of Ophthalmology and Visual science, Graduate School of Biomedical Sciences, Hiroshima University, Hiroshima, Japan, 2 Shibata Eye Clinic, Hyogo, Japan

* okimoto@hiroshima-u.ac.jp

Abstract

Purpose

To compare the optic disc parameters of glaucomatous eyes to those of non-glaucomatous eyes with large discs.

Methods

We studied 225 consecutive eyes with large optic discs (>2.82 mm2): 91 eyes with glaucoma and 134 eyes without glaucoma. An eye was diagnosed with glaucoma when visual field defects were detected by the Humphrey Field Analyzer. All of the Heidelberg Retina Tomograph II (HRT II) parameters were compared between the non-glaucomatous and glaucomatous eyes. A logistic regression analysis of the HRT II parameters was used to establish a new formula for diagnosing glaucoma, and the sensitivity and specificity of the Moorfields Regression Analysis (MRA) was compared to the findings made by our analyses.

Results

The mean disc area was 3.44±0.50 mm2 in the non-glaucomatous group and 3.40±0.52 mm2 in the glaucoma group. The cup area, cup volume, cup-to-disc area ratio, linear cup/disc ratio, mean cup depth, and the maximum cup depth were significantly larger in glaucomatous eyes than in the non-glaucomatous eyes. The rim area, rim volume, cup shape measurement, mean retinal nerve fiber layer (RNFL) thickness, and RFNL cross-sectional area were significantly smaller in glaucomatous eyes than in non-glaucomatous eyes. The cup-to-disc area ratio, the height variation contour (HVC), and the RNFL cross-sectional area were important parameters for diagnosing the early stage glaucoma, and the cup-to-disc area ratio and cup volume were useful for diagnosing advanced stage glaucoma in eyes with a large optic disc. The new formula had higher sensitivity and specificity for diagnosing glaucoma than MRA.

OPEN ACCESS

Citation: Okimoto S, Yamashita K, Shibata T, Kiuchi Y (2015) Morphological Features and Important Parameters of Large Optic Discs for Diagnosing Glaucoma. PLoS ONE 10(3): e0118920. doi:10.1371/journal.pone.0118920

Academic Editor: Sanjoy Bhattacharya, Bascom Palmer Eye Institute, University of Miami School of Medicine;, UNITED STATES

Received: June 16, 2014

Accepted: January 7, 2015

Published: March 23, 2015

Data Availability Statement: All relevant data are within the paper and its Supporting Information files.

Funding: Shibata Eye Clinic provided support in the form of salaries for authors KY and TS, but did not have any additional role in the study design, data collection and analysis, decision to publish, or preparation of the manuscript. The specific roles of these authors are articulated in the "author contributions" section.

Competing Interests: KY and TS are employees of Shibata Eye Clinic. There are no patents, products in

development, or marketed products to declare. This does not alter our adherence to all the PLOS ONE policies on sharing data and materials.

Conclusions

The cup-to-disc area ratio, HVC, RNFL cross-sectional area, and cup volume were important parameters for diagnosing glaucoma in eyes with a large optic disc. The important disc parameters to diagnose glaucoma depend on the stage of glaucoma in patients with large discs.

Introduction

Glaucoma is a progressive optic neuropathy in which morphological changes of the optic disc and the retinal nerve fiber layer (RNFL) progress to visual field defects [1,2]. Because the rim area of the optic disc is reduced in glaucomatous eyes, evaluating the changes of the optic disc morphology is essential for diagnosing glaucoma [3–7]. In general, the optic disc cup area is increased in glaucomatous eyes, and the cup-to-disc ratio is used for diagnosing glaucoma [8]. However, the cup area is also large in eyes with a large optic disc, and these eyes may not be glaucomatous [9,10]. Therefore, a careful examination is needed to discriminate whether a large cup area is due to glaucoma or to a large optic disc.

The Heidelberg Retina Tomograph II (HRT II; Heidelberg Engineering, GmbH, Heidelberg, Germany) can obtain highly reproducible measurements of the stereometric parameters of the optic disc, and these parameters can be used to differentiate normal from glaucomatous eyes. Therefore, the HRT II has been used for glaucoma screening [11–13].

The Moorfields Regression Analysis (MRA) of the stereometric parameters obtained by the HRT II is a useful method of diagnosing glaucoma based on the morphological parameters of optic discs. The MRA program is based on comparing the rim area and disc area of a glaucoma suspect to the normal database embedded in the instrument [11]. From the results of the comparisons, a determination can be made on whether the eye is non-glaucomatous or glaucomatous.

However, when the size of the optic nerve head is smaller or larger than the normal size, it is difficult to diagnose glaucoma by the MRA. Based on the Tajimi study, the diagnostic power of detecting glaucoma by the MRA program is reduced when the disc size becomes larger than the normal size [14].

In addition to the MRA, several statistical methods have been proposed by Mikelberg et al., Lester et al. and Bathija et al. to differentiate normal from glaucomatous optic discs [15–17]. Ford et al. reported that these methods of analysis had similar sensitivities once their specificities were equalized. However, the diagnostic power of these methods decreases when the disc size is large, because these methods are based mainly on the data of eyes with a normal disc size [18].

The purpose of this study was to determine the stereometric parameters of eyes with large optic discs without visual field defects. The parameters were compared to those of diagnosed glaucomatous eyes with large optic discs, and we identified the disc parameters which can be used to diagnose glaucoma. We then created a new formula based on these parameters to diagnose glaucoma in eyes with a large optic disc.

Materials and Methods

Patients

Patients who were being treated at Shibata Clinic of Ophthalmology from November 2005 to July 2007 were studied. Consecutive subjects who were identified with a large optic disc area >2.82 mm^2 by the HRT II parameters during the study period underwent visual field examinations with the Humphrey Field Analyzer (HFA) 30-2 SITA Standard program (Carl Zeiss Meditec Inc, Dublin, CA). All HRT tests were performed within six months of the visual field tests.

All participants underwent a comprehensive ophthalmic examination, including a medical and family history, best-corrected visual acuity (BCVA), slit-lamp biomicroscopy, Goldmann applanation tonometry, gonioscopy and fundus examinations. Patients were excluded if they had other eye diseases that could affect the visual field other than glaucoma, those with a BCVA of 20/33 or worse and patients with a tilted optic disc.

Ethics Statement

All the data were analyzed in the Department of Ophthalmology, Hiroshima University. The study was approved by the Ethics Committee of Hiroshima University (registration number; 957) and was conducted according to the tenets of the Declaration of Helsinki.

In some kind of epidemiological researches like this study design, the Ethics Review Board of the Hiroshima University waived the need for written informed consent from the participants. We didn't get the written or verbal consent in the medical records. However, we announced the details of this study to the participants using the poster, and have disclosed the results of the examinations and study data to all participants. The Ethics committee of the Hiroshima University had approved the study procedures.

Evaluation of Visual Fields

A diagnosis of glaucoma was made based on the visual field results obtained with HFA. The results of the HFA 30-2 SITA Standard program were examined by two glaucoma specialists (SO and YK) who were blinded to other information about the eye being examined. The evaluations were carried out on all eyes, excluding those that were unreliable (fixation loss, $<20\%$; false-positive and false-negative, $<15\%$). Abnormal visual field data were defined by the presence of at least one abnormal hemifield that was based on the criteria proposed by Anderson and Patella [19]. The hemifield was judged to be abnormal when the pattern deviation probability plot showed a cluster of three or more non-edge contiguous points having a sensitivity of less than 5% in the upper or lower hemifield, and in one of these with a probability of less than 1%. Glaucomatous visual field changes were diagnosed when the pattern standard deviation was less than 5%, or when the glaucoma hemifield test was abnormal.

Heidelberg Retinal Tomograph II (HRT II) Parameter Measurements

The optic disc parameters were determined from the HRT II images [11,15,20]. The fundus, including the optic disc, was photographed using the HRT after pupil dilation. The image quality of all the HRT images was checked manually by an experienced operator, and the optic disc margin (contour line) was outlined around the inner margin of the peripapillary scleral rings by the same operator (KY). The analysis was restricted to eyes that had valid optic disc measurements with the HRT II. Good image quality was defined as appropriate focus, brightness and clarity, minimal eye movements, the optic disc centered in the image and a standard deviation of the mean topographic image <40 μm. Eyes in which good-quality images could not be obtained were excluded from the analysis. The results of the MRA were evaluated by classifying borderline cases as being outside the normal limits. The HRT image recording and visual field testing were performed on the same day. All data obtained from the HRT II were analyzed (provide as supplemental data). The RNFL cross sectional area was calculated as the average distance between the retinal surface and a standard point along a contour line of the disc × the length of contour line. The height variation contour (HVC) is the difference in retinal surface height along the contour line of the disc between the highest and lowest points. The cup shape measure represents the overall shape of the optic nerve head and has been shown to have a significant correlation with glaucomatous damage [20,21]. The cup shape measurement is independent of the reference plane and, thus, is unaffected by any variability in the reference plane [22,23]. The reference height is calculated as the average heights of the retina around the disc.

Statistical Analyses

The eyes with normal visual fields (Non-glaucoma group) and the eyes with a glaucomatous visual field (Glaucoma group) were compared based on the results of the HFA. The glaucoma group was divided into two subsets: an early glaucoma group ($\text{MD} > -5$ dB) and the advanced glaucoma group (MD : −5dB). The correlations between the disc area and each of the HRT parameters were examined in a scatter diagram. Important HRT parameters were selected by using the stepwise method, and the odds ratio for the diagnosis of glaucoma by a logistic regression analysis was calculated. The results of the multiple logistic analyses were used to compare the results of the MRA for the global area. The optimal cut-off value of the receiver operating characteristic curve (ROC) was calculated to differentiate glaucomatous and non-glaucomatous eyes.

Comparisons of the mean values among the groups were made using t-tests. The JMP 9.0 Statistical Analysis System software program (SAS Institute Inc. California) was used for the calculations and statistical analyses, and a P value <0.05 was considered to be statistically significant.

Results

Participants

The demographics of the patients are summarized in Table 1. There were 225 eyes in 145 patients that were analyzed (78 eyes of 49 males and 147 eyes of 96 females). The Non-glaucomatous group included 134 eyes and the glaucoma group included 91 eyes.

Comparison of the Disc Parameters in Non-glaucomatous and Glaucomatous Eyes

The disc parameters were compared between the non-glaucomatous group and the glaucomatous group (Table 2). The disc area in the non-glaucomatous group (3.44 ± 0.50 mm^2) was not significantly different from that in the glaucomatous group (3.40 ± 0.52 mm^2). The values of the cup area, cup volume, cup-to-disc area ratio, linear cup/disc ratio, mean cup depth and the maximum cup depth of the glaucomatous group were significantly larger than those of the non-glaucomatous group. The rim area, rim volume, cup shape measure, mean RNFL thickness and RFNL cross-sectional area of the RNFL in the glaucomatous group were significantly smaller than those in the non-glaucomatous group.

Correlations between the Disc Area and the HRT Parameters

A scatter diagram shows that the cup area increased with an increase of the disc area in both the non-glaucomatous and glaucomatous groups (Fig. 1). No other HRT parameter was significantly correlated with the disc area (data not shown).

Table 1. Demographics of the study subjects.

	N	G	P*	Glaucoma			
	(n = 134)	(n = 91)		EG (n = 66)	P†	AG (n = 25)	P‡
Age (y.o)	56.70±15.91	63.59±15.20	0.001	62.55±16.50	0.017	66.36±10.85	0.004
SE (D)	−1.27±3.13	−1.60±3.27	0.456	−1.10±2.79	0.713	−2.91±4.06	0.019
MD (dB)	−0.74±1.34	−5.05±5.78	<0.001	−2.43±1.34	<0.001	−11.98±7.32	<0.001
PSD (dB)	1.79±0.88	5.71±4.35	<0.001	3.71±2.40	<0.001	10.97±3.97	<0.001

The data are expressed as the means ± SD.

N: non-glaucomatous group

G: glaucomatous group

EG: early stage glaucoma group (MD <-5dB)

AG: advanced stage glaucoma group (MD ≦-5dB)

SE: spherical equivalent

MD: mean deviation

PSD: pattern standard deviation

* Difference between the normal group and all glaucoma cases

† Difference between the normal group and the early glaucoma group

‡ Difference between the normal group and the progressive/advanced glaucoma group

doi:10.1371/journal.pone.0118920.t001

The Sensitivity and Specificity of Moorfield's Regression Analysis (MRA)

The sensitivity of the MRA was 59.0% and the specificity was 66.0% for the present patients (Table 3). The sensitivity decreased when the subjects with advanced glaucoma were excluded (Table 4). Otherwise, the sensitivity improved when the subjects in the early glaucoma group were excluded (Table 5).

The Stepwise Logistic Regression Analysis

A stepwise logistic regression analysis showed that an increase of the cup-to-disc area ratio, an increase of the height variation contour (HVC) and a decrease of the RNFL cross-sectional area were risk factors for glaucoma in eyes with a large optic disc (Table 6). The formula generated by the logistic regression analysis showed that the area under the ROC was 0.81. The sensitivity and specificity of diagnosing glaucoma were 83.5% and 68.7%, respectively, if the cut off value used for the classification was −0.69 (Fig. 2A).

The yellow line is a straight line, with an angle of 45 degrees which touches the ROC curve. a) The analysis for all subjects; b) The analysis for the non-glaucomatous and early stage glaucoma groups; c) The analysis for the non-glaucomatous and advanced stage glaucoma groups.

Before stepwise selection, there were 13 factors (disc area, cup area, cup-to-disc area ratio, rim area, height variation contour, cup volume, rim volume, mean cup depth, maximum cup depth, cup shape measure, mean RNFL thickness, RNFL cross-sectional area and reference height). The four factors shown in the table were selected using a stepwise method.

The formula generated by the logistic regression: F = −5.26 + (−1.80) x Cup volume + 9.99 x C/D area + 11.44 x HVC + (−2.461) x RNFL CS.

$R^2 = 0.22$, Significance of the model: $p<0.0001$

The analysis of the subjects in the Non-glaucomatous group and early glaucoma group by the logistic regression analysis with the stepwise method, in which glaucoma was the outcome variable, showed that an increase of the cup-to-disc area ratio, an increase of the HVC and a

Table 2. The HRT II parameters in the non-glaucomatous and glaucomatous eyes.

	N	G	P*	Glaucoma				
	(n = 134)	(n = 91)		EG (n = 66)	P†	AG (n = 25)	P‡	P**
Disc area (mm^2)	3.44±0.50	3.40±0.52	0.610	3.44±0.56	0.970	3.30±0.37	0.200	0.254
Rim area (mm^2)	1.96±0.43	1.57±0.43	<0.001	1.68±0.38	<0.001	1.28±0.40	<0.001	<0.001
Rim volume (mm^3)	0.45±0.19	0.32±0.17	<0.001	0.35±0.16	<0.001	0.25±0.15	<0.001	0.007
Cup area (mm^2)	1.47±0.47	1.83±0.60	<0.001	1.76±0.63	<0.001	2.02±0.46	<0.001	0.063
Cup volume (mm^3)	0.37±0.24	0.50±0.26	<0.001	0.49±0.27	0.002	0.53±0.23	0.002	0.512
C/D area	0.42±0.11	0.53±0.13	<0.001	0.51±0.12	<0.001	0.61±0.12	<0.001	<0.001
C/D linear	0.65±0.088	0.73±0.089	<0.001	0.71±0.085	<0.001	0.78±0.079	<0.001	<0.001
Mean CD (mm)	0.29±0.081	0.33±0.086	0.005	0.32±0.084	0.015	0.33±0.091	0.043	0.756
Maximum CD (mm)	0.70±0.16	0.75±0.16	0.025	0.76±0.16	0.017	0.72±0.17	0.450	0.416
CSM	0.11±0.059	0.085±0.062	0.001	0.098±0.059	0.110	0.052±0.059	<0.001	0.001
RNFLT (mm)	0.23±0.077	0.19±0.073	<0.001	0.20±0.073	0.006	0.17±0.072	<0.001	0.097
RNFL CS (mm^2)	1.48±0.51	1.23±0.50	<0.001	1.29±0.51	0.011	1.08±0.46	<0.001	0.075
HVC (mm)	0.38±0.11	0.38±0.13	0.830	0.39±0.12	0.500	0.36±0.15	0.490	0.345
RH (mm)	0.38±0.10	0.36±0.10	0.300	0.36±0.10	0.170	0.38±0.11	0.910	0.329

The data are expressed as the means ± SD.
N: non-glaucomatous group
G: glaucomatous group
EG: early stage glaucoma group (MD<-5dB)
AG: advanced stage glaucoma group (MD ≧-5dB)
C/D area: cup-to-disc area ratio
C/D linear: linear cup/disc ratio
CD: cup depth
CSM: cup shape measure
RNFLT: mean RNFL thickness
RNFL CS: RNFL cross-sectional area
HVC: height variation contour
RH: reference height
* Difference between the normal patients and all glaucoma cases
† Difference between the normal and early glaucoma groups
‡ Difference between the normal and progressive/advanced glaucoma groups
** Difference between the early glaucoma and progressive/advanced glaucoma groups

doi:10.1371/journal.pone.0118920.t002

decrease of the RNFL cross-sectional area were risk factors for early stage glaucoma (Table 7). The formula generated by the logistic regression analysis showed that the area under the ROC was 0.79. The sensitivity and specificity for diagnosing glaucoma were 92.4% and 57.5%, respectively, if the cut-off value used for the classification was −1.19 (Fig. 2B).

Before the stepwise selection, there were 13 factors (shown in Table 6). The three factors shown in the table were selected using with a stepwise method.

The formula generated by the logistic regression: $F = -4.18 + 5.35 \times C/D\ area + 12.3 \times HVC + (-2.6) \times RNFL\ CS$.

C/D area: cup-to-disc area ratio; HVC: height variation contour;

RNFL CS: RNFL cross-sectional area

$R^2 = 0.16$, Significance of the model: $p<0.0001$

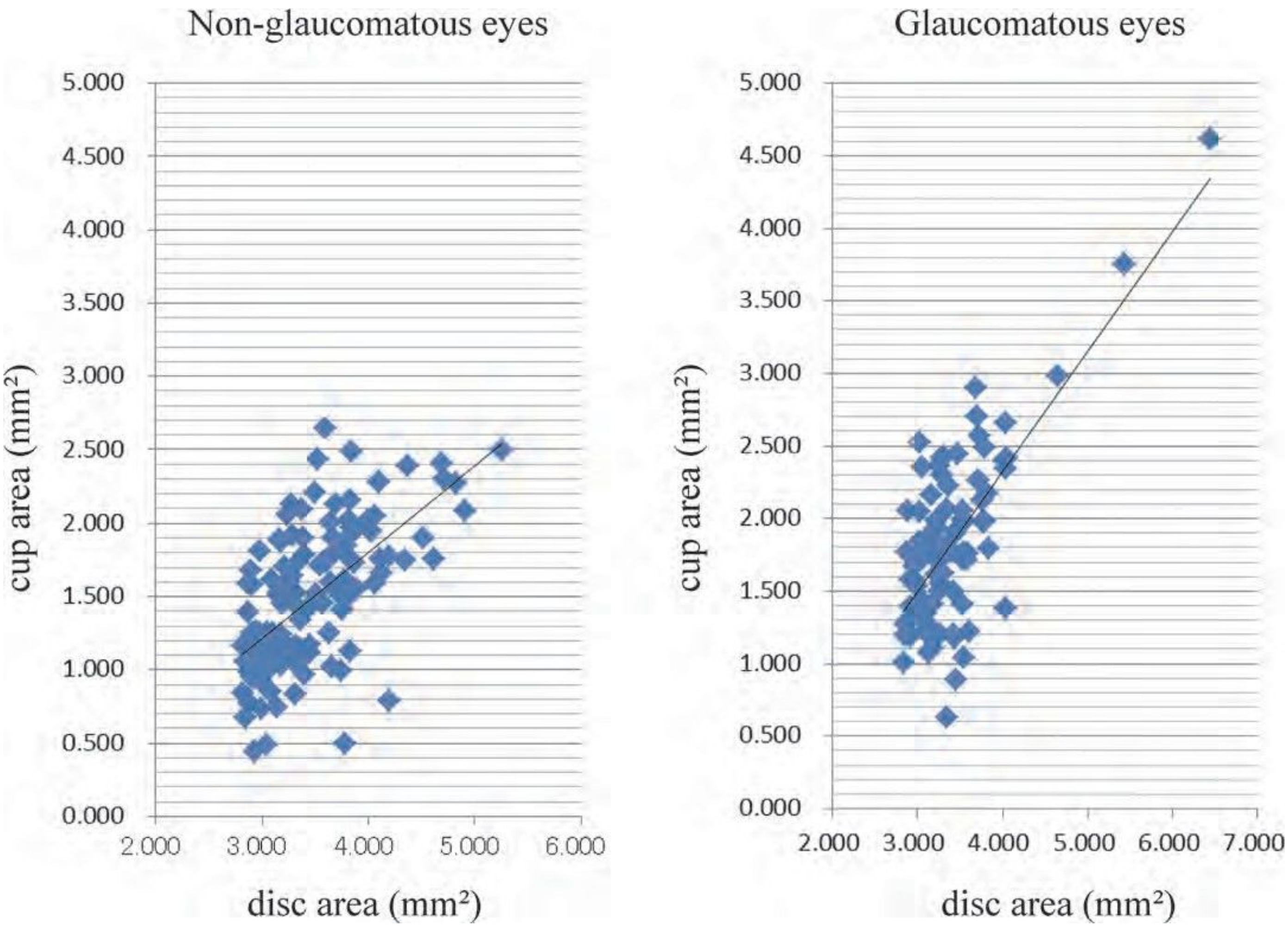

Fig 1. Scatter diagrams showing the correlations between the disc area and cup area. (Left figure) $R^2 = 0.384$, cup area = 0.585 x disc area—0.540. (Right figure) $R^2 = 0.515$, cup area = 0.825 x disc area—0.974.

doi:10.1371/journal.pone.0118920.g001

An analysis of the subjects in the non-glaucomatous group and the advanced glaucoma group by a stepwise logistic regression analysis showed that an increase in the cup-to-disc area ratio and a decrease of the cup volume were risk factors for glaucoma (Table 8). The formula

Table 3. The sensitivity and specificity of the MRA (Moorfield's Regression Analysis) for all subjects (n = 225).

	MRA	Sector						
	Classification	global	temporal	tmp/sup	tmp/inf	nasal	nsl/sup	nsl/inf
Sensitivity (%)	88	59	34	39	65	54	54	66
Specificity (%)	36	66	88	90	66	57	70	61

tmp: temporal
nsl: nasal
sup: superior
inf: inferior

doi:10.1371/journal.pone.0118920.t003

Table 4. The sensitivity and specificity of the MRA (Moorfield's Regression Analysis) for the non-glaucomatous group and the early stage glaucoma group (n = 200).

	MRA	Sector						
	Classification	global	temporal	tmp/sup	tmp/inf	nasal	nsl/sup	nsl/inf
Sensitivity (%)	86	51	25	29	59	48	48	58
Specificity (%)	36	66	88	90	66	57	70	61

tmp: temporal
nsl: nasal
sup: superior
inf: inferior

doi:10.1371/journal.pone.0118920.t004

generated by the logistic regression analysis showed that the area under the ROC was 0.91. The sensitivity and specificity for diagnosing glaucoma were 92.0% and 83.7%, respectively, if the cut-off value used for the classification was −1.94 (Fig. 2C).

Before stepwise selection, there were 13 factors (shown in Table 6). The two factors shown in the table were selected with a stepwise method.

The formula generated by the logistic regression: $F = -11.66 + (-6.17) \times \text{Cup volume} + 24.81 \times \text{C/D area}$.

C/D area: cup-to-disc area ratio

$R^2 = 0.44$, Significance of the model: $p < 0.0001$

Discussion

It is difficult to recognize the morphological changes in a glaucomatous optic disc when the disc size is large because a large disc area is significantly correlated with the optic cup area in both glaucomatous and non-glaucomatous eyes. We therefore determined the morphological features of large optic discs in eyes that were diagnosed with glaucoma by HFA. We were also able to develop a new formula to diagnose glaucoma based on the stereometric parameters in eyes with large optic discs.

Table 5. The sensitivity and specificity of the MRA (Moorfield's Regression Analysis) for the non-glaucomatous group and the advanced stage glaucoma group (n = 159).

	MRA	Sector						
	Classification	global	temporal	tmp/sup	tmp/inf	nasal	nsl/sup	nsl/inf
Sensitivity (%)	96	80	60	68	80	72	72	88
Specificity (%)	36	66	88	90	66	57	70	61

tmp: temporal
nsl: nasal
sup: superior
inf: inferior

doi:10.1371/journal.pone.0118920.t005

Table 6. The results of the logistic regression analysis with a stepwise method, in which glaucoma was the outcome variable among all subjects.

Variable	Odds Ratio	95% Confidence Interval	P
Cup volume ($\times 10^{-1}$)	0.83	0.67 - 1.03	0.10
C/D area ($\times 10^{-1}$)	2.72	1.70 - 4.52	<.0001
HVC ($\times 10^{-1}$)	3.14	1.80 - 5.81	0.0001
RNFL CS	0.085	0.021 - 0.31	0.0003

doi:10.1371/journal.pone.0118920.t006

The Differences in the Morphological Features of Large Discs Between Glaucomatous and Non-glaucomatous Eyes

Our results showed that all of the parameters related to disc cupping, viz., the cup area, cup volume, cup-to-disc area ratio, linear cup/disc ratio, mean cup disc and maximum cup depth, were significantly larger in the eyes with glaucoma than in the eyes without glaucoma. The parameters related to the disc rim, viz., the rim area, rim volume and the circumpapillary nerve fiber layer thickness (mean RNFL thickness, RNFL cross-sectional area) in glaucomatous eyes were significantly smaller than those in eyes without glaucoma.

Similar findings were previously noted in eyes with normal-sized optic discs. For example, Medeiros reported that the rim-related parameters, including the rim area, rim volume and rim-to-disc area, of glaucomatous eyes were significantly smaller than those in eyes without glaucoma [24]. Medeiros also reported statistically significant differences in the cup parameters, viz., the cup-to-disc area ratio and the linear cup-to-disc ratio, between glaucomatous and non-glaucomatous eyes with normal-sized optic discs [24]. Uchida et al. reported that the area and volume of the optic cup were significantly larger in glaucomatous eyes than in normal eyes [20].

Our results on eyes with large optic discs showed that the maximum cup depth and mean cup depth in the early stage glaucoma group was significantly larger than those in the non-glaucomatous group (Table 2). However, the differences in these parameters between the early stage and advanced stage glaucoma groups were small, and the differences were not significant. Thus, the evaluation of whether glaucoma has progressed by using the cup depth parameters does not lead to accurate results. On the other hand, the rim area in advanced glaucomatous eyes was significantly smaller than that in the early stage glaucomatous subjects, and the cup-to-disc area ratio and linear cup/disc ratio were significantly larger in advanced stage than in early stage glaucomatous eyes. These results indicate that the cup depth reaches its maximum change at the early stage of glaucoma, but that the rim thinning continues to decrease for a longer duration in eyes with large optic discs.

Diagnosing Glaucoma by the HRT Stereometric Parameters in Eyes with Large Optic Discs

We used the stereometric parameters determined by HRT II to create a new formula for eyes with a large optic disc. We used the MRA to determine the validity of the new formula, because it is the default program included for the HRT II and is easy to use. The MRA uses the disc rim area, disc area and age for its calculations. In our study, an increase in the cup-to-disc area ratio, an increase in the HVC and a reduction of the RNFL cross-sectional area were risk factors for glaucoma. The HVC is the difference in the height between the highest retinal surface and the lowest retinal surface along the contour line. The RNFL cross-sectional area is the average distance between the retinal surface and a standard point along the contour line of the disc

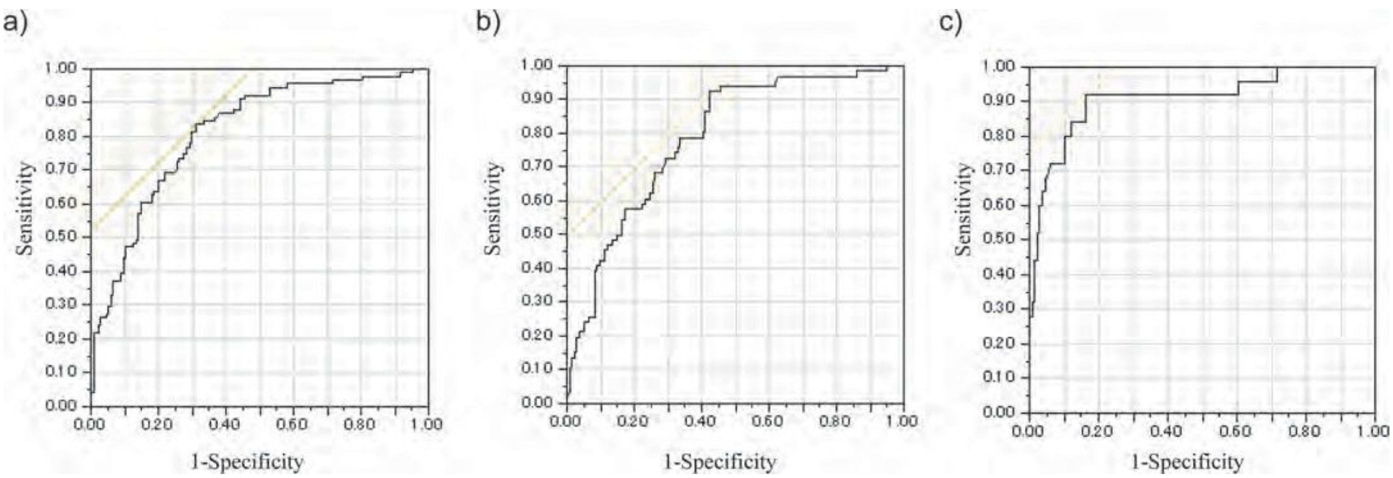

Fig 2. The ROC curves of the logistic regression analyses with the stepwise method in which glaucoma was the outcome variable among all subjects.

doi:10.1371/journal.pone.0118920.g002

x the length of contour line. Both parameters are related to the thickness of the circumpapillary retinal nerve fiber layer. An increase of the HVC and decrease of the RNFL cross-sectional area suggest glaucomatous changes, because the RNFL becomes thinner in glaucomatous eyes. The diagnostic power, which is the sum of the sensitivity and specificity, of our new formula that included the cup volume, cup-to-disc area ratio, HVC and RNFL cross-sectional area was 1.53, whereas the diagnostic power of the MRA was 1.25. The large discs are identical to normal-sized discs in terms of the RNFL thickness [10,25]. Oddone et al. showed that the diagnostic accuracy of quantitative RNFL assessments measured with Cirrus HD-OCT and GDx-VCC is high and insignificantly affected by the size of the optic disc [26]. Furthermore, they reported that it may provide more consistent diagnostic outcomes across small and large discs when compared with the optic nerve head assessment, such as the MRA program measured with HRT [26]. Therefore, it is important to evaluate the parameters related to the retinal nerve fiber thickness, which are not affected by the disc size, to diagnose glaucoma in eyes with large optic discs.

The parameters related to the RNFL thickness were not selected by a logistic regression analysis when we differentiated eyes in the advanced stage and non-glaucomatous groups. These findings are not contradictory to the study by Hood et al., who reported a good correlation between the circumpapillary RNFL thickness obtained by OCT and the visual field loss (Mean Deviation, MD) when the field loss was >-6 dB. This is because when the MD is <-6.0 dB, the RNFL changes are too small to detect the progression of glaucoma [27].

Table 7. The results of the logistic regression analysis with the stepwise method, in which glaucoma was the outcome variable between the non-glaucomatous group and the early stage glaucoma group.

Variable	Odds Ratio	95% Confidence Interval			P
C/D area ($\times 10^{-1}$)	1.71	1.25	-	2.38	0.001
HVC ($\times 10^{-1}$)	3.42	1.93	-	6.45	<.0001
RNFL CS	0.073	0.018	-	0.27	<.0001

doi:10.1371/journal.pone.0118920.t007

Table 8. The results of the logistic regression analysis with the stepwise method, in which glaucoma was the outcome variable between the non-glaucomatous group and the advanced stage glaucoma group.

Variable	Odds Ratio	95% Confidence Interval			P
Cup volume (×10^{-1})	0.54	0.35	-	0.77	0.002
C/D area (×10^{-1})	11.96	5.23	-	33.77	<0.001

doi:10.1371/journal.pone.0118920.t008

Another interesting result of this study was the high incidence, 40.4%, of glaucoma in eyes with a large optic disc. In the general population, the incidence of glaucoma was 5.0% in the Tajimi study and 3.5% in the Namil study [28,29]. It is difficult to draw conclusions about the prevalence of glaucoma in cases with large discs, because this was a single center case-control study. However, all subjects with a disc > 2.82mm^2 by HRT II were included in this study. This suggested that a large optic disc may be a risk factor for glaucoma. Our present findings are similar to past reports suggesting that a large optic disc is a risk factor for glaucoma [30–32].

There are a few limitations associated with our study. First, this was a single center, case-control study, and we analyzed both eyes of each patient when the subjects had large discs in both eyes. Abe et al. reported that all HRT parameters were significantly correlated between right and left eyes. However, their results suggested that subjects with larger discs tended to show greater inter-eye absolute differences in these HRT parameters [33]. In our 147 consecutive cases, 69 subjects had a large disc in one eye and 78 subjects had a large disc in both eyes. The disc features were not correlated between the right and left eyes. This is the reason why we included the data from both eyes even when both eyes had a large disc. Second, we have not confirmed the ability of our new formula to discriminate the glaucoma group from the non-glaucoma group in another set of subjects with a large optic disc area.

In conclusion, our data indicate that the cup-to-disc area ratio, HVC and RNFL cross-sectional area are significant HRT parameters that are more appropriate for diagnosing early stage glaucoma, and an increase in the cup-to-disc area ratio and a decrease of the cup volume were risk factors for advanced glaucoma in eyes with large optic discs.

Supporting Information

S1 Dataset. The patients' information, HFA, and HRT data.
(XLS)

Author Contributions

Conceived and designed the experiments: SO YK TS. Performed the experiments: SO. Analyzed the data: SO KY. Contributed reagents/materials/analysis tools: SO KY TS. Wrote the paper: SO KY.

References

1. Sommer A, Pollack I, Maumenee AE. Optic disc parameters and onset of glaucomatous field loss. II. Static screening criteria. Arch Ophthalmol. 1979; 97: 1449–1454. PMID: 464867
2. Sommer A, Katz J, Quigley HA, Miller NR, Robin AL, Richter RC, et al. Clinically detectable nerve fiber atrophy precedes the onset of glaucomatous field loss. Arch Ophthalmol. 1991; 109: 77–83. PMID: 1987954
3. Quigley HA, Miller NR, George T. Clinical evaluation of nerve fiber layer atrophy as an indicator of glaucomatous optic nerve damage. Arch Ophthalmol. 1980; 98: 1564–1571. PMID: 7425916

4. Quigley HA, Katz J, Derick RJ, Gilbert D, Sommer A. An evaluation of optic disc and nerve fiber layer examinations in monitoring progression of early glaucoma damage. Ophthalmology. 1992; 99: 19–28. PMID: 1741133
5. Quigley HA, Green WR. The histology of human glaucoma cupping and optic nerve damage: clinicopathologic correlation in 21 eyes. Ophthalmology. 1979; 86: 1803–1830. PMID: 553256
6. Pederson JE, Anderson DR. The mode of progressive disc cupping in ocular hypertension and glaucoma. Arch Ophthalmol. 1980; 98: 490–495. PMID: 7362506
7. Jonas JB, Bergua A, Schmitz-Valckenberg P, Papastathopoulos KI, Budde WM. Ranking of optic disc variables for detection of glaucomatous optic nerve damage. Invest Ophthalmol Vis Sci. 2000; 41: 1764–1773. PMID: 10845597
8. Foster PJ, Buhrmann R, Quigley HA, Johnson GJ. The definition and classification of glaucoma in prevalence surveys. Br J Ophthalmol. 2002; 86: 238–242. PMID: 11815354
9. Hoffmann EM, Zangwill LM, Crowston JG, Weinreb RN. Optic disk size and glaucoma. Surv Ophthalmol. 2007; 52: 32–49. PMID: 17212989
10. Onmez FE, Satana B, Altan C, Basarir B, Demirok A. A comparison of optic nerve head topographic measurements by Stratus OCT in patients with macrodiscs and normal-sized healthy discs. J Glaucoma. 2014; 23: e152–156. doi: 10.1097/IJG.0000000000000021 PMID: 24240877
11. Wollstein G, Garway-Heath DF, Hitchings RA. Identification of early glaucoma cases with the scanning laser ophthalmoscope. Ophthalmology. 1998; 105: 1557–1563. PMID: 9709774
12. Miglior S, Guareschi M, Albe E, Gomarasca S, Vavassori M, Orzalesi N. Detection of glaucomatous visual field changes using the Moorfields regression analysis of the Heidelberg retina tomograph. Am J Ophthalmol. 2003; 136: 26–33. PMID: 12834666
13. Miglior S, Albe E, Guareschi M, Rossetti L, Orzalesi N. Intraobserver and interobserver reproducibility in the evaluation of optic disc stereometric parameters by Heidelberg Retina Tomograph. Ophthalmology. 2002; 109: 1072–1077. PMID: 12045046
14. Saito H, Tsutsumi T, Araie M, Tomidokoro A, Iwase A. Sensitivity and specificity of the Heidelberg Retina Tomograph II Version 3.0 in a population-based study: the Tajimi Study. Ophthalmology. 2009; 116: 1854–1861. doi: 10.1016/j.ophtha.2009.03.048 PMID: 19660814
15. Mikelberg FS, Parfitt CM, Swindale NV, Graham SL, Drance SM, Gosine R. Ability of the heidelberg retina tomograph to detect early glaucomatous visual field loss. J Glaucoma. 1995; 4: 242–247. PMID: 19920681
16. Iester M, Mikelberg FS, Drance SM. The effect of optic disc size on diagnostic precision with the Heidelberg retina tomograph. Ophthalmology. 1997; 104: 545–548. PMID: 9082287
17. Bathija R, Zangwill L, Berry CC, Sample PA, Weinreb RN. Detection of early glaucomatous structural damage with confocal scanning laser tomography. J Glaucoma. 1998; 7: 121–127. PMID: 9559499
18. Ford BA, Artes PH, McCormick TA, Nicolela MT, LeBlanc RP, Chauhan BC. Comparison of data analysis tools for detection of glaucoma with the Heidelberg Retina Tomograph. Ophthalmology. 2003; 110: 1145–1150. PMID: 12799239
19. Anderson DR, Patella VM. Automated static perimetry. St. Louis: Mosby; 1999.
20. Uchida H, Brigatti L, Caprioli J. Detection of structural damage from glaucoma with confocal laser image analysis. Invest Ophthalmol Vis Sci. 1996; 37: 2393–2401. PMID: 8933756
21. Teesalu P, Vihanninjoki K, Airaksinen PJ, Tuulonen A, Laara E. Correlation of blue-on-yellow visual fields with scanning confocal laser optic disc measurements. Invest Ophthalmol Vis Sci. 1997; 38: 2452–2459. PMID: 9375562
22. Vihanninjoki K, Burk RO, Teesalu P, Tuulonen A, Airaksinen PJ. Optic disc biomorphometry with the Heidelberg Retina Tomograph at different reference levels. Acta Ophthalmol Scand. 2002; 80: 47–53. PMID: 11906304
23. Tan JC, Hitchings RA. Reference plane definition and reproducibility in optic nerve head images. Invest Ophthalmol Vis Sci. 2003; 44: 1132–1137. PMID: 12601040
24. Medeiros FA, Vizzeri G, Zangwill LM, Alencar LM, Sample PA, Weinreb RN. Comparison of retinal nerve fiber layer and optic disc imaging for diagnosing glaucoma in patients suspected of having the disease. Ophthalmology. 2008; 115: 1340–1346. doi: 10.1016/j.ophtha.2007.11.008 PMID: 18207246
25. Costa AM, Cronemberger S. Optic disc and retinal nerve fiber layer thickness descriptive analysis in megalopapilla. J Glaucoma. 2014; 23: 368–371. doi: 10.1097/IJG.0b013e318279b3af PMID: 23296371
26. Oddone F, Centofanti M, Tanga L, Parravano M, Michelessi M, Schiavone M, et al. Influence of disc size on optic nerve head versus retinal nerve fiber layer assessment for diagnosing glaucoma. Ophthalmology. 2011; 118: 1340–1347. doi: 10.1016/j.ophtha.2010.12.017 PMID: 21474186

27. Hood DC, Anderson SC, Wall M, Raza AS, Kardon RH. A test of a linear model of glaucomatous structure-function loss reveals sources of variability in retinal nerve fiber and visual field measurements. Invest Ophthalmol Vis Sci. 2009; 50: 4254–4266. doi: 10.1167/iovs.08-2697 PMID: 19443710
28. Kim CS, Seong GJ, Lee NH, Song KC. Prevalence of primary open-angle glaucoma in central South Korea the Namil study. Ophthalmology. 2011; 118: 1024–1030. doi: 10.1016/j.ophtha.2010.10.016 PMID: 21269703
29. Iwase A, Suzuki Y, Araie M, Yamamoto T, Abe H, Shirato S, et al. The prevalence of primary open-angle glaucoma in Japanese: the Tajimi Study. Ophthalmology. 2004; 111: 1641–1648. PMID: 15350316
30. Tuulonen A, Airaksinen PJ. Optic disc size in exfoliative, primary open angle, and low-tension glaucoma. Arch Ophthalmol. 1992; 110: 211–213. PMID: 1736870
31. Tomita G, Nyman K, Raitta C, Kawamura M. Interocular asymmetry of optic disc size and its relevance to visual field loss in normal-tension glaucoma. Graefes Arch Clin Exp Ophthalmol. 1994; 232: 290–296. PMID: 8045438
32. Burk RO, Rohrschneider K, Noack H, Volcker HE. Are large optic nerve heads susceptible to glaucomatous damage at normal intraocular pressure? A three-dimensional study by laser scanning tomography. Graefes Arch Clin Exp Ophthalmol. 1992; 230: 552–560. PMID: 1427140
33. Abe H, Shirakashi M, Tsutsumi T, Araie M, Tomidokoro A, Iwase A, et al. Laser scanning tomography of optic discs of the normal Japanese population in a population-based setting. Ophthalmology. 2009; 116: 223–230. doi: 10.1016/j.ophtha.2008.09.013 PMID: 19084274

Retina

Macular Choroidal Thickness and Volume in Healthy Pediatric Individuals Measured by Swept-Source Optical Coherence Tomography

Toshihiko Nagasawa,[1,2] Yoshinori Mitamura,[3] Takashi Katome,[3] Kayo Shinomiya,[3] Takeshi Naito,[3] Daisuke Nagasato,[1] Yukiko Shimizu,[1] Hitoshi Tabuchi,[1] and Yoshiaki Kiuchi[2]

[1]Department of Ophthalmology, Saneikai Tsukazaki Hospital, Himeji, Japan
[2]Department of Ophthalmology and Visual Sciences, Graduate School of Biomedical Sciences, Hiroshima University, Hiroshima, Japan
[3]Department of Ophthalmology, Institute of Health Biosciences, The University of Tokushima Graduate School, Tokushima, Japan

Correspondence: Yoshinori Mitamura, Department of Ophthalmology, Institute of Health Biosciences, The University of Tokushima Graduate School, 3-18-15 Kuramoto, Tokushima 770-8503, Japan; ymita@tokushima-u.ac.jp.

Submitted: May 3, 2013
Accepted: September 22, 2013

Citation: Nagasawa T, Mitamura Y, Katome T, et al. Macular choroidal thickness and volume in healthy pediatric individuals measured by swept-source optical coherence tomography. Invest Ophthalmol Vis Sci. 2013;54:7068–7074. DOI:10.1167/iovs.13-12350

PURPOSE. We evaluated the choroidal thickness and volume in healthy pediatric individuals by swept-source optical coherence tomography (SS-OCT) and compared the findings to those of adults.

METHODS. We examined 100 eyes of 100 healthy pediatric volunteers (3–15 years) and 83 eyes of 83 healthy adult volunteers (24–87 years) by SS-OCT with a tunable long wavelength laser source. The three-dimensional raster scan protocol was used to construct a choroidal thickness map. When the built-in software delineated an erroneous chorioscleral border in the B-scan images, manual segmentation was used.

RESULTS. The central choroidal thickness and volume within a 1.0-mm circle were significantly larger in the children (260.4 6 57.2 1m, 0.205 6 0.045 mm^3) than in the adults (206.1 6 72.5 1m, 0.160 6 0.056 mm^3, both $P < 0.0001$). In the children, the mean choroidal thickness of the nasal area was significantly thinner than that of all other areas ($P < 0.005$). Pediatric choroidal thinning with increasing age in the central area was faster than that in the outer areas. Stepwise regression analysis showed that the axial length and body mass index had the highest correlation with the choroidal thickness (R^2 ¼ 0.313, $P < 0.0001$).

CONCLUSIONS. The macular choroidal thickness and volume in the pediatric individuals were significantly larger than those in the adults. The pediatric choroidal thinning with increasing age is more rapid in the central area. Pediatric choroidal thickness is associated with several systemic or ocular parameters, especially the axial length and body mass index. These differences should be remembered when the choroidal thickness is evaluated in pediatric patients with retinochoroidal diseases.

Keywords: swept-source optical coherence tomography, choroidal thickness, choroidal volume, pediatric individual, adult

---

Enhanced depth imaging (EDI) optical coherence tomography (OCT) based on spectral-domain OCT (SD-OCT) technology has allowed clinicians to examine the choroidal thickness in healthy eyes and eyes with various pathologies.[1–6]

Swept-source OCT (SS-OCT) uses a swept wavelength laser as the light source,[7,8] and a recently developed SS-OCT instrument has an A-scan repetition rate of 100,000 Hz. When the coherence length of the source is appropriate, SS-OCT can achieve much less roll-off in sensitivity with increasing depth than with the standard SD-OCT.[9] In addition, the current SS-OCT instrument uses a longer center wavelength, which improved its ability to penetrate deeply into tissues.

With this SS-OCT instrument, precise evaluations of deeper structures of the eye, such as the choroid and retrobulbar optic nerve, are possible.[10] Ikuno et al.[11] studied the choroidal thickness of healthy adult subjects with an SS-OCT. Because the current SS-OCT instrument has a high scan rate and a relatively low sensitivity roll-off versus depth, a three-dimensional (3D) high contrast image of the choroid can be obtained.[12–14] Recently, Hirata et al.[15] constructed a choroidal thickness map using the 3D raster scan protocol of the SS-OCT, and they investigated the macular choroidal thickness and volume of healthy adults.

The choroidal thickness determined by EDI-OCT or SS-OCT has been reported to decrease with age in healthy adult eyes.[3,11,15–18] However, information on the choroidal thickness in children remains limited.[19–21] In these studies, the choroidal thickness of only a few sampling points[19,20] or the average choroidal thickness on the scan line[21] was examined. Thus, the exact choroidal thickness could not be determined, because the thickness can be affected by focal changes,[22,23] and by irregularities of the chorioscleral border.[5] In addition, the location of the chorioscleral border was done manually. It would be better to construct a map of the choroid with the borders selected objectively to overcome these limitations.

Thus, the purpose of this study was to determine the choroidal thickness and volume by constructing choroidal thickness maps in a pediatric population. To accomplish this,

www.iovs.org j ISSN: 1552-5783

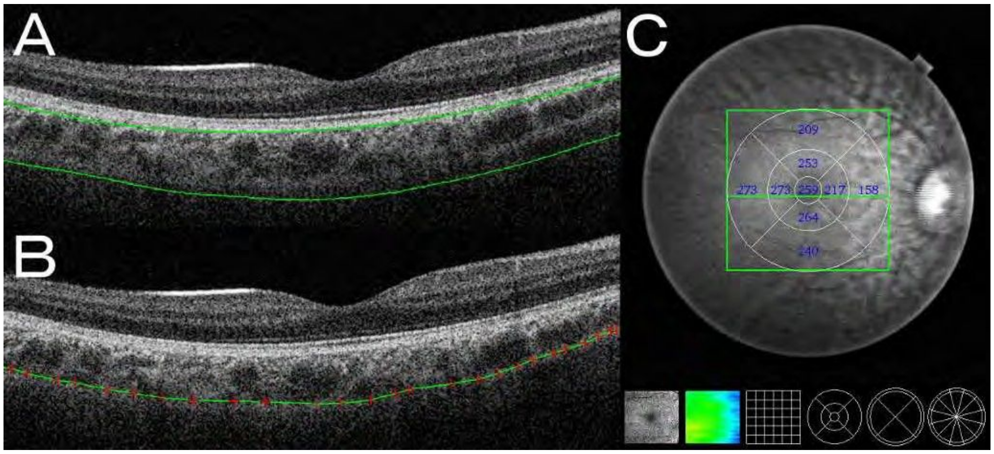

FIGURE 1. Choroidal thickness map of a healthy 7-year-old boy obtained by SS-OCT. The 3D raster scan protocol with 512 A-scans 3 256 B-scans was used to obtain 3D imaging data of the 6 3 6-mm area. (A) Erroneous placement of the chorioscleral border made by the automatic built-in software in one of the B-scan images of the 3D data set. Although the tracing of the retinal pigment epithelium is correct, that of the chorioscleral border is not accurate. (B) Manual segmentation of the chorioscleral border in the same B-scan image. Only when the built-in software delineated an erroneous chorioscleral border, manual segmentation was performed. (C) By analyzing the B-scan images of the 3D data set, a choroidal thickness map of the 6 3 6-mm area centered on the fovea was created. By applying the ETDRS grid to the map, the mean choroidal thickness was obtained for each sector.

we scanned the macular area of healthy pediatric eyes using the 3D raster scan protocol, and constructed a choroidal thickness map. By using the Early Treatment Diabetic Retinopathy Study (ETDRS)[24] grid for the choroidal thickness maps, we were able to determine the mean choroidal thickness and volume in each sector of the grid. The findings obtained from the pediatric individuals were compared to those obtained from adults.

SUBJECTS AND METHODS

We studied 100 eyes of 100 healthy pediatric volunteers, with a mean 6 SD age of 7.9 6 3.1 years and a range from 3 to 15 years (45 boys and 55 girls), and 83 eyes of 83 healthy adult volunteers, with a mean age of 54.5 6 19.3 years and a range from 24 to 87 years (43 men and 40 women) at Saneikai Tsukazaki Hospital and Tokushima University Hospital. All subjects had no ophthalmic or systemic signs or symptoms. One eye was chosen randomly for the statistical analyses. The procedures used conformed to the tenets of the Declaration of Helsinki, and an informed consent was obtained from either the subjects or their legal guardians after explanation of the nature and possible consequences of the study. An approval was obtained from the Institutional Review Board of Saneikai Tsukazaki Hospital and Tokushima University Hospital to perform this study.

All subjects underwent standard ophthalmologic examinations, including measurements of the best-corrected visual acuity (BCVA), applanation tonometry, slit-lamp biomicroscopy, indirect ophthalmoscopy, autorefractometry (ARK1; Nidek, Gamagori, Japan), and axial length measurements with the IOLMaster (Carl Zeiss Meditec, Jena, Germany). All of the examinations were performed on the same day. The BCVA was measured with a standard Japanese Landolt visual acuity chart. All of the healthy pediatric volunteers had a BCVA that ranged from 0.6 to 1.5, and all adults had a BCVA that ranged from 0.9 to 1.5. The body height and weight were recorded, and the body mass index was calculated for each subject. The exclusion criteria included history of intraocular surgery; history or evidence of chorioretinal or vitreoretinal diseases, such as central serous chorioretinopathy; refractive errors (spherical equivalent) greater than 66 diopters (D); and evidence of glaucoma. Subjects with systemic disease that might affect the choroidal thickness, such as diabetes mellitus, also were excluded.

Swept-source Optical Coherence Tomography

The macular area of the eyes was examined with the SS-OCT instrument (DRI OCT-1; Topcon, Tokyo, Japan), which was government approved for use in Japan. The light source of this SS-OCT system is a wavelength tunable laser centered at 1050 nm with an approximate 100-nm tuning range. The tissue imaging depth was 2.6 mm.

After pupillary dilation, the SS-OCT examinations were performed by trained examiners. The 3D volumetric raster scan protocol was used, and 3D volumetric data were acquired in 0.8 seconds. Each 3D scan covered an area of 6 3 6 mm centered on the fovea with 512 A-scans 3 256 B-scans. To improve the image quality, 4 consecutive B-scan images of the same area were averaged. Because of the infrared scanning light, eye movements during the scans were minimized. All examinations were performed from 2:00 PM to 5:00 PM to reduce the effects of diurnal variations.[25,26]

Choroidal Thickness and Volume Measurement

From a series of 64 B-scan OCT images, each of which was created by averaging 4 consecutive B-scans, a choroidal thickness map of a 6 3 6 mm area was created by semiautomatic segmentation. Using the built-in software, the choroidal thickness was measured as the distance between the outer border of the RPE and the inner surface of the chorioscleral border. In the analyses of the 64 B-scan images, each scanned OCT image was examined to be certain that a proper tracing of the chorioscleral border had been made. When the built-in software delineated an inaccurate chorioscleral border (Fig. 1A), a manual segmentation was made by trained observers in a masked fashion (Fig. 1B).

The ETDRS grid was used for the choroidal thickness map (Fig. 1C), and the mean regional thicknesses were calculated for the nine sectors of the grid.[15,27] The inner and outer rings had diameters of 1 to 3 and 3 to 6 mm, respectively, and they were divided into superior, inferior, temporal, and nasal

TABLE 1. Comparisons of the Choroidal Thickness and Volume Between Healthy Pediatric and Adult Individuals

	Pediatric Individuals	Adult Individuals	P Value
Eyes, n	100	83	
Mean age, y	7.9 ± 3.1	54.5 ± 19.3	<0.0001
Mean axial length, mm	23.13 ± 1.37	24.14 ± 1.17	<0.0001
Mean refractive error, D	−0.04 ± 1.96	−0.25 ± 2.42	0.5256
Central choroidal thickness, 1.0-mm circle, μm	260.4 ± 57.2	206.1 ± 72.5	<0.0001
Macular choroidal thickness, 3.0-mm circle, μm	255.2 ± 52.3	201.8 ± 68.6	<0.0001
Macular choroidal thickness, 6.0-mm circle, μm	240.3 ± 45.6	190.8 ± 63.2	<0.0001
Central choroidal volume, 1.0-mm circle, mm^3	0.205 ± 0.045	0.160 ± 0.056	<0.0001

quadrants. The individual sectors are referred to as the central, inner temporal, inner superior, inner inferior, inner nasal, outer temporal, outer superior, outer inferior, and outer nasal sectors. In addition, the macular choroidal thickness within a circle of 3.0- or 6.0-mm diameter, and within an inner or outer ring was calculated. Based on the choroidal thicknesses obtained, we calculated the choroidal volume for each sector of the ETDRS grid.

Measurement of Reproducibility

Because the segmentation was done manually in some images, we evaluated the interobserver reproducibility of the corrections. The chorioscleral border in the OCT images of one raster scan was adjusted by two observers in 14 selected pediatric individuals before the study.[15] The thickness maps and mean choroidal thicknesses were calculated independently, and the intraclass correlation coefficient (ICC) for each ETDRS sector was calculated.

In addition, the methods described by Bland and Altman[28] was used to evaluate interobserver reproducibility.[29] The mean difference between two choroidal thickness measurements (Observer 1 − Observer 2) for each of the 14 individuals represented the bias. The 95% limits of agreement (LoA), the expected difference between two measurements, were calculated as the mean of the differences ± 1.96 × SD of the differences.

Statistical Analyses

Student's t-tests were used to determine the significance of the differences in the age, axial length, refractive errors, central or macular choroidal thickness, and central choroidal volume between the pediatric and adult individuals. Data were analyzed using one factor ANOVA and Fisher's post hoc least significant difference (PSLD) test to compare the choroidal thickness or volume in three or more groups. The correlations between choroidal thickness and systemic or ocular parameters were determined by Pearson's correlation tests for simple regression analysis and forward stepwise multiple regression analysis. The differences in the choroidal thickness between boys and girls were tested by χ^2 tests. All analyses were done with the SPSS version 20.0 (SPSS Japan, Tokyo, Japan). A P value < 0.05 was considered statistically significant.

RESULTS

None of the eyes was excluded because of unreliable measurements of the choroidal thickness. Even in pediatric individuals, none of the eyes was excluded because of eye movements during the scanning procedure.

Comparisons of Choroidal Thickness and Volume Between Pediatric and Adult Individuals

The mean axial length in the pediatric individuals was significantly shorter than that in the adults ($P < 0.0001$, Table 1). The mean refractive error in the pediatric individuals was not significantly different from that of the adults ($P = 0.5256$).

The central choroidal thickness and volume within a 1.0-mm circle were significantly greater in the pediatric individuals (260.4 ± 57.2 μm, 0.205 ± 0.045 mm^3, respectively) than in the adults (206.1 ± 72.5 μm, 0.160 ± 0.056 mm^3, respectively; both $P < 0.0001$; Table 1). The macular choroidal thickness within a circle of 3.0- and 6.0-mm diameter in the children was significantly thicker than that of the adults (both $P < 0.0001$).

Choroidal Thickness and Volume in ETDRS Sectors

In the pediatric individuals, the choroidal thicknesses in the four inner and four outer sectors were significantly different (both $P < 0.0001$, Table 2). The inner and outer nasal choroid

TABLE 2. Choroidal Thickness and Volume in ETDRS Grid Sectors in Pediatric and Adult Individuals

	Pediatric Individuals		Adult Individuals
Area	Choroidal Volume, mm^3	Mean Choroidal Thickness, μm	Mean Choroidal Thickness, μm
Center	0.205 ± 0.045	260.4 ± 57.2	206.1 ± 72.5
Inner temporal	0.423 ± 0.081*	269.4 ± 51.9*	206.3 ± 74.2
Inner superior	0.407 ± 0.086*	259.1 ± 54.4*	212.0 ± 70.6
Inner inferior	0.404 ± 0.084*	257.1 ± 53.8*	202.0 ± 74.7
Inner nasal	0.365 ± 0.091	232.2 ± 58.0	189.6 ± 70.5
Outer temporal	1.388 ± 0.238†	262.0 ± 44.9†	197.7 ± 69.2†
Outer superior	1.327 ± 0.249†	250.3 ± 47.0†	213.4 ± 69.7†
Outer inferior	1.300 ± 0.255†	245.2 ± 48.1†	194.6 ± 68.9†
Outer nasal	0.971 ± 0.296	182.7 ± 53.0	147.8 ± 60.9

* Significantly larger than values of inner nasal area ($P < 0.005$).

† Significantly larger than values of outer nasal area ($P < 0.0001$).

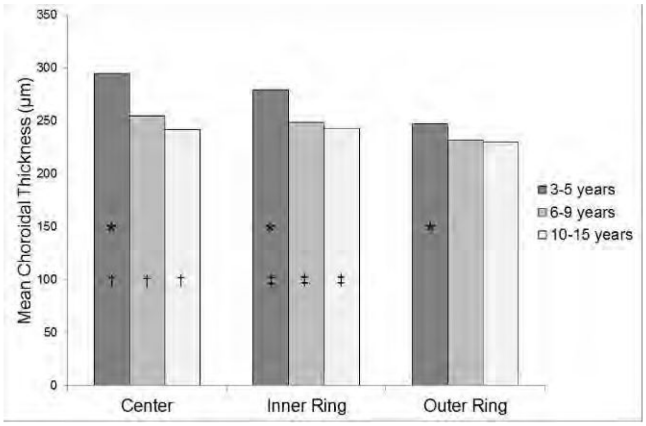

FIGURE 2. Pediatric choroidal thinning with increasing age in the central, inner ring, and outer ring areas of ETDRS grid. The mean choroidal thicknesses in the 3- to 5-year-old (n ¼ 25), 6- to 9-year-old (n ¼ 42), and 10- to 15-year-old (n ¼ 33) age groups are presented. The choroidal thinning with increasing age appears to be more rapid in the central area than in the inner and outer rings. *P ¼ 0.0057, †P ¼ 0.0011, ‡P ¼ 0.0191.

was significantly thinner than choroid of the other three inner and outer sectors (all P < 0.005). The choroidal thickness of the temporal sector was the thickest followed by the superior, inferior, and nasal choroid. However, differences among the temporal, superior, and inferior sectors of the inner and outer rings were not statistically significant.

In the adults, the choroidal thicknesses of the four inner sectors were not significantly different (P ¼ 0.2347), but the outer choroidal thicknesses were significantly different among the four sectors (P < 0.0001). The outer nasal choroid was significantly thinner than that of the other three outer sectors (all P < 0.0001). The superior choroid was thickest, followed by the temporal, inferior, and nasal choroid; however, the majority of the differences were not significant.

Changes of the choroidal thickness maps associated with age are presented in Figure 2 and Table 3. In the pediatric individuals, the choroidal thinning with increasing age appeared to be more rapid in the central area than in the inner and outer rings (Fig. 2). The differences in the mean choroidal thicknesses among the 3- to 5-year-old, 6- to 9-year-old, and 10- to 15-year-old age groups were significant in the central and inner ring areas (P ¼ 0.0011, P ¼ 0.0191, respectively), but not in the outer ring area (P ¼ 0.2551). The differences in the mean choroidal thicknesses of the central, inner ring, and outer ring areas were significant in the 3- to 5-year-old age group (P ¼ 0.0057), but not in the 6- to 9-year-old and 10- to 15-year-old age groups (P ¼ 0.1081, P ¼ 0.4401, respectively), with a rapid decrease in the central choroidal thickness. In pediatric and adult individuals. The most remarkable decrease in choroidal thickness was seen between the 41- to 55-year-old and 56- to 70-year-old groups, although some of the adult age groups had only a small number of eyes (Table 3).

TABLE 3. Changes of the Mean Choroidal Thickness in ETDRS Grid Associated With Age

	Eyes, n	Center, 1m	Inner Ring, 1m	Outer Ring, 1m
Pediatric individuals				
3–15 y	100	260.4 6 57.2	254.4 6 52.0	235.0 6 43.3
Adult individuals				
24–40 y	25	247.7 6 51.6	241.7 6 49.8	229.1 6 44.4
41–55 y	14	221.5 6 67.2	220.1 6 63.4	203.4 6 45.4
56–70 y	19	190.1 6 71.3	189.2 6 68.1	172.8 6 62.9
71–87 y	25	168.1 6 73.3	163.5 6 69.4	151.1 6 57.9

TABLE 4. Simple Regression Analysis for Correlations Between the Mean Choroidal Thickness of the Macular Area and the Age, Axial Length, Body Height, Body Weight, Body Mass Index, or Refractive Error in Pediatric Individuals

	Central Choroidal Thickness, 1.0-mm Circle, 1m	Macular Choroidal Thickness, 6.0-mm Circle, 1m
Age, y	r ¼ −0.404 P < 0.0001	r ¼ −0.274 P ¼ 0.0056
Axial length, mm	r ¼ −0.525 P < 0.0001	r ¼ −0.448 P < 0.0001
Body height, cm	r ¼ −0.419 P < 0.0001	r ¼ −0.299 P ¼ 0.0024
Body weight, kg	r ¼ −0.412 P < 0.0001	r ¼ −0.329 P ¼ 0.0008
Body mass index	r ¼ −0.293 P ¼ 0.0030	r ¼ −0.272 P ¼ 0.0060
Refractive error, D	r ¼ 0.325 P ¼ 0.0009	r ¼ 0.297 P ¼ 0.0025

Simple Regression Analysis for Correlations Between Choroidal Thickness, and Systemic and Ocular Parameters in Pediatric Individuals

Simple linear regression analysis showed that the central choroidal thickness was correlated significantly with the age, axial length, body height, body weight, body mass index, and refractive error (all P < 0.005, Table 4). The central choroidal thickness was significantly thicker in girls (274.1 6 62.1 1m) than in boys (247.9 6 46.6 1m, P ¼ 0.0255). The correlations between the macular choroidal thickness within a circle of 6.0-mm diameter and systemic and ocular parameters were similar to the results for the central choroidal thickness (Table 4).

Multiple Regression Analysis for Correlations Between Choroidal Thickness, and Systemic and Ocular Parameters in Pediatric Individuals

Multiple linear regression analysis of the mean central choroidal thickness by age, axial length, body height, body weight, body mass index, and refractive error was performed. A forward stepwise method was used to determine factors associated most with the choroidal thickness. The highest correlation was between the choroidal thickness, and the axial length and body mass index, with a determination coefficient (R^2) of 0.313 (P < 0.0001, Fig. 3). Using analysis of covariance, the effects of the age group (pediatric or adult group), axial length, and body mass index on the central choroidal thickness were evaluated. After adjustment for the axial length and body mass index, the central choroidal thickness was no longer significantly correlated with the age group (P ¼ 0.632).

Interobserver Reproducibility of Choroidal Thickness

In all the pediatric and adult individuals, manual segmentation was performed in 180 of the 183 eyes. Proportion of the scans needed for manual segmentation to all the 64 scans was calculated in each subject. The mean percentage of manual

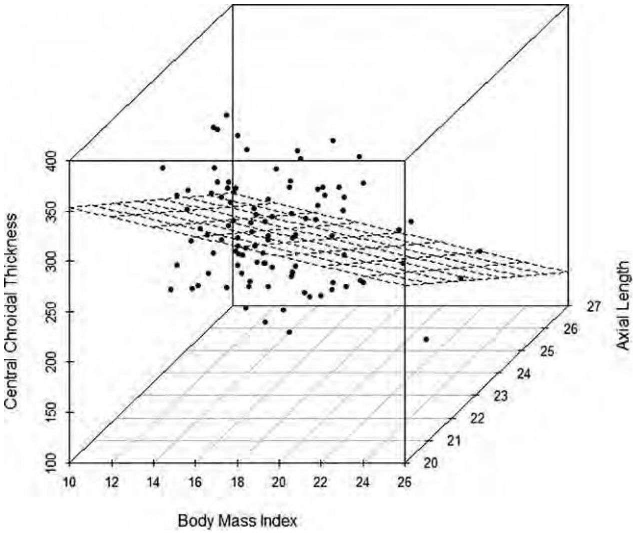

FIGURE 3. Three-dimensional scatterplot of the body mass index (x-axis), central choroidal thickness (y-axis), and axial length (z-axis). The model shows a relatively good coefficient of determination (R^2¼ 0.313, $P < 0.0001$). Mean central choroidal thickness ¼ 807.933 – 20.229 3 axial length – 4.906 3 body mass index.

segmentation required was 25.1 6 20.7%. A proper tracing of the RPE was confirmed in all images of all subjects.

Before this study, the chorioscleral border was corrected independently by the two observers in 14 pediatric individuals.[15] The ICCs for the mean choroidal thickness of each ETDRS grid sector that was measured by the two observers are shown in Table 5. The mean choroidal thickness had a high ICC (from 0.9908–0.9995) between the two observers ($P <$ 0.0001).

For the Bland and Altman plots, the mean difference in the choroidal thickness of the nine ETDRS grid sectors between Observer 1 and Observer 2 varied from –1.9 to 2.9 1m. The 95% LoA for all the ETDRS sectors including zero showed that no fixed bias was present (Table 5). In all of the ETDRS sectors, the mean of choroidal thickness calculated by Observer 1 and Observer 2 was not correlated significantly with the mean difference between the two measurements (Observer 1 – Observer 2, all $P > 0.05$). Thus, no proportional bias was considered to be present.

DISCUSSION

Our findings showed that high ICC values were found between the two observers, and the results of Bland-Altman plots indicated the highly reproducible measurements of the choroidal thickness with semiautomatic segmentation. These findings indicated that we can obtain valid and reproducible results of the choroidal thickness of the images obtained by SS-OCT.

Park and Oh[20] reported that the pediatric subfoveal choroidal thickness determined by EDI-OCT was 343.1 6 79.8 1m. However, the choroidal thickness was measured in a point-by-point way and did not include comparisons with adult subjects. Ruiz-Moreno et al.[19] examined the choroidal thickness in 43 normal pediatric patients using a prototype SS-OCT instrument. They reported that the mean macular choroidal thickness in the pediatric patients (285.2 6 56.7 1m) was not significantly thicker than that in healthy adults (275.2 6 92.7 1m, P ¼ 0.08). However, they measured the choroidal thickness at only 7 points in the horizontal plane. In addition, the mean age of their pediatric subjects was 10 6 3 years, which is older than that of our group. Moreover, both eyes were included in their analyses, which can lead to bias. We examined the mean choroidal thickness and volume in one randomly selected eye of all subjects to create the choroidal thickness maps.

TABLE 5. ICCs and Results of Bland-Altman Method in Choroidal Thickness of ETDRS Grid Sectors Measured by Two Observers in 14 Selected Pediatric Individuals

Area	ICC (P Value)	95% LoA	Correlation Between Mean and Mean Difference
Center	0.9979 (<0.0001)	–13.5~11.5	r ¼ –0.260 P ¼ 0.3783
Inner temporal	0.9995 (<0.0001)	–5.4~4.8	r ¼ –0.271 P ¼ 0.3563
Inner superior	0.9908 (<0.0001)	–20.8~17.1	r ¼ –0.207 P ¼ 0.4869
Inner inferior	0.9992 (<0.0001)	–7.2~6.9	r ¼ –0.147 P ¼ 0.6224
Inner nasal	0.9962 (<0.0001)	–16.1~12.9	r ¼ –0.308 P ¼ 0.2908
Outer temporal	0.9945 (<0.0001)	–9.6~14.6	r ¼ –0.234 P ¼ 0.4284
Outer superior	0.9931 (<0.0001)	–12.6~18.4	r ¼ 0.356 P ¼ 0.2169
Outer inferior	0.9993 (<0.0001)	–7.0~5.6	r ¼ –0.513 P ¼ 0.0602
Outer nasal	0.9953 (<0.0001)	–13.9~17.2	r ¼ 0.151 P ¼ 0.6129

The 95% LoA, expected difference between two measurements was calculated as the mean of the differences 6 1.96 3 SD of the differences.

Using EDI-OCT, Read et al.[21] recently reported that the choroidal thickness increased significantly from early childhood to adolescence. However, only children with refractive error between þ1.25 and –0.50 D were studied, thereby minimizing the potential influence of refractive error or axial length on the choroidal thickness. Indeed, the investigators reported that a strong negative association between axial length and choroidal thickness would be expected to result in a decrease in choroidal thickness with increasing age, rather than an increase in choroidal thickness. They concluded that longitudinal studies of the choroidal thickness in childhood, including myopic participants, will be necessary.

An earlier study reported that the axial length increased by 3 mm between the ages of 9 months and 9 years.[30] Because the choroidal thickness decreases with increases in the axial length in healthy adults,[11,15,16] the choroidal thickness in children is assumed to be thicker than that of adults. We found that the macular choroid was significantly thicker and the volume significantly larger in the pediatric individuals than in the adults. After adjustment for axial length and body mass index, the central choroidal thickness was no longer significantly correlated with the age group. This suggests that the pediatric choroidal thickening may be influenced by the shortening of the axial length and low body mass index. Hirata et al.[15] reported that the central choroidal thickness was 202.6 6 83.5 1m in adults, which is comparable to the 206.1 6 72.5 in our study.

The sectorial choroidal thicknesses were slightly different in the pediatric and adult individuals. Although the thinnest area was nasal in both groups, the thickest area was temporal in the children and superior in the adults. Ruiz-Moreno et al.[19] reported that the pediatric choroidal thickness along the horizontal line was thicker on the temporal side than in the fovea, and it was thinnest on the nasal side. In addition, the adult choroidal thickness in their study was thickest in the fovea, followed by the temporal, and it was thinnest on the nasal side. These results are consistent with our results.

The thinning of pediatric choroid with increasing age appeared to occur more quickly in the central area. Moreno et al.[31] reported that the central choroidal thickness in newborn infants (329 ± 66 μm) was remarkably thicker than that in adults (258 ± 66 μm). In their study, the subfoveal choroid in the newborn infant was significantly thicker than the superior or inferior choroid at 2000 μm from the fovea, and the mean difference between subfoveal and superior choroidal thickness was 87 μm. These results are consistent with our findings.

To the best of our knowledge, there has been only one report on the choroidal volume measured by SS-OCT in adults.[15] The choroidal volume can reflect the vascular changes, for example, vascular hyperpermeability or vasodilation, that can be observed in retinochoroidal diseases, such as central serous chorioretinopathy.[4] At present, the status of the choroid usually is evaluated by the choroidal thickness measured at a few points. However, point-by-point measurements can be affected by focal thickening or thinning of the choroid,[22,23] or by irregularities of the chorioscleral border.[5] Examining the choroidal volume by 3D mapping is a better method for a comprehensive evaluation of the entire macular area.

In pediatric individuals, Ruiz-Moreno et al.[19] reported that the average choroidal thickness at 7 horizontal points of the macular area was correlated significantly with the age and refractive error. We found that the mean central choroidal thickness was correlated significantly with the age, axial length, body height, body weight, body mass index, and refractive error using simple linear regression analyses. In addition, multiple linear regression analysis with the forward stepwise method showed that the model determined by the axial length and body mass index had the highest regression coefficients. In schoolchildren, Selovic et al.[32] found that the axial length increased with increasing age, body height, and weight, but was more highly correlated with the height and weight than with the age. This close relationship between axial length and body height or weight may contribute to the relationship between pediatric choroidal thickness and body mass index, because the axial length is known to be correlated closely with the choroidal thickness.[11,15,16]

A choroidal thickness map of the macular area was created by semiautomatic segmentation. Manual segmentation was performed in 25.1 ± 20.7% of our eyes because of errors in the delineation of the chorioscleral border by the built-in software. To standardize this evaluation further, it will be necessary that a choroidal thickness map can be created by fully automatic segmentation. For this purpose, a software to determine chorioscleral border more accurately and further improvement of the OCT image quality are essential.

One of the limitations of our study was that we examined only Japanese subjects, and the choroidal thickness in children of other races was not determined. In addition, the relatively small sample size might be insufficient to evaluate choroidal thicknesses in a pediatric population.

In conclusion, the macular choroid was significantly thicker and the volume was significantly larger in pediatric individuals than in adults. Although the thinnest area was nasal in both groups, the thickest area was temporal in the children and superior in the adults. Pediatric choroidal thinning with increasing age appears to be more rapid in the central sector than in the outer sectors. Pediatric choroidal thickness was associated significantly with systemic and ocular parameters, especially the axial length and body mass index. Further studies in a larger number of pediatric individuals will be needed to determine precisely the choroidal status in pediatric eyes.

Acknowledgments

The authors alone are responsible for the content and writing of the paper.

Disclosure: T. Nagasawa, None; Y. Mitamura, None; T. Katome, None; K. Shinomiya, None; T. Naito, None; D. Nagasato, None; Y. Shimizu, None; H. Tabuchi, None; Y. Kiuchi, None

References

1. Spaide RF, Koizumi H, Pozzoni MC. Enhanced depth imaging spectral-domain optical coherence tomography. Am J Ophthalmol. 2008;146:496–500.
2. Spaide RF. Enhanced depth imaging optical coherence tomography of retinal pigment epithelial detachment in age-related macular degeneration. Am J Ophthalmol. 2009;147:644–652.
3. Margolis R, Spaide RF. A pilot study of enhanced depth imaging optical coherence tomography of the choroid in normal eyes. Am J Ophthalmol. 2009;147:811–815.
4. Imamura Y, Fujiwara T, Margolis R, Spaide RF. Enhanced depth imaging optical coherence tomography of the choroid in central serous chorioretinopathy. Retina. 2009;29:1469–1473.
5. Chung SE, Kang SW, Lee JH, Kim YT. Choroidal thickness in polypoidal choroidal vasculopathy and exudative age-related macular degeneration. Ophthalmology. 2011;118:840–845.
6. Fong AH, Li KK, Wong D. Choroidal evaluation using enhanced depth imaging spectral-domain optical coherence tomography in Vogt-Koyanagi-Harada disease. Retina. 2011;31:502–509.
7. Ohno-Matsui K, Akiba M, Moriyama M, Ishibashi T, Tokoro T, Spaide RF. Imaging retrobulbar subarachnoid space around optic nerve by swept-source optical coherence tomography in eyes with pathologic myopia. Invest Ophthalmol Vis Sci. 2011;52:9644–9650.
8. Spaide RF, Akiba M, Ohno-Matsui K. Evaluation of peripapillary intrachoroidal cavitation with swept source and enhanced depth imaging optical coherence tomography. Retina. 2012;32:1037–1044.
9. Wojtkowski M, Srinivasan V, Ko T, Fujimoto J, Kowalczyk A, Duker J. Ultrahigh-resolution, high-speed, Fourier domain optical coherence tomography and methods for dispersion compensation. Opt Express. 2004;12:2404–2422.
10. Nagasawa T, Mitamura Y, Katome T, Nagasato D, Tabuchi H. Swept-source optical coherence tomographic findings in morning glory syndrome [published online ahead of print May 28, 2013]. Retina.
11. Ikuno Y, Kawaguchi K, Nouchi T, Yasuno Y. Choroidal thickness in healthy Japanese subjects. Invest Ophthalmol Vis Sci. 2010;51:2173–2176.
12. Potsaid B, Baumann B, Huang D, et al. Ultrahigh speed 1050 nm swept source/Fourier domain OCT retinal and anterior segment imaging at 100,000 to 400,000 axial scans per second. Opt Express. 2010;18:20029–20048.
13. Srinivasan VJ, Huber R, Gorczynska I, et al. High-speed, high resolution optical coherence tomography retinal imaging with a frequency-swept laser at 850 nm. Opt Lett. 2007;32:361–363.
14. Yasuno Y, Hong Y, Makita S, et al. In vivo high-contrast imaging of deep posterior eye by 1-micron swept source optical coherence tomography and scattering optical coherence angiography. Opt Express. 2007;15:6121–6139.

15. Hirata M, Tsujikawa A, Matsumoto A, et al. Macular choroidal thickness and volume in normal subjects measured by swept-source optical coherence tomography. Invest Ophthalmol Vis Sci. 2011;52:4971–4978.
16. Ding X, Li J, Zeng J, et al. Choroidal thickness in healthy Chinese subjects. Invest Ophthalmol Vis Sci. 2011;52:9555–9560.
17. Ouyang Y, Heussen FM, Mokwa N, et al. Spatial distribution of posterior pole choroidal thickness by spectral domain optical coherence tomography. Invest Ophthalmol Vis Sci. 2011;52:7019–7026.
18. Manjunath V, Taha M, Fujimoto JG, Duker JS. Choroidal thickness in normal eyes measured using Cirrus HD optical coherence tomography. Am J Ophthalmol. 2010;150:325–329.
19. Ruiz-Moreno JM, Flores-Moreno I, Lugo F, Ruiz-Medrano J, Montero JA, Akiba M. Macular choroidal thickness in normal pediatric individuals measured by swept-source optical coherence tomography. Invest Ophthalmol Vis Sci. 2013;54:353–359.
20. Park KA, Oh SY. Analysis of spectral-domain optical coherence tomography in preterm children: retinal layer thickness and choroidal thickness profiles. Invest Ophthalmol Vis Sci. 2012;53:7201–7207.
21. Read SA, Collins MJ, Vincent SJ, Alonso-Caneiro D. Choroidal thickness in childhood. Invest Ophthalmol Vis Sci. 2013;54:3586–3593.
22. Yeoh J, Rahman W, Chen F, et al. Choroidal imaging in inherited retinal disease using the technique of enhanced depth imaging optical coherence tomography. Graefes Arch Clin Exp Ophthalmol. 2010;248:1719–1728.
23. Yasuno Y, Okamoto F, Kawana K, Yatagai T, Oshika T. Investigation of multifocal choroiditis with panuveitis by three-dimensional high-penetration optical coherence tomography. J Biophotonics. 2009;2:435–441.
24. Early Treatment Diabetic Retinopathy Study research group. Photocoagulation for diabetic macular edema. Early Treatment Diabetic Retinopathy Study report number 1. Arch Ophthalmol. 1985;103:1796–1806.
25. Brown JS, Flitcroft DI, Ying GS, et al. In vivo human choroidal thickness measurements: evidence for diurnal fluctuations. Invest Ophthalmol Vis Sci. 2009;50:5–12.
26. Tan CS, Ouyang Y, Ruiz H, Sadda SR. Diurnal variation of choroidal thickness in normal, healthy subjects measured by spectral domain optical coherence tomography. Invest Ophthalmol Vis Sci. 2012;53:261–266.
27. Agawa T, Miura M, Ikuno Y, et al. Choroidal thickness measurement in healthy Japanese subjects by three-dimensional high-penetration optical coherence tomography. Graefes Arch Clin Exp Ophthalmol. 2011;249:1485–1492.
28. Bland JM, Altman DG. Statistical methods for assessing agreement between two methods of clinical measurement. Lancet. 1986;1:307–310.
29. Katome T, Mitamura Y, Nagasawa T, Eguchi H, Naito T. Quantitative analysis of cystoid macular edema using scanning laser ophthalmoscope in modified dark-field imaging. Retina. 2012;32:1892–1899.
30. Twelker JD, Mitchell GL, Messer DH, et al. Children's ocular components and age, gender, and ethnicity. Optom Vis Sci. 2009;86:918–935.
31. Moreno TA, O'Connell RV, Chiu SJ, et al. Choroid development and feasibility of choroidal imaging in the preterm and term infants utilizing SD-OCT. Invest Ophthalmol Vis Sci. 2013;54:4140–4147.
32. Selovic A, Juresa V, Ivankovic D, Malcic D, Selovic Bobonj G. Relationship between axial length of the emmetropic eye and the age, body height, and body weight of schoolchildren. Am J Hum Biol. 2005;17:173–177.

OPEN ACCESS Freely available online

PLOS | ONE

The Whole Macular Choroidal Thickness in Subjects with Primary Open Angle Glaucoma

Shunsuke Nakakura[1]*, Minami Yamamoto[1], Etsuko Terao[1], Toshihiko Nagasawa[1], Hitoshi Tabuchi[1], Yoshiaki Kiuchi[2]

1 Department of Ophthalmology, Saneikai Tsukazaki Hospital, Himeji, Japan, 2 Department of Ophthalmology and Visual Sciences, Graduate School of Biomedical Sciences, Hiroshima University, Hiroshima, Japan

Abstract

Purpose: We investigated the whole macular choroidal thickness in subjects with glaucoma in order to evaluate the effects of glaucoma and glaucoma visual field damage on the choroidal thickness.

Subjects and Methods: We examined 40 primary open angle glaucoma patients with only superior visual field defects and 48 normal controls. The macular choroidal thickness was measured using swept-source optical coherence tomography according to the three-dimensional raster scan protocol (666 mm). We used the choroidal thickness within a 1.0-mm circle measured on ETDRS grids as the central sector and then used a 666 rectangular grid to divide the area into six sectors.

Results: No significant differences were found in the choroidal thickness values between the glaucoma and normal subjects in any of the sectors after adjusting for the age and axial length (all P _ 0.4, ANCOVA). According to a stepwise analysis of the glaucoma subjects performed using the parameters of age, axial length, central corneal thickness and mean deviation (MD value) obtained by static perimetry, age was the most predictive and significant factor in all sectors (coefficient = 23.091 to 24.091 and F value = 15.629 to 22.245), followed by axial length (coefficient = 210.428 to 223.458 and F value = 2.454 to 6.369). The central corneal thickness and MD values were not significant predictive factors in any of the sectors. No significant predictive factors were found for the differences in the choroidal thickness values observed between the superior and inferior field sectors.

Conclusions: Neither the glaucoma-related visual field damage nor glaucoma itself have any apparent associations with the whole macular choroidal thickness.

Trial Registration: Japan Clinical Trials Register (http://www.umin.ac.jp/ctr/ number, UMIN 000012527).

Citation: Nakakura S, Yamamoto M, Terao E, Nagasawa T, Tabuchi H, et al. (2014) The Whole Macular Choroidal Thickness in Subjects with Primary Open Angle Glaucoma. PLoS ONE 9(10): e110265. doi:10.1371/journal.pone.0110265

Editor: Demetrios Vavvas, Massachusetts Eye & Ear Infirmary, Harvard Medical School, United States of America

Received July 16, 2014; **Accepted** September 10, 2014; **Published** October 28, 2014

Data Availability: The authors confirm that all data underlying the findings are fully available without restriction. All relevant data are within the paper and its Supporting Information files.

Funding: The authors have no support or funding to report.

Competing Interests: The authors have declared that no competing interests exist.

* Email: shunsukenakakura@yahoo.co.jp

Introduction

Whether the choroidal thickness is truly associated with the etiology or progression of glaucoma remains unknown. The uvea (choroid, iris and ciliary body) contains abundant large and small vessels, and utilizes more than 80% of the ocular blood flow [1]. The factors that influence the ocular blood flow, such as a low systolic perfusion pressure, low systolic blood pressure and history of cardiovascular disease, have been reported to be predictors of long-term glaucoma progression [2]. Recently, the development of enhanced-depth imaging optical coherence tomography (OCT) based on spectral-domain OCT has enabled clinicians to measure the choroidal thickness noninvasively. Previous studies have reported that a thinner choroidal thickness value at the fovea is associated with an older age [3–9], longer axial length [3–6,8,9] and thicker central corneal thickness (CCT) [6,9].

With respect to the association between glaucoma and the choroidal thickness, previous reports have shown no significant differences between glaucoma patients and normal subjects [5,7,9] or among individuals suspected of having glaucoma [6] based on the choroidal thickness value. However, Hirooka et al. reported that, in the setting of normal tension glaucoma (NTG), which was diagnosed when there was an untreated peak IOP#21 mmHg, including the 24-h fluctuations, there was choroidal thinning 3 mm nasal from the fovea compared with that observed in normal subjects [10]. Meanwhile, Usui et al. reported that, in highly myopic eyes (with a spherical equivalent refractive error between -6 and -12 diopters, and an axial length greater than 26.5 mm), NTG patients exhibit thinner choroidal values at the fovea and around the optic disc than subjects without glaucoma [11]. However, even if the choroidal thinning or thickening is associated with glaucoma, whether such changes in the choroidal

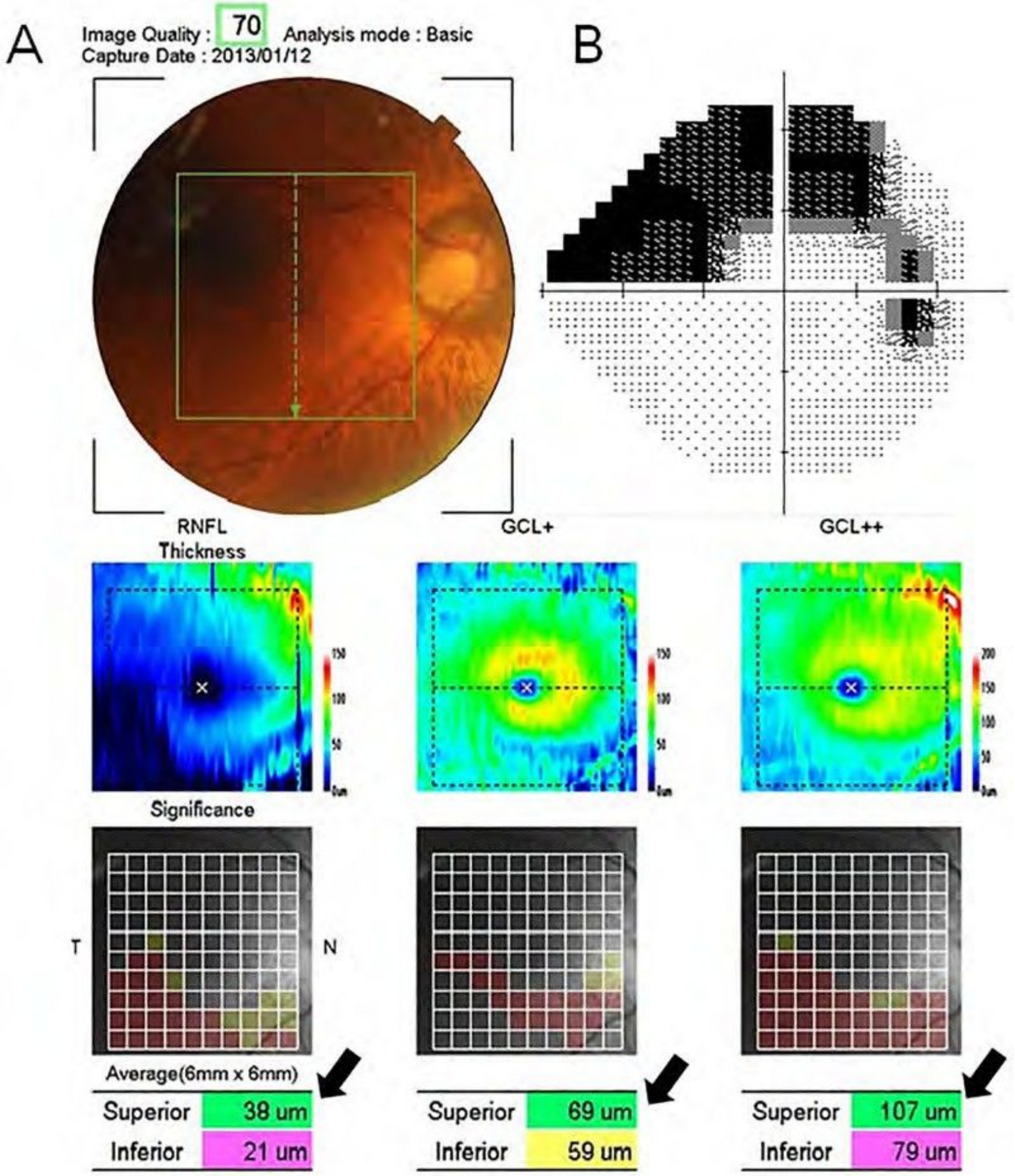

Figure 1. The 3D-OCT map and results of the HFA test in a 71-year-old male subject with glaucoma. (A) The 3D-OCT map provides a 10610 grid map of the macular RNFL (GCL+), ganglion cell layer (GCL)/inner plexiform layer (IPL) thickness (GCL++) and macular RNFL+GCL+IPL. Upper panel: a pseudo-colored map of the measured thickness. Center panel: Each grid in the 10610 grid was color-coded, with no color (within the normal limit), yellow (outside of the 95% normal limit) or red (outside of the 99% normal limit) used to indicate different values. Lower panel: the thicknesses of the total, superior and inferior hemiretinal sectors. The black arrows show the superior hemiretinal thickness, which is displayed as color-coded with green (within the normal limit), yellow (outside of the 95% normal limit) or red (outside of the 99% normal limit) based on the software program's normal built-in dataset. (B) The results of the HFA test. The MD was 29.38 dB (P,0.5%) and the PSD was 14.54 dB (P,0.5%). Superior glaucoma visual field damage corresponds to inferior optic disc rim thinning and the 3D-OCT data. The inferior visual field was intact.
doi:10.1371/journal.pone.0110265.g001

thickness values are primary or occur secondarily due to the progression of glaucoma remains unknown.

Furthermore, most of the previous reports have focused on the subfoveal choroidal thickness and/or choroidal thickness values at +/2 3 mm nasal or temporal to the fovea. Glaucoma is generally characterized by optic disc changes with corresponding nerve fiver defects and visual field defects. The initial changes most frequently occur in the inferior optic disc rim, corresponding to a superior visual field defect, and it does not exceed the central line, since the normal retinal nerve fiber layers run symmetrically in the superior and inferior fields. However, the fovea is free of a nerve fiber layer, as the inner retina and ganglion cells are pushed away to the foveal slope. Therefore, the use of measurement points at the fovea or +/2 3 mm nasal or temporal to the fovea may not be appropriate for evaluating the relationship between glaucoma and the choroidal thickness.

Swept-source optical coherence tomography (SS-OCT) applies a swept wavelength laser as a light source [12,13], with a longer center wavelength that penetrates deeply into tissues. The longer wavelength (1,050 mm) of SS-OCT is attenuated by water absorption; however, SS-OCT can achieve much less roll-off, thus leading to retained sensitivity at increasing depths, and can

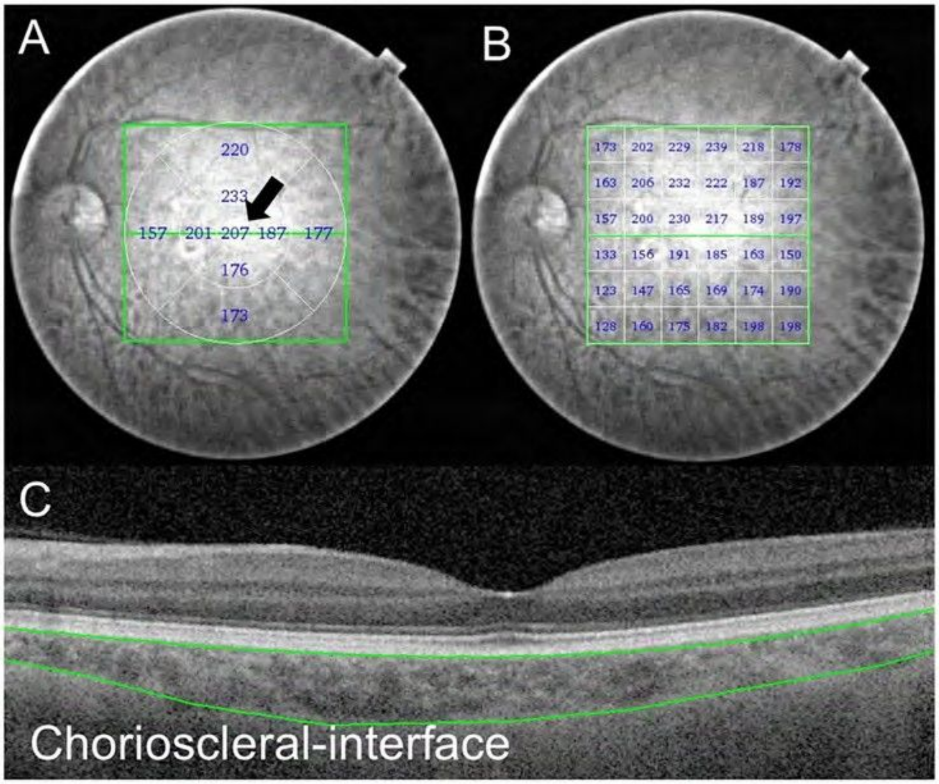

Figure 2. The choroidal thickness map of a 57-year-old normal male obtained using SS-OCT. The 3D raster scan protocol with 512A-scans ×256 B-scans was used to obtain the 3D imaging data for a 6×6-mm area. (A) The black arrow shows the central sector choroidal thickness as measured on the ETDRS grid within a 1×1-mm circular area. (B) The choroidal thickness values presented by the 6×6 rectangular grid map. Each value shows the mean choroidal thickness within a 1×1-mm square area. (C) Manual segmentation of the chorioscleral interface on the B-scan image. All 64 B-scan images were obtained for each subject.
doi:10.1371/journal.pone.0110265.g002

operate at a higher speed than spectral domain OCT to obtain the choroidal thickness maps using the 3D raster scan protocol [14].

The aim of this study was to investigate the whole macular choroidal thickness (6×6 mm) in patients with superior glaucoma visual hemi-field defects in order to: 1) compare these values with those observed in normal subjects after adjusting for the previously identified factors associated with the choroidal thickness (age and axial length) and 2) to investigate whether the degree of glaucoma visual field damage is associated with the choroidal thickness and/

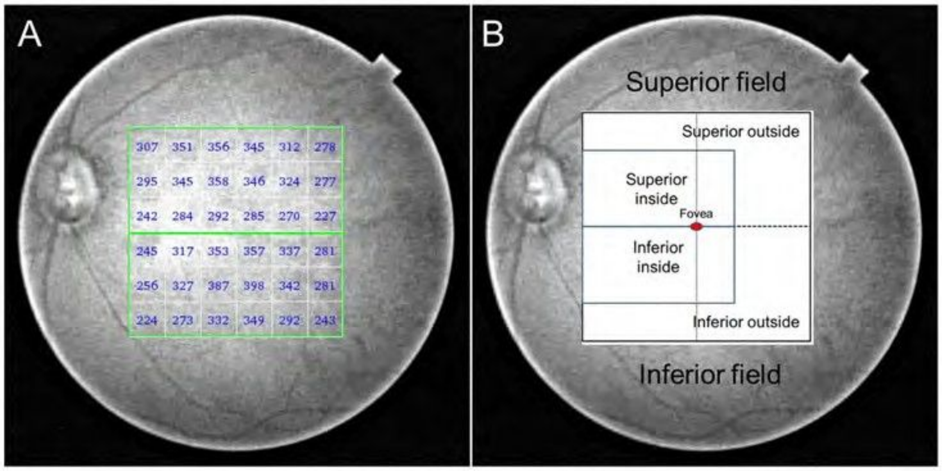

Figure 3. The choroidal thickness map of a 74-year-old female subject with glaucoma obtained using SS-OCT. (A) The choroidal thickness values presented on the 6×6 rectangular grid map. (B) The six sectors used in the present study. Each area was symmetrically divided between the superior and inferior sectors by a horizontal line.
doi:10.1371/journal.pone.0110265.g003

or differences in the choroidal thickness values between the superior and inferior sectors.

Subjects and Methods

We studied 88 subjects (40 glaucoma patients and 48 normal subjects) treated at Saneikai Tsukazaki Hospital from October 2012 to December 2013. This study received approval from the Institutional Review Board of Saneikai Tsukazaki Hospital and was performed according to the tenets of the Declaration of Helsinki. Written informed consent was obtained from each participant prior to enrollment in this study. All subjects received a full ophthalmic examination (conducted by S.N. or T.N) and had a best-correlated visual acuity of more than 0.6, refractive errors (spherical equivalent) within 66 diopters (D) and cylinder correction within 63D. The refraction was measured using an autorefractor (KR-8800, Topcon Corporation, Japan). The axial length (AL) was measured using an IOLMaster, ver. 5.02 (Carl Zeiss Meditec, Jena, Germany), and the mean of five measurements was used in the subsequent analyses. The CCT values in the glaucoma subjects were measured with a specular microscope (SP-3000, Topcon Corporation, Japan). The intraocular pressure was measured using a Goldmann applanation tonometer with the subject in the sitting position.

All glaucoma patients had attended our clinic for at least one year and their disease was well controlled with topical anti-glaucoma eye drops. Each patient received a reliable visual field analysis (Humphry Visual Field Analyzer (HFA), Carl Zeiss Inc., Dublin, CA) according to the thresholding algorithm (SITA-standard) 30-2, and underwent HFA at four- to six-month intervals. The visual field test results used in the study were obtained within 6 three months of the time when the choroidal thickness was measured, and which had fixation losses less than 20%, and the false-positive and false-negative errors were less than 15%. A glaucomatous visual field defect was defined as 1) a glaucoma hemifield test graded ''outside the normal limits'' and 2) a cluster of three contiguous points at the 5% level for the pattern deviation plot, with at least one point being P,1%. The mean deviation value (MD value) was used for the analysis. All patients had primary open angle glaucoma, as defined by 1) the results of a gonioscopic examination that revealed an open angle and 2) the presence of visual field defects in least one of the eyes whose locations corresponded to glaucomatous disc excavation, namely, the presence of a focal or diffuse defect of the optic disc rim with or without retinal nerve fiver layer (RNFL) defects.

In the present study, we recruited glaucoma patients who exhibited only focal or diffuse inferior optic rim thinning with corresponding superior visual field loss. Patients with a history of any previous glaucoma surgery or systemic diseases, such as diabetes mellitus or uncontrolled hypertension, the use of an oral carbonic anhydrase inhibitor (acetazolamide) and/or an unknown previous refraction before cataract surgery were excluded. Patients who displayed any optic disc changes suspected to be due to glaucoma at the superior optic disc rim confirmed based on the presence of ganglion cell-loss on three-dimensional OCT were also excluded (3D-OCT; Topcon, Inc., Tokyo, Japan). The 3D-OCT provides a 10610 grid map of the macula RNFL and ganglion cell layer (GCL)/inner plexiform layer (IPL) thickness, and uses a software program that displays a deviation map indicating if there is a significant reduction of the total macular retinal thickness, superior hemiretinal thickness or inferior hemiretinal thickness compared to that observed in a built-in normal database in three areas (the mean macular RNFL, mean GCL/IPL and mean macular RNFL+ mean GCL/IPL), with a probability of less than 1% [15]. All glaucoma patients exhibited only inferior hemiretinal thickness abnormalities (displayed in yellow or red), with a normal superior hemiretinal thickness (displayed in green). Figure 1 shows the macular retinal thickness values in the glaucoma patients measured on 3D-OCT and the glaucoma visual field defects measured on HFA (The 3D-OCT data are provided in Table S1).

The inclusion criteria for normal subjects were 1) IOP #21 mm Hg 2) normal ophthalmoscopic appearance of the optic nerve (cup-to-disc ratio ,0.5 in both eyes, cup-to disc ratio asymmetry ,0.2, the absence of hemorrhage, or the presence of localized or diffuse rim thinning).^{5} The exclusion criteria for the normal controls were as follows: 1) a history of intraocular surgery, 2) a history or evidence of chorioretinal or vitreoretinal disease and 3) systemic disease, such as diabetes mellitus or uncontrolled hypertension. Normal subjects did not undergo HFA testing.

Swept-source Optical Coherence Tomography (SS-OCT)

The macula area (666mm) of the eyes was examined with the SS-OCT instrument (DR1 OCT-1; Topcon, Tokyo, Japan). The SS-OCT has an acquisition rate of 100,000 A-scans per second when operated with the 1-mm wavelength tunable laser centered at 1,050 nm, with an approximate 100-nm tuning range and a tissue imaging depth of 2.6 mm [14]. Following pupil dilation, the SS-OCT examinations were performed by experienced certified orthoptists (M.Y and E.T) from 1:00 PM to 5:00 PM to reduce the effects of diurnal fluctuations [16,17]. The 3D volumetric raster

Table 1. The patient demographics.

	Glaucoma N = 40		Normal N = 48		
	mean ±SD	range	mean ±SD	range	P value
Age (years)	65.2611.8	40–85	66.4611.8	31–87	0.631*
Sex/female (%)	31(78)		24(50)		0.007{
Right eye (%)	19(47)		27(56)		0.413{
IOP (mmHg)	15.862.6	12–21	15.662.8	9–21	0.832*
Axial length (mm)	23.761.2	20.6–26.0	23.961.1	21.8–27.6	0.514*
CCT (mm)	502.9628.9	445–558	-	-	-
Mean deviation (dB)	25.164.7	219.64–0.24	-	-	-

*, Student's t-test
{, chi-square test.
doi:10.1371/journal.pone.0110265.t001

Table 2. Comparisons among the sectors between the glaucoma and normal groups.

	Glaucoma	95% CI	Normal	95% CI	P value
The central sector	219.1±11.2	196.7–241.6	216.6±10.2	196.1–237.1	0.869
a: superior field ave	208.6±8.9	190.8–226.5	200.9±8.1	184.6–217.2	0.531
b: inferior field ave	193.2±9.1	174.9–211.5	185.4±8.3	168.8–202.1	0.536
c: superior inside ave	198.8±9.9	179.1–218.5	193.8±9.0	175.8–211.8	0.712
d: superior outside ave	216.7±8.5	199.7–233.6	206.6±7.7	191.1–222.1	0.390
e: inferior inside ave	188.0±10.1	167.8–208.1	183.0±9.2	164.7–201.4	0.720
f: inferior outside ave	197.3±8.7	179.8–214.7	187.4±8.0	171.4–203.3	0.408

Ave, average.
The data are presented as the age- and axial length-adjusted mean ± standard error of the mean (SEM) and 95% CI (confidence interval) (μm).
All P values were obtained with an ANCOVA using the age and axial length as covariates.
doi:10.1371/journal.pone.0110265.t002

scan protocol was used, which covered an area measuring 6×6 mm centered on the fovea, with 512 A-scans × 256 B-scans. All images had image quality scores ≥45 (of 160), according to the manufacturer's recommendations.

Using a series of 64 B-scan images, each of which was created by averaging four consecutive B-scans, a choroidal thickness map was created via semiautomatic segmentation. The choroidal thickness was measured as the distance from the outer border of the retinal pigment epithelium to the inner surface of the chorioscleral interface. However, semiautomatic segmentation does not always provide the correct chorioscleral interface; therefore, manual segmentation using the built-in software program was performed on all 64 B-scan images in each patient by experienced certified orthoptists (M.Y and E.T). The interobserver reproducibility of the choroidal thickness values obtained using this manual segmentation method has previously been reported by our group, and the ICC for the choroidal thickness values between the two observers was very good (from 0.990 to 0.999) [14].

The central sector, the center of the 1.0-mm circle on the ETDRS grid (Figure 2) and the 6×6 rectangular grid (Figure 2) (1×1 mm for each section), was used for the subsequent sector analysis. The 6×6 rectangular grid (36 sections) was divided horizontally into the superior field (18 sections) and inferior field (18 sections). The superior field was divided superiorly inside (including the fovea, eight sections) and outside (the remaining 10 sections), and a similar partition was attempted on the inferior field (Figure 3). This deviation was developed for the present study based on the RNFL lanes.

Statistical Analysis

We used the JMP, version 10.0.0 software package (SAS Institute Inc., Cary, NC, USA) for the statistical analyses, and the data were expressed as the means ± standard deviation (SD). Values of $p < 0.05$ were considered to be statistically significant. For comparisons of the demographic data between the glaucoma and normal subjects, we used Student's t-test for the age, IOP and axial length and the chi-square test for sex and the target eye.

We compared the macular choroidal thickness values between the glaucoma patients and normal subjects using an analysis of covariance, with covariance considered for age and the axial length. We used a stepwise regression analysis to evaluate the significant factors affecting the choroidal thickness and the differences in the choroidal thickness values between the sectors in the glaucoma patients based on the following representative factors: age, axial length, CCT and MD. The independent variable criterion of $P = 0.2$ was set for the analysis.

The sample size required to detect a 20% (approximately 40 μm) difference between the glaucoma and normal subjects with a significance level of 5% and a power of 80%, based on the

Table 3. The choroidal thickness values in the glaucoma group.

	mean ±SD	range
The central sector	222.6±71.7	77.0–397.0
a: superior field ave	210.4±57.1	103.7–346.8
b: inferior field ave	195.8±54.8	88.3–318.6
c: superior inside ave	202.3±64.1	90.0–359.6
d: superior outside ave	219.8±53.1	119.1–332.6
e: inferior inside ave	190.9±62.6	77.6–355.0
f: inferior outside ave	199.7±50.8	96.9–295.4
difference 1 (a-b)	14.5±29.6	−55.5–74.8
difference 2 (c-e)	11.4±24.6	−45.2–60.1
difference 3 (d-f)	20.0±33.2	−64.7–101.8

The values are presented as the means±SD (μm).
The values are slightly different from those in Table 2 because these are the raw data.
doi:10.1371/journal.pone.0110265.t003

Table 4. The results of symmetrical comparisons between two sectors in the glaucoma group.

Comparison between two sectors	P value
superior vs inferior ave	0.001
superior inside vs inferior inside ave	<0.001
superior outside vs inferior outside ave	<0.001
superior inside vs outside ave	<0.001
inferior inside vs outside ave	0.004

Ave, average.
All p values were obtained using the paired t-test.
doi:10.1371/journal.pone.0110265.t004

standard deviation of 54.8 mm in the inferior field choroidal thickness average in the glaucoma subjects, was estimated to be 30 patients per group.

Results

The patient demographics of the two groups and the MD values in the glaucoma patients are shown in Table 1. The glaucoma group consisted of more female patients than the normal group ($P < 0.01$). No significant differences were found between the two groups in terms of the age, the target eye, IOP or axial length.

Table 2 shows the results of a comparison of the choroidal thickness values following adjustment for age and the axial length in all sectors, and the p values of the ANCOVA analysis. No significant differences were found between the glaucoma group and the normal group in any sector ($P > 0.4$).

The raw data for the choroidal thickness values in the glaucoma group are shown in Table 3, and Table 4 shows a comparison between the superior field sectors and inferior field sectors (symmetrical comparison). The choroidal thickness values were significantly thinner in the inferior sectors in all symmetrical comparisons ($P < 0.05$). We also compared the inside and outside choroidal thickness values, and found that the outside choroidal thickness values were significantly thicker in both the superior and inferior fields (all $P < 0.05$). These data differ from the values in Table 2 because they were obtained without adjustment for age or the axial length.

The results of a stepwise regression analysis of independent predictors of the choroidal thickness, and the differences in the choroidal thickness values in all symmetrical sectors among the glaucoma subjects

Table 5 shows the results of the stepwise analyses to determine the predictors of the choroidal thickness using the previously reported factors; age, axial length, CCT and MD. According to these analyses, the age was found to be the most predictive and significant factor for the choroidal thickness in all seven sectors ($P < 0.001$). The axial length was the second most predictive factor and was found to be a statistically significant predictor in almost all sectors. The CCT was identified as the only predictive factor in the symmetrical comparisons; however, all adjusted R2 values in the symmetrical comparison were low (0.037–0.063) and were not statistically significant (all $p > 0.05$). The MD value was not identified as a significant factor in any sector or in the symmetrical comparisons.

Discussion

In the present study, we first reported that the whole macular choroidal thickness values in glaucoma subjects do not differ significantly from those of normal subjects. Previous reports have only shown pinpoint measurements of the choroidal thickness obtained using the enhanced-depth imaging method; however, by using SS-OCT, we were able to analyze the whole macular choroidal thickness and compare different sectors. The subjects evaluated in the present study exhibited only focal or diffuse inferior optic rim thinning with corresponding superior visual field damage. We first assumed that in such patients, the inferior macular choroidal thickness might be thinner due to the glaucoma-related damage compared with the superior macular choroidal thickness or the thickness in normal subjects.

However, no significant differences in the macular choroidal thickness were found between glaucoma patients and normal subjects in any of the sectors (All $p > 0.4$). Furthermore, our results obtained by a stepwise regression analysis showed that the differences in the choroidal thickness values observed between the superior and inferior sectors had no association with glaucoma damage (MD value), suggesting that the secondary changes due to the progression of glaucoma may not extend to the choroid. This observation was also confirmed by the results of a comparison among sectors in the glaucoma patients (Table 4). The glaucoma patients had thicker values in the superior field than in the inferior field and in the temporal field (outside sector) compared to the nasal field (inside sector) in our study, similar to the findings observed in normal subjects [4,5,18]. The macular choroidal thickness value was affected by age and the axial length, but not the CCT or MD values, according to the stepwise regression analysis performed in this study. Therefore, this result suggests that the whole macular choroidal thickness values of our glaucoma patients were similar to those obtained in normal subjects, as demonstrated in previous reports [5,7,8]. Moreover, the values were not affected by either glaucoma itself or by glaucoma visual field progression.

Both glaucoma patients and normal subjects had a decreased choroidal thickness in inferior sections (Table 2), which is supported by the data form normal adults and children reported by Nagasawa et al. [12]. In addition, the initial changes in glaucoma frequently occur in the inferior optic disc rim, with superior visual field defects being found in glaucoma patients. It has been speculated that inferior choroidal thinning plus some other factors (not choroidal thinning alone) might be associated with the initial glaucomatous changes. However, no mechanism responsible for these changes has been proven. Ikuno et al., advocated two mechanisms underlying the inferior choroidal

Table 5. The results of the stepwise regression analyses of the choroidal thickness values using the age, axial length, CCT and MD as variables in the glaucoma group.

	Independent variables												
	Age			Axial length			CCT			MD value			
Dependent variables	Coefficient	F value	P value	Coefficient	F value	P value	Coefficient	F value	P value	Coefficient	F value	P value	Adjusted R^2
The central sector	−4.091	17.718	<0.001	−23.458	5.646	0.022	-			-			0.287
a: superior field average	−3.309	18.515	<0.001	−16.963	4.715	0.036	-			-			0.297
b: inferior field average	−3.237	19.713	<0.001	−15.246	4.239	0.046	-			-			0.313
c: superior inside average	−3.568	16.545	<0.001	−22.536	6.369	0.015	-			-			0.274
d: superior outside average	−3.191	20.158	<0.001	−13.531	3.510	0.069	0.325	1.753	0.193	-			0.318
e: inferior inside average	−3.418	15.629	<0.001	−21.267	5.863	0.020	-			-			0.261
f: inferior outside average	−3.091	22.245	<0.001	−10.428	2.454	0.125	-			-			0.355
Difference 1 (a-b)	-			-			0.275	3.631	0.064	-			0.063
Difference 2 (c-e)	-			-			0.212	2.533	0.119	-			0.037
Difference 3 (d-f)	-			-			0.329	3.395	0.073	-			0.057

-: excluded variables.

Statistically significant independent factors for the dependent variables are shown in bold.

doi:10.1371/journal.pone.0110265.t005

thinning in normal subjects; one is the choroidal watershed, which isolates the choroidal circulation, and the other is the fetal choroidal fissure, which closes inferiorly at 16 weeks [19]. It also remains unclear as to why the initial changes due to glaucoma occur in the inferior rim; although gravity may be the simplest explanation.

In a comparison of the group characteristics, our glaucoma patients included more females than the normal control group (P < 0.01). This was likely due to patient selection, because typical notches or rim thinning are usually observed in patients with focal ischemic type discs, as classified by Nicolela and Drance [20]. They classified the glaucoma disc morphology into four subtypes: focal ischemic, myopic glaucomatous, senile sclerotic and generalized enlargement. The focal ischemic type is most commonly observed in female patients with primary open angle glaucoma [20], and similar findings have been noted in patients with normal tension glaucoma (NTG) [21].

However, Roberts et al. reported that there was a relationship between these glaucoma optic disc types and the peripapillary choroidal thickness values, in that patients with focal ischemic and generalized enlargement exhibited no statistically significant differences compared to healthy subjects [22]. No significant differences were found in the central sector choroidal thickness between the normal females and males (208.9 mm vs 218.6 mm, P = 0.678 by Student's t-test). Furthermore, no significant differences were found in the central sector choroidal thickness between female and male glaucoma patients (216.7 mm vs 242.6 mm, P = 0.347 according to Student's t-test). These data support our results, and previous reports have shown that sex is not a useful factor for predicting the choroidal thickness [6,8].

Other assessments to clarify the relationship between glaucoma and the choroidal thickness have been carried out by investigating the choroidal thickness values in peripapillary areas [6,22–24]. Because the blood supply of the prelaminar region of the optic nerve head is supplied by peripapillary choroidal vessels, and because the laminar cribrosa is supplied by the arterial circle of Zinn or the branches of the posterior ciliary arteries that supply the choroid [25], investigating the relationship between the peripapillary choroidal thickness and glaucoma is interesting. However, Maul et al. reported that the peripapillary choroidal thickness values were not significantly different between glaucoma and suspected glaucoma patients, and were not associated with glaucoma-related damage or the RNFL thickness [6]. Ehrlich et al. [23]. also reported that the peripapillary choroidal thickness values were not associated with the glaucoma damage, the RNFL thickness or the zone of b clock hours parapapillary choroidal atrophy, which are associated with glaucoma damage [26], in either glaucoma subjects or suspected cases. In addition, Suh et al. used spectral-domain OCT and reported that the peripapillary choroidal thickness values correlated with the subject age and axial length, but not with the CCT, MD, IOP or the presence of systemic disease [24].

These previous reports showed no apparent evidence of a relationship between glaucoma and the peripapillary choroidal thickness, which supports our results showing that neither glaucoma-related visual damage nor glaucoma itself have any apparent associations with the whole macular choroidal thickness.

Meanwhile, Usui et al. hypothesized that the 50% thinning in the choroidal thickness values observed in patients with highly myopic NTG results in reduced choroidal circulation, which may be associated with narrowing of the posterior ciliary arteries due to axial length elongation [11]. The differences in the anatomical structure caused by an abnormal refractive error may account for the differences in conclusions between the present and that study [11].

One limitation of the present study is that the adjusted R^2 values obtained in the stepwise analysis were ≤0.4. The age and axial length are representative predictive factors for the CT value. However, Aksoy et al. reported that the choroidal thickness is affected by more factors than was previously estimated; for example, the diurnal choroidal thickness changes occur at 30–60 mm, and the use of intravenous acetazolamide increases the CT values [27]. Therefore, we measured the choroidal thickness values during a limited time period (from 1:00 PM to 5:00 PM), and patients receiving an oral topical carbonic inhibitor (acetazolamide) were excluded. However, some patients use topical carbonic inhibitors, which can be absorbed through the mucous membranes in the nose, which then enter the intravenous circulation. In addition, topical prostaglandin analogues and beta blockers have the potential to affect the choroidal thickness. Furthermore, the systolic blood pressure values [16] and hypercholesterolemia [28] may also affect the choroidal thickness; however, these parameters were not examined in this study.

A second limitation is that this study included a relatively small number of subjects. However, it fulfilled a strict power analysis to detect a 20% difference in the choroidal thickness (40 mm) between glaucoma subjects and normal subjects compared with previous reports of 63 mm [5,8]. A third limitation is that whether the choroidal thickness truly represents the choroidal blood flow remains to be elucidated. In healthy younger subjects, the choroidal thickness was not associated with either the total choroidal blood flow or the subfoveal choroidal blood flow [29]. However, systemic administration of sildenafil citrate (Viagra, Pfizer, New York, NY) has been reported to increase the choroidal blood flow and the choroidal thickness in healthy subjects [30]. Further studies are therefore necessary to clarify the relationship between the choroidal thickness and the choroidal blood flow.

The fourth limitation is that we used manual segmentation techniques, according to previous reports. However, Mansouri et al. recently reported that the findings of automated segmentation obtained using SS-OCT are not affected by operator effects, and exhibit a high level of repeatability, and that the main artifact is blinking, not segmentation errors [31]. The fifth limitation associated with this study is that SS-OCT could cover only 20 degrees in the macula area which thus correlated with the first and second test-points in the 30-2 test program. The 10-2 test program was too small for the region and could not reflect the glaucoma visual field damage, therefore the 24-2 test program might closely correlate with the macula area obtained by SS-OCT. In summary, this study demonstrated that neither glaucoma-related visual damage nor glaucoma itself has any apparent association with the whole macular choroidal thickness.

Supporting Information

Table S1 The 3D-OCT values in the glaucoma group. All p values were obtained using the paired t-test. The values are presented as the mean6SD (mm).
(DOCX)

Data S1
(XLSX)

Acknowledgments

The authors thank Hajime Yamakage for his advice on the statistical analyses performed in this study.

Author Contributions

Conceived and designed the experiments: SN TN HT YK. Performed the experiments: SN TN ET MY. Analyzed the data: SN HT. Contributed reagents/materials/analysis tools: SN. Wrote the paper: SN.

References

1. Alm A (1992) Ocular circulation. In: Moses R, Hart W (ed.) Adlerãs physiology of the eye; clinical applications.9th ed.St Louis C.V Mosby; 198–227.
2. Leske MC, Heijl A, Hyman L, Bengtsson B, Dong L, et al (2007) Predictors of long-term progression in the early manifest glaucoma trial. Ophthalmology 114(11):1965–1972.
3. Ikuno Y, Kawaguchi K, Nouchi T, Yasuno Y (2010) Choroidal thickness in healthy Japanese subjects. Invest Ophthalmol Vis Sci 51(4):2173–2176.
4. Hirata M, Tsujikawa A, Matsumoto A, Hangai M, Ooto S, et al (2011) Macular choroidal thickness and volume in normal subjects measured by swept-source optical coherence tomography. Invest Ophthalmol Vis Sci 52(8):4971–4978.
5. Mwanza JC, Hochberg JT, Banitt MR, Feuer WJ, Budenz DL (2011) Lack of association between glaucoma and macular choroidal thickness measured with enhanced depth-imaging optical coherence tomography. Invest Ophthalmol Vis Sci 52(6):3430–3435.
6. Maul EA, Friedman DS, Chang DS, Boland MV, Ramulu PY, et al (2011) Choroidal thickness measured by spectral domain optical coherence tomography: factors affecting thickness in glaucoma patients. Ophthalmology 118(8):1571–1579.
7. Rhew JY, Kim YT, Choi KR (2014) Measurement of subfoveal choroidal thickness in normal-tension glaucoma in Korean patients. J Glaucoma 23(1):46–49.
8. Mwanza JC, Sayyad FE, Budenz DL (2012) Choroidal thickness in unilateral advanced glaucoma. Invest Ophthalmol Vis Sci 53(10):6695–6701.
9. Arora KS, Jefferys JL, Maul EA, Quigley HA (2012) The choroid is thicker in angle closure than in open angle and control eyes. Invest Ophthalmol Vis Sci 53(12):7813–7818.
10. Hirooka K, Fujiwara A, Shiragami C, Baba T, Shiraga F (2012) Relationship between progression of visual field damage and choroidal thickness in eyes with normal-tension glaucoma. Clin Experiment Ophthalmol 40(6):576–582.
11. Usui S1, Ikuno Y, Miki A, Matsushita K, Yasuno Y, et al (2012) Evaluation of the choroidal thickness using high-penetration optical coherence tomography with long wavelength in highly myopic normal-tension glaucoma. Am J Ophthalmol 153(1):10–16.
12. Ohno-Matsui K, Akiba M, Moriyama M, Ishibashi T, Tokoro T, et al (2011) Imaging retrobulbar subarachnoid space around optic nerve by swept-source optical coherence tomography in eyes with pathologic myopia. Invest Ophthalmol Vis Sci 52(13):9644–9650.
13. Spaide RF, Akiba M, Ohno-Matsui K (2012) Evaluation of peripapillary intrachoroidal cavitation with swept source and enhanced depth imaging optical coherence tomography. Retina 2012:1037–44.
14. Nagasawa T, Mitamura Y, Katome T, Shinomiya K, Naito T, et al (2013) Macular choroidal thickness and volume in healthy pediatric individuals measured by swept-source optical coherence tomography. Invest Ophthalmol Vis Sci 54(10):7068–7074.
15. Kanamori A, Naka M, Akashi A, Fujihara M, Yamada Y, et al (2013) Cluster analyses of grid-pattern display in macular parameters using optical coherence tomography for glaucoma diagnosis. Invest Ophthalmol Vis Sci 54(9):6401–6408.
16. Usui S, Ikuno Y, Akiba M, Maruko I, Sekiryu T, et al (2012) Circadian changes in subfoveal choroidal thickness and the relationship with circulatory factors in healthy subjects. Invest Ophthalmol Vis Sci 53(4):2300–2307.
17. Tan CS, Ouyang Y, Ruiz H, Sadda SR (2012) Diurnal variation of choroidal thickness in normal, healthy subjects measured by spectral domain optical coherence tomography. Invest Ophthalmol Vis Sci 53(1):261–266.
18. Margolis R, Spaide RF (2009) A pilot study of enhanced depth imaging optical coherence tomography of the choroid in normal eyes. Am J Ophthalmol 147(5):811–815.
19. Ikuno Y, Kawaguchi K, Nouchi T, Yasuno Y (2010) Choroidal thickness in healthy Japanese subjects. Invest Ophthalmol Vis Sci 51(4):2173–2176.
20. Nicolela MT, Drance SM (1996) Various glaucomatous optic nerve appearances: clinical correlations. Ophthalmology 103(4):640–649.
21. Nakazawa T, Shimura M, Ryu M, Himori N, Nitta F, et al (2012) Progression of visual field defects in eyes with different optic disc appearances in patients with normal tension glaucoma. J Glaucoma 21(6):426–430.
22. Roberts KF, Artes PH, O'Leary N, Reis AS, Sharpe GP, et al (2012) Peripapillary choroidal thickness in healthy controls and patients with focal, diffuse, and sclerotic glaucomatous optic disc damage. Arch Ophthalmol 130(8):980–986.
23. Ehrlich JR, Peterson J, Parlitsis G, Kay KY, Kiss S, et al (2011) Peripapillary choroidal thickness in glaucoma measured with optical coherence tomography. Exp Eye Res 92(3):189–194.

24. Suh W, Cho HK, Kee C (2014) Evaluation of peripapillary choroidal thickness in unilateral normal-tension glaucoma. Jpn J Ophthalmol 58(1):62–67.
25. Hayreh SS (1969) Blood supply of the optic nerve head and its role in optic atrophy, glaucoma, and oedema of the optic disc. Br J Ophthalmol 53(11):721–748.
26. Manjunath V, Shah H, Fujimoto JG, Duker JS (2011) Analysis of peripapillary atrophy using spectral domain optical coherence tomography. Ophthalmology 118(3):531–536.
27. Aksoy Y, Çolakoglu K, Kar T, Sevinc MK, Eyi YE (2014) Choroidal thickness is affected by more factors than estimated. Invest Ophthalmol Vis Sci 55(3):1311.
28. Wong IY, Wong RL, Zhao P, Lai WW (2013) Choroidal thickness in relation to hypercholesterolemia on enhanced depth imaging optical coherence tomography. Retina 33(2):423–428.
29. Sogawa K, Nagaoka T, Takahashi A, Tanano I, Tani T, et al (2012) Relationship between choroidal thickness and choroidal circulation in healthy young subjects. Am J Ophthalmol 153(6):1129–1132.
30. Kim DY, Silverman RH, Chan RV, Khanifar AA, Rondeau M, et al (2013) Measurement of choroidal perfusion and thickness following systemic sildenafil (Viagra). Acta Ophthalmol 91(2):183–188.
31. Mansouri K, Medeiros FA, Tatham AJ, Marchase N, Weinreb RN (2014) Evaluation of retinal and choroidal thickness by swept-source optical coherence tomography: repeatability and assessment of artifacts. Am J Ophthalmol 157(5):1022–1032.

Changes in Outer Retinal Microstructures during Six Month Period in Eyes with Acute Zonal Occult Outer Retinopathy-Complex

Yoshitsugu Matsui[1], Hisashi Matsubara[1], Shinji Ueno[2], Yasuki Ito[2], Hiroko Terasaki[2], Mineo Kondo[1]*

1 Department of Ophthalmology, Mie University Graduate School of Medicine, Tsu, Japan, 2 Department of Ophthalmology, Nagoya University Graduate School of Medicine, Nagoya, Japan

Abstract

Purpose: To study the changes in the outer retinal microstructures during a six month period after the onset of acute zonal occult outer retinopathy (AZOOR)-complex by spectral-domain optical coherence tomography (SD-OCT).

Methods: Seventeen eyes of 17 patients with the AZOOR-complex were studied. The integrity of the external limiting membrane (ELM), ellipsoid zone (EZ; also called the inner/outer segment junction), and interdigitation zone (IDZ; also called the cone outer segment tips) were evaluated in the SD-OCT images obtained at the initial visit and at six months. The three highly reflective bands were divided into three types; continuous, discontinuous, and absent. The integrity of the outer nuclear layer (ONL) was also assessed.

Results: Among the three highly reflective bands, the IDZ was most altered at the initial visit and least recovered at six months. Fifteen of 17 eyes (88%) had a recovery of at least one of the three bands at six months in the retinal area where the ONL was intact, and these areas showed an improvement of visual field. Three eyes (18%) had retinal areas where the ONL was absent at the initial visit, and there was no recovery in both the retinal structures and visual fields in these areas.

Conclusions: Our results indicate that more than 85% eyes with AZOOR-complex show some recovery in the microstructures of the outer retina during a six month period if the ONL is intact. We conclude that SD-OCT is a useful method to monitor the changes of the outer retinal microstructure in eyes with the AZOOR-complex.

Citation: Matsui Y, Matsubara H, Ueno S, Ito Y, Terasaki H, et al. (2014) Changes in Outer Retinal Microstructures during Six Month Period in Eyes with Acute Zonal Occult Outer Retinopathy-Complex. PLoS ONE 9(10): e110592. doi:10.1371/journal.pone.0110592

Editor: Steven Barnes, Dalhousie University, Canada

Received May 28, 2014; Accepted September 19, 2014; Published October 30, 2014

Data Availability: The authors confirm that all data underlying the findings are fully available without restriction. All relevant data are within the paper.

Funding: Grant-in-Aid for Scientific Research C (#20592603) from Ministry of Education, Culture, Sports, Science and Technology (http://www.jsps.go.jp/). The funders had no role in study design, data collection and analysis, decision to publish, or preparation of the manuscript.

Competing Interests: The authors have declared that no competing interests exist.

* Email: mineo@clin.medic.mie-u.ac.jp

Introduction

Acute zonal occult outer retinopathy (AZOOR) is a retinal disease that was first reported by Gass [1]. AZOOR is characterized by an acute loss of one or more zones of outer retinal function, photopsia, minimal funduscopic changes, and electroretinographic (ERG) abnormalities [1–4]. AZOOR occurs predominantly in young women, and some patients have a viral-like illness before the onset [1,4,5]. The exact pathogenesis of AZOOR is still uncertain, but two possible hypotheses have been advanced; virus infection of the photoreceptors [6] and common genetic hypothesis of autoimmune/inflammatory disease [7].

In 2003, Gass suggested that retinal diseases similar to AZOOR, e.g., multiple evanescent white dot syndrome (MEWDS), multifocal choroiditis and panuveitis (MFP), punctate inner choroidopathy (PIC), acute idiopathic blind spot enlargement (AIBSE), acute macular neuroretinopathy (AMN), and AZOOR, were part of a spectrum of a single disease with similar clinical signs, symptoms, and ophthalmological findings [6]. He recommended that these should be placed in a single clinical entity called the AZOOR-complex. There are several studies that reported that two of these diseases can occur in the same patient at the same time or at different times [8–12].

Optical coherence tomography (OCT) is a useful method to detect subtle morphological changes in retinas affected by various pathological conditions. Past studies have demonstrated the diagnostic value of time-domain (TD) and spectral-domain (SD) OCT in eyes with AZOOR-complex. The findings showed that the integrity of the external limiting membrane (ELM), ellipsoid zone (EZ; originally called the inner/outer segment junction [13]) and/or interdigitation zone (IDZ; also called the cone outer segment tips [14]) were disrupted at the retinal areas of visual field defects in eyes with the AZOOR-complex [15–24]. It was also reported that the abnormalities in the outer retinal microstructures can recover during the follow-up period in some patients with the AZOOR-complex [18–20,22]. However, there has not a study that analyzed how these three highly reflective bands change with time during a fixed time period for many patients.

Therefore, the purpose of this study was to determine by SD-OCT the changes in the outer retinal microstructures during a six month period after the initial visit in eyes with AZOOR-complex.

Subjects and Methods

Subjects

We reviewed the medical records of patients who were diagnosed with AZOOR-complex who visited the Mie University Hospital or the Nagoya University Hospital from September 2007 to June 2013. Because the purpose of this study was to determine the changes of the retinal microstructures at the early stages of AZOOR-complex, only the patients whose initial examination was #3 months from the onset were studied. In addition, only the patients who were followed for at least six months after the initial visit were included. Based on these criteria, seventeen eyes of 17 patients with the AZOOR-complex were studied.

All patients had undergone a complete eye examination including best-corrected visual acuity (BCVA) measured by a standard Japanese decimal visual acuity chart at 5 m, slit-lamp biomicroscopy, color fundus photography, Humphrey static perimetry (30-2 program), and SD-OCT. Fluorescein angiography was performed only at the initial visit. Full-field electroretinograms (ERGs) or multifocal ERGs were recorded at the initial visit for a correct diagnosis of the AZOOR-complex [2,3].

The procedures used conformed to the tenets of the World Medical Association's Declaration of Helsinki. Mie University Institutional Ethics Review Board approved this retrospective study of the patients' medical records. Written informed consent was not given by participants for their clinical records to be used in this study, but patient information was anonymized and de-identified prior to analysis.

Spectral-domain optical coherence tomography (SD-OCT)

All of the patients had undergone SD-OCT examinations with the Spectralis OCT (HRA+OCT, Heidelberg Engineering) or the Cirrus HD-OCT (version 5.1, Carl Zeiss Meditec). Following the dilation of the pupils, the retinal tomographic images of 9 mm (approximately 30u) horizontal scans for Spectralis or horizontal 6 mm scans for Cirrus were obtained across the fovea. Depending on the image quality, B-scans were averaged.

We evaluated the SD-OCT findings at the initial visit and at six months. The reason why we selected the SD-OCT findings at 6 months was because Gass et al. [4] had reported that the alterations of the patients' vision stabilized within six months of the onset in 77% of the patients. We evaluated the integrity of the three highly reflective bands at the outer retina obtained by the SD-OCT; the external limiting membrane (ELM), ellipsoid zone (EZ) [13], and interdigitation zone (IDZ) [14]. The integrity of these bands was divided into three types; ''continuous'', ''discontinuous'', or ''absent''. The bands were defined as ''continuous'' when they were seen clearly and appeared to be continuous. The bands were defined as being ''discontinuous'' when they were blurred or interrupted. The bands were defined as ''absent'' when they were not identified at the area of the visual field defect. These decisions were made by two retinal specialists (YM and HM) independently and were masked to the other clinical findings. In addition, the preservation of outer nuclear layer (ONL) was also assessed.

To evaluate the changes in the outer retinal highly reflective bands more quantitatively, a longitudinal reflectivity profile (LRP) was created by previously described methods [13,25,26]. In brief, one vertical straight line was drawn at the retinal area of the visual field defect. The LRPs were made by calculating median values of pixels across each level of 20 adjacent A-scans using ImageJ (National Institutes of Health, Bethesda, MA; available at rsbweb.nih.gov/ij/download.html).

Results

The clinical characteristics and SD-OCT findings of the 17 Japanese patients with AZOOR-complex (three men and 14 women; age, 19–49 years) are summarized in Table 1. The diagnosis of our 17 patients included 10 with AZOOR, 4 with MEWDS, and 3 with AIBSE. The average interval between the onset of symptoms and examination in our hospital was 3.6 weeks with a range of 1 to 12 weeks. The average spherical equivalent refractive error was -4.4 diopters (D) with a range of -0.5 to -13.5 D. The type of visual field defects included two with a central scotoma, six with a paracentral scotoma, two with a temporal scotoma, and seven with a centro-temporal scotoma (Table 1).

Case Presentations

Case 11: MEWDS Associated with ONL Loss. A 35-year-old myopic woman presented with complaints of acute vision reduction and photopsia in her right eye. Her decimal best-corrected visual acuity (BCVA) was 0.5 OD, and perimetry showed a visual field defect within 30 degrees of the fovea (Fig. 1A). Fundus examination showed multiple small, gray-white patches at the level of RPE and outer retina in the mid-peripheral region, and these white patches disappeared within four weeks without treatment. Based on these clinical findings, she was diagnosed with MEWDS. She was followed up without any treatments.

Her SD-OCT findings at the initial visit are shown in Figures 1B and 1C. In the central retinal area where the ONL was intact (yellow dotted square, Fig. 1B), the ELM was judged to be ''discontinuous'', and the EZ and IDZ were classified as being ''absent''. This was because these two lines were merged with the RPE-Bruch's membrane complex and were not identified as independent bands (Fig. 1C).

At six months after the initial visit, the decimal BCVA had improved to 1.2, and the visual field had recovered at many points (Fig. 1D). SD-OCT also showed an improvement in the outer retinal microstructures but only at the area of the intact ONL (yellow dotted square, Figs. 1E and 1F). At this time, the ELM and EZ were judged as ''continuous'', but the IDZ was still judged as ''discontinuous'' at the central area.

We also noted that this patient had an area of the retina where the ONL was completely absent at the initial visit (red square, Fig. 1B), and there was no recovery of the both the visual field and the SD-OCT image in this area at 6 months (red square, Fig. 1E).

Case 1: AZOOR with Recovery of Outer Retinal Microstructures. A 30-year-old emmetropic woman had an acute onset of photopsia and vision reduction in her right eye. Her decimal BCVA was 1.0 OD, and fundus examination and fluorescein angiography were essentially normal. However, perimetry showed severely decreased retinal sensitivities within 20 degrees of the fovea in the right eye (Fig. 2A). Multifocal ERGs also showed reduced focal ERGs within 20 degrees of the fovea. Based on these findings, this patient was diagnosed with AZOOR. She was followed without any treatments.

Her SD-OCT findings at the initial visit are shown in Figures 2B and 2C. The ELM and EZ were judged to be ''discontinuous'', because they were disrupted away from the macula (Figs. 2B and 2C). The IDZ was judged to be ''absent'' because this band was not identified over the entire 9 mm scan.

Table 1. Clinical Characteristics and SD-OCT findings of Patients with AZOOR-Complex.

Case/Sex/Age (y)/Eye	Diagnosis	Initial visit from the onset (week)	Spherical equivalent refractive error (dioptor)	Type of Scotoma	BCVA initial/6M	ELM initial/6M	EZ initial/6M	IDZ initial/6M	Improvement in visual field
1/F/30/Right	AZOOR	2	20.5	Paracentral	1.0/1.2	II/I	II/I	III/II	Significant
2/M/35/Right	AZOOR	4	20.5	Paracentral	1.2/1.5	I/I	I/I	II/I	Significant
3/F/34/Right	AZOOR	1	211.5	Centro-temporal	0.5/0.7	II/II	III/III	III/III	None
4/F/19/Right	AZOOR	2	23.0	Temporal	0.9/1.2	II/I	II/I	III/III	Mild
5/F/49/Left	AZOOR	12	213.5	Centro-temporal	0.8/0.6	III/III	III/III	III/III	None
6/F/30/Right	AZOOR	4	27.0	Centro-temporal	0.5/0.8	I/I	II/I	II/III	Mild
7/F/37/Left	AZOOR	1	28.5	Centro-temporal	0.6/1.0	II/I	II/I	III/III	Mild
8/F/25/Left	AZOOR	8	26.6	Centro-temporal	0.2/0.8	I/I	II/I	III/III	Mild
9/M/42/Right	AZOOR	2	26.0	Paracentral	1.2/1.2	I/I	II/I	III/II	Mild
10/F/19/Right	AZOOR	1	24.5	Centro-temporal	0.6/1.2	II/II	II/I	III/II	Significant
11/F/35/Right	MEWDS	2	210.0	Central	0.5/1.2	II/I	III/I	III/II	Significant
12/F/31/Left	MEWDS	1	26.5	Central	0.3/1.2	II/I	II/I	III/I	Significant
13/M/39/Right	MEWDS	8	20.5	Centro-temporal	0.2/1.2	II/I	III/I	III/II	Significant
14/F/24/Right	MEWDS	1	22.75	Paracentral	0.8/1.2	II/I	II/I	III/II	Significant
15/F/47/Right	AIBSE	1	22.0	Temporal	1.2/1.2	I/I	II/I	III/III	None
16/F/37/Left	AIBES	3	20.5	Paracentral	1.2/1.0	II/I	II/I	III/I	Significant
17/F/29/Left	AIBSE	8	25.75	Paracentral	1.0/1.2	I/I	II/I	III/II	Significant

Abbreviations: AZOOR, acute zonal occult outer retinopathy; MEWDS, multiple evanescent white dot syndrome; AIBSE, acute idiopathic blind spot enlargement; BCVA, best-corrected visual acuity; ELM, external limiting membrane; EZ, ellipsoid zone; IDZ, interdigitation zone; I, continuous; II, discontinuous; III, absent.

doi:10.1371/journal.pone.0110592.t001

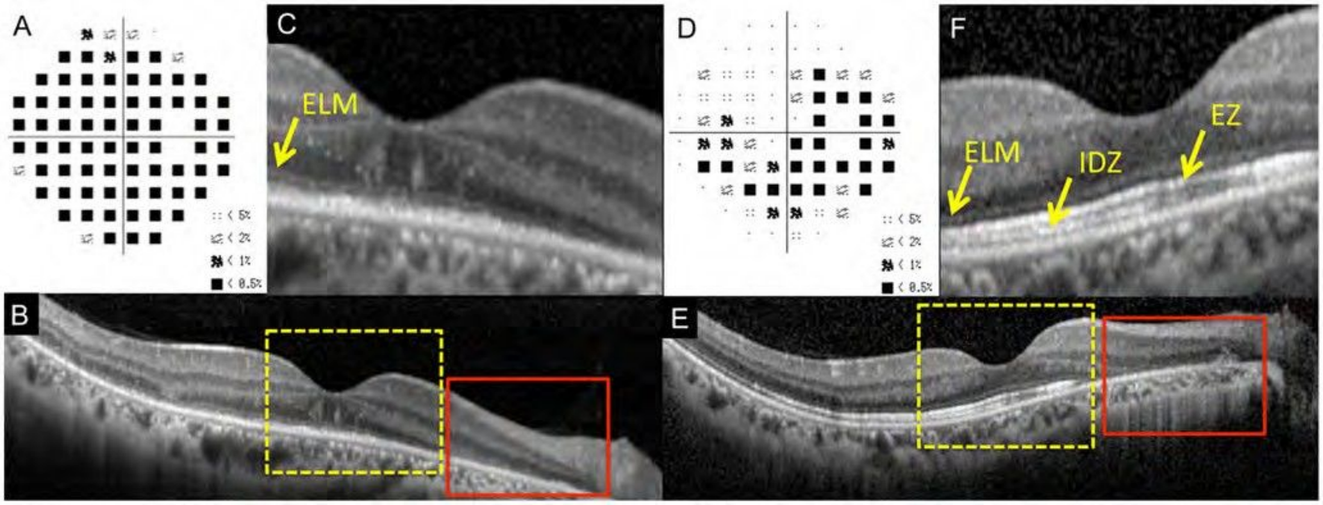

Figure 1. Static visual field and spectral-domain optical coherence tomographic (SD-OCT) results of the right eye of Case 11 at the initial visit (A–C) and six months after the initial visit (D–F). A: Deviation plot obtained by the Humphrey 30-2 program at the initial visit. B: Horizontal SD-OCT image through the fovea at the initial visit. C: Magnified view of the area outlined by dashed yellow line box in the image of B. D: Deviation plot obtained with the Humphrey 30-2 program at six months after the initial visit. E: Horizontal SD-OCT image through the fovea at six months after the initial visit. F: Magnified view of the area outlined by dashed yellow line box in the image of E. ELM, external limiting membrane. EZ, ellipsoid zone. IDZ, interdigitation zone. This case had the retinal area where the outer nuclear layer (ONL) was completely absent (red line boxes).
doi:10.1371/journal.pone.0110592.g001

Interestingly, the retina had highly reflective materials in columns which passed through the ONL from the RPE at the area of visual field defect (red arrows, Fig. 2C). Similar highly reflective materials have been reported in a patient with MEWDS [20].

After six months, there was a marked improvement in her visual fields (Fig. 2D), and SD-OCT showed a recovery of the outer retinal microstructures. At this time, the ELM and EZ were judged to be ''continuous''. However, the IDZ was still ''discontinuous'', because it was only identified in the central area (Figs. 2E and 2F). We also noticed that the columnar highly reflective materials were not present at six months. The ONL was preserved in the initial and 6 months SD-OCT images.

Case 2: AZOOR with Intact EZ at Initial Visit. A 35-year-old healthy emmetropic man reported that he had an acute paracentral visual field depression and photopsia in his right eye. His decimal BCVA was 1.2 OD. His fundus and fluorescein angiography were normal, but visual field showed extensive defects outside the fovea in the right eye (Fig. 3A). His scotopic and photopic full-field ERGs were reduced but only in the right eye.

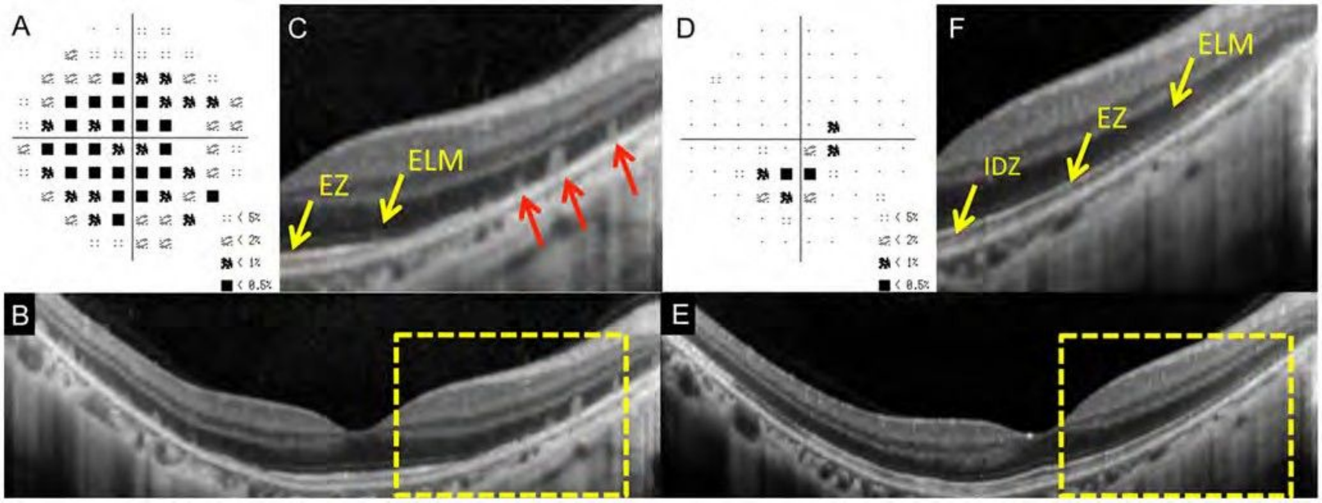

Figure 2. Static visual field and spectral-domain optical coherence tomography (SD-OCT) results of the right eye of Case 1 at the initial visit (A–C) and six months after the initial visit (D–F). A: Deviation plot obtained with the Humphrey 30-2 program at the initial visit. B: Horizontal SD-OCT image through the fovea at the initial visit. C: Magnified view of the area outlined by dashed yellow line box in B. D: Deviation plot obtained with the Humphrey 30-2 program at six months after the initial visit. E: Horizontal SD-OCT image through the fovea at six months after the initial visit. F: Magnified view of the area outlined by dashed yellow line box in the image of B. ELM, external limiting membrane. EZ, ellipsoid zone. IDZ, interdigitation zone. Several column-shaped highly reflective materials are seen at the outer retinal area of visual field defect at the initial visit (red arrows).
doi:10.1371/journal.pone.0110592.g002

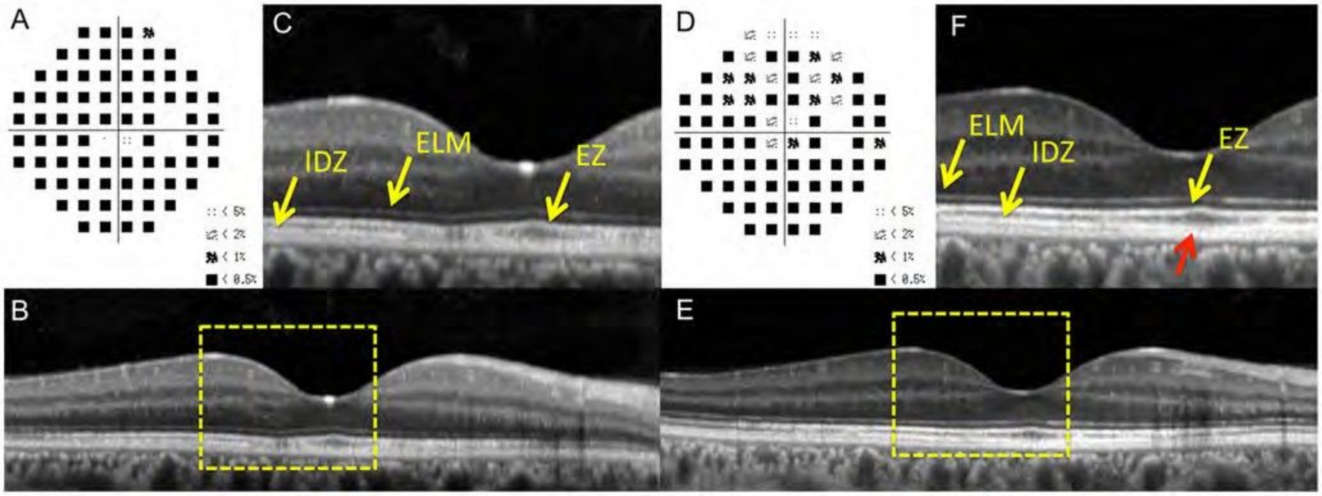

Figure 3. Static visual field and spectral-domain optical coherence tomographic (SD-OCT) results in the right eye of Case 2 at the initial visit (A–C) and six months after the initial visit (D–F). A: Deviation plot obtained with the Humphrey 30-2 program at the initial visit. B: Horizontal SD-OCT image through the fovea at the initial visit. C: Magnified view of the area outlined by dashed yellow line box in the image of B. D: Deviation plot obtained by the Humphrey 30-2 program at six months after the initial visit. E: Horizontal SD-OCT image through the fovea at six months after the initial visit. F: Magnified view of the area outlined by dashed yellow line box in the image of B. The COST line is still blurred near the fovea (red arrow). ELM, external limiting membrane. EZ, ellipsoid zone. IDZ, interdigitation zone.
doi:10.1371/journal.pone.0110592.g003

Based on these findings, he was diagnosed with AZOOR. He was treated with intravenous drip methylprednisolone.

His SD-OCT findings at the initial visit are shown in Figures 3B and 3C. The ELM and EZ were judged to be ''continuous'', but the IDZ was judged to be ''discontinuous'' (Fig. 3B & 3C).

Six months later, he reported some improvements of his visual symptoms, and his visual field showed recovery at several points (Fig. 3D). At this time, the ELM and EZ were judged to be ''continuous'', but the IDZ was judged to be ''discontinuous'', because it was still blurred near the fovea (yellow arrow, Fig. 3F, red arrow). The ONL was intact both at the initial visit and at 6 months.

To evaluate the changes in outer retinal high-reflective bands more quantitatively, a longitudinal reflectivity profile (LRP) was created in the retina of Case 2 (Fig. 4). One vertical straight line was drawn at 0.5 mm temporal retina from the foveola (red dotted lines of Fig. 4). We found that that IDZ was undetectable at the initial visit, but it became detectable as a third highly reflective band six month later (Figs. 4C and 4E).

Case 3: AZOOR with Worsening of Visual Fields. A 34-year-old myopic woman reported experiencing photophobia and vision reduction of one month duration in her right eye. She had a history of Basedow disease for eight years. Her decimal BCVA was 0.5 OD. Fundus examination and fluorescein angiography were normal, but Humphrey visual field tests revealed a temporal scotoma extending into the fixation point in the right eye (Fig. 5A). The multifocal ERGs were reduced in the centro-temporal field. Based on these clinical findings, she was diagnosed with AZOOR. She was treated with intravenous drip methylprednisolone.

Her SD-OCT findings of the right eye at the initial visit are shown in Figures 5B and 5C. Her ELM and EZ were judged to be ''discontinuous'', and the IDZ was judged to be ''absent''. Despite intravenous drip methylprednisolone and following orally administrated predonisolone for six months, she felt that there was a gradual worsening of her visual decrease, and visual field tests showed an enlargement of the temporal scotoma (Fig. 5D). At this time, the ELM and EZ were judged to be ''discontinuous'', and the IDZ still remained ''absent'' (Figs. 5E and 5F). The ONL thickness was also reduced at the areas of the visual field defects.

Summary of SD-OCT findings

The changes in the ELM, EZ, and IDZ at the initial visit and six months later are summarized in Figure 6 (see also Table 1). The status of the three highly reflective bands were evaluated at the retinal areas with visual field defects. In this evaluation, we excluded the retinal areas of undetectable ONL, because we noted that the retinal areas with loss of ONL at the initial visit did not show any improvement both in the SD-OCT findings and the visual field defects. Therefore in Figure 6, the results are shown only at the retinal areas of intact ONL.

We found that the IDZ was most vulnerable among the three outer retinal bands at the initial visit. There were no AZOOR-complex patients who had a continuous IDZ at the area of visual field defect at the initial visit. The IDZ was also most slow to recover at six months after the initial visit. Even at six months, the IDZ was continuous only in three eyes (18%), discontinuous in six eyes (35%), and still absent in eight eyes (47%).

When compared to the IDZ, the ELM and EZ were relatively well preserved at six months. The ELM was continuous in 14 of 17 eyes (82%) at six months. Similarly, the EZ was continuous in 15 of 17 eyes (88%) at six months (Fig. 5).

We also found that 15 of 17 eyes (88.3%) had a recovery of at least one of the three bands during six months (Table 1) if the ONL was intact, and these 15 eyes also showed an improvement of the visual field defects.

Discussion

We investigated the changes in the outer retinal microstructures at the initial visit and six months later in 17 eyes with AZOOR-complex using the SD-OCT. There have been many case series which described the change of OCT findings with time in AZOOR-complex patients [12,15–24], but the best of our knowledge, this is the first systematic report focusing on the

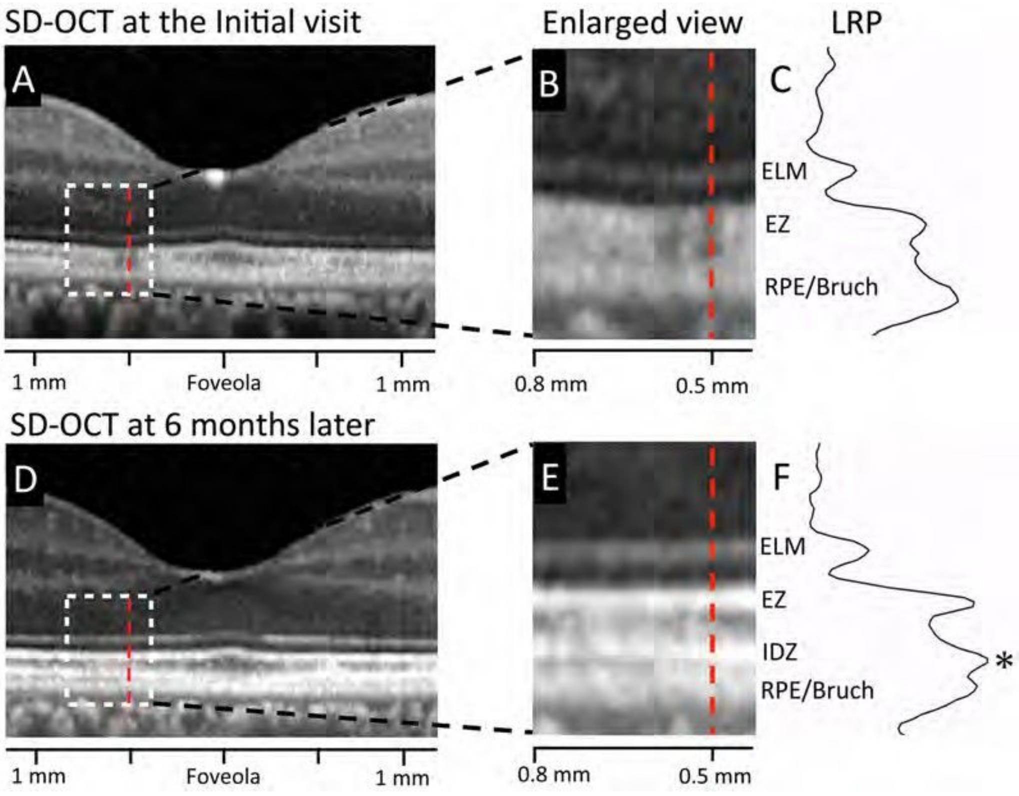

Figure 4. Results of longitudinal reflectivity profile (LRP) in the retina of Case 2. A. Horizontal SD-OCT scan through the fovea at the initial visit. B. Magnified view of the area outlined by dashed white line box in the image of A. C. Longitudinal reflectivity profile (LRP) along the vertical line at 0.5 mm temporal from the foveola (red dotted line) at the initial visit. D. Horizontal SD-OCT scan through the fovea at six months after the initial visit. E. Magnified view of the area outlined by dashed white line box in the image of D at six months after the initial visit. F. Longitudinal reflectivity profile (LRP) along the vertical line at 0.5 mm temporal from the foveola (red dotted line) at six months after the initial visit. At the retinal area of 0.5 mm temporal from the foveola, IDZ was nearly undetectable at the initial visit, but the peak of IDZ was clearly detectable as a third highly reflective band at six month later (asterisk). ELM, external limiting membrane. EZ, ellipsoid zone. IDZ, interdigitation zone. RPE/Bruch, retinal pigment epithelium/Bruch's membrane complex. LRP, longitudinal reflectivity profile.
doi:10.1371/journal.pone.0110592.g004

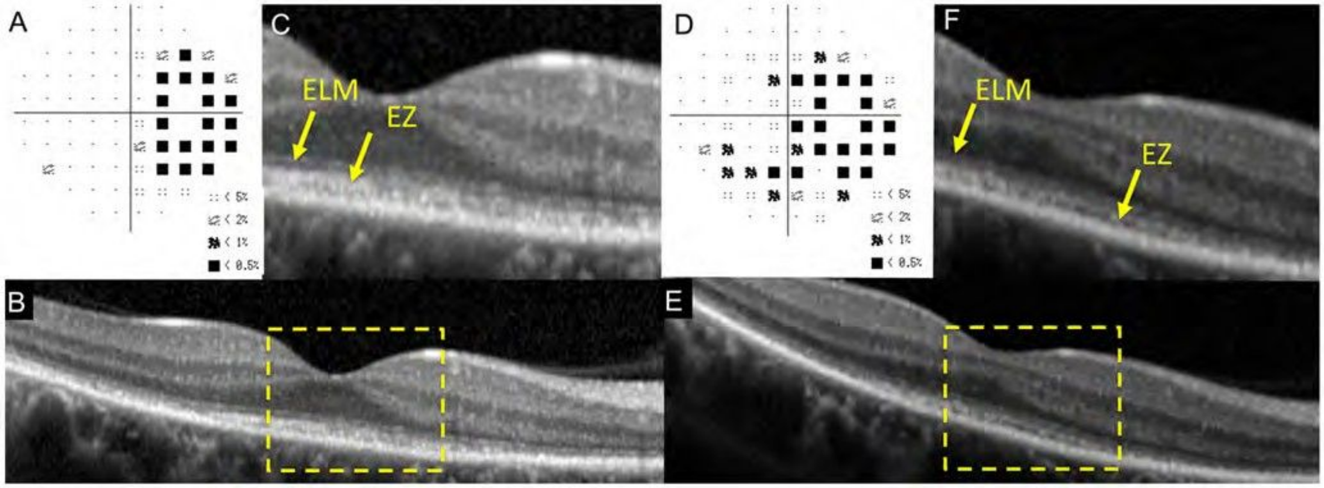

Figure 5. Static visual field and spectral-domain optical coherence tomographic (SD-OCT) results in the right eye of Case 3 at the initial visit (A–C) and six months after the initial visit (D–F). A: Deviation plot obtained by the Humphrey 30-2 program at the initial visit. B: Horizontal SD-OCT image through the fovea at the initial visit. C: Magnified view of the area outlined by dashed yellow line box in the image of B. D: Deviation plot obtained by the Humphrey 30-2 program at six months after the initial visit. E: Horizontal SD-OCT image through the fovea at six months after the initial visit. F: Magnified view of the area outlined by dashed yellow line box in the image of E. ELM, external limiting membrane. EZ, ellipsoid zone. IDZ, interdigitation zone.
doi:10.1371/journal.pone.0110592.g005

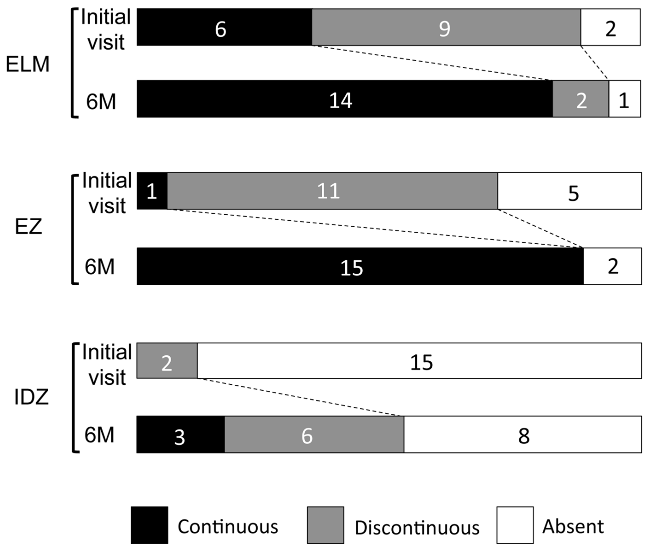

Figure 6. Summary of findings of the three highly reflective bands at the outer retina obtained by SD-OCT at the initial visit and six months later. These three lines were divided into three types; "continuous", "discontinuous" and "absent". ELM, external limiting membrane. EZ, ellipsoid zone. IDZ, interdigitation zone.
doi:10.1371/journal.pone.0110592.g006

changes in the three outer retinal bands of SD-OCT during a fixed time period.

We found that the IDZ was most vulnerable among the three outer retinal bands in the retina of AZOOR-complex. At the initial visit, the IDZ was abnormal, i.e., discontinuous or absent, in all 17 eyes (100%), while the ELM and EZ were abnormal in 11 (65%) and 16 eyes (94%), respectively (Fig. 6). Similarly, at six months after the initial visit, the IDZ was still abnormal in 14 eyes (82%), while the ELM and EZ were abnormal in only three (18%) and two eyes (12%), respectively. These results indicate that the IDZ is the most vulnerable microstructure and can be used to detect and follow the alterations of the outer retina in eyes with AZOOR-complex.

The origin of IDZ has not been established, and is currently thought to correspond to the junction [14] or contact cylinder [13] between the RPE apical processes and the external portion of the cones. Thus, this band is thought to be a useful indicator of the integrity of outer segments of the photoreceptors. Recent studies have reported that the integrity of the IDZ was significantly correlated with visual function in different retinal diseases including occult macular dystrophy [27,28], epiretinal membrane [29–31], and central serous chorioretinopathy [32]. On the other hand, it is also known that the IDZ cannot be identified clearly even in some normal subjects [33,34]. Thus, Rii et al. reported that the incidence of eyes with an intact foveal IDZ was about 95% in normal individuals [33]. Taken together, we now interpret our findings by concluding that the IDZ is the most vulnerable microstructure in eyes with our AZOOR-complex patients. This is because the visibility of the IDZ is most easily affected when the photoreceptors are damaged and not necessarily because this region is the primary site of this disorder.

There are several reports suggesting that the abnormality of EZ was present in the region of the visual field defects in AZOOR-complex [12,15–24]. Our results agree with this because most of our patients (16 of 17 eyes, 94%) had abnormal EZ at the region of the visual field defect at the initial visit. However, we also noted that one of our patients had a ''continuous'' EZ even at the retinal area of visual field defect at the initial visit (Case 2). In this area, only the IDZ was ''discontinuous'' (Fig. 3C). Tsunoda et al. [23] recently described two AZOOR patients whose EZ was normal, but the IDZ was not present or indistinct at the retinal area of visual field defect. So et al. [22] also reported an AZOOR patient whose EZ recovered, but the IDZ was still absent at the one month follow-up examination. We recommend focusing on not only the EZ but also the IDZ to enhance the detection of abnormal retinal microstructures in eyes with the AZOOR-complex [22,23].

Spaide et al. [18] reported that there was no visual field or anatomic improvements in the retinal regions where there was outer nuclear loss and that the improvement of scotoma and restoration of EZ were only seen in areas that had no loss of outer nuclear layers. Our results agree with their findings. We noted that three of 17 eyes (18%, Case 5, 11, and 16) that had retinal regions with a loss of the ONL at the initial visit did not show any recovery both in the retinal microstructures or the visual fields at these regions during six months (red squares of Fig. 1). These results support the idea that the photoreceptor outer segments can recover by the process of renewal only when the photoreceptor cell bodies are intact [18,20], and also suggests that the OCT findings of ONL can be useful in predicting whether the visual field defect can recover in eyes with AZOOR-complex.

Many of our patients with AZOOR-complex had myopia, and the average spherical equivalent refractive error in our 17 eyes was -4.4 D. This is consistent with past reports showing a high prevalence of myopia in eyes with AZOOR-complex [4,35]. In this study, we also noted that the eyes with more severe myopia of -≥5.0 D tended to have worse outcomes with abnormal EZ or IDZ at 6 months (Table 1). It should be interesting to study the correlation between the degree of myopia and the severity of outer retinal damage in more patients with AZOOR-complex.

There are two major limitations in this study. The first limitation is the small number of patients who were studied retrospectively. Because the AZOOR-complex is a very rare disease, we could not collect many patients from only two institutions. In addition, some patients were excluded because of insufficient SD-OCT or clinical data. Longer prospective studies with a larger number of patients may clarify more detailed information on the structural and functional changes with time in AZOOR-complex.

The second limitation is that we have combined the three different subtypes of the AZOOR-complex, MEWDS, AZOOR, and AIBSE. Although Gass et al. [6] suggested that these diseases may be part of a spectrum of a single disease, the prognosis is clearly different among the different types of AZOOR-complex [36]. Therefore, subgroup analysis for each type of disease may add more useful information.

Despite these limitations, our results demonstrated that 15 of 17 eyes (88%) with AZOOR-complex have some recovery of the retinal microstructures during six months if the ONL is intact. We also showed that the IDZ was the most vulnerable at the initial visit, and difficult to recover in this disorder. The SD-OCT was very useful for monitoring the changes of the outer retinal microstructure in eyes with the AZOOR-complex.

Acknowledgments

We thank Professor Duco Hamasaki of the Bascom Palmer Eye Institute of the University of Miami for critical discussion and final manuscript revisions.

Author Contributions

Conceived and designed the experiments: YM HM SU YI HT MK. Performed the experiments: YM HM MK. Analyzed the data: YM HM SU YI HT MK. Contributed reagents/materials/analysis tools: YM HM SU YI HT MK. Wrote the paper: YM MK.

References

1. Gass JDM (1993) Acute zonal occult outer retinopathy. Donders lecture—The Netherlands Ophthalmological Society, Maastricht, Holland, June 19, 1992. J Clin Neurol Ophthalmol 13: 79–97.
2. Jacobson SG, Morales DS, Sun XK, Feuer WJ, Cideciyan AV, et al. (1995) Pattern of retinal dysfunction in acute zonal occult outer retinopathy. Ophthalmology 102: 1187–1198.
3. Francis PJ, Marinescu A, Fitzke FW, Bird AC, Holder GE (2005) Acute zonal occult outer retinopathy: towards a set of diagnostic criteria. Br J Ophthalmol 89: 70–73.
4. Gass JD, Agarwal A, Scott IU (2002) Acute zonal occult outer retinopathy: a long-term follow-up study. Am J Ophthalmol 134: 329–339.
5. Monson DM, Smith JR (2011) Acute zonal occult outer retinopathy. Surv Ophthalmol 56: 23–35.
6. Gass JD (2003) Are acute zonal occult outer retinopathy and the white spot syndromes (AZOOR complex) specific autoimmune diseases? Am J Ophthalmol 135: 380–381.
7. Jampol LM, Becker KG (2003) White spot syndromes of the retina: a hypothesis based on the common genetic hypothesis of autoimmune/inflammatory disease. Am J Ophthalmol 135: 376–379.
8. Gass JD, Hamed LM (1989) Acute macular neuroretinopathy and multiple evanescent white dot syndrome occurring in the same patients. Arch Ophthalmol 107: 189–193.
9. Holz FG, Kim RY, Schwartz SD, Harper CA, Wroblewski J, et al. (1994) Acute zonal occult outer retinopathy (AZOOR) associated with multifocal choroidopathy. Eye (Lond) 8(Pt1): 77–83.
10. Bryan RG, Freund KB, Yannuzzi LA, Spaide RF, Huang SJ, et al. (2002) Multiple evanescent white dot syndrome in patients with multifocal choroiditis. Retina 22: 317–322.
11. Taira K, Nakazawa M, Takano Y, Ota T (2006) Acute zonal occult outer retinopathy in the fellow eye 5 years after presentation of punctate inner choroidopathy. Graefes Arch Clin Exp Ophthalmol 244: 880–882.
12. Fine HF, Spaide RF, Ryan EH Jr, Matsumoto Y, Yannuzzi LA (2009) Acute zonal occult outer retinopathy in patients with multiple evanescent white dot syndrome. Arch Ophthalmol 127: 66–70.
13. Spaide RF, Curcio CA (2011) Anatomical correlates to the bands seen in the outer retina by optical coherence tomography: literature review and model. Retina 31: 1609–1619.
14. Srinivasan VJ, Monson BK, Wojtkowski M, Bilonick RA, Gorczynska I, et al. (2008) Characterization of outer retinal morphology with high-speed, ultrahigh-resolution optical coherence tomography. Invest Ophthalmol Vis Sci 49: 1571–1579.
15. Li D, Kishi S (2007) Loss of photoreceptor outer segment in acute zonal occult outer retinopathy. Arch Ophthalmol 125: 1194–1200.
16. Nguyen MH, Witkin AJ, Reichel E, Ko TH, Fujimoto JG, et al. (2007) Microstructural abnormalities in MEWDS demonstrated by ultrahigh resolution optical coherence tomography. Retina 27: 414–418.
17. Zibrandtsen N, Munch IC, Klemp K, Jorgensen TM, Sander B, et al. (2008) Photoreceptor atrophy in acute zonal occult outer retinopathy. Acta Ophthalmol 86: 913–916.
18. Spaide RF, Koizumi H, Freund KB (2008) Photoreceptor outer segment abnormalities as a cause of blind spot enlargement in acute zonal occult outer retinopathy-complex diseases. Am J Opthalmol 146: 111–120.
19. Hangai M, Fujimoto M, Yoshimura N (2009) Features and function of multiple evanescent white dot syndrome. Arch Ophthalmol 127: 1307–1313.
20. Li D, Kishi S (2009) Restored photoreceptor outer segment damage in multiple evanescent white dot syndrome. Ophthalmology 116: 762–770.
21. Fujiwara T, Imamura Y, Giovinazzo VJ, Spaide RF (2010) Fundus autofluorescence and optical coherence tomographic findings in acute zonal occult outer retinopathy. Retina 30: 1206–1216.
22. So K, Shinoda K, Matsumoto CS, Satofuka S, Imamura Y, et al. (2011) Focal functional and microstructural changes of photoreceptors in eyes with acute zonal occult outer retinopathy. Case Rep Ophthalmol 2: 307–313.
23. Tsunoda K, Fujinami K, Miyake Y (2011) Selective abnormality of cone outer segment tip line in acute zonal occult outer retinopathy as observed by spectral-domain optical coherence tomography. Arch Ophthalmol 129: 1099–1101.
24. Mkrtchyan M, Lujan BJ, Merino D, Thirkill CE, Roorda A, et al. (2012) Outer retinal structure in patients with acute zonal occult outer retinopathy. Am J Ophthalmol 153: 757–768.
25. Murakami T, Nishijima K, Akagi T, Uji A, Horii T, et al. (2012) Optical coherence tomographic reflectivity of photoreceptors beneath cystoid spaces in diabetic macular edema. Invest Ophthalmol Vis Sci. 53: 1506–1511.
26. Cideciyan AV, Hufnagel RB, Carroll J, Sumaroka A, Luo X, et al. (2013) Human cone visual pigment deletions spare sufficient photoreceptors to warrant gene therapy. Hum Gene Ther. 24: 993–1006.
27. Park SJ, Woo SJ, Park KH, Hwang JM, Chung H (2010) Morphologic photoreceptor abnormality in occult macular dystrophy on spectral-domain optical coherence tomography. Invest Ophthalmol Vis Sci. 51: 3673–3679.
28. Tsunoda K, Usui T, Hatase T, Yamai S, Fujinami K, et al. (2012) Clinical characteristics of occult macular dystrophy in family with mutation of RP1l1 gene. Retina 32: 1135–1147.
29. Shimozono M, Oishi A, Hata M, Matsuki T, Ito S, et al. (2012) The significance of cone outer segment tips as a prognostic factor in epiretinal membrane surgery. Am J Ophthalmol. 153: 698–704,
30. Watanabe K, Tsunoda K, Mizuno Y, Akiyama K, Noda T (2013) Outer retinal morphology and visual function in patients with idiopathic epiretinal membrane. JAMA Ophthalmol 131: 172–177.
31. Itoh Y, Inoue M, Rii T, Hirota K, Hirakata A (2013) Correlation between foveal cone outer segment tips line and visual recovery after epiretinal membrane surgery.Invest Ophthalmol Vis Sci 54: 7302–7208.
32. Fujita K, Shinoda K, Imamura Y, Matsumoto CS, Mizutani Y, et al. (2012) Correlation of integrity of cone outer segment tips line with retinal sensitivity after half-dose photodynamic therapy for chronic central serous chorioretinopathy. Am J Ophthalmol 154: 579–585.
33. Rii T, Itoh Y, Inoue M, Hirakata A (2012) Foveal cone outer segment tips line and disruption artifacts in spectral-domain optical coherence tomographic images of normal eyes. Am J Ophthalmol 153: 524–529.
34. Terasaki H, Shirasawa M, Yamashita T, Yamashita T, Yamakiri K, et al. (2012) Comparison of foveal microstructure imaging with different spectral domain optical coherence tomography machines. Ophthalmology. 119: 2319–2327.
35. Asano T, Kondo M, Kondo N, Ueno S, Terasaki H, et al. (2004) High prevalence of myopia in Japanese patients with multiple evanescent white dot syndrome. Jpn J Ophthalmol. 48: 486–489.
36. Jampol LM, Wiredu A (1995) MEWDS, MFC, PIC, AMN, AIBSE, and AZOOR: one disease or many? Retina 15: 373–378.

Ophthalmic Genetics, 2014; 35(1): 25–34
© Informa Healthcare USA, Inc.
ISSN: 1381-6810 print/1744-5094 online
DOI: 10.3109/13816810.2013.768673

RESEARCH REPORT

Clinical Phenotype in Ten Unrelated Japanese Patients with Mutations in the EYS Gene

Kimiko Suto[1], Katsuhiro Hosono[1], Masayo Takahashi[2], Yasuhiko Hirami[3], Yuki Arai[3], Yasunori Nagase[1], Shinji Ueno[4], Hiroko Terasaki[4], Shinsei Minoshima[5], Mineo Kondo[6], and Yoshihiro Hotta[1]

[1]Department of Ophthalmology, Hamamatsu University School of Medicine, Hamamatsu, Japan, [2]Laboratory for Retinal Regeneration, RIKEN Center for Developmental Biology, Kobe, Japan, [3]Department of Ophthalmology, Institute of Biomedical Research and Innovation Hospital, Kobe, Japan, [4]Department of Ophthalmology, Nagoya University Graduate School of Medicine, Nagoya, Japan, [5]Department of Photomedical Genomics, Basic Medical Photonics Laboratory, Medical Photonics Research Center, Hamamatsu University School of Medicine, Hamamatsu, Japan, and [6]Department of Ophthalmology, Mie University Graduate School of Medicine, Tsu, Japan

ABSTRACT

Background: To characterize the clinical phenotypes associated with previously-reported mutations of the eyes shut homolog (EYS) gene, including a truncating mutation, c.4957_4958insA, which is a major causative mutation for retinitis pigmentosa (RP) in Japan.

Materials and Methods: The study population comprised ten unrelated RP subjects with very likely pathogenic mutations in both alleles, four of them with a homozygous c.4957_4958insA mutation. The phenotype analysis was based on ophthalmic examination, Goldmann perimetry, and digital fundus photography.

Results: The study population included six men and four women aged 34–74 years. The average age at first visit was 31 years (range, 14–44 years), and the patients typically presented with night blindness as the initial symptom and subsequently developed progressive constriction of the visual field. Myopia was noted in 9/20 affected eyes. For most patients, central visual acuity was preserved relatively well up to their thirties, after which it deteriorated rapidly over the next two decades. The visual acuity of patients homozygous for the c.4957_4958insA mutation was uniform. Visual fields were constricted symmetrically, and the extent of constriction seemed to be better correlated with age than visual acuity. The fundus displayed bone spicules, which increased in density with age, and attenuated retinal vessels.

Conclusions: Although additional studies with more patients with mutations of the EYS gene are required, it appears that patients share a relatively uniform phenotype with near-normal central visual function up to their twenties. The patients homozygous for the c.4957_4958insA mutation showed a uniform course of visual acuity changes.

Keywords: Autosomal recessive, eyes shut homolog (EYS) gene, founder effect, Japanese patient, retinitis pigmentosa

INTRODUCTION

Retinitis pigmentosa (RP [MIM 268000]) is a genetically highly heterogeneous retinal degeneration characterized by night blindness and visual field constriction, which eventually lead to severe visual impairment. The disease can be inherited via an autosomal recessive (ar), autosomal dominant (ad), or X-linked recessive mode or may occur in isolation; more than half the cases in Japan are isolated.[1]

Received 23 May 2012; revised 16 January 2013; accepted 17 January 2013; published online 20 February 2013

Correspondence: Yoshihiro Hotta, MD, Department of Ophthalmology, Hamamatsu University School of Medicine, 1-20-1 Handayama, Hamamatsu 431-3192, Japan. Tel: +81 53 435 2256. Fax: +81 53 435 2372. E-mail: hotta@hama-med.ac.jp

Rod dysfunction precedes cone dysfunction; this results in the typical symptoms of night blindness, which is followed by the loss of the peripheral visual field in most cases. Subsequently, the cones in the central retina may also be affected, causing loss of visual acuity in the later stages of the disease. Ophthalmoscopic abnormalities include a waxy pallor of the optic disc, attenuation of retinal vessels, and peripheral bone spicule pigmentations as well as atrophy of the retinal pigment epithelium (RPE).

To date, 55 causative genes and eight loci have been found to be associated with RP (http://www.sph.uth.tmc.edu/Retnet/; accessed May 20, 2012). The eyes shut homolog (EYS) gene encodes an ortholog of Drosophila spacemaker (spam) and a protein essential for maintaining the photoreceptor morphology. EYS spans over 2 Mb, making it one of the largest genes known to be expressed in the human eye.[2,3] EYS gene mutations, which include primarily truncating and some missense mutations, have been detected in arRP-affected families of different ancestral origin and are reported to account for 5–16% of arRP cases.[4–7] Recently, we screened all EYS gene exons in 100 unrelated Japanese RP patients and, found EYS gene mutations in at least 20% of the arRP patients (see the Supplementary Table in the Supplementary Material – available online).[8] In the current study, we examined the clinical features of ten unrelated Japanese patients with RP caused by the EYS gene mutation and compared the phenotype of four patients with the homozygous c.4957_4958insA (p.S1653KfsX2) mutation, which is a major causative mutation of RP in Japan, to that of the other RP patients.

MATERIALS AND METHODS

Ethics Statements

This study was approved by the Institutional Review Board for Human Genetic and Genome Research at the three participating institutions (Hamamatsu University School of Medicine, RIKEN Center for Developmental Biology, and Nagoya University Graduate School of Medicine), and its procedures conformed to the tenets of the Declaration of Helsinki. Written informed consent was obtained from all participants before molecular genetic studies. Ten RP patients who carried homozygous or compound heterozygous mutations in the EYS gene were clinically re-evaluated at either the Department of Ophthalmology, Hamamatsu University Hospital in Hamamatsu (by YH); the Department of Ophthalmology, Kobe City Medical Center General Hospital in Kobe (by MT); or the Department of Ophthalmology, Nagoya University Hospital in Nagoya (by MK and SU).

Patients and Clinical Evaluation

The study subjects were ten unrelated Japanese RP patients residing in various geographical regions, ranging from Tokyo to Osaka. The cohort comprised nine unrelated patients with previously-reported homozygous or compound heterozygous EYS mutations[8] and one patient with a homozygous c.4957_4958insA mutation (RP115N). The doctors were asked to inquire about the family history of patients in as much detail as possible, and they confirmed that the parents of the patients with homozygous mutations were not consanguineous. The complete history and medical records of all the patients were reviewed. In addition, the patients were also clinically evaluated by the measurement of the best-corrected visual acuity, slit-lamp biomicroscopy, and ophthalmoscopy after pupillary dilatation. Refraction was determined using an auto-refractometer. Additional examinations included fundus photography and Goldmann kinetic perimetry (targets, V-4e, III-4e, and I-4e to I-1e) to assess the size and extent of the visual field and spectral-domain optical coherence tomography (OCT; Spectralis, Heidelberg Engineering, Heidelberg, Germany or Cirrus, Carl Zeiss Meditec Inc., Dublin, CA, USA), to visualize the in vivo retinal architecture. Electroretinograms (ERGs) were recorded according to the protocol set by the International Society for Clinical Electrophysiology of Vision.[9]

Goldmann visual fields were scanned with a Canon or Epson scanner and analyzed using the ImageJ software (available at http://rsbweb.nih.gov/ij/) in the following manner: transparent layers were added to each field, and the isopters of the visual fields were manually traced onto these layers. The areas of fields that were circular or elliptical were calculated using the appropriate equations, while those with other irregular forms were calculated using ImageJ. Further, the area of the fields for the V-4e and I-4e targets were measured and compared with the normal area.[10]

Mutation Analyses

Genomic DNA of one proband, RP115N, was extracted from the peripheral lymphocytes by using standard procedures. All 44 exons of EYS and their flanking sequences were studied initially. DNA was amplified by PCR. The PCR and sequencing procedures used have been described previously.[8]

P21H was homozygous for a deletion in exon 32 of the EYS gene, which is an in-frame deletion that results in the replacement of amino acids from D2142 to S2191 with G2142 (p.D2142_S2191delinsG).[8] To precisely determine the deletion breakpoints, PCR amplification was performed using a specially-designed primer pair: forward primer 5′-ATGGCTGTAGGAAACAATACAATGA-3′, located in intron 31, and reverse primer 5′-TTACTTCCAA ATTTCATGGTCATCT-3′, in intron 32 (see the Supplementary Figure – available online). Direct sequencing analysis was performed using the following primers: forward primer, 5′-ATAGATTC AATGCCATCCCCATCAAGCT-3′ and reverse primer, 5′-TGAGAAGTGTCTGTTCATATCCTTCA-3′ (Supplementary Figure). The amplification conditions were as follows: PCR was performed using the KOD FX PCR kit (TOYOBO, Japan) for 35 cycles at 98 °C for 10 s, 60 °C for 30 s, and 68 °C for 18 min in an automated thermal cycler.

RESULTS

Clinical and functional findings are summarized in Table 1. The patients' ages ranged from 14–37 years at the time of initial diagnosis (average, 31 years), while their ages at the time of initial examination for this study ranged from 34–74 years (average, 53 years). The patients were from diverse geographical regions, ranging from Tokyo to Osaka in Japan. Six patients' pedigrees were compatible with a recessive mode of inheritance, while the remaining four were considered isolated cases (data not shown). All ten patients had night blindness, with age at onset ranging from childhood to age 50 years (median, 17 years).

Mutation Analysis

A p.D2142_S2191delinsG mutation was detected by PCR by using a specially designed primer in the severest case (patient RP21H). In brief, after failing to amplify exon 32 in this case, we hypothesized that the patient may have homozygous deletion of a long genomic region, including exon 32. We successfully obtained an amplified product by using a primer pair, of which one (forward) was in intron 31 and the other (reverse) was in intron 32 (Supplementary Figure). Sequence analyses showed that the amplified DNA contained truncated intron 31 and truncated intron 32. The boundary between truncated intron 31 and 32 had a 58-nucleotide sequence string, GGGCAA. . .ATTGAC. We could not determine the precise breakpoints in both introns because the exact sequence identity around possible breakpoints could not be delineated; however, the deletion size was elucidated to be 12197 nucleotides, irrespective of the position of the break. We denoted the deletion as c.6425 -?_6571 þ ?del, as per the nomenclature guidelines provided by the Human Genome Variation Society (http://www.hgvs.org/mutnomen/).

Visual Acuity

Clinical examination revealed that corrected visual acuity varied considerably and ranged from 0 logMAR unit to light perception; the differences were attributable to the different stages of macular involvement (Table 1 and Figure 1). From the findings, a common pattern emerged: relatively well-preserved visual acuity up to the 3rd or 4th decade, with subsequent rapid deterioration to less than 1.0 logMAR unit at approximately 60 years of age. This pattern was noted in all cases, except one eye (left) of the youngest patient (patient RP44K; Table 1) who had visual acuity of counting fingers at the age of 34 years. Patient RP21H exhibited complete deletion of exon 32, which was the severest phenotype with vision being limited to light perception. The visual acuity of patients homozygous for the c.4957_4958insA mutation was of a uniform phenotype.

Refractive Error

Twelve eyes were ametropic; three exhibited slight hyperopia, and nine had various degrees of myopia ranging from −1 D to −6 D. The remaining eight eyes were emmetropic. Patients with severe forms of myopia (over −8 D), hypermetropia (over þ4 D), or astigmatism (over 3 D) were not found in this study.

Visual Fields

Constriction of the visual fields was symmetric, except for one patient who had no testable visual field in the central area or any targets in one eye (left eye of patient RP44K; Table). The extent of vi constriction correlated with age (Table 1 and Figure 1B). The visual field at the time of the study ranged from constriction to 10–12° for the V-4 target in a 63-year-old man (RP87N) to no light perception for the V-4 target in a 55-year-old man (RP21H). Figure 1B shows that the disease progressed relatively rapidly over the 3rd and 4th decades.

Cataracts and Anterior Segment Abnormalities

Cataract was observed in seven of the ten affected subjects, including four individuals who had pseudophakia (seven eyes).

Retinal and Macular Findings

Retinal changes were relatively uniform among the subjects. The optic disc appeared to be relatively

TABLE 1. Genotypes and phenotypes in Japanese patients with mutations in the EYS gene.

										Visual Acuity		Refraction						
Patient	Age at onset (years)	Age at first visit (years)	Current age (years)	Follow-up duration (years)	Gender	Origin	Family history	Type of change	Nucleotide change	Right Eye	Left Eye	Right Eye (D)	Left Eye (D)	Lens Status	Goldmann Perimetry (V-4e)	Fundoscopy Results	OCT Results	ERG Results
RP3H	14	35	67	12	Female	Tochigi	ar	Homozygous	c.4957_4958insA[8,12]/ c.4957_4958insA [8,12]	0.07	0.08	þ1	þ1.25	Bilateral pseudophakia	OD: 8º; OS: 7º	Waxy optic disc, attenuated retinal vasculature, RPE changes in the periphery, extensive bone spicules throughout periphery	No data	Extinguished
RP21H	20	35	55	17	Male	Hamamatsu	ar	Homozygous	c.6425-?_6571þ?del[8]/ c.6425-?_6571þ?del[8]	LP	LP	−3.0	−3.0	Bilateral pseudophakia	Unmeasurable	Waxy optic disc, attenuated retinal vasculature, RPE changes in the periphery and posterior pole, extensive bone spicules throughout periphery	Relatively preserved foveal lamination	Extinguished
RP35K	20	30s	39	3	Male	Toyooka	iso	Homozygous	c.8868C4A[8,12]/ c.8868C4A[8,12]	1	1	−6.0	−5.25	Clear	OD, OS: concentric constriction with remaining central island; remaining peripheral island. P0	Normal optic disc, slightly attenuated vessels, RPE changes in the periphery, bone spicules sprinkled throughout periphery	No data	No data
RP44K	14	14	34	4	Female	Tokyo	ar	Heterozygous/ Heterozygous	c.4957_4958insA[8,12]/ c.6557G4A[4,7,8]	0.4	CF	›0.5	0	Bilateral cataract	OD: concentric constriction with remaining central island. OS: concentric constriction with remaining peripheral island	Normal optic disc, attenuated retinal vasculature, RPE changes in the periphery and posterior pole, extensive bone spicules	No data	Extinguished

																throughout periphery		
RP48K	13	26	36	2	Male	Osaka	iso	Homozygous	c.4957_4958insA^{8,12}/ c.4957_4958insA ^{8,12}	0.6	0.6	−1.25	−1.0	Clear	OD: 6°; OS: 7°	Normal optic disc, slightly attenuated vessels, RPE changes in the periphery and posterior pole, extensive bone spicules throughout periphery	No data	No data
RP54K	20 s	30	53	2	Male	Himeji	ar	Homozygous	c.4957_4958insA^{8,12}/ c.4957_4958insA ^{8,12}	0.7	0.3	−2.25	−1.5	Right cataract Left pseudophakia	OD: 8°; OS: 8°	Waxy optic disc, attenuated retinal vasculature, RPE changes in the periphery and posterior pole, extensive bone spicules throughout periphery	Foveal thinning	No data
RP56K	20	37	74	5	Male	Tokyo	ar	Compound Heterozygous	c.4957_4958insA^{8,12}/ c.8351T>G^{8}	0.04	0.2	−1.5	−1.5	Bilateral pseudophakia	OD: 8°; OS: 9°	Waxy optic disc, attenuated retinal vasculature, RPE changes in the periphery and posterior pole, extensive bone spicules throughout periphery	Foveal thinning	No data
RP81K	Childhood	20	51	2	Female	Higashi-Osaka	ar	Compound Heterozygous	c.2522_2523insA^{8}/ c.6557G>A^{4,7,8}	0.6	0.6	0	+1.5	Bilateral cataract	OD: 11°; OS: 11°	Waxy optic disc, attenuated retinal vasculature, RPE changes in the periphery and posterior pole, some drusen-like deposits	No data	No data
7N	50*	44*	64	8	Male	Nagoya	iso	Heterozygous/							H		eterozygous	

c.4957_4958insA[8,12]/ c.7793G>A[8]	1	0.8	0	−1.0	Bilateral cataract	OD: 10º; OS: 10º OS: concentric constriction with remaining peripheral island	Normal optic disc, attenuated ret-inal vascula-ture, RPE changes in the periphery and posterior pole, extensive bone spicules	No data	No data

(continued)

TABLE 1. Continued.

										Visual Acuity		Refraction						
Patient	Age at onset (years)	Age at first visit (years)	Current age (years)	Follow-up duration (years)	Gender	Origin	Family history	Type of change	Nucleotide change	Right Eye	Left Eye	Right Eye (D)	Left Eye (D)	Lens Status	Goldmann Perimetry (V-4e)	Fundoscopy Results	OCT Results	ERG Results
																periphery, extensive bone spicules throughout periphery		
RP115N	6–12 years	30 s	52	7	Female	Aichi	iso	Homozygous	c.4957_4958insA[8,12]/ c.4957_4958insA [8,12]	0.6	0.6	0	0	Clear	OD, OS: concentric constriction with remaining central island; remaining peripheral island	Waxy optic disc, attenuated retinal vasculature, RPE changes in the periphery, extensive bone spicules throughout periphery	No data	No data

* Subject RP87N was diagnosed with retinitis pigmentosa by fundoscopy at the age of 44 years, when he was asymptomatic; thereafter, he developed night blindness at the age of 50 years.

‘‘Age at Onset’’ was based on history and ‘‘Age at First Visit’’ was based on medical records.

Tochigi, Tokyo, Osaka, and Aichi are prefectures and Hamamatsu, Toyooka, Himeji, Higashi-Osaka, and Nagoya are cities.

References for previously-reported mutations are indicated in the column labeled ‘‘Nucleotide Change’’.

All clinical data were obtained from the latest examinations, but the refraction of the eyes that underwent cataract surgery was assessed on the basis of the latest phakic data.

ar, autosomal recessive; iso, isolated case; D, diopter; LP, light perception; CF, counting fingers; OD, oculis dextra (right eye); OS, oculis sinistra (left eye); OCT, optical coherence tomography; ERG: electroretinogram

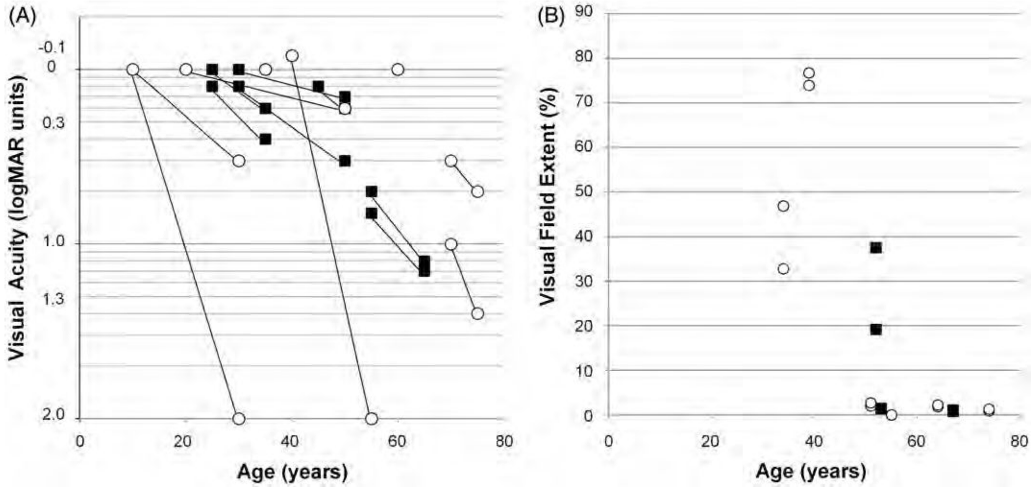

FIGURE 1. (A) Visual acuity was expressed in logMAR units, as a function of age of the subjects. The graph shows a decrease in visual acuity (y-axis) with age in years (x-axis). Symbols indicate the time points of assessment. g, subjects with homozygous c.4957_4958insA mutation; *, other subjects. The visual acuity was preserved well into the thirties or forties, after which it declined. Visual acuity of subjects with the homozygous c.4957_4958insA mutation was uniform. (B) The extent of the visual field (kinetic perimetry with V-4e test target) loss was expressed as a percentage of the normal mean and plotted as a function of age in the ten subjects. g, subjects with the homozygous c.4957_4958insA EYS mutation; *, other subjects. The extent of visual constriction correlated with age.

well-preserved, and compared to the venules, the arterioles showed mild to moderate attenuation. Profound atrophy of the retinal pigment epithelium (RPE), choriocapillaris, and outer segment at the mid-peripheral retina were observed in all patients. In the later stages of the disease, the macular region and, sometimes, the fovea were abnormal. We also observed varying amounts of bone spicule-like pigmentation dispersed in the posterior pole, mid-periphery, and anterior portions of the fundus; the deposits were more prominent in the older patients, but were detected in all the cases in mid-peripheral retina (Figure 2A, B, C). Only one patient had a history of cystoid macular edema (CME) (10%) at 66 years of age; this frequency is less than that reported-previously.[13]

OCT Images

High-resolution OCT images showed a marked reduction of retinal thickness resulting from the loss of photoreceptor layers (Figure 2D, E, F). The photoreceptor inner segment/outer segment junction (IS/OS line) was either completely absent or only detectable at the fovea in four subjects. Although patient RP21H, with complete deletion of exon 32, had light perception in both eyes, the OCT image demonstrated relatively preserved foveal structures, including the IS/OS line (Figure 2D).

ERG Recordings

ISCEV-standard full-field ERGs were recorded for three patients [patients RP3H (at the age of 59 years), RP21H (at the age of 41 years), and RP44K (at the age of 27 years)] and were nearly undetectable for all patients in both rod and cone components.

DISCUSSION

In this report, we describe the phenotype of ten unrelated Japanese patients affected with arRP caused by EYS gene mutations. Our previous study on 100 Japanese arRP patients indicated very likely pathogenic mutations and possible pathogenic mutations in 18% (18/100) and 8% (8/100), respectively, of the study population; these values are higher than those previously reported.[4–7] Our previous study has shown that 16% of Japanese patients with arRP displayed either the c.4957_4958insA or the c.8868C4A mutation, which accounted for 57% (15 þ 5/35) of the mutated alleles and seem to be frequent among Japanese patients with arRP.[8] However, a detailed haplotype analysis of the EYS gene has not been performed, and therefore, currently, we cannot verify whether each mutation occurred in an ancient common ancestor. This high prevalence of EYS gene mutations, including two frequent mutations, has recently been confirmed by another study in the Japanese population.[12] Together, these findings strongly suggest that EYS gene mutations play a major role in the pathogenesis of arRP affecting the Japanese population. In this study, we only recruited patients with very likely pathogenic mutations and involvement of both alleles because a second mutant allele could not be detected by direct sequencing in 17/26 patients in the previous study, and the genotype of such patients could not be determined.

FIGURE 2. Fundus photographs of patients carrying mutations in the EYS gene. The entire retina of the right eye of patient RP21H at age 55 years showed extensive bone-spicule pigmentation throughout the fundus (A). The central retina of the left eye of patient RP54K, aged 51 years, showed a waxy optic disc, severely attenuated retinal vasculature, and extensive chorioretinal atrophy with minimal residual retinal pigment epithelium in the macular region (B). The central retina of the right eye of patient RP56K (age, 73 years) showed the fundus appearance of the end-stage of the disease (C). Illustration of macular changes by spectral-domain optical coherence tomography showed a marked reduction of retinal thickness. Relatively preserved foveal lamination was observed in the right eye of patient RP21H at the age of 55 years (D). Marked foveal thinning was observed in the left eye of patient RP54K at the age of 51 years (E) and in the right eye of patient RP56K at the age of 73 years (F).

The genotype includes truncated mutations and few missense mutations (Supplementary Table). No patient with missense mutations in both alleles was included. We recruited four patients with the homozygous c.4957_4958insA mutation and one patient with the homozygous c.8868C4A mutation.

Overall, most patients showed relatively well-preserved visual acuity into their thirties, after which rapid deterioration was observed in their forties or fifties. The constriction of the visual fields was symmetric, although the extent seemed to correlate better with age than visual acuity. Cataract was frequently observed among patients in their thirties. In one case (RP21H), visual acuity improved noticeably from 0.5 logMAR units to −0.1 logMAR units in both eyes after cataract extraction by the age of 37 years, but gradually progressed to light perception by the age of 40 years. In all cases, the fundus displayed typical changes of retinitis pigmentosa (RP), including attenuated retinal vessels and bone-spicule deposits over 360° of the fundus, all of which increased in density with age. Electroretinographic (ERG) responses were consistent with severe generalized rod–cone dysfunction.

Reports have been published on the phenotype of RP caused by EYS gene mutations in Indonesian, Pakistani, Chinese, Israeli, Spanish, French, British, Dutch, and Palestinian patient populations[4–7,13–16];

these reports contain only a brief description of the clinical features. The subjects in this study shared a relatively uniform phenotype, characterized by a symptom-free interval in the first two decades of life (median age at onset, 23 years) followed by a rapid decline in visual function. The patient RP87N was diagnosed with RP by funduscopy at the age of 44 years, when he was subjectively asymptomatic; later, he developed night blindness at the age of 50 years. The clinical features reported in this study are consistent with those reported previously. For instance, the visual acuities were relatively well-preserved up to the 3rd or 4th decades, as reported in a study of a population of European ancestry.[7] The visual acuities were relatively better and photophobia less frequent than that in seven Spanish arRP subjects carrying mutations of the ceramide kinase-like (CERKL) gene, which is involved in sphingolipid-mediated apoptosis in the retina.[17] The visual field loss noted among our study population was less than that reported for patients with mutations of the dehydrodolichyl diphosphate synthase (DHDDS) gene, which encodes an enzyme required for dolichol-pyrophosphate synthesis.[18]

To date, extensive studies focusing on the clinical features of a large number of RP patients with EYS gene mutations have been limited to Dutch and French arRP cohorts.[5,7] However, these studies included only a few non-European patients and showed a change in visual acuity with age in patients carrying EYS gene mutations; this was similar to the pattern noted in our Japanese subjects.

X-linked RP has been associated with myopia of 2 diopters or more, whereas dominant inheritance is associated with hyperopia.[19–21] In this study, 12 of the investigated eyes were ametropic (three slightly hyperopic and nine with various degrees of myopia) and eight were emmetropic. Myopia has a greater prevalence in Asian countries, including Japan, compared to Western populations.[22] Thus, our data together with those of a previous French study[5] suggest that most patients with arRP due to EYS mutations may have no or mild (mostly myopic) refractive error.

Three severe cases with retinal atrophy involving the posterior pole have been described previously (Family A: II-3[3], CIC01223[5] and CIC00492[5]);[3,5] however, most patients in this study presented with typical signs of progressive rod–cone dystrophy with relatively well-preserved central vision until late in the course of the disorder. It is plausible that a larger cohort of Japanese patients with EYS mutation may yield patients with greater involvement of the cones than rods. Two cases of sector RP with distinct fundus abnormalities with predominance of pigmentary changes in the inferior part of both retinas have been reported previously (CIC01222[5] and MOL0640 III:1[13]).[5,13] Although none of our patients had sector RP at the time of the study, we cannot rule out its presence in the earlier stages of the disease, before the patients were enrolled in this study. It is difficult to establish a clear genotype–phenotype association since we could only investigate ten patients.

We recruited six homozygous patients for this clinical and molecular study. Among them, four patients (RP3H, RP48K, RP54K, and RP115N) were homozygous for the c.4957_4958insA mutation (p.S1653KfsX2; truncating mutation in exon 26), which, as shown in our previous report, is a major causative mutation of RP in Japan. The course of visual acuity changes in homozygous patients with the c.4957_4958insA mutation was uniform. However, no remarkable clinical pattern emerged among the ten patients with variable genotypes, including the c.4957_4958insA mutation, in this study. The patients had near-normal visual function up to their twenties; this implies that slowing the progression of degeneration may be a possible therapeutic approach for preventing blindness in RP patients.

ACKNOWLEDGMENTS

We would like to thank the patients who participated in the study.

DECLARATION OF INTEREST

The authors report no conflict of interest. The authors alone are responsible for the content and writing of the paper.

This study was supported by research grants from the Ministry of Health, Labour and Welfare (Research on Measures for Intractable Diseases) and from the Japan Society for the Promotion of Science (Grant-in-Aid for Scientific Research (C) 23592561 and Grant-in Aid for Young Scientists (B) 23791975).

REFERENCES

1. Hayakawa M, Fujiki K, Kanai A, et al. Multicenter genetic study of retinitis pigmentosa in Japan: I. Genetic heterogeneity in typical retinitis pigmentosa. Jpn J Ophthalmol 1997;41:1–6.
2. Abd El-Aziz MM, Barragán I, O'Driscoll CA, et al. EYS, encoding an ortholog of Drosophila spacemaker, is mutated in autosomal recessive retinitis pigmentosa. Nat Genet 2008;40:1285–1287.
3. Collin RW, Littink KW, Klevering BJ, et al. Identification of a 2 Mb human ortholog of Drosophila eyes shut/spacemaker that is mutated in patients with retinitis pigmentosa. Am J Hum Genet 2008;83:594–603.
4. Abd El-Aziz MM, O'Driscoll CA, Kaye RS, et al. Identification of novel mutations in the ortholog of Drosophila eyes shut gene (EYS) causing autosomal

recessive retinitis pigmentosa. Invest Ophthalmol Vis Sci 2010;51:4266–4272.

5. Audo I, Sahel JA, Mohand-Saïd S, et al. EYS is a major gene for rod-cone dystrophies in France. Hum Mutat 2010;31:E1406–1435.
6. Barragán I, Borrego S, Pieras JI, et al. Mutation spectrum of EYS in Spanish patients with autosomal recessive retinitis pigmentosa. Hum Mutat 2010;31:E1772–1800.
7. Littink KW, van den Born LI, Koenekoop RK, et al. Mutations in the EYS gene account for approximately 5% of autosomal recessive retinitis pigmentosa and cause a fairly homogeneous phenotype. Ophthalmology 2010; 117:2026–2033.
8. Hosono K, Ishigami C, Takahashi M, et al. Two novel mutations in the EYS gene are possible major causes of autosomal recessive retinitis pigmentosa in the Japanese population. PLoS ONE 2012;7:e31036.
9. Marmor MF, Fulton AB, Holder GE, et al. ISCEV Standard for full-field clinical electroretinography (2008 update). Doc Ophthalmol 2009;118:69–77.
10. Schindler EI, Nylen EL, Ko AC, et al. Deducing the pathogenic contribution of recessive ABCA4 alleles in an outbred population. Hum Mol Genet 2010;19:3693–3701.
11. Hajali M, Fishman GA, Anderson RJ. The prevalence of cystoid macular oedema in retinitis pigmentosa patients determined by optical coherence tomography. Br J Ophthalmol 2008;92:1065–1068.
12. Iwanami M, Oshikawa M, Nishina T, et al. High prevalence of mutations in the EYS genes in Japanese patients with autosomal recessive retinitis pigmentosa. Invest Ophtalmol Vis Sci 2012;53:1033–1040.
13. Bandah-Rozenfeld D, Littink KW, Ben-Yosef T, et al. Novel null mutations in the EYS gene are a frequent cause of autosomal recessive retinitis pigmentosa in the Israeli population. Invest Ophthalmol Vis Sci 2010;51:4387–4394.
14. Huang Y, Zhang J, Li C, et al. Identification of a novel homozygous nonsense mutation in EYS in a Chinese family with autosomal recessive retinitis pigmentosa. BMC Med Genet 2010;11:121.
15. Khan MI, Collin RW, Arimadyo K, et al. Missense mutations at homologous positions in the fourth and fifth laminin A G-like domains of eyes shut homolog cause autosomal recessive retinitis pigmentosa. Mol Vis 2010;16:2753–2759.
16. Pieras JI, Barragán I, Borrego S, et al. Copy-number variations in EYS: a significant event in the appearance of arRP. Invest Ophthalmol Vis Sci 2011;52:5625–5631.
17. Avila-Fernandez A, Riveiro-Alvarez R, Vallespin E. CERKL mutations and associated phenotypes in seven Spanish families with autosomal recessive retinitis pigmentosa. Invest Ophthalmol Vis Sci 2008;49:2709–2713.
18. Zelinger L, Banin E, Obolensky A, et al. A missense mutation in DHDDS, encoding dehydrodolichyl diphosphate synthase, is associated with autosomal-recessive retinitis pigmentosa in Ashkenazi Jews. Am J Hum Genet 2011;88:207–215.
19. Berson EL, Rosner B, Simonoff E. Risk factors for genetic typing and detection in retinitis pigmentosa. Am J Ophthalmol 1980;89:763–75.
20. Hartong DT, Berson E, Dryja TP. Retinitis pigmentosa. Lancet 2006;368:1795–1809.
21. Fishman GA, Farber MD, Derlacki DJ. X-linked retinitis pigmentosa: profile of clinical findings. Arch Ophthalmol 1988;106:369–75.
22. Sawada A, Tomidokoro A, Araie M, et al. Refractive errors in an elderly Japanese population: the Tajimi study. Ophthalmology 2008;115:363–370.

Changes in angle of optic nerve and angle of ocular orbit with increasing age in Japanese children

Hideyuki Tsukitome,[1] Yoshikazu Hatsukawa,[2] Tomoko Morimitsu,[2] Teiji Yagasaki,[3] Mineo Kondo[1]

[1]Department of Ophthalmology, Mie University Graduate School of Medicine, Tsu, Japan
[2]Department of Ophthalmology, Osaka Medical Center and Research Institute for Maternal and Child Health, Osaka, Japan
[3]Yagasaki Eye Clinic, Ichinomiya, Japan

Correspondence to
Dr Mineo Kondo, Department of Ophthalmology, Mie University Graduate School of Medicine, 2-174 Edobashi, Tsu, Mie 514-8507, Japan; mineo@clin.medic.mie-u.ac.jp

Received 13 March 2014
Revised 29 June 2014
Accepted 25 July 2014
Published Online First
21 August 2014

To cite: Tsukitome H, Hatsukawa Y, Morimitsu T, et al. Br J Ophthalmol 2015;99:263–266.

ABSTRACT

Purpose To study changes in the opening angle of the optic nerve and the angle of the ocular orbit with increasing age in normal Japanese children.

Methods We studied 147 normal children (aged 6 months to 18 years) who had undergone CT as a diagnostic procedure. Measurements were performed on axial CT images that included the entire optic nerve of both eyes. The opening angle of the optic nerve was defined as the angle formed by the intersection of a line running through the left optic nerve and a vertical line passing through the centre of the nose. The opening angle of the orbit was defined as the angle formed by the intersection of a line running tangentially along the deep lateral wall of the left orbit and a vertical line passing through the centre of the nose. The relationship between age and these opening angles was analysed by regression analysis.

Results The correlation between age and opening angle of the optic nerve was not significant. In contrast, the opening angle of the orbit decreased relatively rapidly until about 2–3 years of age, and then it stabilised. The decrease in the opening angle of the orbit with increasing age was significant ($p<0.001$). The relationship between these two parameters was best fitted by a logarithmic regression curve.

Conclusions Because the opening angle of the orbit decreased significantly with increasing age, this factor must be considered when diagnosing and treating strabismus in children.

INTRODUCTION

The morphology of the orbit is known to change during normal development. The angle of the orbit is wide during early fetal development and gradually becomes narrower as gestation progresses.[1] Examining normal developmental changes in orbital morphology after birth should provide important information on the management of strabismus in children with and without skull or orbital abnormalities.

There have been a number of studies on changes in the volume of the orbit and the diameter of the orbital opening during development.[2–6] However, there are only three studies on the opening angle of the optic nerve or the orbit.[7–9] Therefore, the purpose of this study was to determine changes in the opening angle of the optic nerve and orbit with increasing age using axial CT images in normal Japanese children.

SUBJECTS AND METHODS

Subjects

We studied 147 children (aged 6 months to 18 years) who had been examined at the Osaka Medical Center and Research Institute for Maternal and Child Health from 2008 to 2011. These children had undergone head CT because they had suffered a blow to the head or had headaches of unknown origin. The attending doctors needed to rule out intracranial injuries or diseases. Children found not to have head or orbital abnormalities served as subjects. Children whose height or weight fell outside the mean±2SD for their age group were excluded. In addition, children with conditions potentially affecting the normal formation of the skull or facial bones, such as hydrocephalus or craniosynostosis, and also children with apparent eye position abnormalities were excluded. The procedures used conformed to the tenets of the World Medical Association's Declaration of Helsinki. The institutional ethics review board approved this retrospective study of the patients' medical records (approved No 675).

The children were divided into year age groups; to minimise age variations in each age group due to the date of birth, subjects were selected by the following method. Ten infants who underwent CT at 6 ±1 months of age were placed in the 6-month age group. For the 1–8-year groups, 10 children who had undergone CT on their date of birth ±1 month were selected. Similarly, of the children who underwent a CT on their date of birth ±2 months from ages 9–12 and ages 15–17 years, 10 of each age were selected. Seven children who underwent a CT at age 18 years ±2 months were also selected. In total, 147 children were studied. A histogram of the age and sex of these children is shown in figure 1.

CT and measurement of opening angles

A CT system (Aquilion16; Toshiba, Japan) was used to obtain tomographic images of the head including both orbits with the optic nerves and the surrounding orbital walls (figure 2). The CT scan was performed with the subject in the supine position with their face directed upward, and measurements were made on the CT image in which the face position was straight upward. Imaging conditions were: tube voltage, 120 kV; tube current, 200 mA; slice thickness, 0.5 mm; 16 data acquisition system channels; helical scan with a pitch of 0.67. The slice thickness for images used for the measurements was 1 mm. Opening angles of the optic nerve and orbit were measured in the axial CT images.

The opening angle of the optic nerve was defined as the angle formed by the intersection of a

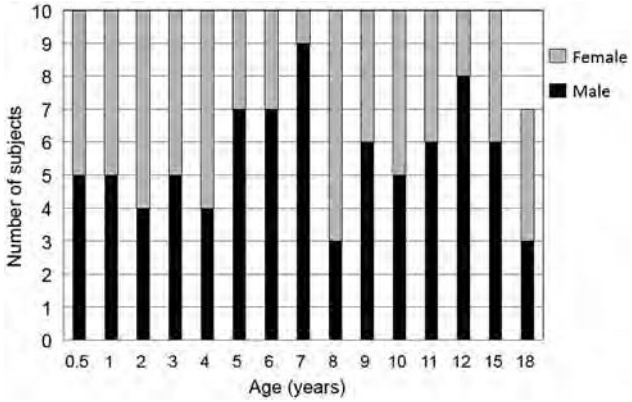

Figure 1 Histogram showing the age and sex of the 147 children who were subjects of this study.

line running through the left optic nerve and a vertical line passing through the centre of the nose (figure 2, left panel). The opening angle of the orbit was defined as the angle formed by the intersection of a line running tangentially along the deep lateral wall of the left orbit and a vertical line passing through the centre of the nose (figure 2, right panel). We measured these angles when the optic nerve appeared in one CT slice. An automatic measuring tool, which was included in the electronic medical charts, was used to measure these angles. To reduce interobserver variation, all measurements were performed by two independent observers (HT and TM), who were blinded to the age of the subject. The mean values of the two observers were used for the statistical analyses.

Statistical analyses

Mann–Whitney U tests were used to compare opening angles between two groups of different ages. In addition, the following three types of regression analysis were performed to examine the relationship between age and opening angle of the optic nerve or opening angle of the orbit: linear regression analysis using the actual values, linear regression analysis in which the relationship between angle and age was approximated with an exponential function, and linear regression analysis in which the relationship between angle and age was approximated with a logarithmic function. The coefficient of determination (r^2) and p values were determined on the basis of these regression analyses. $p<0.05$ was considered significant.

RESULTS

The opening angles of the optic nerve in each age group are shown in figure 2. The mean opening angle of the optic nerve was 23.9±4.1° (mean±SD) in the 10 infants in the 6-month age group and 21.7±1.7° in the 10 in the 3-year age group (figure 3). The difference between these two groups was not significant ($p=0.82$; Mann–Whitney U test). The relationship between age and opening angle of the optic nerve was analysed using three regression analyses (table 1). We found that there was no significant correlation between age and angle of the optic nerve ($p>0.40$), and the coefficient of determination (r^2) of age to the opening angle of the optic nerve was less than 0.01 (1%) for all three regression analyses (table 1).

The opening angles of the orbit in each age group are plotted in figure 4. The mean opening angle of the orbit was 50.8±4.1° in 10 infants who were 6 months old, and this was significantly larger than that (45.2±1.9°) in 10 infants who were 3 years of age ($p<0.001$; Mann–Whitney U test). In addition, the data show that the angle decreased asymptotically up until the age of 2–3 years.

The relationship between age and opening angle of the orbit was analysed using three regression analyses. We found that there were significant correlations between age and angle of orbit for all regression analyses ($p<0.001$, table 1). The coefficient of determination (r^2) of age to the opening angle of the orbit was about 0.13 (13%) and 0.12 (12%) according to linear and exponential regression analyses, respectively, and 0.19 (19%) in the logarithmic regression analysis (table 1).

DISCUSSION

Body parts change considerably during the fetal period and early childhood. A number of studies have examined morphological changes in the orbit with increasing age,[1–9] but only a few studies have measured changes in the opening angle of the optic nerve and orbit after birth in normal subjects.[7–9] We

Figure 2 Opening angle of the optic nerve and opening angle of the orbit for representative typical infants measured on the axial CT image at 6 months and 5 years of age. The opening angle of the optic nerve was defined as the angle formed by the intersection of a line running through the left optic nerve and a vertical line passing through the centre of the nose (left panel). The opening angle of the orbit was defined as the angle formed by the intersection of a line running tangentially along the deep lateral wall of the left orbit and a vertical line passing through the centre of the nose (right panel). There were no major differences in the opening angle of the optic nerve (left panel) in infants at 6 months and 5 years of age, but the opening angle of the orbit (right panel) was less in the 5-year-old infant.

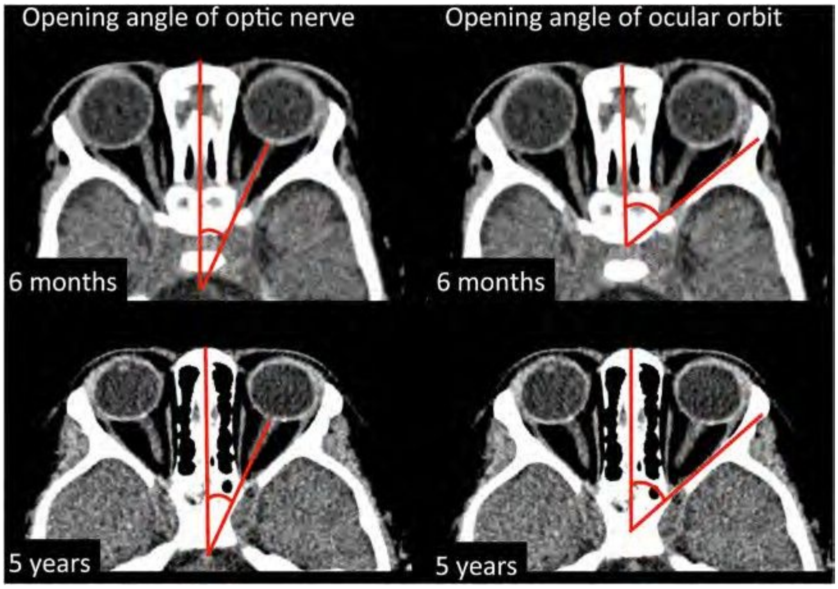

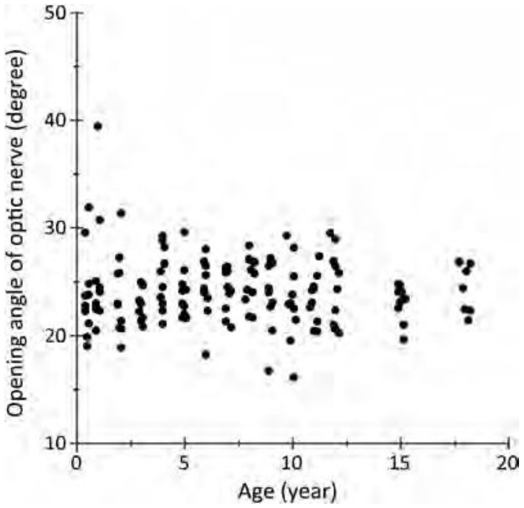

Figure 3 Changes in the opening angle of the optic nerve during development. The results of regression analyses showed no significant changes in the opening angle of the optic nerve with increasing age.

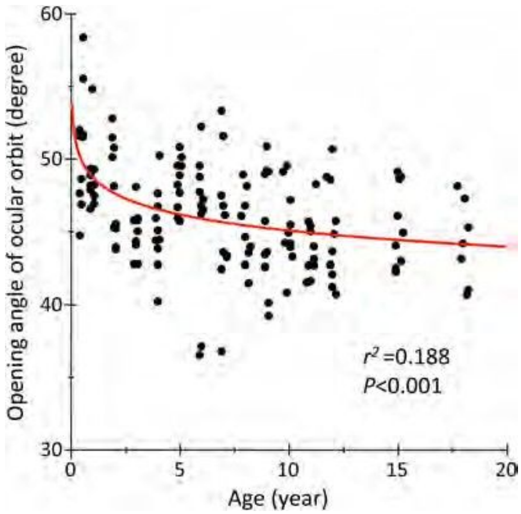

Figure 4 Changes in the opening angle of the orbit during development. The opening angle of the orbit was found to decrease significantly during development. The red line is the logarithmic curve generated by regression analysis (r^2=0.188, p<0.001). Equation: y (angle of ocular orbit, degrees)=48.7–3.7 log x age (years).

measured the opening angle of the optic nerve and orbit using axial CT images in 147 normal Japanese children aged from 6 months to 18 years.

In an autopsy study, Zimmermann et al[7] measured the angle formed by two lines running from the optic chiasm to the site where the optic nerves are attached to each eye. They reported that the opening angle of the optic nerve measured by this method decreased slightly during the fetal period, and that the angle was 71.5° at birth and 68° in adults. This early study involved measurements on autopsied heads, and the method used to measure the opening angle of the optic nerve differed from that used in our study, so a direct comparison may not be meaningful. However, they found that the opening angle of the optic nerve changed very little during development, which is consistent with our results.

Escaravage et al[8] measured the angle formed by the central axis of the two orbits. They reported that the angle formed by the central axes of the two orbits decreased until about 1 year of age, but changed little thereafter. Although their measurement method was similar to our method for the angle of optic nerves, it was not identical. In addition, Escaravage et al obtained data from many infants whose ages ranged from birth to 6 months, whereas our study included infants ≥6 months of age. Their findings clearly detected changes from birth to the age of 1 year.

Table 1 Coefficient of determination (r^2) and p values between age and opening angle of the optic nerve, and between age and opening angle of the ocular orbit obtained by three different regression analyses

	Age and opening angle of optic nerve		Age and opening angle of ocular orbit	
	Coefficient of determination (r^2)	p Value	Coefficient of determination (r^2)	p Value
Linear regression analysis	0.005	0.411	0.126	<0.001
Exponential regression analysis	0.003	0.517	0.121	<0.001
Logarithmic regression analysis	0.003	0.505	0.188	<0.001

There were considerable variations in the opening angle of the optic nerve, particularly in infants younger than 1 year (figure 3). One possible reason for this is that there is a variation in the position of the optic nerve on the CT images of infants younger than 1 year. Another possibility is that the opening angle of the optic nerve was affected by the direction of the eyes during the CT scans, especially in infants younger than 1 year. Alternatively, this variation in the opening angle of the optic nerve may simply be caused by a large variation in the growth of the head and orbit.

There have been studies on changes in the opening angle of the orbit during development. Lemke and Lucarelli[9] used CT images to measure the opening angle of both orbits, and they reported that the opening angle of the orbits was 90° in adults. This angle is similar to that of the teenage group in our study whose ages ranged from 15 to 18 years (unilateral orbital angle, 45.5±3.5°, n=18).

The measurements in our study indicate that the opening angle of the orbit changed substantially before the age of 3 and changed less thereafter (figure 4). In addition, the results indicate that the changes in the opening angle of the orbit can be fitted by a logarithmic curve. Escaravage et al[8] reported that the angle of the orbit decreased until the age of 1 year and then changed little thereafter. They measured the angle formed by a line connecting the orbital apex and the orbital process of the zygomatic bone and the medial and lateral wall of the orbit (the angle between the medial and lateral orbital wall). We measured the angle formed by the intersection of a line running tangentially along the deep lateral wall of the left orbit and a vertical line passing through the centre of the nose. Thus, a direct comparison is not possible.

We measured the angle formed by the deep lateral wall of the orbit because this wall is where the extraocular muscles are in contact with the orbital bone via a pulley system. This site is closely associated with eye movements and eye alignment.

Although the relationship between the morphology of the orbit and the presence of strabismus has not been well investigated, strabismus is common in craniosynostosis, with a complication rate of 39–90.9%. Exotropia is the major type of strabismus in Crouzon syndrome and Apert syndrome.[10] Kreiborg and Cohen[11] reported that the incidence of exotropia in Crouzon syndrome was 76.6% and both the inner and the outer interorbital distances were significantly greater than that of normal orbits, resulting in an increase in the opening angle of the orbits between both lateral walls. Morax[12] studied changes in the position of the eye in patients with Crouzon syndrome after a sagittal expansion of the orbit. Eight of nine patients were exotropic before the craniofacial surgery, and the exotropia was corrected to orthophoria after the surgery without a strabismic procedure. This change in ocular alignment most likely resulted from the decrease in the opening angle of the orbits between the two lateral walls caused by the surgical procedures. In Apert syndrome, the ocular alignment changed from exotropia to esotropia after craniofacial surgery.[13 14] These findings suggest that the greater the opening angle of the orbits, the more often exotropia is present.

The results of several studies examining the relationship between exotropia and the increase in the opening angle of the orbits have been reported. It is known that 70% of newborns have an exodeviation, but the deviation gradually disappears in most cases by 2–4 months of age.[15] The reason why this happens has not been determined, but our findings suggest that the decrease in the opening angle of the orbit may contribute to this decrease in exodeviation.

It is known that strabismus often recurs after strabismic surgery. One of the authors (TY) has reported that exotropic patients who have a recurrence soon after surgery tended to have a larger opening angle of the orbit, and that resection of the medial rectus rather than recession of the lateral rectus muscle resulted in fewer recurrences after the surgery.[16] If this is correct, then the opening angle of the orbit should be considered when the type of exotropia surgery is selected.

Intermittent exotropia is known to be more prevalent in Asians than in Caucasians.[17] One way to determine the reasons for this would be to study changes in opening angle of the orbit with increasing age in Caucasians and compare them with changes in Asians. Such research might yield interesting findings.

This study has four limitations. The first is that it did not include data from newborns to examine changes soon after birth. This is because there was a lack of data from normal newborns who had undergone CT soon after birth. The second limitation is that this study measured the angle along the optic nerve for the measurement of the opening angle of the optic nerve. However, children have difficulty controlling their eye movements, so measurements may differ from the actual opening angle of the optic nerve. The third limitation is that we did not determine the eye position and eye movements before the CT recordings. The fourth limitation is that there are no data on the changes in angles in one child at different ages—that is, a longitudinal study.

In spite of these limitations, this study revealed that the opening angle of the orbit changes logarithmically with age. The results provide important information for the management of strabismus in children with and without skull or orbital abnormalities.

Acknowledgements The authors thank Professor Duco I Hamasaki of Bascom Palmer Eye Institute for his critical discussion and editing of the final version of manuscript.

Contributors HT, YH, TY and MK planned this study. HT, YH and TM measured the angle of optic nerves and orbits. HT, YH, TM and MK analysed the data. HT, YH, TY and MK wrote the manuscript.

Funding Grant support: Grant-in-Aid for Scientific Research C (No 20592603) from the Ministry of Education, Culture, Sports, Science and Technology (http://www.jsps.go.jp/).

Competing interests None.

Ethics approval Institutional Ethics Review Board of Osaka Medical Center and Research Institute for Maternal and Child Health (No 675).

Provenance and peer review Not commissioned; externally peer reviewed.

REFERENCES

1 Duke-Elder S, Cook C. The post-natal period. In: Duke-Elder S, ed. System of ophthalmology, normal and abnormal development, part 1. Embryology Vol III. London: Henry Kimpton, 1963:304–13.
2 Farkas LG, Posnick JC, Hreczko TM, et al. Growth patterns in the orbital rejoin: a morphometric study. Cleft Palate Craniofac J 1992;29:315–18.
3 Furuta M. Measurement of orbital volume by computed tomography: especially on the growth of orbit. Jpn J Ophthalmol 2001;45:600–6. (in Japanese with English abstract).
4 Bentley RP, Sqouros S, Natarajan K, et al. Normal changes in orbital volume during childhood. J Neurosurg 2002;96:742–6.
5 Yang G, Wang J, Chang Q, et al. Digital evaluation of orbital development in Chinese children with congenital microphthalmia. Am J Ophthalmol 2012;154:601–9.
6 Chau A, Fung K, Yip L, et al. Orbital development in Hong Kong Chinese subjects. Ophthalamic Physiol Opt 2004;24:436–9.
7 Zimmermann AA, Armstrong EL, Scammon RE. The change in position of the eyeballs during fetal life. Anat Rec 1934;59:109–34.
8 Escaravage GK Jr, Dutton JJ. Age-related changes in the pediatric human orbit on CT. Ophthal Plast Reconstr Surg 2013;29:150–6.
9 Lemke BN, Lucarelli MJ. Anatomy of the ocular adnexa, orbit, and related facial structures. In: Black EH, Nesi FA, Gladstone GJ, Levine MR, Calvano CJ, eds. Smith and Nesi's ophthalmic plastic and reconstructive surgery. New York: Springer, 2012:3–58.
10 Rosenberg JB, Tepper OM, Medow NB. Strabismus in craniosynostosis. J Pediatr Ophthalmol Strabismus 2013;50:140–8.
11 Kreiborg S, Cohen MM Jr. Ocular manifestations of Apert and Crouzon syndromes: qualitative and quantitative findings. J Craniofac Surg 2010;21:1354–7.
12 Morax S. Change in eye position after cranio-facial surgery. J Maxillofac Surg 1984;12:47–55.
13 Khong JJ, Anderson P, Gray TL, et al. Ophthalmic findings in Apert syndrome prior to craniofacial surgery. Am J Ophthalmol 2006;142:328–30.
14 Khong JJ, Anderson P, Gray TL, et al. Ophthalmic findings in Apert's syndrome after craniofacial surgery: twenty-nine years' experience. Ophthalmology 2006;113:347–52.
15 Archer SM, Sondhi N, Helveston EM. Strabismus in infancy. Ophthalmology 1989;96:133–7.
16 Yagasaki T, Yokoyama Y, Maeda M, et al. Larger biorbital angle in cases with immediate recurrence after surgery for intermittent exotropia. Presented at 2nd World Congress of Pediatric Ophthalmology and Strabismus; 7–9 September 2012, Milano.
17 Chia A, Roy L, Seenyen L. Comitant horizontal strabismus: an Asian perspective. Br J Ophthalmol 2007;91:1337–40.

Downloaded from http://bjo.bmj.com/ on January 21, 2015 - Published by group.bmj.com

Changes in angle of optic nerve and angle of ocular orbit with increasing age in Japanese children

Hideyuki Tsukitome, Yoshikazu Hatsukawa, Tomoko Morimitsu, Teiji Yagasaki and Mineo Kondo

Br J Ophthalmol 2015 99: 263-266 originally published online August 21, 2014
doi: 10.1136/bjophthalmol-2014-305236

Updated information and services can be found at:
http://bjo.bmj.com/content/99/2/263

These include:

References This article cites 15 articles, 1 of which you can access for free at:
http://bjo.bmj.com/content/99/2/263#BIBL

Open Access This is an Open Access article distributed in accordance with the Creative Commons Attribution Non Commercial (CC BY-NC 4.0) license, which permits others to distribute, remix, adapt, build upon this work non-commercially, and license their derivative works on different terms, provided the original work is properly cited and the use is non-commercial. See: http://creativecommons.org/licenses/by-nc/4.0/

Email alerting service Receive free email alerts when new articles cite this article. Sign up in the box at the top right corner of the online article.

Topic Collections Articles on similar topics can be found in the following collections

Open access (171)
Muscles (238)
Neurology (1228)

Notes

To request permissions go to:
http://group.bmj.com/group/rights-licensing/permissions

To order reprints go to:
http://journals.bmj.com/cgi/reprintform

To subscribe to BMJ go to:
http://group.bmj.com/subscribe/

© 2014 Informa Healthcare USA, Inc.

Ophthalmic Genetics, 2014; 35(1): 25–34
© Informa Healthcare USA, Inc.
ISSN: 1381-6810 print/1744-5094 online
DOI: 10.3109/13816810.2013.768673

RESEARCH REPORT

Clinical Phenotype in Ten Unrelated Japanese Patients with Mutations in the EYS Gene

Kimiko Suto[1], Katsuhiro Hosono[1], Masayo Takahashi[2], Yasuhiko Hirami[3], Yuki Arai[3], Yasunori Nagase[1], Shinji Ueno[4], Hiroko Terasaki[4], Shinsei Minoshima[5], Mineo Kondo[6], and Yoshihiro Hotta[1]

[1]Department of Ophthalmology, Hamamatsu University School of Medicine, Hamamatsu, Japan, [2]Laboratory for Retinal Regeneration, RIKEN Center for Developmental Biology, Kobe, Japan, [3]Department of Ophthalmology, Institute of Biomedical Research and Innovation Hospital, Kobe, Japan, [4]Department of Ophthalmology, Nagoya University Graduate School of Medicine, Nagoya, Japan, [5]Department of Photomedical Genomics, Basic Medical Photonics Laboratory, Medical Photonics Research Center, Hamamatsu University School of Medicine, Hamamatsu, Japan, and [6]Department of Ophthalmology, Mie University Graduate School of Medicine, Tsu, Japan

ABSTRACT

Background: To characterize the clinical phenotypes associated with previously-reported mutations of the eyes shut homolog (EYS) gene, including a truncating mutation, c.4957_4958insA, which is a major causative mutation for retinitis pigmentosa (RP) in Japan.

Materials and Methods: The study population comprised ten unrelated RP subjects with very likely pathogenic mutations in both alleles, four of them with a homozygous c.4957_4958insA mutation. The phenotype analysis was based on ophthalmic examination, Goldmann perimetry, and digital fundus photography.

Results: The study population included six men and four women aged 34–74 years. The average age at first visit was 31 years (range, 14–44 years), and the patients typically presented with night blindness as the initial symptom and subsequently developed progressive constriction of the visual field. Myopia was noted in 9/20 affected eyes. For most patients, central visual acuity was preserved relatively well up to their thirties, after which it deteriorated rapidly over the next two decades. The visual acuity of patients homozygous for the c.4957_4958insA mutation was uniform. Visual fields were constricted symmetrically, and the extent of constriction seemed to be better correlated with age than visual acuity. The fundus displayed bone spicules, which increased in density with age, and attenuated retinal vessels.

Conclusions: Although additional studies with more patients with mutations of the EYS gene are required, it appears that patients share a relatively uniform phenotype with near-normal central visual function up to their twenties. The patients homozygous for the c.4957_4958insA mutation showed a uniform course of visual acuity changes.

Keywords: Autosomal recessive, eyes shut homolog (EYS) gene, founder effect, Japanese patient, retinitis pigmentosa

INTRODUCTION

Retinitis pigmentosa (RP [MIM 268000]) is a genetically highly heterogeneous retinal degeneration characterized by night blindness and visual field constriction, which eventually lead to severe visual impairment. The disease can be inherited via an autosomal recessive (ar), autosomal dominant (ad), or X-linked recessive mode or may occur in isolation; more than half the cases in Japan are isolated.[1]

Received 23 May 2012; revised 16 January 2013; accepted 17 January 2013; published online 20 February 2013

Correspondence: Yoshihiro Hotta, MD, Department of Ophthalmology, Hamamatsu University School of Medicine, 1-20-1 Handayama, Hamamatsu 431-3192, Japan. Tel: +81 53 435 2256. Fax: +81 53 435 2372. E-mail: hotta@hama-med.ac.jp

Rod dysfunction precedes cone dysfunction; this results in the typical symptoms of night blindness, which is followed by the loss of the peripheral visual field in most cases. Subsequently, the cones in the central retina may also be affected, causing loss of visual acuity in the later stages of the disease. Ophthalmoscopic abnormalities include a waxy pallor of the optic disc, attenuation of retinal vessels, and peripheral bone spicule pigmentations as well as atrophy of the retinal pigment epithelium (RPE).

To date, 55 causative genes and eight loci have been found to be associated with RP (http://www.sph.uth.tmc.edu/Retnet/; accessed May 20, 2012). The eyes shut homolog (EYS) gene encodes an ortholog of Drosophila spacemaker (spam) and a protein essential for maintaining the photoreceptor morphology. EYS spans over 2 Mb, making it one of the largest genes known to be expressed in the human eye.[2,3] EYS gene mutations, which include primarily truncating and some missense mutations, have been detected in arRP-affected families of different ancestral origin and are reported to account for 5–16% of arRP cases.[4–7] Recently, we screened all EYS gene exons in 100 unrelated Japanese RP patients and, found EYS gene mutations in at least 20% of the arRP patients (see the Supplementary Table in the Supplementary Material – available online).[8] In the current study, we examined the clinical features of ten unrelated Japanese patients with RP caused by the EYS gene mutation and compared the phenotype of four patients with the homozygous c.4957_4958insA (p.S1653KfsX2) mutation, which is a major causative mutation of RP in Japan, to that of the other RP patients.

MATERIALS AND METHODS

Ethics Statements

This study was approved by the Institutional Review Board for Human Genetic and Genome Research at the three participating institutions (Hamamatsu University School of Medicine, RIKEN Center for Developmental Biology, and Nagoya University Graduate School of Medicine), and its procedures conformed to the tenets of the Declaration of Helsinki. Written informed consent was obtained from all participants before molecular genetic studies. Ten RP patients who carried homozygous or compound heterozygous mutations in the EYS gene were clinically re-evaluated at either the Department of Ophthalmology, Hamamatsu University Hospital in Hamamatsu (by YH); the Department of Ophthalmology, Kobe City Medical Center General Hospital in Kobe (by MT); or the Department of Ophthalmology, Nagoya University Hospital in Nagoya (by MK and SU).

Patients and Clinical Evaluation

The study subjects were ten unrelated Japanese RP patients residing in various geographical regions, ranging from Tokyo to Osaka. The cohort comprised nine unrelated patients with previously-reported homozygous or compound heterozygous EYS mutations[8] and one patient with a homozygous c.4957_4958insA mutation (RP115N). The doctors were asked to inquire about the family history of patients in as much detail as possible, and they confirmed that the parents of the patients with homozygous mutations were not consanguineous. The complete history and medical records of all the patients were reviewed. In addition, the patients were also clinically evaluated by the measurement of the best-corrected visual acuity, slit-lamp biomicroscopy, and ophthalmoscopy after pupillary dilatation. Refraction was determined using an auto-refractometer. Additional examinations included fundus photography and Goldmann kinetic perimetry (targets, V-4e, III-4e, and I-4e to I-1e) to assess the size and extent of the visual field and spectral-domain optical coherence tomography (OCT; Spectralis, Heidelberg Engineering, Heidelberg, Germany or Cirrus, Carl Zeiss Meditec Inc., Dublin, CA, USA), to visualize the in vivo retinal architecture. Electroretinograms (ERGs) were recorded according to the protocol set by the International Society for Clinical Electrophysiology of Vision.[9]

Goldmann visual fields were scanned with a Canon or Epson scanner and analyzed using the ImageJ software (available at http://rsbweb.nih.gov/ij/) in the following manner: transparent layers were added to each field, and the isopters of the visual fields were manually traced onto these layers. The areas of fields that were circular or elliptical were calculated using the appropriate equations, while those with other irregular forms were calculated using ImageJ. Further, the area of the fields for the V-4e and I-4e targets were measured and compared with the normal area.[10]

Mutation Analyses

Genomic DNA of one proband, RP115N, was extracted from the peripheral lymphocytes by using standard procedures. All 44 exons of EYS and their flanking sequences were studied initially. DNA was amplified by PCR. The PCR and sequencing procedures used have been described previously.[8]

P21H was homozygous for a deletion in exon 32 of the EYS gene, which is an in-frame deletion that results in the replacement of amino acids from D2142 to S2191 with G2142 (p.D2142_S2191delinsG).[8] To precisely determine the deletion breakpoints, PCR amplification was performed using a specially-designed primer pair: forward primer 5′-ATGGCTGTAGGAAACAATACAATGA-3′, located in intron 31, and reverse primer 5′-TTACTTCCAAATTTCATGGTCATCT-3′, in intron 32 (see the Supplementary Figure – available online). Direct sequencing analysis was performed using the following primers: forward primer, 5′-ATAGATTCAATGCCATCCCCATCAAGCT-3′ and reverse primer, 5′-TGAGAAGTGTCTGTTCATATCCTTCA-3′ (Supplementary Figure). The amplification conditions were as follows: PCR was performed using the KOD FX PCR kit (TOYOBO, Japan) for 35 cycles at 98 °C for 10 s, 60 °C for 30 s, and 68 °C for 18 min in an automated thermal cycler.

RESULTS

Clinical and functional findings are summarized in Table 1. The patients' ages ranged from 14–37 years at the time of initial diagnosis (average, 31 years), while their ages at the time of initial examination for this study ranged from 34–74 years (average, 53 years). The patients were from diverse geographical regions, ranging from Tokyo to Osaka in Japan. Six patients' pedigrees were compatible with a recessive mode of inheritance, while the remaining four were considered isolated cases (data not shown). All ten patients had night blindness, with age at onset ranging from childhood to age 50 years (median, 17 years).

Mutation Analysis

A p.D2142_S2191delinsG mutation was detected by PCR by using a specially designed primer in the severest case (patient RP21H). In brief, after failing to amplify exon 32 in this case, we hypothesized that the patient may have homozygous deletion of a long genomic region, including exon 32. We successfully obtained an amplified product by using a primer pair, of which one (forward) was in intron 31 and the other (reverse) was in intron 32 (Supplementary Figure). Sequence analyses showed that the amplified DNA contained truncated intron 31 and truncated intron 32. The boundary between truncated intron 31 and 32 had a 58-nucleotide sequence string, GGGCAA. . .ATTGAC. We could not determine the precise breakpoints in both introns because the exact sequence identity around possible breakpoints could not be delineated; however, the deletion size was elucidated to be 12197 nucleotides, irrespective of the position of the break. We denoted the deletion as c.6425 -?_6571 + ?del, as per the nomenclature guidelines provided by the Human Genome Variation Society (http://www.hgvs.org/mutnomen/).

Visual Acuity

Clinical examination revealed that corrected visual acuity varied considerably and ranged from 0 logMAR unit to light perception; the differences were attributable to the different stages of macular involvement (Table 1 and Figure 1). From the findings, a common pattern emerged: relatively well-preserved visual acuity up to the 3rd or 4th decade, with subsequent rapid deterioration to less than 1.0 logMAR unit at approximately 60 years of age. This pattern was noted in all cases, except one eye (left) of the youngest patient (patient RP44K; Table 1) who had visual acuity of counting fingers at the age of 34 years. Patient RP21H exhibited complete deletion of exon 32, which was the severest phenotype with vision being limited to light perception. The visual acuity of patients homozygous for the c.4957_4958insA mutation was of a uniform phenotype.

Refractive Error

Twelve eyes were ametropic; three exhibited slight hyperopia, and nine had various degrees of myopia ranging from −1 D to −6 D. The remaining eight eyes were emmetropic. Patients with severe forms of myopia (over −8 D), hypermetropia (over +4 D), or astigmatism (over 3 D) were not found in this study.

Visual Fields

Constriction of the visual fields was symmetric, except for one patient who had no testable visual field in the central area or any targets in one eye (left eye of patient RP44K; Table). The extent of vi constriction correlated with age (Table 1 and Figure 1B). The visual field at the time of the study ranged from constriction to 10–12° for the V-4 target in a 63-year-old man (RP87N) to no light perception for the V-4 target in a 55-year-old man (RP21H). Figure 1B shows that the disease progressed relatively rapidly over the 3rd and 4th decades.

Cataracts and Anterior Segment Abnormalities

Cataract was observed in seven of the ten affected subjects, including four individuals who had pseudophakia (seven eyes).

Retinal and Macular Findings

Retinal changes were relatively uniform among the subjects. The optic disc appeared to be relatively

TABLE 1. Genotypes and phenotypes in Japanese patients with mutations in the EYS gene.

										Visual Acuity		Refraction						
Patient	Age at onset (years)	Age at first visit (years)	Current age (years)	Follow-up duration (years)	Gender	Origin	Family history	Type of change	Nucleotide change	Right Eye	Left Eye	Right Eye (D)	Left Eye (D)	Lens Status	Goldmann Perimetry (V-4e)	Fundoscopy Results	OCT Results	ERG Results
RP3H	14	35	67	12	Female	Tochigi	ar	Homozygous	c.4957_4958insA[8,12]/ c.4957_4958insA [8,12]	0.07	0.08	þ1	þ1.25	Bilateral pseudophakia	OD: 8º; OS: 7º	Waxy optic disc, attenuated retinal vasculature, RPE changes in the periphery, extensive bone spicules throughout periphery	No data	Extinguished
RP21H	20	35	55	17	Male	Hamamatsu	ar	Homozygous	c.6425-?_6571þ?del[8]/ c.6425-?_6571þ?del[8]	LP	LP	−3.0	−3.0	Bilateral pseudophakia	Unmeasurable	Waxy optic disc, attenuated retinal vasculature, RPE changes in the periphery and posterior pole, extensive bone spicules throughout periphery	Relatively preserved foveal lamination	Extinguished
RP35K	20	30s	39	3	Male	Toyooka	iso	Homozygous	c.8868C4A[8,12]/ c.8868C4A[8,12]	1	1	−6.0	−5.25	Clear	OD, OS: concentric constriction with remaining central island; remaining peripheral island. P0	Normal optic disc, slightly attenuated vessels, RPE changes in the periphery, bone spicules sprinkled throughout periphery	No data	No data
RP44K	14	14	34	4	Female	Tokyo	ar	Heterozygous/ Heterozygous	c.4957_4958insA[8,12]/ c.6557G4A[4,7,8]	0.4	CF	›0.5	0	Bilateral cataract	OD: concentric constriction with remaining central island.	Normal optic disc, attenuated retinal vasculature, RPE changes in the	No data	Extinguished

																throughout periphery		
RP48K	13	26	36	2	Male	Osaka	iso	Homozygous	c.4957_4958insA[8,12]/ c.4957_4958insA[8,12]	0.6	0.6	−1.25	−1.0	Clear	OD: 6°; OS: 7°	Normal optic disc, slightly attenuated vessels, RPE changes in the periphery and posterior pole, extensive bone spicules throughout periphery	No data	No data
RP54K	20 s	30	53	2	Male	Himeji	ar	Homozygous	c.4957_4958insA[8,12]/ c.4957_4958insA[8,12]	0.7	0.3	−2.25	−1.5	Right cataract Left pseudophakia	OD: 8°; OS: 8°	Waxy optic disc, attenuated retinal vasculature, RPE changes in the periphery and posterior pole, extensive bone spicules throughout periphery	Foveal thinning	No data
RP56K	20	37	74	5	Male	Tokyo	ar	Compound Heterozygous	c.4957_4958insA[8,12]/ c.8351T>G[8]	0.04	0.2	−1.5	−1.5	Bilateral pseudophakia	OD: 8°; OS: 9°	Waxy optic disc, attenuated retinal vasculature, RPE changes in the periphery and posterior pole, extensive bone spicules throughout periphery	Foveal thinning	No data
RP81K	Childhood	20	51	2	Female	Higashi-Osaka	ar	Compound Heterozygous	c.2522_2523insA[8]/ c.6557G>A[4,7,8]	0.6	0.6	0	+1.5	Bilateral cataract	OD: 11°; OS: 11°	Waxy optic disc, attenuated retinal vasculature, RPE changes in the periphery and posterior pole, some drusen-like deposits	No data	No data
															OS: concentric constriction with remaining peripheral island	periphery and posterior pole, extensive bone spicules		

RP87N	50*	44*	64	8	Male	Nagoya	iso	Heterozygous/ Heterozygous	c.4957_4958insA[8,12]/ c.7793G4A[8]	1	0.8	0	−1.0	Bilateral cataract	OD: 10°; OS: 10°	Normal optic disc, attenuated retinal vasculature, RPE changes in the	No data	No data

(continued)

TABLE 1. Continued.

										Visual Acuity		Refraction						
Patient	Age at onset (years)	Age at first visit (years)	Current age (years)	Follow-up duration (years)	Gender	Origin	Family history	Type of change	Nucleotide change	Right Eye	Left Eye	Right Eye (D)	Left Eye (D)	Lens Status	Goldmann Perimetry (V-4e)	Fundoscopy Results	OCT Results	ERG Results
																periphery, extensive bone spicules throughout periphery		
RP115N	6–12 years	30 s	52	7	Female	Aichi	iso	Homozygous	c.4957_4958insA[8,12]/ c.4957_4958insA [8,12]	0.6	0.6	0	0	Clear	OD, OS: concentric constriction with remaining central island; remaining peripheral island	Waxy optic disc, attenuated retinal vasculature, RPE changes in the periphery, extensive bone spicules throughout periphery	No data	No data

* Subject RP87N was diagnosed with retinitis pigmentosa by fundoscopy at the age of 44 years, when he was asymptomatic; thereafter, he developed night blindness at the age of 50 years.

''Age at Onset'' was based on history and ''Age at First Visit'' was based on medical records.

Tochigi, Tokyo, Osaka, and Aichi are prefectures and Hamamatsu, Toyooka, Himeji, Higashi-Osaka, and Nagoya are cities.

References for previously-reported mutations are indicated in the column labeled ''Nucleotide Change''.

All clinical data were obtained from the latest examinations, but the refraction of the eyes that underwent cataract surgery was assessed on the basis of the latest phakic data.

ar, autosomal recessive; iso, isolated case; D, diopter; LP, light perception; CF, counting fingers; OD, oculis dextra (right eye); OS, oculis sinistra (left eye); OCT, optical coherence tomography; ERG: electroretinogram

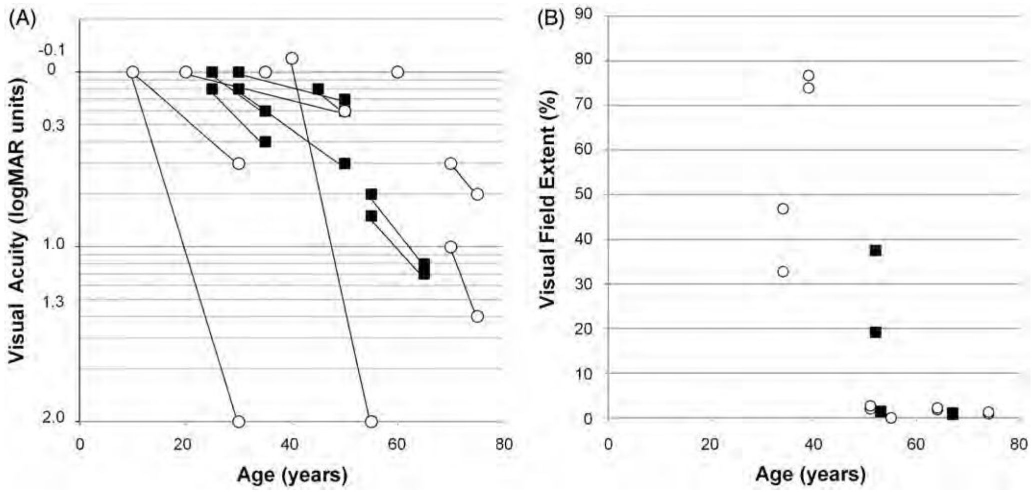

FIGURE 1. (A) Visual acuity was expressed in logMAR units, as a function of age of the subjects. The graph shows a decrease in visual acuity (y-axis) with age in years (x-axis). Symbols indicate the time points of assessment. g, subjects with homozygous c.4957_4958insA mutation; *, other subjects. The visual acuity was preserved well into the thirties or forties, after which it declined. Visual acuity of subjects with the homozygous c.4957_4958insA mutation was uniform. (B) The extent of the visual field (kinetic perimetry with V-4e test target) loss was expressed as a percentage of the normal mean and plotted as a function of age in the ten subjects. g, subjects with the homozygous c.4957_4958insA EYS mutation; *, other subjects. The extent of visual constriction correlated with age.

well-preserved, and compared to the venules, the arterioles showed mild to moderate attenuation. Profound atrophy of the retinal pigment epithelium (RPE), choriocapillaris, and outer segment at the mid-peripheral retina were observed in all patients. In the later stages of the disease, the macular region and, sometimes, the fovea were abnormal. We also observed varying amounts of bone spicule-like pigmentation dispersed in the posterior pole, mid-periphery, and anterior portions of the fundus; the deposits were more prominent in the older patients, but were detected in all the cases in mid-peripheral retina (Figure 2A, B, C). Only one patient had a history of cystoid macular edema (CME) (10%) at 66 years of age; this frequency is less than that reported-previously.[13]

OCT Images

High-resolution OCT images showed a marked reduction of retinal thickness resulting from the loss of photoreceptor layers (Figure 2D, E, F). The photoreceptor inner segment/outer segment junction (IS/OS line) was either completely absent or only detectable at the fovea in four subjects. Although patient RP21H, with complete deletion of exon 32, had light perception in both eyes, the OCT image demonstrated relatively preserved foveal structures, including the IS/OS line (Figure 2D).

ERG Recordings

ISCEV-standard full-field ERGs were recorded for three patients [patients RP3H (at the age of 59 years), RP21H (at the age of 41 years), and RP44K (at the age of 27 years)] and were nearly undetectable for all patients in both rod and cone components.

DISCUSSION

In this report, we describe the phenotype of ten unrelated Japanese patients affected with arRP caused by EYS gene mutations. Our previous study on 100 Japanese arRP patients indicated very likely pathogenic mutations and possible pathogenic mutations in 18% (18/100) and 8% (8/100), respectively, of the study population; these values are higher than those previously reported.[4–7] Our previous study has shown that 16% of Japanese patients with arRP displayed either the c.4957_4958insA or the c.8868C4A mutation, which accounted for 57% (15 þ 5/35) of the mutated alleles and seem to be frequent among Japanese patients with arRP.[8] However, a detailed haplotype analysis of the EYS gene has not been performed, and therefore, currently, we cannot verify whether each mutation occurred in an ancient common ancestor. This high prevalence of EYS gene mutations, including two frequent mutations, has recently been confirmed by another study in the Japanese population.[12] Together, these findings strongly suggest that EYS gene mutations play a major role in the pathogenesis of arRP affecting the Japanese population. In this study, we only recruited patients with very likely pathogenic mutations and involvement of both alleles because a second mutant allele could not be detected by direct sequencing in 17/26 patients in the previous study, and the genotype of such patients could not be determined.

FIGURE 2. Fundus photographs of patients carrying mutations in the EYS gene. The entire retina of the right eye of patient RP21H at age 55 years showed extensive bone-spicule pigmentation throughout the fundus (A). The central retina of the left eye of patient RP54K, aged 51 years, showed a waxy optic disc, severely attenuated retinal vasculature, and extensive chorioretinal atrophy with minimal residual retinal pigment epithelium in the macular region (B). The central retina of the right eye of patient RP56K (age, 73 years) showed the fundus appearance of the end-stage of the disease (C). Illustration of macular changes by spectral-domain optical coherence tomography showed a marked reduction of retinal thickness. Relatively preserved foveal lamination was observed in the right eye of patient RP21H at the age of 55 years (D). Marked foveal thinning was observed in the left eye of patient RP54K at the age of 51 years (E) and in the right eye of patient RP56K at the age of 73 years (F).

The genotype includes truncated mutations and few missense mutations (Supplementary Table). No patient with missense mutations in both alleles was included. We recruited four patients with the homozygous c.4957_4958insA mutation and one patient with the homozygous c.8868C4A mutation.

Overall, most patients showed relatively well-preserved visual acuity into their thirties, after which rapid deterioration was observed in their forties or fifties. The constriction of the visual fields was symmetric, although the extent seemed to correlate better with age than visual acuity. Cataract was frequently observed among patients in their thirties. In one case (RP21H), visual acuity improved noticeably from 0.5 logMAR units to –0.1 logMAR units in both eyes after cataract extraction by the age of 37 years, but gradually progressed to light perception by the age of 40 years. In all cases, the fundus displayed typical changes of retinitis pigmentosa (RP), including attenuated retinal vessels and bone-spicule deposits over 360° of the fundus, all of which increased in density with age. Electroretinographic (ERG) responses were consistent with severe generalized rod–cone dysfunction.

Reports have been published on the phenotype of RP caused by EYS gene mutations in Indonesian, Pakistani, Chinese, Israeli, Spanish, French, British, Dutch, and Palestinian patient populations[4–7,13–16];

these reports contain only a brief description of the clinical features. The subjects in this study shared a relatively uniform phenotype, characterized by a symptom-free interval in the first two decades of life (median age at onset, 23 years) followed by a rapid decline in visual function. The patient RP87N was diagnosed with RP by funduscopy at the age of 44 years, when he was subjectively asymptomatic; later, he developed night blindness at the age of 50 years. The clinical features reported in this study are consistent with those reported previously. For instance, the visual acuities were relatively well-preserved up to the 3rd or 4th decades, as reported in a study of a population of European ancestry.[7] The visual acuities were relatively better and photophobia less frequent than that in seven Spanish arRP subjects carrying mutations of the ceramide kinase-like (CERKL) gene, which is involved in sphingolipid-mediated apoptosis in the retina.[17] The visual field loss noted among our study population was less than that reported for patients with mutations of the dehydrodolichyl diphosphate synthase (DHDDS) gene, which encodes an enzyme required for dolichol-pyrophosphate synthesis.[18]

To date, extensive studies focusing on the clinical features of a large number of RP patients with EYS gene mutations have been limited to Dutch and French arRP cohorts.[5,7] However, these studies included only a few non-European patients and showed a change in visual acuity with age in patients carrying EYS gene mutations; this was similar to the pattern noted in our Japanese subjects.

X-linked RP has been associated with myopia of 2 diopters or more, whereas dominant inheritance is associated with hyperopia.[19–21] In this study, 12 of the investigated eyes were ametropic (three slightly hyperopic and nine with various degrees of myopia) and eight were emmetropic. Myopia has a greater prevalence in Asian countries, including Japan, compared to Western populations.[22] Thus, our data together with those of a previous French study[5] suggest that most patients with arRP due to EYS mutations may have no or mild (mostly myopic) refractive error.

Three severe cases with retinal atrophy involving the posterior pole have been described previously (Family A: II-3[3], CIC01223[5] and CIC00492[5]);[3,5] however, most patients in this study presented with typical signs of progressive rod–cone dystrophy with relatively well-preserved central vision until late in the course of the disorder. It is plausible that a larger cohort of Japanese patients with EYS mutation may yield patients with greater involvement of the cones than rods. Two cases of sector RP with distinct fundus abnormalities with predominance of pigmentary changes in the inferior part of both retinas have been reported previously (CIC01222[5] and MOL0640 III:1[13]).[5,13] Although none of our patients had sector RP at the time of the study, we cannot rule out its presence in the earlier stages of the disease, before the patients were enrolled in this study. It is difficult to establish a clear genotype–phenotype association since we could only investigate ten patients.

We recruited six homozygous patients for this clinical and molecular study. Among them, four patients (RP3H, RP48K, RP54K, and RP115N) were homozygous for the c.4957_4958insA mutation (p.S1653KfsX2; truncating mutation in exon 26), which, as shown in our previous report, is a major causative mutation of RP in Japan. The course of visual acuity changes in homozygous patients with the c.4957_4958insA mutation was uniform. However, no remarkable clinical pattern emerged among the ten patients with variable genotypes, including the c.4957_4958insA mutation, in this study. The patients had near-normal visual function up to their twenties; this implies that slowing the progression of degeneration may be a possible therapeutic approach for preventing blindness in RP patients.

ACKNOWLEDGMENTS

We would like to thank the patients who participated in the study.

DECLARATION OF INTEREST

The authors report no conflict of interest. The authors alone are responsible for the content and writing of the paper.

This study was supported by research grants from the Ministry of Health, Labour and Welfare (Research on Measures for Intractable Diseases) and from the Japan Society for the Promotion of Science (Grant-in-Aid for Scientific Research (C) 23592561 and Grant-in Aid for Young Scientists (B) 23791975).

REFERENCES

1. Hayakawa M, Fujiki K, Kanai A, et al. Multicenter genetic study of retinitis pigmentosa in Japan: I. Genetic heterogeneity in typical retinitis pigmentosa. Jpn J Ophthalmol 1997;41:1–6.
2. Abd El-Aziz MM, Barragán I, O'Driscoll CA, et al. EYS, encoding an ortholog of Drosophila spacemaker, is mutated in autosomal recessive retinitis pigmentosa. Nat Genet 2008;40:1285–1287.
3. Collin RW, Littink KW, Klevering BJ, et al. Identification of a 2 Mb human ortholog of Drosophila eyes shut/spacemaker that is mutated in patients with retinitis pigmentosa. Am J Hum Genet 2008;83:594–603.
4. Abd El-Aziz MM, O'Driscoll CA, Kaye RS, et al. Identification of novel mutations in the ortholog of Drosophila eyes shut gene (EYS) causing autosomal

recessive retinitis pigmentosa. Invest Ophthalmol Vis Sci 2010;51:4266–4272.

5. Audo I, Sahel JA, Mohand-Saïd S, et al. EYS is a major gene for rod-cone dystrophies in France. Hum Mutat 2010;31:E1406–1435.
6. Barragán I, Borrego S, Pieras JI, et al. Mutation spectrum of EYS in Spanish patients with autosomal recessive retinitis pigmentosa. Hum Mutat 2010;31:E1772–1800.
7. Littink KW, van den Born LI, Koenekoop RK, et al. Mutations in the EYS gene account for approximately 5% of autosomal recessive retinitis pigmentosa and cause a fairly homogeneous phenotype. Ophthalmology 2010; 117:2026–2033.
8. Hosono K, Ishigami C, Takahashi M, et al. Two novel mutations in the EYS gene are possible major causes of autosomal recessive retinitis pigmentosa in the Japanese population. PLoS ONE 2012;7:e31036.
9. Marmor MF, Fulton AB, Holder GE, et al. ISCEV Standard for full-field clinical electroretinography (2008 update). Doc Ophthalmol 2009;118:69–77.
10. Schindler EI, Nylen EL, Ko AC, et al. Deducing the pathogenic contribution of recessive ABCA4 alleles in an outbred population. Hum Mol Genet 2010;19:3693–3701.
11. Hajali M, Fishman GA, Anderson RJ. The prevalence of cystoid macular oedema in retinitis pigmentosa patients determined by optical coherence tomography. Br J Ophthalmol 2008;92:1065–1068.
12. Iwanami M, Oshikawa M, Nishina T, et al. High prevalence of mutations in the EYS genes in Japanese patients with autosomal recessive retinitis pigmentosa. Invest Ophtalmol Vis Sci 2012;53:1033–1040.
13. Bandah-Rozenfeld D, Littink KW, Ben-Yosef T, et al. Novel null mutations in the EYS gene are a frequent cause of autosomal recessive retinitis pigmentosa in the Israeli population. Invest Ophthalmol Vis Sci 2010;51:4387–4394.
14. Huang Y, Zhang J, Li C, et al. Identification of a novel homozygous nonsense mutation in EYS in a Chinese family with autosomal recessive retinitis pigmentosa. BMC Med Genet 2010;11:121.
15. Khan MI, Collin RW, Arimadyo K, et al. Missense mutations at homologous positions in the fourth and fifth laminin A G-like domains of eyes shut homolog cause autosomal recessive retinitis pigmentosa. Mol Vis 2010;16:2753–2759.
16. Pieras JI, Barragán I, Borrego S, et al. Copy-number variations in EYS: a significant event in the appearance of arRP. Invest Ophthalmol Vis Sci 2011;52:5625–5631.
17. Avila-Fernandez A, Riveiro-Alvarez R, Vallespin E. CERKL mutations and associated phenotypes in seven Spanish families with autosomal recessive retinitis pigmentosa. Invest Ophthalmol Vis Sci 2008;49:2709–2713.
18. Zelinger L, Banin E, Obolensky A, et al. A missense mutation in DHDDS, encoding dehydrodolichyl diphosphate synthase, is associated with autosomal-recessive retinitis pigmentosa in Ashkenazi Jews. Am J Hum Genet 2011;88:207–215.
19. Berson EL, Rosner B, Simonoff E. Risk factors for genetic typing and detection in retinitis pigmentosa. Am J Ophthalmol 1980;89:763–75.
20. Hartong DT, Berson E, Dryja TP. Retinitis pigmentosa. Lancet 2006;368:1795–1809.
21. Fishman GA, Farber MD, Derlacki DJ. X-linked retinitis pigmentosa: profile of clinical findings. Arch Ophthalmol 1988;106:369–75.
22. Sawada A, Tomidokoro A, Araie M, et al. Refractive errors in an elderly Japanese population: the Tajimi study. Ophthalmology 2008;115:363–370.

Cell Biology International ISSN 1065-6995
doi: 10.1002/cbin.10174

RESEARCH ARTICLE

Interaction between optineurin and the bZIP transcription factor NRL

Chunxia Wang[1, 2, 3], Katsuhiro Hosono[1, 2], Masafumi Ohtsubo[2], Kentaro Ohishi[2], Jie Gao[1, 2], Nobuo Nakanishi[2], Akiko Hikoya[1], Miho Sato[1], Yoshihiro Hotta[1] and Shinsei Minoshima[2]*

1 Department of Ophthalmology, Hamamatsu University School of Medicine, 1-20-1 Handayama, Hamamatsu 431-3192, Japan
2 Department of Photomedical Genomics, Basic Medical Photonics Laboratory, Medical Photonics Research Center, Hamamatsu University School of Medicine, 1-20-1 Handayama, Hamamatsu 431-3192, Japan
3 Department of Ophthalmology, The Fourth Affiliated Hospital of China Medical University, Shenyang 110005, China

Abstract

Although the gene encoding optineurin (OPTN) is a causative gene for glaucoma and amyotrophic lateral sclerosis, it is ubiquitously expressed in all body tissues, including the retina. To study the function of OPTN in retinal ganglion cells as well as the whole retina, we previously isolated OPTN-interacting proteins and identified the gene encoding the bZIP transcription factor neural retina leucine zipper (NRL), which is a causative gene for retinitis pigmentosa. Herein, we investigated the binding between OPTN and NRL proteins in HeLaS3 cells. Co-expression of HA-tagged NRL and FLAG-tagged OPTN in HeLaS3 cells followed by immunoprecipitation and Western blotting with anti-tag antibodies demonstrated the binding of these proteins in HeLaS3 cells, which was confirmed by proximity ligation assay. NRL is the first OPTN-binding protein to show eye-specific expression. A series of partial-deletion OPTN plasmids demonstrated that the tail region (423–577 amino acids [aa]) of OPTN was necessary for binding with NRL. Immunostaining showed that Optn (rat homologue of OPTN) was expressed in rat photoreceptors and localised in the cytoplasm of photoreceptor cells. This is a novel demonstration of Optn expression in photoreceptor cells. OPTN was not detected in photoreceptor nuclei under our experimental conditions. Further analyses are necessary to elucidate the function of OPTN and the significance of its possible binding with NRL in photoreceptor cells.

Keywords: co-immunoprecipitation; NRL; optineurin; photoreceptor; protein interaction; proximity ligation assay

Introduction

The cellular protein optineurin (OPTN) was originally given the name FIP-2 and characterised by its binding of the adenovirus E3 14.7-kDa protein and induction by tumour necrosis factor alpha (Li et al., 1998). OPTN was also described as a huntingtin interacting protein HYPL, a transcription factor IIIA-interacting protein (TFIIIA-intP) (Faber et al., 1998; Moreland et al., 2000), and an NF-kB essential modulator (NEMO)-related protein with the name NRP (Schwamborn et al., 2000). Following the discovery that mutations in the *OPTN* gene were causative for adult-onset primary open-angle glaucoma (POAG), the gene was named optineurin (Rezaie et al., 2002) and OPTN was thought to have a neuroprotective function, which was subsequently supported by studies in limited cell culture systems (De Marco et al., 2006; Chalasani et al., 2007).

OPTN is ubiquitously expressed in tissues, including the heart, brain, skeletal muscle, adrenal cortex and retina (Li et al., 1998; Rezaie et al., 2002). For this reason, OPTN is thought to play roles in various tissues and cell types in addition to retinal ganglion cells to maintain their normal functions. The function of OPTN in tissues other than retinal ganglion cells was exemplified by a recent report that several *OPTN* mutations cause amyotrophic lateral sclerosis (ALS) but not POAG (Maruyama et al., 2010). This discovery supports the neuroprotective function of OPTN not only in the retina but also in the spinal cord.

OPTN expression is seen in ocular tissues such as the trabecular meshwork, non-pigmented ciliary epithelium and retina (Rezaie et al., 2002). Retinal ganglion cells have the highest level of OPTN expression in the retina (Rezaie and Sarfarazi, 2005; Rezaie et al., 2005; Kroeber et al., 2006). To study the general functions of OPTN not only in ganglion

---

*Corresponding author: e-mail: mino@hama-med.ac.jp

Abbreviations: aa, amino acid; NEMO, NF-kB essential modulator; OPTN, optineurin (human); Optn, optineurin (rat); NRL, neural retina leucine zipper (human); Nrl, neural retina leucine zipper (rat); IP, immunoprecipitation; WB, Western blotting; PLA, proximity ligation assay cells, but in other types of retinal cells, we isolated cDNA clones of OPTN-binding candidate proteins by yeast two-hybrid screening from a human retinal cDNA library (Ohtsubo et al., unpublished). We found that one of these cDNA clones encodes a neural retina-specific leucine zipper protein, the bZIP transcription factor (NRL). The NRL gene is expressed in rod nuclei in adults and has important functions in the differentiation of various types of ocular cells (Mears et al., 2001; Swain et al., 2001). Mutations of the NRL gene also cause retinitis pigmentosa (RP) (Bessant et al., 1999).

We report here interactions between OPTN and NRL proteins in cultured cells as well as the expression of Optn in rat photoreceptor cells.

Materials and methods

The study was approved by the Institutional Ethics Committee for Genetic and Genomic Research and the Animal Use Committee of Hamamatsu University School of Medicine.

Antibodies

Rabbit anti-HA-tag antibody (561) was purchased from MBL International Corporation (Woburn, MA), and mouse anti-FLAG M2 monoclonal antibody (F3165) was purchased from Sigma–Aldrich, Japan, K.K. (Tokyo, Japan). We confirmed by Western blot analysis that the anti-HA-tag and anti-FLAG M2 monoclonal antibodies do not cross-react. Anti-OPTN antibody (Cat. No. 10837-1-AP) was purchased from ProteinTech Group, Inc. (Chicago, IL), and anti-NRL antibody (sc-10971) was purchased from Santa Cruz Biotechnology, Inc. (Santa Cruz, CA), both of which detect human proteins. Anti-NRL antibody cross-reacts with the rat counterpart of NRL (Nrl). We confirmed that the anti-OPTN antibody can be used for the rat counterpart of OPTN (Optn) by Western blot analysis, as also that the anti-NRL and the anti-OPTN antibodies do not cross-react. Goat anti-mouse IgG/HRP (P0447), goat anti-rabbit IgG/HRP (P0448), and rabbit anti-goat IgG/HRP (P0449) were purchased from DAKO (Tokyo, Japan). AlexaFluor488-donkey anti-goat IgG (A11055), AlexaFluor488-donkey anti-mouse IgG (A21202) and AlexaFluor594-donkey anti-rabbit IgG (A21207) were purchased from Invitrogen (Carlsbad, CA).

cDNA cloning

cDNA for the NRL and OPTN genes was amplified by polymerase chain reaction (PCR) with human retina marathon cDNA (TAKARA, Japan). The nucleotide sequences of NRL (Acc. No. NM_006177) and OPTN (NM_001008211) cDNA were obtained from RefSeq, NCBI (http://www.ncbi.nlm.nih.gov/). The open reading frame sizes were 714 and 1,734 bp for NRL and OPTN, respectively. PCR primers were designed from these sequences, and the recognition sites for restriction endonuclease HindIII and EcoRI for NRL and BsaI and EcoRI for OPTN were introduced into each primer. The names and sequences of the PCR primers for NRL are as follows: NRL. HindIII.F, CCCAGCaagcttATGGCCCTGCCCCCCAGCCCCCT; and NRL.EcoRI.R, GCTCTGgaattcTCAGAGGAAGAGGTGGGAGGG. Those for OPTN are as follows: OPTN. BsaI.F, TTCCACggtctcAAGCTTATGTCCCATCAACCTCTCAG; and OPTN.EcoRI.R, ATACATgaattcTTAAATGATGCAATCCATCA.

After PCR amplification, NRL cDNA was cut with HindIII and EcoRI and inserted into the HindIII and EcoRI sites of a 3 ×HA vector (a gift of Drs. A. Takayanagi and N. Shimizu) (Lim et al., 2007). Similarly, OPTN cDNA was amplified, cut with BsaI and EcoRI, and inserted into the HindIII and EcoRI sites of a p3 ×FLAG-CMV-7.1 expression vector (Sigma–Aldrich). The PCR primer OPTN.Bsa1.F was designed to obtain the same protruding sequence as that produced by HindIII when the amplified product was cut by BsaI to enable a ligation reaction with the vector edge cut by HindIII. For NRL and OPTN cDNA mock experiments, we used YPEL5 cDNA (Hosono et al., 2010), which shares no homology to the sequences of NRL and OPTN and was not expected to interact with them. YPEL5 cDNA was inserted into the 3 ×HA vector and p3 ×FLAG-CMV-7.1 expression vector. The nucleotide sequences of all clones were confirmed as the same as the designed sequences.

Construction of a deletion series of OPTN-expression plasmids

A series of deletion OPTN plasmids was constructed using the KOD-Plus-Mutagenesis Kit (TOYOBO) with the following PCR primers: OPTN_Lc1st-R, AAGCTTGTCATCGTCATCCTTGTAATC, and OPTN_Lc1st-F, TCATCTGAGGACCCCACTGATG for OPTNdel1st (1–120); OPTN_LcM-R, CCTTTCTGATTTCCCTTTTAG, and OPTN_LcM-F, GAAGAGAAAGGCCCGGAGA for OPTNdel2nd (121–287); OPTN_Lc3rd-R, ATCATTCTCTTTCTCTGTGCT- CCC, and OPTN_Lc3rd-F, CTGAAGGAACTGAGTGAAAAACTGGA for OPTNdel3rd (288–422) and OPTN_Lc4th-R, CACTGCCCTGTCCACTTTTTCTG, and OPTN_Lc4th-F, TAAGAATTCATCGATAGATCTGATATCGG for OPTNdel4th (423–577).

Cell culture, DNA transfection and immunofluorescent staining

HeLaS3 cells were cultured on coverslips in Dulbecco's modified Eagle medium containing 10% foetal bovine serum under standard cell culture conditions. DNA transfection involved FuGENE6 (Roche, Indianapolis, IN). Briefly, the cells were treated with FuGENE6 in the same serum-containing medium for 24 h. They were fixed in 4% paraformaldehyde after permeabilization by 0.5% Triton X-100 in phosphate buffered saline lacking Ca^{2þ} and Mg^{2þ}. Binding of the primary and secondary antibodies was done at room temperature for 1 h and 30 min, respectively. Fluorescent signals were observed using a fluorescence microscope [Axioskop-2plus (Zeiss, Goetingen, Germany)].

Proximity ligation assay

Cells cultured on coverslips were co-transfected with HA-NRL and FLAG-OPTN plasmids. After fixation and binding of the rabbit anti-HA and mouse anti-FLAG primary antibodies, cells were treated with secondary antibodies, that is, anti-rabbit Ig conjugated with a specific oligonucleotide (PLA probe MINUS) and anti-mouse Ig with another specific oligonucleotide (PLA probe PLUS). Next, AlexaFluor488-donkey anti-mouse IgG was applied to detect FLAG-OPTN, which was followed by PLA probe hybridisation, the ligation reaction to form closed circular DNA, amplification by the rolling circle reaction, and final hybridisation of the amplified DNA-specific fluorescent oligo DNA probe. PLA hybridisation signals were detected using a fluorescent microscope (Axioskop-2plus, Zeiss).

Cell fractionation

Cell fractionation was done in 50 mM Tris–HCl/0.15 M NaCl/1 mM EDTA (pH 7.4) (TBS) and 1% Triton X-100 in TBS (Triton-TBS). Protease inhibitor complete EDTA-free (Roche) cocktail was added to TBS and Triton-TBS. Cells were suspended in Triton-TBS for disruption to prepare the cell lysate. The whole cell lysate was centrifuged at 500g for 5 min and the supernatant used for immunoprecipitation. To prepare nuclear and cytoplasmic fractions, cells were mildly disrupted in hypotonic buffer (10 mM Tris–HCl, 10 mM KCl, 1.5 mM $MgCl_2$, 0.5 mM DTT, pH 7.9 and the protease inhibitor) using a homogeniser, and the undisrupted cells were removed by low-speed centrifugation. High-speed centrifugation (5000g, 10 min) was used to separate the cytoplasmic fraction (supernatant) and nuclei (precipitate). Nuclei were destroyed in hypertonic buffer (20 mM Tris–HCl, 420 mM NaCl, 1.5 mM $MgCl_2$, 0.5 mM DTT, 25% glycerol, pH 7.9 and the protease inhibitor), using an ultrasonic disruptor (Sonicator UD-201, TOMY, Tokyo, Japan) on ice at power level 2 for 20 s (50% duty cycle). The supernatant from the same high-speed centrifugation was used as the nuclear fraction.

Immunoprecipitation

Protein G Sepharose 4 Fast Flow (GE Healthcare, Piscataway, NJ) was equilibrated with Triton-TBS, and the appropriate antibody was added to the solution for 三 2 h. After washing in Triton-TBS, the whole-cell, cytoplasmic or nuclear lysate was added to allow antigen–antibody binding overnight. After the lysates had been washed with Triton-TBS, sample buffer for sodium dodecyl sulphate–polyacrylamide gel electrophoresis (SDS–PAGE) was added, and the samples were boiled. The supernatant was applied to an SDS–PAGE gel.

Western blotting

Proteins in the SDS–PAGE gel were electroblotted to Immobilon-P (MILLIPORE, Chelmsford, MA) membrane filters in a semi-dry apparatus at 1.2 mA/cm^2 for 60 min. Primary and HRP-labelled secondary antibodies were bound using a standard protocol, and 5% skim milk was used to block non-specific binding. Luminescent detection was performed using ImmunoStar Reagent (Wako, Tokyo, Japan), and the luminescent images were analysed by LAS1000 mini (Fuji Film, Tokyo, Japan).

Immunofluorescent staining of rat retina

Rats were handled in adherence to the ARVO statement for the use of animals in ophthalmic and vision research.

Ten-week old male Wistar rats, purchased from Japan SLC Co., Ltd. (Hamamatsu, Japan), were anaesthetised by ether inhalation, and perfused and fixed with 2% paraformaldehyde-containing 0.1 M phosphate buffer (pH 7.4) at 48C. The eyes were enucleated and immersed in the same fixative for 10 min, and the cornea, lens and vitreous humour were removed to form an eyecup under a stereoscopic microscope. The eyecup was immersed in the fixative for 4 h at 48C, cryoprotected sequentially in PBS(−) containing 15%, 20% and 25% sucrose at 48C for 4 h each and promptly frozen in Tissue-Tek O.C.T. compound (Sakura Finetek USA, Inc., Torrance, CA, USA) in liquid nitrogen. The frozen block was sectioned in the sagittal plane using a cryostat (CM 1510-11, Leica Microsystems GmbH, Wetzlar, Germany; Finetec, Co. Ltd., Tokyo, Japan) to generate sections of 4 and 10 mm. The frozen sections were mounted onto MAS-coated slides (Matsunami Glass Ind., Ltd., Osaka, Japan) and dried using a handheld hair dryer for 1 h.

Immediately before use, the sections on slides were immersed in methanol at −258C for 1 h and treated with 2% skim milk in PBS(−) for 2 h at room temperature to block non-specific binding of antibodies. They were incubated with rabbit anti-OPTN (1:100) and goat anti-NRL (1:50) antibodies in PBS(−) containing 1% bovine serum albumin (BSA) for 1 h at room temperature. After washing with PBS(−) three times for 5 min each, the sections were treated with 2% non-immune donkey serum in PBS(−) for further blocking. Incubation with the secondary antibodies AlexaFluor488-donkey anti-rabbit immunoglobulin

(IgG) (1:500) and AlexaFluor594 donkey anti-goat IgG (1:500) in PBS(−) containing 1% BSA was performed for 1 h at room temperature. After washing, nuclei were counter-stained with 4′,6-diamidino-2-phenylindole (DAPI) (Invitrogen, Tokyo, Japan). The sections were mounted under a coverslip in Fluoromount medium (Diagnostic Biosystems, Pleasanton, CA, USA) and observed using a fluorescence microscope (Axioskop 2 plus; Carl Zeiss Co., Ltd., Tokyo, Japan). For negative staining, non-immune rabbit IgG and goat IgG (Novagen, Madison, WI, USA) were used instead of the primary antibody.

Results

Interaction of tagged NRL and OPTN in HeLaS3 cells

Coding regions of human NRL and OPTN cDNA were prepared by PCR, cloned into N-terminal-HA-tagged and N-terminal-FLAG-tagged vectors, respectively, and co-transfected into HeLaS3 cells. The expression and localisation of HA-tagged NRL (HA-NRL) and FLAG-tagged OPTN (FLAG-OPTN) in the cells were followed by double immunofluorescence staining using anti-tag antibodies. Anti-HA antibody stained the nuclei (Figure 1C), which is consistent with the localisation of NRL (Swain et al., 2001). In contrast, anti-FLAG antibody staining was found not only in the cytoplasm, but in the nucleus (Figure 1D). The staining signal in the nucleus was weaker than in the cytoplasm, but still appeared non-artifactual, which suggests that a small amount of FLAG-OPTN is localised to the nucleus. The intensity of the FLAG-OPTN (green) signal in the nucleus varied among cells, and nuclei with a stronger signal showed more yellow colour mixed with the HA-NRL (red) signal (Figure 1A). The staining profile of FLAG-OPTN in the cytoplasm was fairly even, probably because of overexpression. Therefore, we transfected cells with only the HA-NRL plasmid (Figures 1E–1H). Endogenous OPTN was detected using its specific antibody (Figure 1H). The signal intensity was generally lower than that of FLAG-OPTN, but the Golgi apparatus staining near the nucleus was seen as previously reported (Rezaie et al., 2002). In this case, the anti-OPTN signal in the nuclei was also clear, although it was weaker than in the cytoplasm (Figure 1H), which suggests that OPTN is at least partially localised to the nuclei.

We examined the interaction between HA-NRL and FLAG-OPTN co-expressed in HeLaS3 cells in two ways. First, we immunoprecipitated it for Western blot analysis (IP-WB analysis) to determine whether NRL and OPTN might be co-immunoprecipitated. Second, we did a proximity ligation assay (PLA). For IP-WB analysis, plasmid cDNA encoding HA-NRL and FLAG-OPTN was co-transfected into HeLaS3 cells, and whole cell lysates were prepared using Triton-TBS, with the negative controls being plasmids containing the coding sequence of an unrelated protein; YPEL5 (HA-YPEL5 or FLAG-YPEL5) were used rather than HA-NRL or FLAG-OPTN. Following immunoprecipitation with the anti-FLAG antibody, the immunoprecipitate was detected by Western blotting using anti-HA antibody, and a 33-kDa band corresponding to the size of NRL (29 kDa) with the HA-tag (4 kDa) (left lane of the upper panel in Figure 2A) was found. Immunoprecipitation with the anti-HA antibody gave a 75-kDa band with anti-FLAG antibody (left lane of lower panel in Figure 2C). Although the calculated size of FLAG-OPTN is 69 kb (66 kDa of OPTN plus the 3-kDa FLAG-tag), the 75-kDa band was considered to be FLAG-OPTN because this apparently larger size of FLAG-OPTN in SDS–PAGE was seen previously (Park et al., 2006, 2010). Mock transfection with plasmids expressing YPEL5 cDNA did not produce

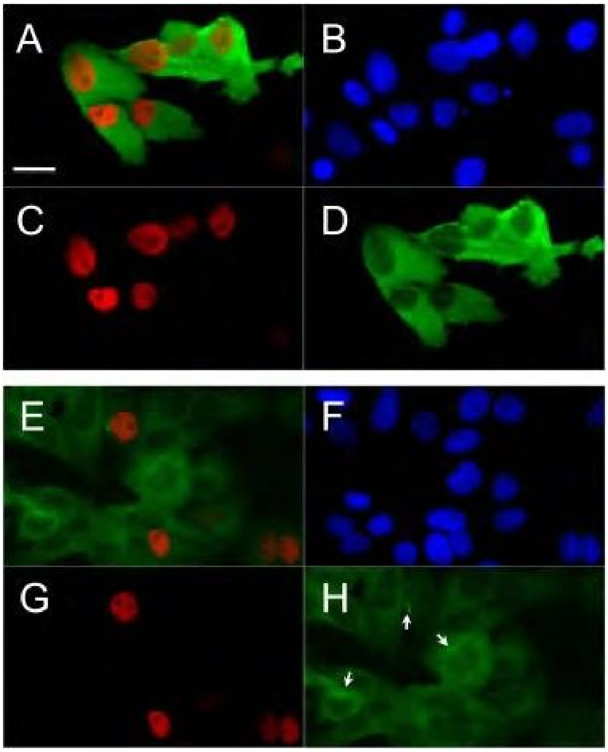

Figure 1 Immunofluorescence staining of HeLaS3 cells using anti-HA and anti-FLAG or anti-OPTN. HeLaS3 cells were transfected with HA-NRL and FLAG-OPTN plasmids (A–D) or with HA-NRL plasmid only (E–H). (A–D) Cells were stained with anti-HA antibody (red) and anti-FLAG antibody (green). (A) Merged image of (C) and (D); (B) DAPI staining of nuclei; (C) staining with anti-HA antibody; (D) staining with anti-FLAG antibody. (E–H) Cells were stained with anti-HA antibody (red) and anti-OPTN antibody (green). (E) merged image of (G) and (H); (F) DAPI staining of nuclei; (G) staining with anti-HA antibody; (H) staining with anti-OPTN antibody. Arrows in (H) show Golgi-apparatus-like staining near the nuclei. Scale bar is 20 mm. Only cells in which plasmids were successfully transfected showed immunofluorescent signals (C, D and G). FLAG-OPTN signals in nuclei were weaker than those in the cytoplasm, but still non-artifactual (D and H).

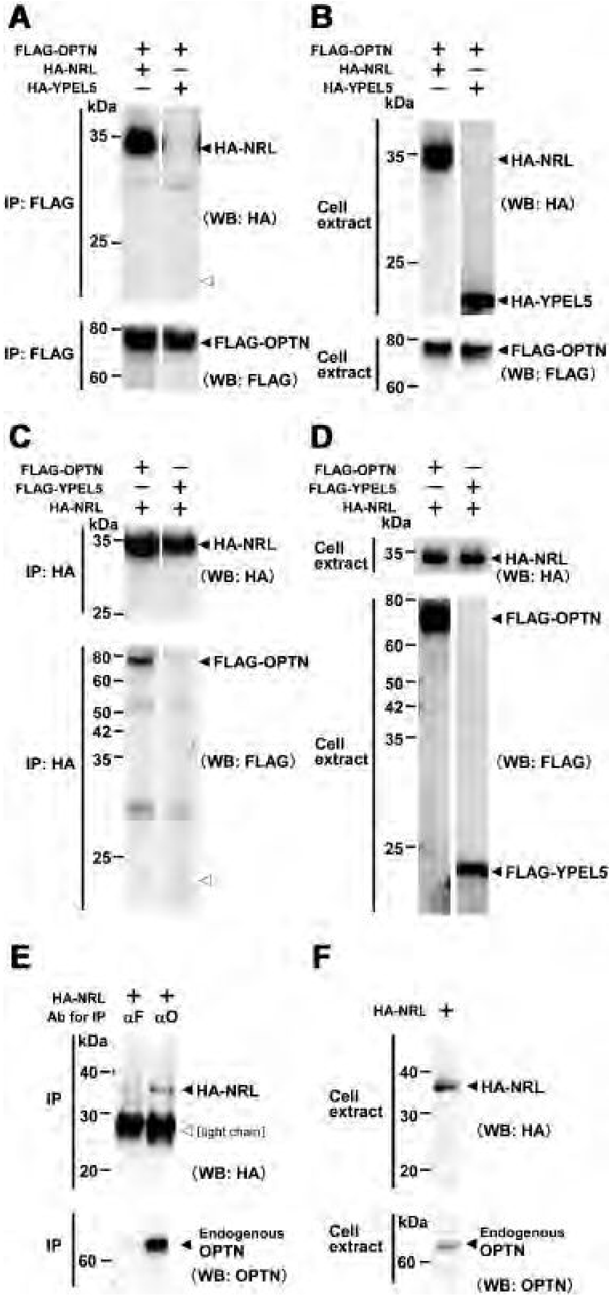

Figure 2 Co-immunoprecipitation of HA-NRL and FLAG-OPTN expressed in HeLaS3 cells. (A) Immunoprecipitation performed with the anti-FLAG antibody. The presence of transfected plasmid DNA is indicated at the top by plus (þ) and minus (−). Western blotting was used with the anti-HA antibody (upper panel) and the anti-FLAG antibody (lower panel). The open arrowhead shows the position around 22–23 kDa corresponding to the size of HA-YPEL5. (B) Western blot analysis of input proteins used for the immunoprecipitation shown in (A). The presence of transfected plasmid DNA is indicated at the top by plus (þ) and minus (−). Western blotting was used with the anti-HA antibody (upper panel) and anti-FLAG antibody (lower panel). (C) Immunoprecipitation performed with the anti-HA antibody. The presence of transfected plasmid DNA is indicated at the top by plus (þ) and minus (−). Western blotting was used with the anti-HA antibody (upper panel) and the anti-FLAG antibody (lower panel). The open arrowhead shows the position around 22–23 kDa corresponding to the size of HA-YPEL5. (D) Western blot analysis of input proteins used for the immunoprecipitation shown in (C). The presence of transfected plasmid DNA is indicated at the top by plus (þ) and minus (−). Western blotting was used with the anti-HA antibody (upper panel) and anti-FLAG antibody (lower panel). (E) Immunoprecipitation performed with the anti-FLAG or anti-OPTN antibody. Antibodies (Ab) used for immunoprecipitation in the left and right lanes are anti-FLAG (aF) and anti-OPTN (aO), respectively. Western blotting was used with the anti-HA antibody (upper panel) and the anti-OPTN antibody (lower panel). The thick band shown with an open arrowhead is the light chain of the antibody. (F) Western blot analysis of input proteins used for immunoprecipitation shown in (E). Western blotting was done with the anti-HA antibody (upper panel) and anti-OPTN antibody (lower panel). IP, immunoprecipitation; WB, Western blotting.

bands at the corresponding size of 22–23 kDa (open arrowheads shown in right lanes of the upper panel in Figure 2A and the lower panel in Figure 2C). Cell extracts without immunoprecipitation were directly assayed, and the respective tagged proteins were found (Figures 2B and 2D), confirming the presence of tagged proteins in cell lysates. These results show that the HA-tagged NRL and FLAG-tagged OPTN proteins were co-immunoprecipitated and suggest that these two proteins interact when co-expressed in HeLaS3 cells.

IP-WB analysis was used for cells transfected with only the HA-NRL plasmid to assay the interaction between HA-NRL and endogenous OPTN. Cell lysate was prepared and used for immunoprecipitation with an anti-OPTN antibody, and the immunoprecipitate was probed with anti-HA antibody. A 66-kb band (right lane of the lower panel in Figure 2E) was considered to be endogenous OPTN. Thus, HA-NRL was co-immunoprecipitated with endogenous OPTN, which indicates interaction between OPTN and NRL.

To confirm that FLAG-OPTN and HA-NRL interact with each other intracellularly, PLA analysis was used. HeLaS3 cells were co-transfected with HA-NRL and FLAG-OPTN plasmids. Strong PLA signals were seen in cell nuclei (Figures 3D and 3H). Because DNA amplification in PLA occurs only when two proteins exist in close proximity, this finding indicates that HA-NRL and FLAG-OPTN interacted with each other in the nucleus, ruling out the possibility of their interacted during preparation of the lysate.

Determination of the region of OPTN necessary for NRL binding

A set of plasmids was constructed with different partial deletions of the OPTN-coding sequence (Figure 4) to determine the region of OPTN necessary for NRL binding. The boundaries of these deletions were decided according to a previously reported homology analysis with NEMO

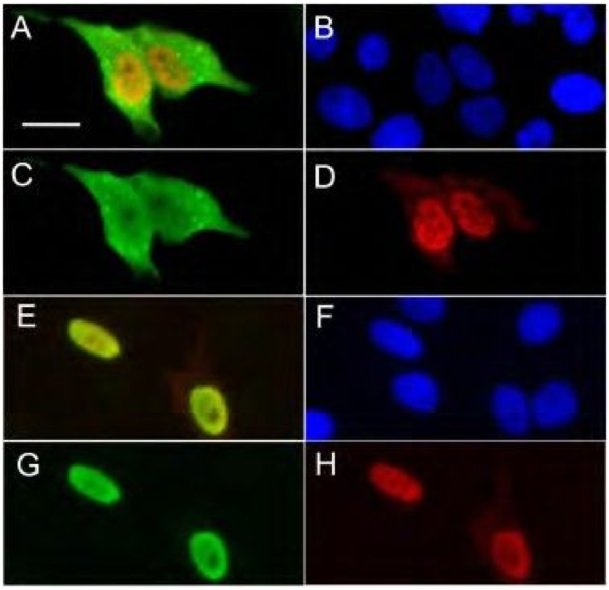

Figure 3 Detection of probable binding between FLAG-OPTN and HA-NRL using the proximity ligation assay in HeLaS3 cells. (A–D) and (E–H) are the same views. (A) Merged image of (C) and (D). (E) Merged image of (G) and (H). (B and F) DAPI staining of nuclei. (C) Staining with anti-FLAG antibody detected by fluorescent secondary antibody (Alexa-Fluor488-donkey anti-mouse IgG). (G) Staining with anti-HA antibody detected by fluorescent secondary antibody (AlexaFluor594-donkey anti-mouse IgG). (D and H) Signals from proximity ligation assay (PLA) using anti-FLAG and anti-HA antibodies. Scale bar is 20 mm. Only cells in which plasmids were successfully transfected showed immunofluorescent signals (C and G). Strong PLA signals were detected in the nuclei (D and H).

(Schwamborn et al., 2000). The tail region (423–577 aa) with the highest NEMO homology; the left middle region (121–287 aa), which does not have a corresponding region in NEMO; and the first and third regions (1–120 and 288–422 aa, respectively) with low NEMO homology were selected for deletion (see the plasmid constructs in Figure 4). The corresponding deletion clones were named del1st, del2nd, del3rd and del4th in order of their position in OPTN. The calculated protein sizes for partial OPTN with the FLAG tag expressed from these four plasmids were 55, 50, 53 and 51 kDa, respectively.

These plasmids were co-transfected with HA-NRL. For the following immunoprecipitation experiments, cytoplasmic and nuclear fractions were used rather than whole cell lysates to analyse the protein localisation in greater detail. Immunoprecipitation used anti-FLAG antibody for the cytoplasmic and nuclear fractions of cells transfected with one of the four deletions OPTN plasmids, followed by Western blot analysis with anti-HA-tag antibody (Figure 5A, lanes 3–6). In the nuclear fractions of cells transfected with the del1st, del2nd or del3rd plasmid, a band of co-immunoprecipitated HA-NRL was detected (arrows in lanes 3Nu, 4Nu and 5Nu in Figure 5A). However, the del4th plasmid did not produce a band (Figure 5A, lane 6Nu), which suggests that the NRL-binding region of OPTN is located in the fourth region (Figure 4). A higher-brightness picture of lane 6Nu (lane 6′ in Figure 5A) confirmed that there was no band in the HA-NRL position. The NRL band was not found in cytoplasmic fractions from cells transfected with any of the deletion plasmids or with the whole-length OPTN plasmid (Figure 5A, lanes 3–6Cy and 1Cy). The same immunoblot used in Figure 5A was analysed by Western blotting with anti-FLAG antibody (Figure 5B). Bands sized 63 kDa (lanes 3Cy and 3Nu), 55 kDa (4Cy and 4Nu), 60 kDa (5Cy and 5Nu) and 58 kDa (6Cy and 6Nu) were detected in the cytoplasmic and nuclear fractions (bracket in Figure 5B), which appear to correspond to FLAG-OPTN with partial deletions. All these apparent sizes were greater than the calculated sizes, which is

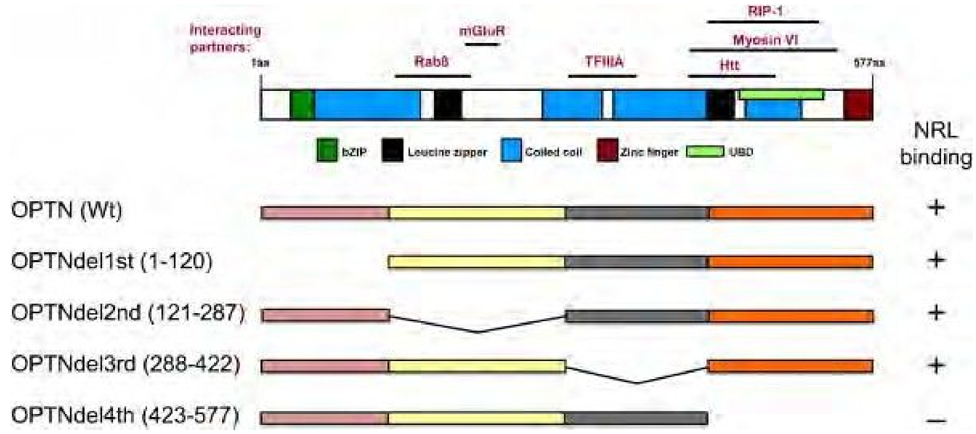

Figure 4 Construction of partial-deletion OPTN plasmids. The four deleted regions are shown. The top part of this figure was compiled from a previous report (Chalasani et al., 2009) with several modifications. bZIP, Leucine zipper, Coiled coil, Zinc finger and UBD represent the functional domains of OPTN. Horizontal bars show the binding regions of various proteins. The ability of NRL to bind each of the partial-deletion OPTN proteins from these plasmids in the assay described in Figure 5 is indicated by a plus or minus sign.

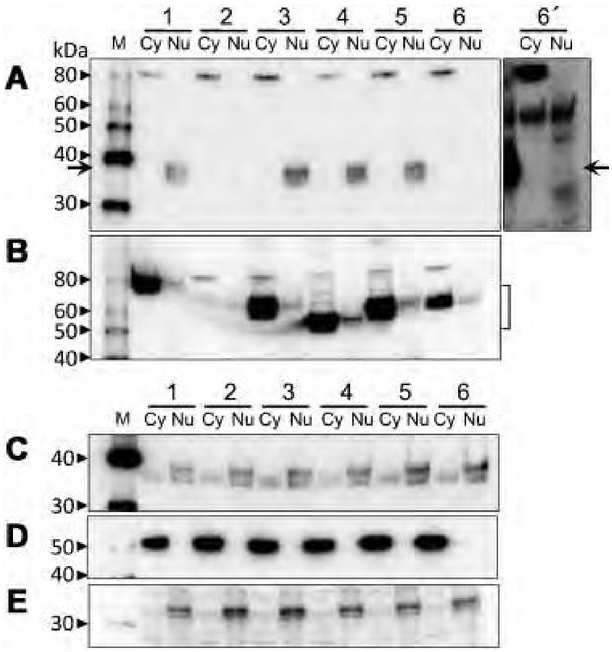

Figure 5 Determination of the OPTN region necessary for NRL binding. (A) Western blot analysis using the anti-HA antibody on immunoprecipitates obtained with the anti-FLAG antibody from the cytoplasmic (Cy) and nuclear (Nu) fractions after transfection with a series of partial deletion FLAG-OPTNs together with the HA-NRL plasmid. The arrow indicates the position of HA-NRL. (B) Western blot analysis using the anti-FLAG antibody in the same blot shown in (A). The bracket shows the band positions of partial-deletion FLAG-OPTN proteins. (C) Western blot analysis of all fractions without immunoprecipitation using the anti-HA antibody. (D) Western blot analysis of all fractions without immunoprecipitation using the anti-alpha-tubulin antibody. (E) Western blot analysis of all fractions without immunoprecipitation using the anti-histone H1 antibody. In Lanes 1–6, the following plasmids were used for transfection: Lane 1, full-length FLAG-OPTN; Lane 2, no plasmids; Lane 3, OPTNdel1st (1–120); Lane 4, OPTNdel2nd (121–287); Lane 5, OPTNdel3rd (288–422); and Lane 6, OPTNdel4th (423–577). Arrows in (A) show the position of HA-NRL. Lane 6′ shows the same blot as Lane 6 but with longer exposure time for signal detection, in which no specific HA-NRL band appeared. The bands seen in Lanes 1–6 Cy in (A) are non-specific. M stands for the molecular weight markers.

similar to the case for full-length FLAG-OPTN described above. The amount of full-length or deletion FLAG-OPTN found in nuclear fractions was much lower than that in the cytoplasm, but was clearly non-artifactual (Figure 5B, lanes 1, 3–6Nu). This finding indicates that a small amount of nuclear-localised FLAG-OPTN, with the exception of del4th, bound to HA-NRL. Western blot analysis of all fractions without immunoprecipitation using the anti-HA antibody also detected HA-NRL bands with modest intensity in the cytoplasm fractions (Figure 5C), which indicates that HA-NRL was present in the cytoplasmic fractions, but did not bind to FLAG-OPTN. The amount of alpha-tubulin and histone H1, marker proteins for the cytoplasm and nuclear fractions, respectively, was analysed to detect contamination of the nuclear fraction by cytoplasmic components or vice versa, but no significant contamination was detected (Figures 5D and 5E). These results show that FLAG-OPTN binds to HA-NRL in the nucleus and that the NRL-binding region of OPTN is located in its tail region (423–577 aa).

Expression and localisation of Optn and Nrl in the rat retina

To investigate the localisation of rat homologues of OPTN and NRL (Optn and Nrl) in the rat retina, we immunostained rat retinal sections with anti-OPTN and anti-NRL antibodies, for which cross-reactivity to rat Nrl and Optn had been confirmed. Strong fluorescent signals from the anti-OPTN antibody were seen in the outer plexiform layer (OPL), the outer nuclear layer (ONL) and the inner segments of the photoreceptors (IS) (Figures 6A and 6B). Medium-intensity signals were detected in ganglion cells, and weaker but clear signals were also detected in the inner plexiform and inner nuclear layer (IPL and INL). Anti-NRL immunoreactivity was seen in the ONL and IS (Figure 6D). High-power images of ONL for anti-OPTN staining showed fluorescent signals in the cytoplasm of most photoreceptor cells (Figure 6G). However, the nuclei of these cells did not show anti-OPTN staining even though they were stained with the anti-NRL antibody (Figures 6G, 6I and 6J). These results indicate that Optn is expressed in rat photoreceptor cells, and is localised in the cytoplasm, but no detectably in the nucleus.

Discussion

Having shown co-immunoprecipitation of FLAG-OPTN and HA-NRL that had been co-transfected in HeLaS3 cells, and that endogenous OPTN co-immunoprecipitated with HA-NRL with close proximity of FLAG-OPTN and HA-NRL in the nucleus with close proximity, it seems that OPTN and NRL interact in the nuclei. Various OPTN-binding proteins have been reported, including huntingtin, TFIIIA, Rab8 and myosin VI (Chalasani et al., 2008), all of which are expressed in the eyes and various other tissues. However, NRL is a rod-specific protein (Swain et al., 2001), and is the first OPTN-binding protein identified to have eye-specific expression. NRL-binding region of OPTN is limited to the tail portion (423–577 aa), which contains binding regions for other proteins, including RIP-1, myosin VI and huntingtin (Figure 4). This information will be useful in analysing the interaction between OPTN and NRL. We have also shown OPTN expression in photoreceptor cells, which seems to be a novel finding.

Since the first report on NRL (Swaroop et al., 1992), many studies have considered its relevance in ocular diseases. NRL and its animal homologue control the differentiation of rods from their progenitor cells during eye morphogenesis and regulate the expression of various rod-specific genes, such as

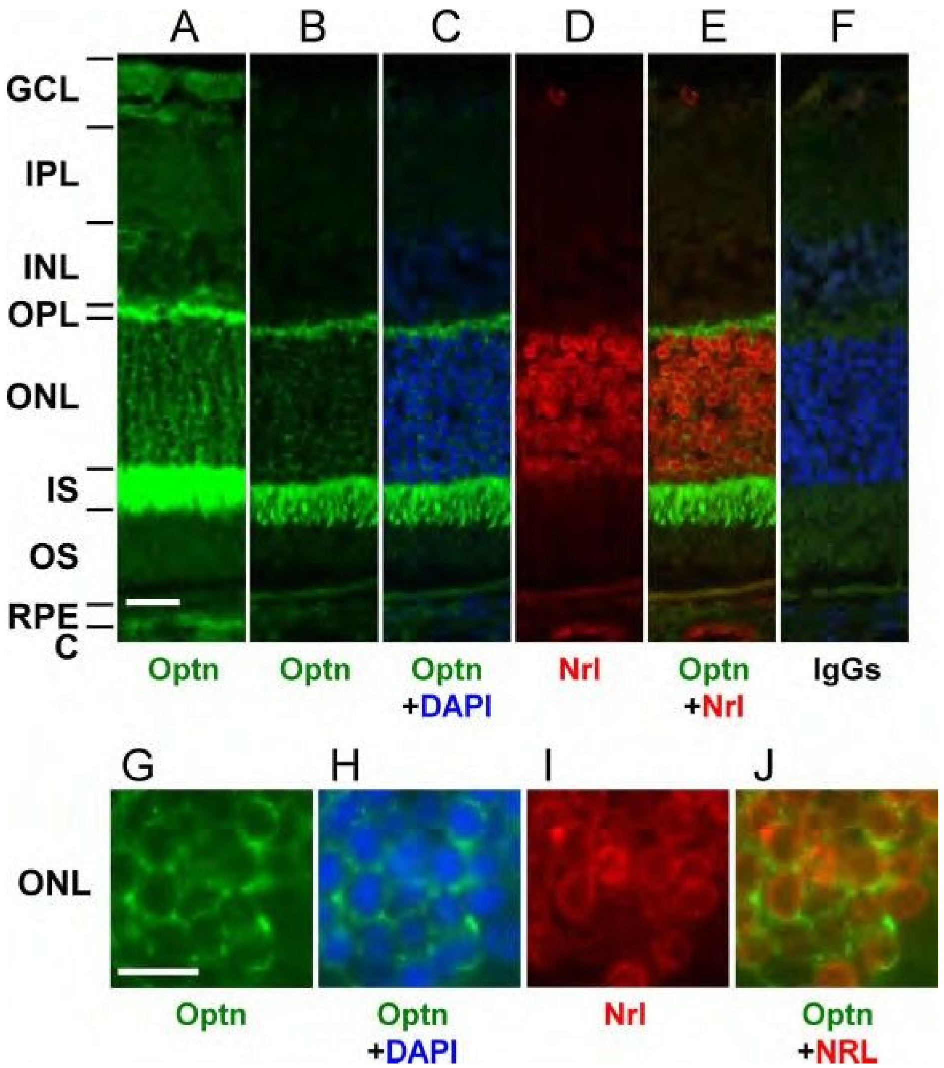

Figure 6 Expression of Optn in rat photoreceptor cells. Sections of rat retina were stained with anti-OPTN and anti-NRL antibodies. (A, B and G) Fluorescent images with anti-OPTN antibody. (D and I) Fluorescent images with anti-NRL antibody. (E and J) Merged images of (A and D) and (G and I), respectively. (C and H) Merged images of (B) or (G) with DAPI counterstaining, respectively. (F) A negative control image using non-immunised IgG to show no significant signals of anti-OPTN and anti-NRL antibodies. (B–E) are images of the same field. (B–E) are images of the same field at positions similar to those of (A–F) under high power. The thickness of the sections was 10 mm in (A) and 4 mm in (B–J). The scale bar is 20 mm in (A–F) and 10 mm in (G–J). GCL, ganglion cell layer; IPL, inner plexiform layer; INL, inner nuclear layer; OPL, outer plexiform layer; ONL, outer nuclear layer; IS, inner segment. The doughnut-ring-like staining of nuclei with the anti-NRL antibody was reproducible, and similar staining of Nr2e3 and Otx2 proteins in mouse photoreceptor nuclei was previously reported (Chen et al., 2005; Fossat et al., 2007).

rhodopsin, in adults (Kumar et al., 1996; Rehemtulla et al., 1996; Oh et al., 2007). Mutations in the NRL gene cause RP (Bessant et al., 1999). Thus, the characteristics of NRL as a transcriptional regulator and an RP-causing factor are well documented. However, the interaction of NRL with OPTN, which causes glaucoma, remains unclear.

OPTN partially relocates from the cytoplasm to the nucleus in a Rab8-dependent manner under stressed conditions, such as H_2O_2 exposure (De Marco et al., 2006). We have shown that a small amount of endogenous OPTN and FLAG-OPTN localises in the nucleus of HeLaS3 cells in the absence of stress. However, Optn was not detected in the nuclei of rat photoreceptor cells, and therefore it is possible that Optn in rat photoreceptors is relocated to the nucleus under some type of stress. Detailed analyses of OPTN localisation and possible interaction with NRL in photoreceptor cells are necessary to elucidate the significance of the binding of OPTN with NRL.

Acknowledgements and funding

The authors thank Dr. A. Takayanagi (Department of Molecular Biology, Keio University School of Medicine, Tokyo, Japan) and Prof. Emeritus N. Shimizu (Advanced Research Center for Genome Super Power, Keio University, Tsukuba, Japan) for providing the 3 ×HA vector, Mr. Katsuhisa Ishii for his persistent efforts to obtain PLA signals in a lab course, and Prof. Duco Hamasaki (Bascom Palmer Eye Institute, University of Miami School of Medicine, Miami, FL) for his helpful comments and editorial support in manuscript preparation. This study was supported in part by a Grant-in-Aid for Scientific Research on Priority Areas from the Ministry of Education, Culture, Sports, Science and Technology (MEXT) and a Grant-in-Aid for Scientific Research from the Japan Society for the Promotion of Science (JSPS). Chunxia Wang is the scholarship student of the Japanese Government (Monbukagakusho: MEXT) (2003–2008); 2009 Santen Pharmaceutical Travel Grant from the Association for Research in Vision and Ophthalmology (ARVO).

References

Bessant DA, Payne AM, Mitton KP, Wang QL, Swain PK, Plant C, Bird AC, Zack DJ, Swaroop A, Bhattacharya SS (1999) A mutation in NRL is associated with autosomal dominant retinitis pigmentosa. Nat Genet 21: 355–6.

Chalasani ML, Radha V, Gupta V, Agarwal N, Balasubramanian D, Swarup G (2007) A glaucoma-associated mutant of optineurin selectively induces death of retinal ganglion cells which is inhibited by antioxidants. Invest Ophthalmol Vis Sci 48: 1607–14.

Chalasani ML, Balasubramanian D, Swarup G (2008) Focus on molecules: optineurin. Exp Eye Res 87: 1–2.

Chalasani ML, Swarup G, Balasubramanian D (2009) Optineurin and its mutants: molecules associated with some forms of glaucoma. Ophthalmic Res 42: 176–84.

Chen J, Rattner A, Nathans J (2005) The Rod photoreceptor-specific nuclear receptor Nr2e3 represses transcription of multiple cone-specific genes. J Neurosci 25: 118–29.

De Marco N, Buono M, Troise F, Diez-Roux G (2006) Optineurin increases cell survival and translocates to the nucleus in a Rab8-dependent manner upon an apoptotic stimulus. J Biol Chem 281: 16147–56.

Faber PW, Barnes GT, Srinidhi J, Chen J, Gusella JF, MacDonald ME (1998) Huntingtin interacts with a family of WW domain proteins. Hum Mol Genet 7: 1463–74.

Fossat N, Le Greneur C, Béby F, Vincent S, Godement P, Chatelain G, Lamonerie T (2007) A new GFP-tagged line reveals unexpected Otx2 protein localization in retinal photoreceptors. BMC Dev Biol 7: 122.

Hosono K, Noda S, Shimizu A, Nakanishi N, Ohtsubo M, Shimizu N, Minoshima S (2010) YPEL5 protein of the YPEL gene family is involved in the cell cycle progression by interacting with two distinct proteins RanBPM and RanBP10. Genomics 96: 102–11.

Kroeber M, Ohlmann A, Russell P, Tamm ER (2006) Transgenic studies on the role of optineurin in the mouse eye. Exp Eye Res 82: 1075–85.

Kumar R, Chen S, Scheurer D, Wang QL, Duh E, Sung CH, Rehemtulla A, Swaroop A, Adler R, Zack DJ (1996) The bZIP transcription factor Nrl stimulates rhodopsin promoter activity in primary retinal cell cultures. J Biol Chem 271: 29612–8.

Li Y, Kang J, Horwitz MS (1998) Interaction of an adenovirus E3 14.7-kilodalton protein with a novel tumor necrosis factor alpha-inducible cellular protein containing leucine zipper domains. Mol Cell Biol 18: 1601–10.

Lim MK, Kawamura T, Ohsawa Y, Ohtsubo M, Asakawa S, Takayanagi A, Shimizu N (2007) Parkin interacts with LIM kinase 1 and reduces its cofilin-phosphorylation activity via ubiquitination. Exp Cell Res 313: 2858–74.

Maruyama H, Morino H, Ito H, Izumi Y, Kato H, Watanabe Y, Kinoshita Y, Kamada M, Nodera H, Suzuki H, Komure O, Matsuura S, Kobatake K, Morimoto N, Abe K, Suzuki N, Aoki M, Kawata A, Hirai T, Kato T, Ogasawara K, Hirano A, Takumi T, Kusaka H, Hagiwara K, Kaji R, Kawakami H (2010) Mutations of optineurin in amyotrophic lateral sclerosis. Nature 465: 223–6.

Mears AJ, Kondo M, Swain PK, Takada Y, Bush RA, Saunders TL, Sieving PA, Swaroop A (2001) Nrl is required for rod photoreceptor development. Nat Genet 29: 447–52.

Moreland RJ, Dresser ME, Rodgers JS, Roe BA, Conaway JW, Conaway RC, Hanas JS (2000) Identification of a transcription factor IIIA-interacting protein. Nucleic Acids Res 28: 1986–93.

Oh EC, Khan N, Novelli E, Khanna H, Strettoi E, Swaroop A (2007) Transformation of cone precursors to functional rod photoreceptors by bZIP transcription factor NRL. Proc Natl Acad Sci USA 104: 1679–84.

Park BC, Shen X, Samaraweera M, Yue BY (2006) Studies of optineurin, a glaucoma gene: Golgi fragmentation and cell death from overexpression of wild-type and mutant optineurin in two ocular cell types. Am J Pathol 169: 1976–89.

Park B, Ying H, Shen X, Park JS, Qiu Y, Shyam R, Yue BY (2010) Impairment of protein trafficking upon overexpression and mutation of optineurin. PLoS ONE 5: e11547.

Rehemtulla A, Warwar R, Kumar R, Ji X, Zack DJ, Swaroop A (1996) The basic motif-leucine zipper transcription factor Nrl can positively regulate rhodopsin gene expression. Proc Natl Acad Sci USA 93: 191–5.

Rezaie T, Sarfarazi M (2005) Molecular cloning, genomic structure, and protein characterization of mouse optineurin. Genomics 85: 131–8.

Rezaie T, Child A, Hitchings R, Brice G, Miller L, Coca-Prados M, Héon E, Krupin T, Ritch R, Kreutzer D, Crick RP, Sarfarazi M (2002) Adult-onset primary open-angle glaucoma caused by mutations in optineurin. Science 295: 1077–9.

Rezaie T, Waitzman DM, Seeman JL, Kaufman PL, Sarfarazi M (2005) Molecular cloning and expression profiling of optineurin in the rhesus monkey. Invest Ophthalmol Vis Sci 46: 2404–10.

Schwamborn K, Weil R, Courtois G, Whiteside ST, Israël A (2000) Phorbol esters and cytokines regulate the expression of the NEMO-related protein, a molecule involved in a NF-kappa B-independent pathway. J Biol Chem 275: 22780–9.

Swain PK, Hicks D, Mears AJ, Apel IJ, Smith JE, John SK, Hendrickson A, Milam AH, Swaroop A (2001) Multiple phosphorylated isoforms of NRL are expressed in rod photoreceptors. J Biol Chem 276: 36824–30.

Swaroop A, Xu JZ, Pawar H, Jackson A, Skolnick C, Agarwal N (1992) A conserved retina-specific gene encodes a basic motif/leucine zipper domain. Proc Natl Acad Sci USA 89: 266–70.

Received 30 January 2013; accepted 22 July 2013.

Journal of Human Genetics (2014) 59, 521–528
© 2014 The Japan Society of Human Genetics All rights reserved 1434-5161/14
www.nature.com/jhg

ORIGINAL ARTICLE

The first USH2A mutation analysis of Japanese autosomal recessive retinitis pigmentosa patients: a totally different mutation profile with the lack of frequent mutations found in Caucasian patients

Yang Zhao[1,2], Katsuhiro Hosono[1], Kimiko Suto[1], Chie Ishigami[3], Yuuki Arai[4], Akiko Hikoya[1], Yasuhiko Hirami[4], Masafumi Ohtsubo[2], Shinji Ueno[5], Hiroko Terasaki[5], Miho Sato[1], Hiroshi Nakanishi[6], Shiori Endo[6], Kunihiro Mizuta[6], Hiroyuki Mineta[6], Mineo Kondo[7], Masayo Takahashi[3], Shinsei Minoshima[2] and Yoshihiro Hotta[1]

Retinitis pigmentosa (RP) is a highly heterogeneous genetic disease. The USH2A gene, which accounts for approximately 74–90% of Usher syndrome type 2 (USH2) cases, is also one of the major autosomal recessive RP (arRP) causative genes among Caucasian populations. To identify disease-causing USH2A gene mutations in Japanese RP patients, all 73 exons were screened for mutations by direct sequencing. In total, 100 unrelated Japanese RP patients with no systemic manifestations were identified, excluding families with obvious autosomal dominant inheritance. Of these 100 patients, 82 were included in this present study after 18 RP patients with very likely pathogenic EYS (eyes shut homolog) mutations were excluded. The mutation analysis of the USH2A revealed five very likely pathogenic mutations in four patients. A patient had only one very likely pathogenic mutation and the others had two of them. Caucasian frequent mutations p.C759F in arRP and p.E767fs in USH2 were not found. All the four patients exhibited typical clinical features of RP. The observed prevalence of USH2A gene mutations was approximately 4% among Japanese arRP patients, and the profile of the USH2A gene mutations differed largely between Japanese patients and previously reported Caucasian populations.

Journal of Human Genetics (2014) 59, 521–528; doi:10.1038/jhg.2014.65; published online 31 July 2014

INTRODUCTION

Usher syndrome (USH; Mendelian inheritance in man (MIM) 276900) is an autosomal recessive disorder characterized by retinitis pigmentosa (RP) and hearing loss, with or without vestibular dysfunction. The syndrome is clinically and genetically heterogeneous and can be clinically classified into three subtypes on the basis of severity and progression of hearing loss and the presence or absence of vestibular dysfunction.[1] Specifically, USH type 2 (USH2), the most common type accounting for >50% of USH cases, is characterized by congenital mild-to-severe hearing loss and a normal vestibular response.[2] The USH2A (Usher syndrome 2A) gene, which encodes usherin, accounts for approximately 80% of USH2 cases.[3–5] Previous mutation analyses of the full-length USH2A coding region (exons 2–72) in Caucasian patients have revealed a frequent mutation c.2299delG (p.E767fs) in exon 13.[4–12] In our recent analysis of the USH2A gene in Japanese USH2 patients, in which the p.E767fs mutation was not identified, we reported 19 novel mutations among 19 patients, as well as the splicing mutation c.8559-2A>G in 4 of the 19 patients, indicating that the incidence of mutations in the Japanese individuals was similar to that in Caucasian individuals, even though the mutation spectrum of the USH2A gene considerably differed between the two populations.[13–15]

RP (MIM 268000) is a highly heterogeneous genetic retinal degeneration characterized by night blindness and visual field constriction, which would eventually lead to severe visual impairment. The disease can be inherited via an autosomal recessive (ar), autosomal dominant (ad) or X-linked recessive mode or may occur in isolation; in fact, more than half of the cases in Japan are isolated cases.[16] To date, 63 causative genes and 7 loci have been found to be associated with RP (http://www.sph.uth.tmc.edu/Retnet/; accessed

---

[1]Department of Ophthalmology, Hamamatsu University School of Medicine, Hamamatsu, Japan; [2]Department of Photomedical Genomics, Basic Medical Photonics Laboratory, Medical Photonics Research Center, Hamamatsu University School of Medicine, Hamamatsu, Japan; [3]Laboratory for Retinal Regeneration, RIKEN Center for Developmental Biology, Kobe, Japan; [4]Department of Ophthalmology, Institute of Biomedical Research and Innovation Hospital, Kobe, Japan; [5]Department of Ophthalmology, Nagoya University Graduate School of Medicine, Nagoya, Japan; [6]Department of Otorhinolaryngology/Head and Neck Surgery, Hamamatsu University School of Medicine, Hamamatsu, Japan and [7]Department of Ophthalmology, Mie University Graduate School of Medicine, Tsu, Japan
Correspondence: Dr Y Hotta, Department of Ophthalmology, Hamamatsu University School of Medicine, 1-20-1 Handayama, Hamamatsu-shi, Higashi-ku, Shizuoka 431-3192, Japan.
E-mail: hotta@hama-med.ac.jp

Received 8 March 2014; revised 20 May 2014; accepted 3 July 2014; published online 31 July 2014

19 February 2014). The *EYS* (eyes shut homolog) gene encodes an ortholog of *Drosophila* spacemaker (spam), which is a protein essential for maintaining the photoreceptor morphology. *EYS* gene mutations have been detected in arRP-affected families of different ancestral origins and have been reported to account for 5–16% of arRP cases.[17–22] Mutations in the *USH2A* gene were also found to cause non-syndromic RP.[23] Although some studies on the *USH2A* gene employed mostly USH patients and included a few non-syndromic RP patients,[5,24,25] a few groups analyzed large sets of non-syndromic RP patients and reported that *USH2A* mutations, including the frequent mutation c.2276G>T (p.C759F), cause a substantial number of cases of non-syndromic RP in North America and Spain (7–23%).[23,26–29] We previously screened all *EYS* gene exons in 100 unrelated Japanese RP patients and, surprisingly, found *EYS* gene mutations in at least 18% of the arRP patients.[30] Of these 100 patients, 82 were included in the present study after 18 RP patients with very likely pathogenic (deleterious) *EYS* gene mutations were excluded.[30] Here we report the results of our study of all *USH2A* exons in 82 Japanese arRP patients.

MATERIALS AND METHODS

Patients

We previously screened all *EYS* gene exons in 100 unrelated Japanese RP patients with no systemic manifestations, excluding families with obvious autosomal dominant inheritance.[30] Among them, some pedigrees showed a pattern compatible with the recessive mode of inheritance, whereas other patients were considered as isolated cases. Excluding 18 RP patients with very likely pathogenic *EYS* gene mutations, 82 out of these 100 patients were employed in this study. An audiological examination, including pure-tone audiometry, was not performed before the mutation analysis; however, none of the patients had documented hearing loss. In addition, 200 unrelated and non-RP Japanese individuals were screened as controls to evaluate the frequency of mutations found in patient samples. Japanese patients with RP were examined at the Department of Ophthalmology, Hamamatsu University Hospital in Hamamatsu (by YH); the Department of Ophthalmology, Kobe City Medical Center General Hospital in Kobe (by MT); the Department of Ophthalmology, Institute of Biomedical Research and Innovation Hospital in Kobe (by MT); or the Department of Ophthalmology, Nagoya University Hospital in Nagoya (by MK and SU). These patients were from the areas of Tokyo to Osaka in Japan.

Ethics statements

This study was approved by the Institutional Review Board for Human Genetic and Genome Research at the four participating institutions (Hamamatsu University School of Medicine, RIKEN Center for Developmental Biology, Institute of Biomedical Research and Innovation Hospital and Nagoya University Graduate School of Medicine). All the procedures conformed to the tenets of the Declaration of Helsinki. Written informed consent was obtained from all participants before the molecular genetic studies were performed.

Mutation analysis

Genomic DNA extracted from peripheral lymphocytes of patients using standard procedures was amplified by PCR using the primer sets described in Supplementary Table S1. The PCR and sequencing procedures used were described previously.[30] A total of 73 exons, including a non-coding exon (exon 1) that covers the 5′ untranslated region, 71 coding exons (exons 2–72) and an alternatively spliced variant of exon 71,[31] were analyzed in both sense and antisense directions. Alternatively spliced exon 71 encodes a 24-amino-acid peptide in the murine inner ear and is considered to be well conserved in humans, even though its presence in human transcripts has not yet been directly confirmed. The accession numbers for the two alternative splicing isoforms (long isoform,[8] consisting of 72 exons, and longer isoform, consisting of 73 exons that included an alternatively spliced variant of exon 71) of *USH2A* genes were NM_206933 (long isoform) and ENST00000366943 (longer isoform). The latter is the Ensembl Transcript ID number in the Ensembl database, which is presented here, because the entry of the longer isoform was not found in the DDBJ/EMBL/GenBank database.

Assessment of pathogenicity

A sequence variant was considered pathogenic when it represented a nonsense mutation, a frameshift mutation, a deletion mutation affecting amino-acid sequences, a mutation in the first two bases of canonical intron splice donor or acceptor sites, a missense mutation affecting a conserved amino-acid residue, a previously described pathogenic mutation or a mutation identified in ≥2 unrelated patients and did not appear in 200 unrelated and non-RP Japanese control samples or a public single-nucleotide polymorphism (SNP) database (NCBI dbSNP database, http://www.ncbi.nlm.nih.gov/projects/SNP/; 1000 Genomes database, http://www.1000genomes.org/). In particular, a missense mutation was described as very likely pathogenic when it fulfilled at least two of the following criteria: (1) it was found together with a second variant, especially a nonsense mutation or frameshift mutation; (2) it was segregated with the disease phenotype within the family; and (3) the *in silico* analysis predicted a pathogenic effect.

In silico analysis to assess the pathogenicity of a missense or deletion mutation

We used the five following computational algorithms to evaluate the pathogenicity of missense mutations: SIFT (http://sift.jcvi.org/www/SIFT_seq_submit2.html), PolyPhen2 (http://genetics.bwh.harvard.edu/pph2/), PMut (http://mmb.pcb.ub.es/PMut/), SNAP (http://rostlab.org/services/snap/), and Align-GVGD (http://agvgd.iarc.fr/agvgd_input.php). The SIFT analysis results are given by a probability of 0–1; specifically, mutations with a probability ≤ 0.05 are predicted to be deleterious (affect protein function), whereas those with a probability >0.05 are predicted to be tolerated. In this study, a mutation predicted to 'affect protein function' was considered as a suspected pathogenic mutation. Polyphen2 describes mutations as 'benign', 'possibly damaging' or 'probably damaging'. In this study, both 'possibly damaging' and 'probably damaging' were classified as suspected pathogenic mutations. The results from the SNAP analysis are classified into 'neutral' or 'non-neutral'. In this study, 'non-neutral' was considered as a suspected pathogenic mutation. The results from the PMut analysis are classified into 'neutral' or 'pathological'. In this study, 'pathological' was considered as a suspected pathogenic mutation. The Align-GVGD analysis results are given by a grade from C0 to C65, where C0 is benign and C65 is most likely pathogenic. In this study, a grade of C65 was considered as a suspected pathogenic mutation.

The secondary structure of usherin was predicted by PSIPRED v3.3 on the PSIPRED server (http://bioinf.cs.ucl.ac.uk/psipred/).

Clinical evaluation

The doctors were asked to obtain as much detail as possible about the family history of patients in whom we identified very likely pathogenic mutations (RP7H, RP10H, RP15H and RP66K) and possible pathogenic mutations (RP82K and RP85N). The complete history and medical records of these four patients were reviewed. In addition, patients were also clinically evaluated by standard procedures, including spectral-domain optical coherence tomography (Spectralis OCT; Heidelberg Engineering, Heidelberg, Germany or Cirrus OCT; Carl Zeiss Meditec, Inc., Dublin, CA, USA). Electroretinograms were also performed in some cases. Audiological examination, including pure-tone audiometry, was performed for patients (RP7H, RP10H and RP15H) who consented to the study.

RESULTS

Mutation analysis

Our mutation analysis of the *USH2A* gene in 82 unrelated Japanese patients revealed 5 very likely pathogenic mutations among 4 patients. A patient had only one very likely pathogenic mutation

Table 1 Mutation spectrum of the USH2A gene among Japanese families

Family ID	Nucleotide change	Predicted effect	Domain[a]	Location in gene	Type of change	Reference
Families with very likely pathogenic mutations						
RP7H[b]	c.685G4C/c.3595_3597delGAA	p.G229R/p.E1199del	LamGL/FN3	Exon 4/exon 17	Compound heterozygous	This study/this study
RP10H[C]	c.685G4C;c.2776C4T	p.G229R;p.R926C	LamGL;EGF_Lam	Exon 4;exon 13	Heterozygous;heterozygous	This study;this study
RP15H	c.8559-2A4G/c.8559-2A4G			Intron 42/intron 42	Homozygous	Nakanishi et al.,[13,15] Dai et al.[32]
RP66K	c.468-14G4A			Intron 2	Heterozygous	Le Guédard-Méreuze et al.[33]
Families with novel possible pathogenic mutations						
RP82K	c.7156G4T	p.V2386F	FN3	Exon 38	Heterozygous	This study
RP85N	c.14243C4T	p.S4748F	FN3	Exon 65	Heterozygous	This study

Nucleotide numbering reflects cDNA numbering with þ1 corresponding to A of the ATG translation initiation codon in the reference sequence NM_206933, according to the nomenclature recommended by the Human Genome Variation Society (www.hgvs.org/mutnomen).
The initiation codon was designated as codon 1. None of these seven mutations were found in the Japanese control individuals.
[a] USH2A has a signal peptide, a laminin G-like domain (LamGL), a laminin N-terminal domain, a laminin-type EGF-like domain (EGF_Lam), a fibronectin type 3 domain (FN3), a laminin G domain, a transmembrane domain, and a PDZ-binding domain. See Figure 2.
[b] Segregation analysis was performed for the patient. See Figure 1a.
[c] No segregation analysis could be performed in this patient owing to difficulties in collecting samples from the patient's family. Therefore, it was not confirmed that two mutations were located on different chromosomes.

Table 2 Summary of very likely and possible pathogenic mutations identified in 82 Japanese patients with autosomal recessive retinitis pigmentosa

					Allele frequency				Computational prediction[b]				
Nucleotide change	Predicted effect	Location in gene	Domain[a]	Conservation in H/B/D/R/M/C/Z[c]	Control frequency	Patient frequency	Family ID	Population	SIFT	PolyPhen2	PMut	SNAP	Align-GVGD
Very likely pathogenic mutations													
Splicing													
c.468-14G4A		Intron 2		Not applicable	0/400	1/164	RP66K	Japanese, French[33]					
c.8559-2A4G		Intron 42		Not applicable	0/400	2/164	RP15H	Japanese,[13,15] Chinese[32]					
Deletion													
c.3595_3597delGAA	p.E1199del	Exon 17	FN3	E/E/E/E/E/E/T	0/400	1/164	RP7H	Japanese					
Missense													
c.685G4C	p.G229R	Exon 4	LamGL	G/G/G/G/G/G/G	0/400	2/164	RP7H, RP10H	Japanese	Affect (score 0.00)	Probably damaging	Neutral	Non-neutral	C65
c.2776C4T	p.R926C	Exon 13	EGF_Lam	R/R/R/R/R/R/R	0/400	1/164	RP10H	Japanese	Affect (score 0.00)	Probably damaging	Neutral	Non-neutral	C65
Possible pathogenic mutations													
Missense													
c.7156G4T	p.V2386F	Exon 38	FN3	V/I/V/T/T/I/E	0/400	1/164	RP82K	Japanese	Affect (score 0.05)	Benign	Neutral	Non-neutral	C45
c.14243C4T	p.S4748F	Exon 65	FN3	S/A/S/S/S/S/S	0/400	1/164	RP85N	Japanese	Affect (score 0.01)	Probably damaging	Pathological	Non-neutral	C65

[a] USH2A has a signal peptide, a laminin G-like domain (LamGL), a laminin N-terminal domain, a laminin-type EGF-like domain (EGF_Lam), a fibronectin type 3 domain (FN3), a laminin G domain, a transmembrane domain and a PDZ-binding domain. See Figure 2.
[b] SIFT, PolyPhen2, PMut, SNAP and Align-GVGD were used to evaluate the pathogenicity of missense mutations. See Materials and methods. Suspected pathogenic mutations are shown in bold.
[c] H/B/D/R/M/C/Z denotes human/bovine/dog/rat/mouse/chicken/zebrafish USH2A orthologs, the sequences of which were selected from the DDBJ/EMBL/GenBank database. Accession numbers were NM_206933 (human), NM_001191425 (bovine), XM_545710 (dog), NM_001244757 (rat), NM_021408 (mouse), XM_419417 (chicken) and XM_692343 (zebrafish).

and the others had two of them (Tables 1 and 2). These very likely pathogenic mutations consisted of a deletion mutation, two splicing mutations and two missense mutations. In addition, we identified two possible pathogenic mutations in two individual patients (Tables 1 and 2).

Families with very likely pathogenic mutations

Among the four patients carrying very likely pathogenic mutations, RP7H, RP10H and RP15H each had two pathogenic mutations. In RP7H and RP15H, the two mutated alleles were considered to be located on different chromosomes (Figures 1a and c).

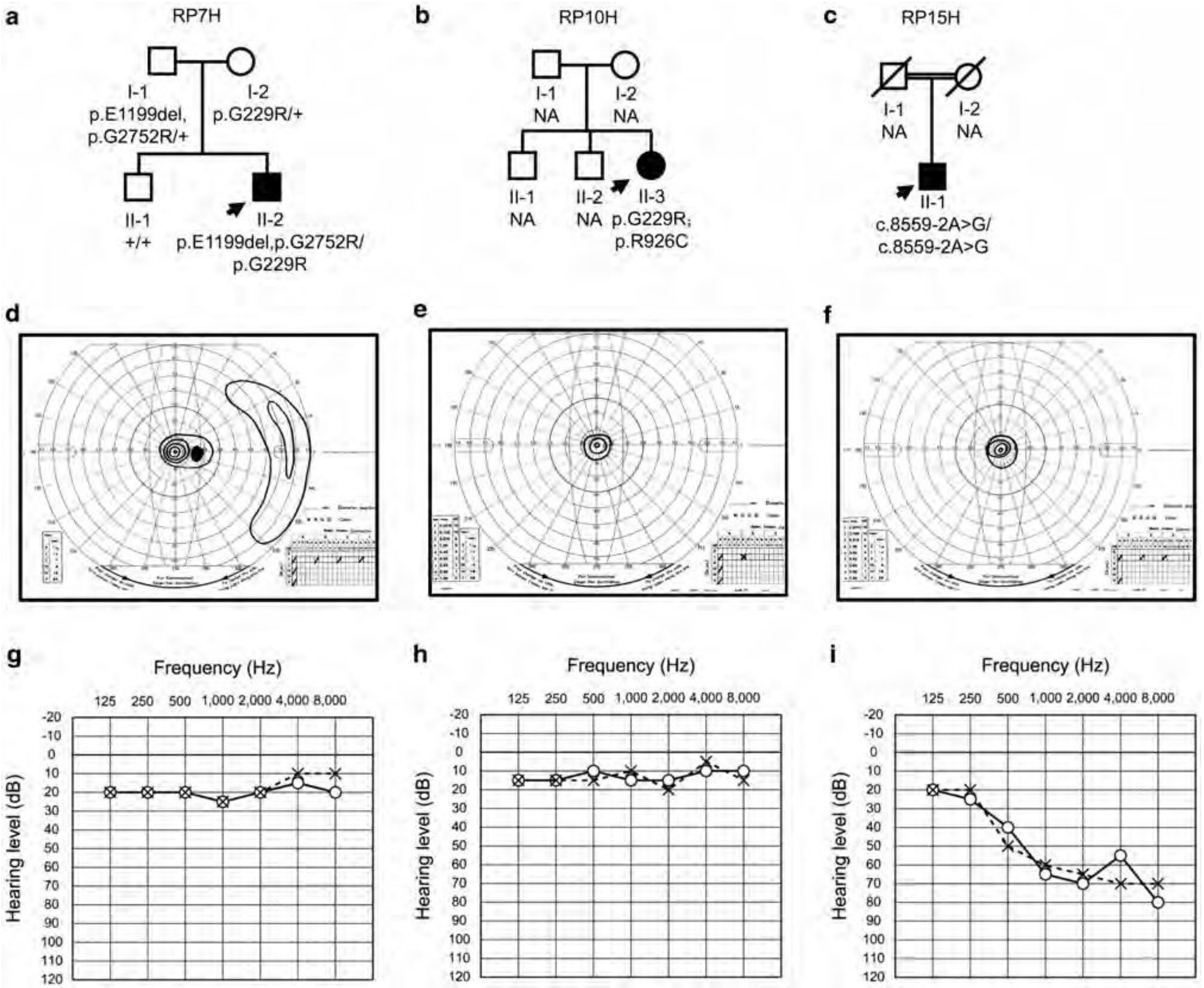

Figure 1 Pedigree and clinical examination data of patients with mutations in the USH2A gene. (a–c) Pedigrees of patients RP7H (a), RP10H (b) and RP15H (c). The genotypes are presented for p.E1199del, p.G229R, p.G2752R, p.R926C and c.8559-2A>G. The genotype of each evaluated individual is indicated below the symbol: square boxes and circles denote male and female individuals, respectively; black symbols indicate affected individuals; and slashed symbols indicate deceased individuals. The probands are indicated with arrows. NA, unavailable DNA samples. For example, c.8559-2A>G/c.8559-2A>G, homozygous mutation carriers; p.G229R/+, heterozygous carriers; +/+, individuals carrying two wild-type alleles; p.E1199del/p.G229R, individuals who were compound heterozygous for both mutations. p.G229R;p.R926C could not be segregated (See Table 1 footnote). (d–f) Right visual fields of patients RP7H (d), RP10H (e) and RP15H (f). The constriction of visual fields was found to be symmetric. The concentric constriction started in their twenties or thirties, and no effective residual visual field was observed after their fifties. (g–i) Audiograms of patients RP7H (g), RP10H (h) and RP15H (i). Circles and crosses indicate hearing thresholds of the right and left ears, respectively.

Patient RP7H was born in the Hamamatsu area and was considered as an isolated case (Figure 1a). In RP7H, the proband (II-2) was compound heterozygous for the novel missense mutation c.685G>C (p.G229R) and the novel deletion mutation c.3595_3597delGAA (p.E1199del) (Figure 1a). p.G229R was also identified in patient RP10H, who was unrelated to RP7H (Tables 1 and 2). The amino-acid residue at G229 of human USH2A was compared with those encoded by the orthologous genes of some vertebrates (bovine, dog, rat, mouse, chicken and zebrafish) and was found to be highly conserved across species (Table 2). p.G229R was predicted to be pathogenic by four different computational prediction programs (SIFT, Polyphen2, SNAP and Align-GVGD). On the other hand, p.E1199del is a 3-base pair (bp) in-frame deletion that results in the loss of the amino-acid residue E1199 in the second fibronectin type 3 domain (Figure 2). E1199 was also compared with the equivalent residue in other species' orthologous genes and was highly conserved among mammals and chicken (Table 2). p.E1199del was analyzed by the PSIPRED program to determine its effect on the secondary structure of usherin. The predicted effect was the shortening of the beta-sheet stretch from seven contiguous amino acids (QPCVSYE-1199) to five (QPCVS-1197), which suggests that the mutation affected the normal protein structure and was pathogenic. Interestingly, we also found another missense mutation c.8254G>A (p.G2752R), which we previously found in USH2 patient C212 as one of thee candidates for probable pathogenic mutations, but we could not determine the pathogenicity because of difficulty in the

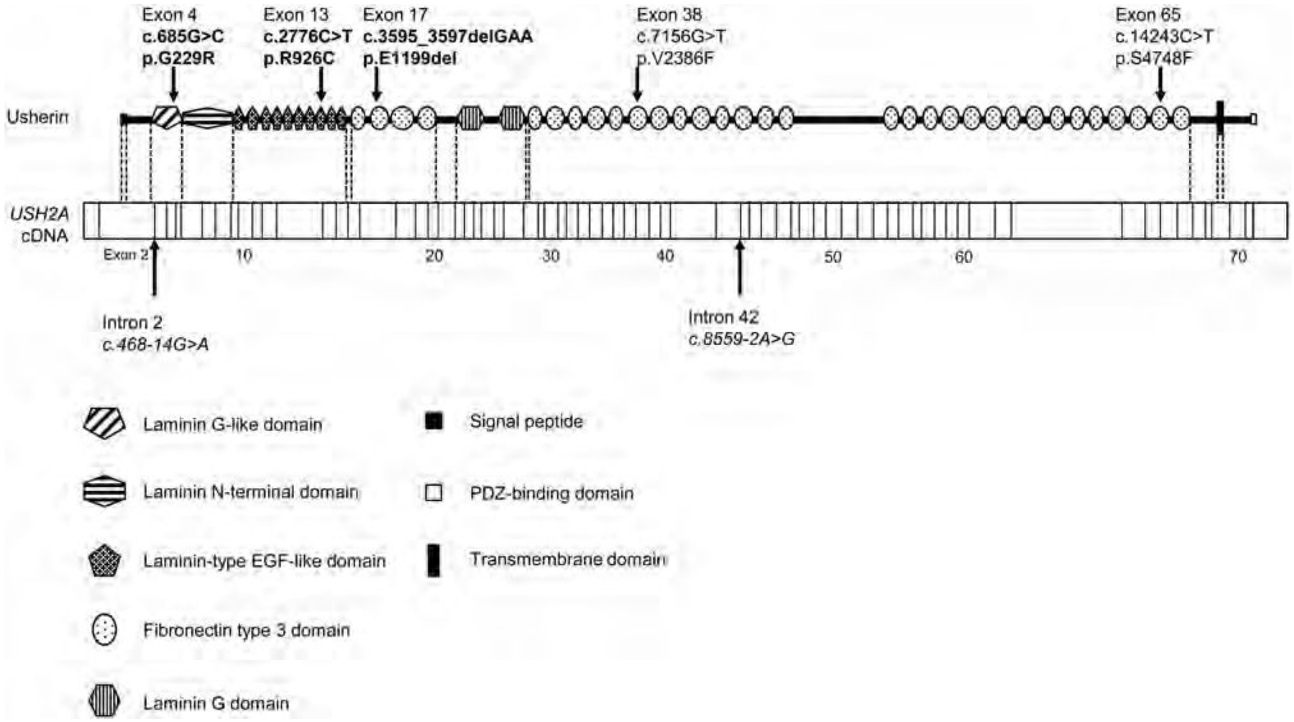

Figure 2 Schematic distribution of the USH2A mutations identified in this study. Upper, usherin domains encoded by USH2A; lower, USH2A cDNA with exon boundaries. Novel very likely pathogenic mutations, novel possible pathogenic mutations and previously described mutations are shown in bold, normal and italic fonts, respectively. Identified mutations were widely distributed throughout almost the entire USH2A gene without any clear hot spot.

segregation analysis.[13] However, in this study, p.G2752R was assigned to the group of possible non-pathogenic sequence alterations (Supplementary Table S2), because it has been described in the dbSNP database (rs201863550) and the 1000 Genomes database. As shown in Figure 1a, the mutations were found to co-segregate with the disease phenotype as follows. The unaffected father (I-1) and mother (I-2) were heterozygous for p.E1199del and p.G229R, respectively, whereas the unaffected brother (II-1) carried the wild-type alleles. In addition, p.G2752R was identified in *cis* to p.E1199del in the unaffected father, indicating that these two mutations were genetically linked in this family.

Patient RP10H was born in the Hamamatsu area and was considered to be an isolated case (Figure 1b). RP10H was heterozygous for two missense mutations, c.685G4C (p.G229R) and c.2776C4T (p.R926C). p.G229R, also found in RP7H, was classified as very likely pathogenic as described above. Similarly, the novel missense mutation p.R926C was predicted to be pathogenic by four different computational prediction programs (SIFT, Polyphen2, SNAP and Align-GVGD) (Table 2). Like G229, the R926 residue was also found to be highly conserved across species (Table 2). No segregation analysis could be performed in this patient owing to difficulties in collecting samples from the patient's family. Although both these two missense mutations were considered pathogenic, we were not able to confirm whether they were located on different chromosomes (Figure 1b, Table 1).

Patient RP15H carried the homozygous c.8559-2A4G mutation; RP15H was an isolated case and his parents were second cousins from the Hamamatsu area; that is, he was the product of a consanguineous marriage (Figure 1c). The proband (II-1) was homozygous for the splicing mutation c.8559-2A4G. No segregation analysis was performed, because both parents were deceased. Although the mutation has been previously reported as disease causing in four Japanese and one Chinese USH2 patients,[13,15,32] all of these five patients were heterozygous for c.8559-2A4G. To the best of our knowledge, this study is the first to report of a patient homozygous for the c.8559-2A4G mutation.

Patient RP66K was born in Kobe and was considered as an isolated case. In RP66K, we found the splicing mutation, c468-14G4A, which has been previously reported as disease causing in a French USH2 patient and shown to create a new AG (acceptor consensus) sequence, resulting in abnormal splicing.[33]

None of these five very likely pathogenic mutations was found among the Japanese controls or in a public SNP database (Table 2).

Families with novel possible pathogenic mutations

Here we report two novel missense mutations in two different patients (RP82K and RP85N), none of which was identified in 400 Japanese control alleles or a public SNP database. Patients RP82K and RP85N were born in the Kansai and Hiroshima areas, respectively, and were considered as isolated cases. RP82K and RP85N each had one novel missense mutation (p.V2386F and p.S4748F, respectively; Tables 1 and 2). The amino-acid residues of USH2A affected by the two novel missense mutations (V2386 and S4748) are not evolutionally conserved compared with those encoded by the orthologous genes of some vertebrate species (Table 2). For pathogenicity, the *in silico* analysis with at least two of the five different computational programs described these two mutations as pathogenic but did not exclude the possibility that these mutations were non-pathogenic (Table 2). Nevertheless, these two mutations were assigned to the group of possible pathogenic mutations, and further analyses are necessary to determine the precise nature of these mutations.

Summary of the possible non-pathogenic sequence alterations in the USH2A gene identified in this study

Overall, 78 possible sequence alterations were identified among 82 patients, and 7 of them have never been reported (Supplementary Table S2). These alterations did not fulfill the assessment of pathogenicity in this study (See Materials and methods); therefore, they were assigned to the group of possible non-pathogenic sequence alterations (Supplementary Table S2).

Clinical findings

The age of the four patients with one or two deleterious mutations ranged from 19 to 52 years at the time of diagnosis and from 37 to 60 years at the time of initial examination for this study. In addition, all the four patients had night blindness. The constriction of visual fields was found to be symmetric. The concentric constriction started in their twenties or thirties, and no effective residual visual field was observed after their fifties (Figures 1d–f). In all cases, the fundus displayed changes typical of RP, including attenuated retinal vessels and bone spicule deposits over 3601 of the fundus, all of which were increased in density with age. Spectral-domain OCT images also showed a marked reduction in retinal thickness resulting from the loss of photoreceptor layers. The photoreceptor inner segment/outer segment junction was either completely absent or was only detectable at the fovea of four subjects. The electroretinographic responses were consistent with severe generalized rod-cone dysfunction. On the other hand, none of these four patients had difficulties in daily conversation. Although the hearing tests for RP7H and RP10H yielded normal results (Figures 1g and h), the test for RP15H showed moderate hearing loss, suggesting USH2 (Figure 1i).

The age of the two patients with one possible mutation (RP82K and RP85N) was 40–46 years at the time of diagnosis and 50–66 years at the time of the initial examination for this study. Both patients had night blindness. The ocular findings including visual field, fundus, OCT and electroretinogram were compatible with the ocular findings in four patients with one or two deleterious mutations. Audiological examination, including pure-tone audiometry, was not performed, because the patients did not consent to the study.

DISCUSSION

This study is the first to analyze mutations in the USH2A gene among Japanese arRP patients with no systemic manifestations. In total, we detected 85 USH2A sequence alterations, of which 12 were novel. Among these 85 sequence alterations, 5 were classified as very likely pathogenic mutations (1 deletion, 2 splicing and 2 missense mutations), 2 were possibly pathogenic mutations (2 missense mutations) and 78 were possible non-pathogenic sequence alterations (Tables 1 and 2, and Supplementary Table S2). Among the 7 very likely and possible pathogenic mutations, a deletion and 4 missense mutations were novel, whereas the other 2 splicing mutations have been reported as disease causing in USH2 patients.[13,15,32,33] Similar to our previous study of Japanese USH2 patients, our current study did not detect the most prevalent mutations, p.E767fs and p.C759F, which account for approximately 23–39% and 1–14% of mutated alleles, respectively, in Caucasian individuals.[7–11] These results indicate that the profile of USH2A gene mutations differs largely between Japanese patients and previously reported Caucasian populations.[4–12,23,24,26–29]

We previously screened all EYS gene exons in 100 unrelated Japanese arRP patients with no systemic manifestations, with the exclusion of families showing obvious autosomal dominant inheritance, and, as a result, detected EYS gene mutations in 18–26% of the patients.[30] Excluding 18 RP patients with very likely pathogenic EYS gene mutations, 82 of these 100 patients were employed in this study. Among them, we found at least one very likely pathogenic or possible pathogenic USH2A gene mutation in six cases, of which three had two mutations and three had one mutation (Tables 1 and 2). Previous studies reported that 23 out of the 96 USH2 patients carried heterozygous USH2A gene mutations,[5] implying that this finding could be due to relatively large heterozygous deletions or deep intronic mutations.[34] In this study, because the direct sequences of PCR-amplified samples were used, we were not able to detect large deletions, insertions or rearrangements. In addition, because audiograms were not obtained from all patients with USH2A gene mutations, some of them may be USH2 patients without documented hearing loss. Therefore our results can only provide an estimate of the prevalence of USH2A mutations among Japanese arRP patients without documented systemic manifestations, including hearing loss. Considering only one or two deleterious mutations, the minimum observed prevalence of distinct USH2A gene mutations is 4% (4/100). If the patients with one heterogeneous possible pathogenic mutation are included in the estimation, the prevalence increases to 6% (6/100). A few previous studies on USH2A mutations employed large sets of non-syndromic RP patients, which accounted for 7–23% of arRP patients.[23,26–29] A possible reason for why the estimated prevalence in our study was lower than that of previous reports may be the fact that the Japanese population does not carry the p.E767fs or p.C759F mutation.

A previous report employing Japanese USH2 patients detected the c.8559-2A4G mutation in 4 out of the 19 cases, suggesting a possible frequent USH2A gene mutation among the Japanese population.[13,15] Here we identified that RP15H was homozygous for the c.8559-2A4G mutation, supporting the possibility of a frequent USH2A gene mutation among the Japanese population. To the best of our knowledge, this study is the first to report a patient homozygous for the c.8559-2A4G mutation. Although RP15H did not have documented hearing loss or communication problems, the hearing test demonstrated that the patient had moderate sensorineural hearing loss. A detailed medical interview revealed that the patient, a 61-year-old male, noticed a slight difficulty in hearing but considered it as age-appropriate. Elderly subjects, especially those aged 460 years, are affected by age-related hearing deterioration that makes it difficult to distinguish hearing loss from age-appropriate hearing. Therefore, auditory examination, including pure-tone audiometry, may be recommended for accurate evaluation of auditory function in elderly subjects. However, in our opinion, we could determine the presence or absence of hearing loss and select RP patients without auditory examination, because most of the subjects included in this study were middle-aged or younger.

In RP85N, we also found another missense mutation, c.2802T4G (p.C934W), which was previously reported as disease causing in a Chinese RP patient without hearing loss, although it has also been identified in two Chinese individuals among 100 normal Chinese controls.[25] p.C934W was also listed in the dbSNP database (rs201527662) and the 1000 Genomes database and was detected in 1 of the 400 control alleles in this study. Therefore we evaluated p.C934W as a possible non-pathogenic sequence alteration in this study (Supplementary Table S2).

In our previous report, we were unable to assign three sequence alterations (p.C691T, p.G2752R and p.T3747R) identified in patient C212 or determine which one of them was pathogenic.[13] In this study, we found that RP7H was heterozygous for p.G2752R, which was absent from 400 control alleles. However, because p.G2752R was described in the public SNP database (rs201863550) and was found to be genetically linked to the 3-bp in-frame deletion mutation p.E1199del in the patient's family (Figure 1a), it was assigned to the group of possible non-pathogenic sequence alterations. We speculate that patient C212 may be compound heterozygous for p.C691T and p.T3747R.

Studies have reported the phenotype of non-syndromic RP caused by USH2A gene mutations among the Caucasian.[35] The patients in this present study shared a relatively uniform phenotype, characterized by a symptom-free interval in the first and second decades of life, followed by a rapid decline in visual functions due to concentric constriction. The four patients with one or two deleterious mutations did not have any documented hearing loss or pronunciation problems. Although the hearing test results for RP7H and RP10H were normal (Figures 1g and h), the results for RP15H showed moderate hearing loss, indicating USH2 (Figure 1i). These findings suggest that RP without documented hearing loss occasionally includes moderate type of USH2.

In conclusion, the profile of USH2A gene mutations in arRP patients with no systemic manifestations differs largely between Japanese and Caucasian. Considering only one or two deleterious mutations, the observed prevalence of distinct USH2A gene mutations among Japanese arRP patients with no systemic manifestations was 4% (4/100). Based on these data, if both EYS and USH2A genes are analyzed among Japanese arRP patients with no systemic manifestations, gene defects could be detected in 22–32% of the patients in total (18–26% and 4–6%, respectively). We believe that screening for these two genes is effective for genetic testing and counseling of RP patients in Japan.

CONFLICT OF INTEREST

The authors declare no conflict of interest.

ACKNOWLEDGEMENTS

We thank the patients who participated in the study. This study was supported by research grants from the Ministry of Health, Labour and Welfare (Research on Measures for Intractable Diseases) and from Japan Society for the Promotion of Science (Grant-in-Aid for Scientific Research (C) 23592561 and Grant-in Aid for Young Scientists (B) 23791975).

---

1 Yan, D. & Liu, X. Z. Genetics and pathological mechanisms of Usher syndrome. J. Hum. Genet. 55, 327–335 (2010).
2 Rosenberg, T., Haim, M., Hauch, A. M. & Parving, A. The prevalence of Usher syndrome and other retinal dystrophy-hearing impairment associations. Clin. Genet. 51, 314–321 (1997).
3 Eudy, J. D., Weston, M. D., Yao, S., Hoover, D. M., Rehm, H. L., Ma-Edmonds, M. et al. Mutation of a gene encoding a protein with extracellular matrix motifs in Usher syndrome type IIa. Science 280, 1753–1757 (1998).
4 Weston, M. D., Eudy, J. D., Fujita, S., Yao, S., Usami, S., Cremers, C. et al. Genomic structure and identification of novel mutations in usherin, the gene responsible for Usher syndrome type IIa. Am. J. Hum. Genet. 66, 1199–1210 (2000).
5 Le Quesne Stabej, P., Saihan, Z., Rangesh, N., Steele-Stallard, H. B., Ambrose, J., Coffey, A. et al. Comprehensive sequence analysis of nine Usher syndrome genes in the UK National Collaborative Usher Study. J. Med. Genet. 49, 27–36 (2012).
6 Dreyer, B., Tranebjaerg, L., Brox, V., Rosenberg, T., Möller, C., Beneyto, M. et al. A common ancestral origin of the frequent and widespread 2299delG USH2A mutation. Am. J. Hum. Genet. 69, 228–234 (2001).
7 Bernal, S., Medà, C., Solans, T., Ayuso, C., Garcia-Sandoval, B., Valverde, D. et al. Clinical and genetic studies in Spanish patients with Usher syndrome type II: description of new mutations and evidence for a lack of genotype–phenotype correlation. Clin. Genet. 68, 204–214 (2005).
8 Aller, E., Jaijo, T., Beneyto, M., Nájera, C., Oltra, S., Ayuso, C. et al. Identification of 14 novel mutations in the long isoform of USH2A in Spanish patients with Usher syndrome type II. J. Med. Genet. 43, e55 (2006).
9 Baux, D., Larrieu, L., Blanchet, C., Hamel, C., Ben Salah, S., Vielle, A. et al. Molecular and in silico analyses of the full-length isoform of usherin identify new pathogenic alleles in Usher type II patients. Hum. Mutat. 28, 781–789 (2007).
10 Dreyer, B., Brox, V., Tranebjaerg, L., Rosenberg, T., Sadeghi, A. M., Möller, C. et al. Spectrum of USH2A mutations in Scandinavian patients with Usher syndrome type II. Hum. Mutat. 29, 451 (2008).
11 Yan, D., Ouyang, X., Patterson, D. M., Du, L. L., Jacobson, S. G. & Liu, X. Z. Mutation analysis in the long isoform of USH2A in American patients with Usher syndrome type II. J. Hum. Genet. 54, 732–738 (2009).
12 Aller, E., Larrieu, L., Jaijo, T., Baux, D., Espinós, C., González-Candelas, F. et al. The USH2A c.2299delG mutation: dating its common origin in a Southern European population. Eur. J. Hum. Genet. 18, 788–793 (2010).
13 Nakanishi, H., Ohtsubo, M., Iwasaki, S., Hotta, Y., Mizuta, K., Mineta, H. et al. Identification of 11 novel mutations in USH2A among Japanese patients with Usher syndrome type 2. Clin. Genet. 76, 383–391 (2009).
14 Nakanishi, H., Ohtsubo, M., Iwasaki, S., Hotta, Y., Mizuta, K., Mineta, H. et al. Hair roots as an mRNA source for mutation analysis of Usher syndrome-causing genes. J. Hum. Genet. 55, 701–703 (2010).
15 Nakanishi, H., Ohtsubo, M., Iwasaki, S., Hotta, Y., Usami, S., Mizuta, K. et al. Novel USH2A mutations in Japanese Usher syndrome type 2 patients: marked differences in the mutation spectrum between the Japanese and other populations. J. Hum. Genet. 56, 484–490 (2011).
16 Hayakawa, M., Fujiki, K., Kanai, A., Matsumura, M., Honda, Y., Sakaue, H. et al. Multicenter genetic study of retinitis pigmentosa in Japan: I. Genetic heterogeneity in typical retinitis pigmentosa. Jpn J. Ophthalmol. 41, 1–6 (1997).
17 Abd El-Aziz, M. M., Barragán, I., O'Driscoll, C. A., Goodstadt, L., Prigmore, E., Borrego, S. et al. EYS, encoding an ortholog of Drosophila spacemaker, is mutated in autosomal recessive retinitis pigmentosa. Nat. Genet. 40, 1285–1287 (2008).
18 Collin, R. W., Littink, K. W., Klevering, B. J., van den Born, L. I., Koenekoop, R. K., Zonneveld, M. N. et al. Identification of a 2 Mb human ortholog of Drosophila eyes shut/spacemaker that is mutated in patients with retinitis pigmentosa. Am. J. Hum. Genet. 83, 594–603 (2008).
19 Abd El-Aziz, M. M., O'Driscoll, C. A., Kaye, R. S., Barragán, I., El-Ashry, M. F., Borrego, S. et al. Identification of novel mutations in the ortholog of Drosophila eyes shut gene (EYS) causing autosomal recessive retinitis pigmentosa. Invest. Ophthalmol. Vis. Sci. 51, 4266–4272 (2010).
20 Audo, I., Sahel, J. A., Mohand-Saïd, S., Lancelot, M. E., Antonio, A., Moskova-Doumanova, V. et al. EYS is a major gene for rod-cone dystrophies in France. Hum. Mutat. 31, E1406–E1435 (2010).
21 Barragán, I., Borrego, S., Pieras, J. I., González-del Pozo, M., Santoyo, J., Ayuso, C. et al. Mutation spectrum of EYS in Spanish patients with autosomal recessive retinitis pigmentosa. Hum. Mutat. 31, E1772–E1800 (2010).
22 Littink, K. W., van den Born, L. I., Koenekoop, R. K., Collin, R. W., Zonneveld, M. N., Blokland, E. A. et al. Mutations in the EYS gene account for approximately 5% of autosomal recessive retinitis pigmentosa and cause a fairly homogeneous phenotype. Ophthalmology 117, 2026–2033 (2010).
23 Rivolta, C., Sweklo, E. A., Berson, E. L. & Dryja, T. P. Missense mutation in the USH2A gene: association with recessive retinitis pigmentosa without hearing loss. Am. J. Hum. Genet. 66, 1975–1978 (2000).
24 Aller, E., Nájera, C., Millán, J. M., Oltra, J. S., Pérez-Garrigues, H., Vilela, C. et al. Genetic analysis of 2299delG and C759F mutations (USH2A) in patients with visual and/or auditory impairments. Eur. J. Hum. Genet. 12, 407–410 (2004).
25 Xu, W., Dai, H., Lu, T., Zhang, X., Dong, B. & Li, Y. Seven novel mutations in the long isoform of the USH2A gene in Chinese families with non-syndromic retinitis pigmentosa and Usher syndrome Type II. Mol. Vis. 17, 1537–1552 (2011).
26 Bernal, S., Ayuso, C., Antiñolo, G., Gimenez, A., Borrego, S., Trujillo, M. J. et al. Mutations in USH2A in Spanish patients with autosomal recessive retinitis pigmentosa: high prevalence and phenotypic variation. J. Med. Genet. 40, e8 (2003).
27 Seyedahmadi, B. J., Rivolta, C., Keene, J. A., Berson, E. L. & Dryja, T. P. Comprehensive screening of the USH2A gene in Usher syndrome type II and non-syndromic recessive retinitis pigmentosa. Exp. Eye Res. 79, 167–173 (2004).
28 McGee, T. L., Seyedahmadi, B. J., Sweeney, M. O., Dryja, T. P. & Berson, E. L. Novel mutations in the long isoform of the USH2A gene in patients with Usher syndrome type II or non-syndromic retinitis pigmentosa. J. Med. Genet. 47, 499–506 (2010).
29 Ávila-Fernández, A., Cantalapiedra, D., Aller, E., Vallespín, E., Aguirre-Lambán, J., Blanco-Kelly, F. et al. Mutation analysis of 272 Spanish families affected by autosomal recessive retinitis pigmentosa using a genotyping microarray. Mol. Vis. 16, 2550–2558 (2010).
30 Hosono, K., Ishigami, C., Takahashi, M., Park, D. H., Hirami, Y., Nakanishi, H. et al. Two novel mutations in the EYS gene are possible major causes of autosomal recessive retinitis pigmentosa in the Japanese population. PLoS ONE 7, e31036 (2012).
31 Adato, A., Lefèvre, G., Delprat, B., Michel, V., Michalski, N., Chardenoux, S. et al. Usherin, the defective protein in Usher syndrome type IIA, is likely to be a component

of interstereocilia ankle links in the inner ear sensory cells. Hum. Mol. Genet. 14, 3921–3932 (2005).

32 Dai, H., Zhang, X., Zhao, X., Deng, T., Dong, B., Wang, J. et al. Identification of five novel mutations in the long isoform of the USH2A gene in Chinese families with Usher syndrome type II. Mol. Vis. 14, 2067–2075 (2008).

33 Le Guédard-Méreuze, S., Vaché, C., Baux, D., Faugère, V., Larrieu, L., Abadie, C. et al. Ex vivo splicing assays of mutations at noncanonical positions of splice sites in USHER genes. Hum. Mutat. 31, 347–355 (2010).

34 Steele-Stallard, H. B., Le Quesne Stabej, P., Lenassi, E., Luxon, L. M., Claustres, M., Roux, A. F. et al. Screening for duplications, deletions and a common intronic mutation detects 35% of second mutations in patients with USH2A monoallelic mutations on Sanger sequencing. Orphanet. J. Rare Dis. 8, 122 (2013).

35 Sandberg, M. A., Rosner, B., Weigel-DiFranco, C., McGee, T. L., Dryja, T. P. & Berson, E. L. Disease course in patients with autosomal recessive retinitis pigmentosa due to the USH2A gene. Invest. Ophthalmol. Vis. Sci. 49, 5532–5539 (2008).

Supplementary Information accompanies the paper on Journal of Human Genetics website (http://www.nature.com/jhg)

Fluorescein angiographic observations of peripheral retinal vessel growth in infants after intravitreal injection of bevacizumab as sole therapy for zone I and posterior zone II retinopathy of prematurity

Sjakon G Tahija,[1] Rini Hersetyati,[1] Geoffrey C Lam,[2] Shunji Kusaka,[3] Paul G McMenamin[4]

[1]Klinik Mata Nusantara, Jakarta, Indonesia
[2]Department of Ophthalmology, Princess Margaret Hospital for Children, University of Western Australia, Perth, Australia
[3]Department of Ophthalmology, Sakai Hospital, Kinki University Faculty of Medicine, Osaka, Japan
[4]Faculty of Medicine, Nursing and Health Sciences, Department of Anatomy and Developmental Biology, Monash University, Melbourne, Australia

Correspondence to
Sjakon G Tahija, Klinik Mata Nusantara, Jalan R A Kartini No. 99, Jakarta 12440, Indonesia; sjakon.tahija@gmail.com

Received 31 July 2013
Revised 17 November 2013
Accepted 11 December 2013
Published Online First 8 January 2014

To cite: Tahija SG, Hersetyati R, Lam GC, et al. Br J Ophthalmol 2014;98:507–512.

ABSTRACT

Aim To evaluate vascularisation of the peripheral retina using fluorescein angiography (FA) digital recordings of infants who had been treated with intravitreal bevacizumab (IVB) as sole therapy for zone I and posterior zone II retinopathy of prematurity (ROP).

Methods A retrospective evaluation was performed of medical records, RetCam fundus images and RetCam fluorescein angiogram videos of 10 neonates (20 eyes) who received intravitreal bevacizumab injections as the only treatment for zone I and posterior zone II ROP between August 2007 and November 2012.

Results All eyes had initial resolution of posterior disease after IVB injection as documented by RetCam colour fundus photographs. Using a distance of 2 disc diameters from the ora serrata to vascular termini as the upper limit of allowable avascular retina in children, the FA of these infants demonstrated that 11 of 20 eyes had not achieved normal retinal vascularisation.

Conclusions Although bevacizumab appears effective in bringing resolution of zone I and posterior zone II ROP and allowing growth of peripheral retinal vessels, in our series of 20 eyes, complete normal peripheral retinal vascularisation was not achieved in half of the patients.

INTRODUCTION

The incidence of retinopathy of prematurity (ROP) has increased globally due to advances in the care of very-low-weight premature infants. In a recent review on the incidence of ROP,[1] the incidence of all ROP was found to be approximately 60% for infants less than 1500 g in high-income countries. Most cases of ROP regress spontaneously; however, more severe cases need treatment to prevent blindness. In middle-income countries greater numbers of premature infants are being saved; however, screening and treatment of severe ROP is often lacking, which in turn is leading to an increase in blindness due to ROP. Six different studies in India have reported the incidence of severe ROP, ranging from 6.3% to 44.9%.[1] Aggressive posterior ROP (AP-ROP) is a severe form of ROP located in zone I or posterior zone II of the retina, and is characterised by rapid progression to advanced stages of disease.[2 3] Even with early laser treatment as suggested in the 'Early Treatment for ROP' (ETROP) study,[4] poor outcomes are still frequently seen in AP-ROP.[5 6] Recently, there have been several encouraging reports of the use of intravitreal

Table 1 Patient characteristics

Patient no.	GA in weeks PMA	Weight (g)	Diagnosis at IVB	PMA at IVB	PMA at last FA (weeks)	Weeks IVB to Last FA	Eye	Avascular peripheral retina, Y/N	Leakage, Y/N
1	28	1200	AP-ROP	37	64	27	Right	N	N
							Left	N	N
2	35	1700	AP-ROP	37	64	27	Right	Y	Y
							Left	Y	Y
3	28	1700	POST-ROP	35	46	42	Right	N	N
							Left	N	N
4	31	1700	AP-ROP	38	84	46	Right	N	N
							Left	N	N
5	28	1200	AP-ROP	32	78	46	Right	N	N
							Left	N	N
6	30	1700	AP-ROP	34	92	58	Right	Y	Y
							Left	Y	Y
7	30	1200	POST-ROP	37	123	86	Right	Y	Y
							Left	N	N
8	30	1150	POST-ROP	34	123	89	Right	Y	Y
							Left	Y	Y
9	29	1200	AP-ROP	36	202	166	Right	Y	N
							Left	Y	N
10	31	1182	AP-ROP	35	259	224	Right	Y	Y
							Left	Y	Y

AP-ROP, aggressive posterior retinopathy of prematurity; FA, fluorescein angiogram; GA, gestational age; IVB, intravitreal bevacizumab injection; PMA, postmenstrual age; POST-ROP, posterior retinopathy of prematurity.

bevacizumab as an off-label first line of treatment in neonates with severe ROP.[7–13]

One of the reported benefits of intravitreal bevacizumab as treatment for zone I and posterior zone II ROP is that the development of peripheral retinal vessels continues after treatment, whereas conventional laser therapy leads to permanent destruction of the peripheral retina.[14] In the present work, we report on the results of fluorescein angiography (FA) performed on 10 neonates (20 eyes), which we had treated up to 5 years previously with intravitreal bevacizumab as sole therapy for zone I and posterior zone II ROP. We have evaluated the extent of peripheral retinal vessel growth and remaining avascular retina after a single injection of intravitreal bevacizumab.

All cases were treated and examined at Klinik Mata Nusantara (KMN), an eye hospital in Jakarta, Indonesia. This retrospective study was approved by the Medical Committee of KMN.

Patients

In this retrospective study, we reviewed the records of 17 neonates who had FA after IVB for zone I and posterior zone II ROP. For the purposes of this study, we included 10 neonates who had achieved regression of posterior disease in both eyes with a single injection of bevacizumab and had a minimal follow-up period of 24 weeks after IVB. We excluded six neonates who did not achieve resolution of posterior disease or needed additional treatment before resolution of ROP: one neonate with AP-ROP had resolution of zone I ROP in one eye but developed stage 5 ROP in the other eye; another neonate with AP-ROP needed a second IVB injection to achieve resolution of zone I disease in both eyes; two neonates had not achieved resolution of posterior zone II disease at the last follow-up, and another two neonates needed vitrectomy. One neonate had to be excluded because the child was lost to follow-up after 10 weeks.

At time of IVB, 7 of these 10 cases had been diagnosed as having AP-ROP and 3 cases as having posterior zone II ROP without plus disease. When FA was performed more than once, we evaluated the last FA. Fluorescein angiograms of 10 neonates (20 eyes) were thus evaluated. These neonates had been treated with IVB as a first-line therapy between August 2007 and November 2012. In all cases, regression of posterior disease was documented by RetCam fundus photographs. Gestational age at birth ranged from 28–35 weeks post menstrual age (PMA) (mean=30 weeks), birth weight ranged from 1150–1700 g (mean=1393.2 g), PMA at time of IVB ranged from 32–38

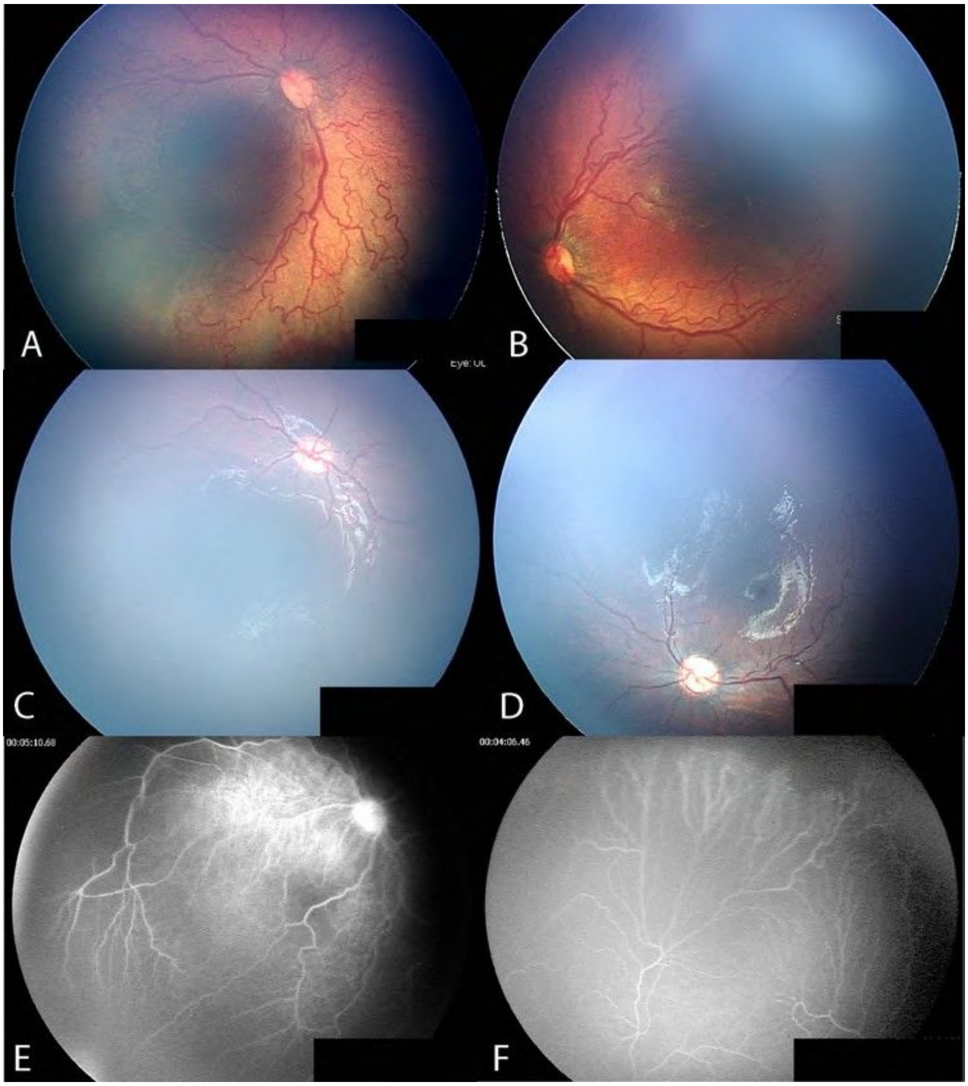

Figure 1 Case no. 5: aggressive posterior retinopathy of prematurity. Posterior fundus before intravitreal bevacizumab injection (IVB) (A,B); after injection of IVB (C,D); fluorescein angiography 46 weeks after IVB, demonstrates less than 2 disc diameters (DD) of avascular retina (E,F).

weeks (mean=35.5 weeks). The interval between treatment with IVB and FA ranged from 27–224 weeks.

RetCam FA was performed under general anaesthesia in an operating room at KMN. A 10% solution of fluorescein was injected intravenously at a dose of 0.1 mL/kg followed by an isotonic saline flush. None of the patients experienced systemic complications related to FA.

METHODS

A retrospective analysis of the medical records of all infants that had been treated with IVB at KMN was performed. We extracted medical records of infants who had demonstrated resolution of zone I and posterior zone II ROP with IVB as sole treatment as documented by RetCam colour fundus photographs. Although we have been treating zone I and posterior zone II ROP with IVB since 2006, RetCam FA only became available to us in the latter part of 2011. The medical records of 10 neonates (20 eyes) who had RetCam FA after IVB were used to document resolution of posterior disease. We reviewed the fluorescein digital videos of these 20 eyes to evaluate the extent of remaining avascular retina.

An estimate of the peripheral retinal non-perfusion in the infants was compared to previously published descriptions of FA in children.[15] Blair et al[15] concluded that avascular retina extending more than 2 disc diameters (DD) from the ora serrata should be considered abnormal.

RESULTS

General patterns

Digital video recordings of RetCam FA allowed us to distinctly visualise the anterior border of retinal vessel growth and the vascular–avascular junction of 10 infants who had achieved RetCam documented resolution of posterior disease after treatment with IVB for zone I and posterior zone II ROP. Of 20 eyes examined with FA, 11 had incomplete peripheral retina vascularisation (table 1). Of these 11 eyes, 9 had fluorescein leakage at the vascular–avascular junction. The IVB-FA interval of these eyes with incomplete vascularisation ranged from 27 to 224 weeks (median 87.5 weeks). At the time of IVB, the diagnosis in these children with incomplete retinal vascularisation was AP-ROP in seven cases and posterior zone II ROP without plus disease in three cases. The birth weight of these infants ranged

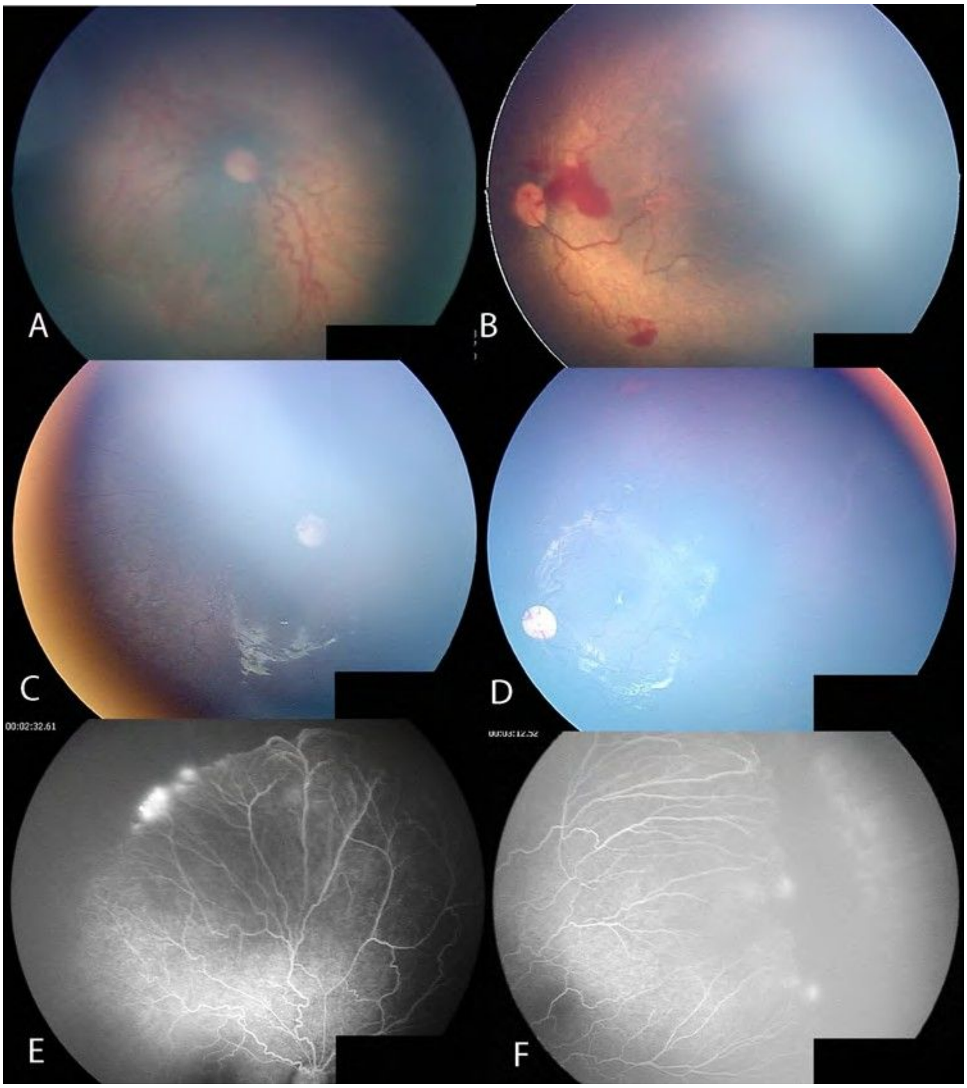

Figure 2 Case no. 10: aggressive posterior retinopathy of prematurity. Posterior fundus before intravitreal bevacizumab injection (IVB) (A,B); resolution of posterior disease after IVB (C,D). The peripheral retina remains avascular with fluorescein leakage more than 4 years after IVB (E,F).

from 1150–1700 g with a mean of 1393.2 g. The gestational age ranged from 28–35 weeks with a mean of 30 weeks PMA.

Case reports

Case no. 5 was a case of AP-ROP (figure 1A,B), which resolved after a single injection of IVB (figure 1C,D). FA performed at 46 weeks after IVB (figure 1E,F) shows less than 2 DD of avascular peripheral retina and no vascular leakage.

Case no. 10 was a case of AP-ROP (figure 2A,B), where there was resolution of posterior disease after IVB (figure 2C,D) but the peripheral retina remained avascular with fluorescein leakage at the vascular–avascular junction more than 4 years after IVB treatment (figure 2E,F).

Cases no. 8 and no. 7 are twin neonates who presented with posterior ROP (figures 3A,B and 4A,B, respectively). Case no. 8 had avascular peripheral retinas without fluorescein leakage 21 weeks after IVB treatment (figure 3C,D). FA at 89 weeks after IVB demonstrated that the retina in both eyes remained avascular with fluorescein leakage at the vascular–avascular junction (figure 3E,F).

Case no. 7 had avascular peripheral retinas without leakage 18 weeks after IVB treatment (figure 4C,D). FA performed at 86 weeks after IVB demonstrated that the left peripheral retina was vascularised while the right peripheral retina remained unvascularised and had fluorescein leakage at the vascular–avascular junction (figure 4E,F).

DISCUSSION

Although numerous authors have reported their experience using bevacizumab in the management of ROP,[9 10 13] at the time of writing there has been only one controlled trial comparing intravitreal bevacizumab to conventional treatment of ROP, the BEAT ROP trial.[10] In that study, the authors concluded that development of peripheral retinal vessels continued after treatment with IVB. In our study, we aimed to evaluate the extent of peripheral retinal growth in eyes with zone I and posterior zone II ROP that were treated with a single injection of intravitreal bevacizumab. Fluorescein angiographic imaging was chosen, as it allowed us to accurately visualise the extent of peripheral retinal vessel growth in these eyes.

In our series of 20 eyes from 10 patients we found that, despite resolution of zone I and posterior zone II ROP after a single injection of IVB, the peripheral retina remained incompletely vascularised in 11 (55%) of the eyes. In addition, we

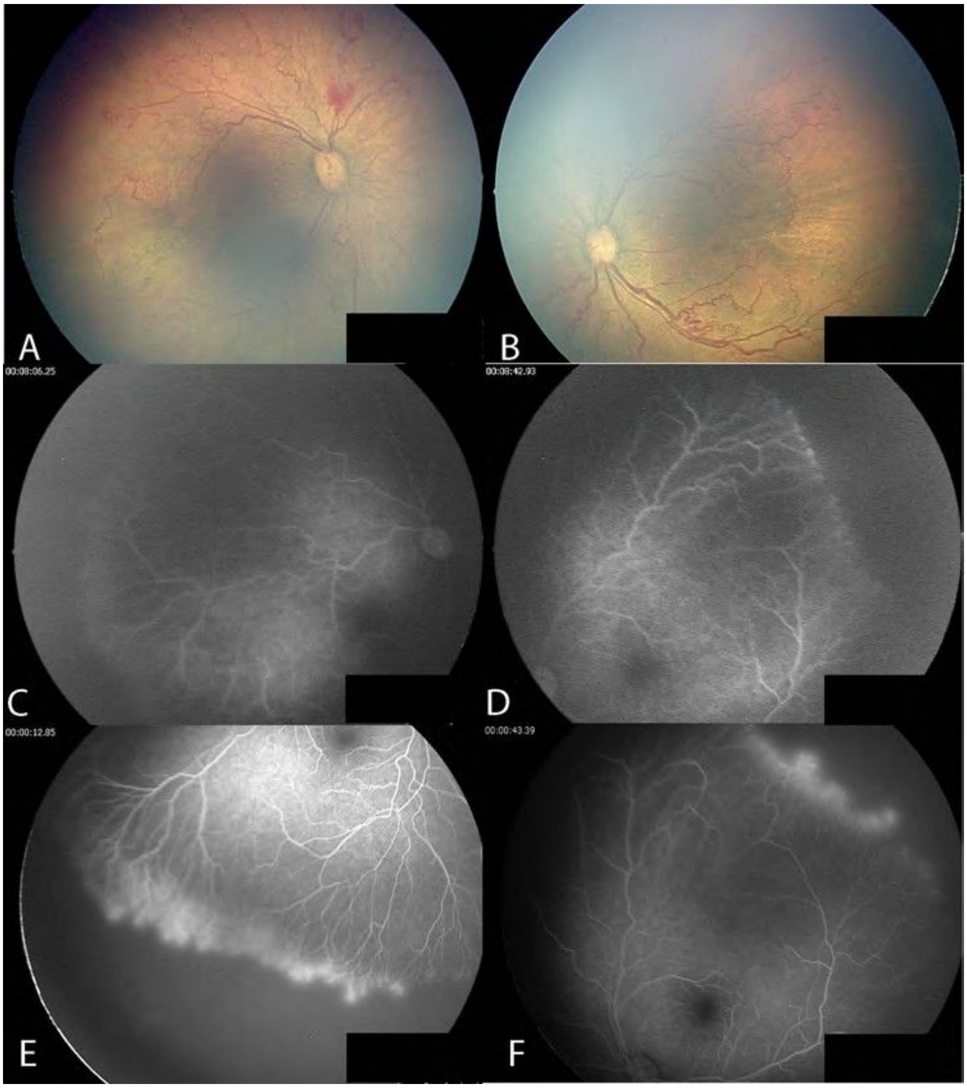

Figure 3 Case no. 8: posterior retinopathy of prematurity. Posterior fundus before intravitreal bevacizumab injection (IVB) (A,B); avascular peripheral retina without leakage 21 weeks after IVB (C,D); avascular peripheral retina with fluorescein leakage in both eyes 89 weeks after IVB (E,F).

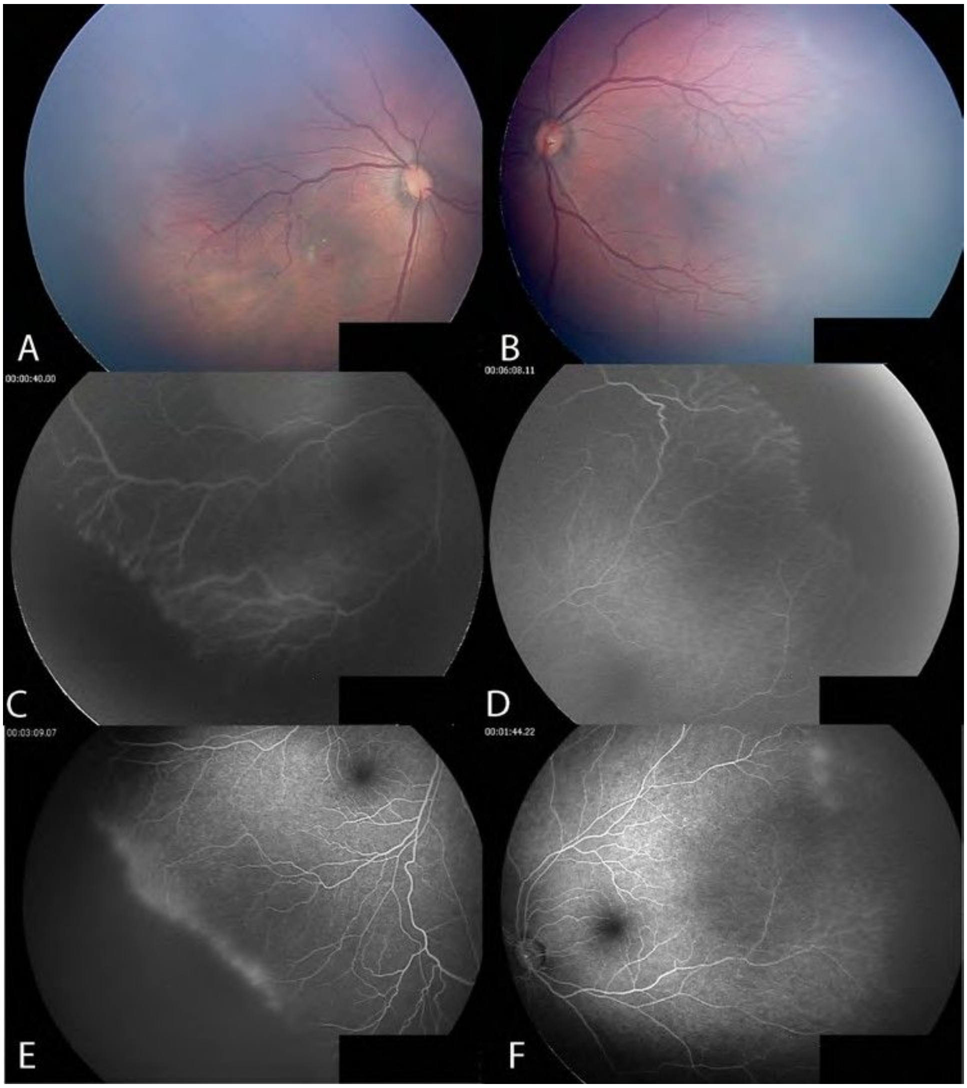

Figure 4 Case no. 7: posterior retinopathy of prematurity, the twin sister of case no. 8. Posterior fundus before intravitreal bevacizumab injection (IVB) (A,B); avascular peripheral retina without fluorescein leakage in both eyes 18 weeks after IVB (C,D); fully vascularised peripheral retina in the left eye, and avascular retina with fluorescein leakage in the right eye 86 weeks after IVB (E,F).

observed fluorescein leakage at the vascular–avascular junction in 9 of these 11 eyes with avascular peripheral retina (82% of total).

The safety of FA in neonates has been established since 2006.[16] [17] In 2011, Lepore et al, published an atlas of fluorescein angiographic findings in eyes undergoing laser treatment for ROP. The authors concluded that FA clearly defined the zone I junction between vascularised and non-vascularised retina.[18] Recently, Velia et al,[19] investigated retinal development in premature infants using FA and revealed vascular changes in ROP eyes, such as loss of the normal dichotomous branching, vessel branching at the junction between vascular and avascular retina, arteriovenous shunts, and other abnormalities that were thought to be related to the immaturity of the vascular network. We observed similar findings such as irregular branching of large arterioles and circumferential vessel formation (figure 4C), and fluorescein leakage (figure 3E,F). Of significance, Velia et al[19] determined that dye leakage is the most significant sign of progression to severe ROP.

Blair et al[15] estimated the normal extent of peripheral retinal non-perfusion in normal children at various postnatal ages. In that study, the authors—using RetCam FA on 33 eyes from 31 normal children—estimated avascular retina using scleral indentation during FA to determine the distance of vascular termini to the ora serrata. None of these normal eyes had a distance greater than 1.5 disk diameters up to 13 years of age. The authors concluded that, conservatively, a distance of greater than 2 DD from the ora to the vascularised retinal margin should be considered abnormal. This data provided a useful practical standard to document the extent of peripheral retinal vascular development when screening infants with ROP using FA.

All neonates in our study had resolution of zone I and posterior zone II ROP documented by RetCam colour imaging at the time FA was performed. Previous studies have reported the favourable response of zone I and posterior zone II ROP to intravitreal injections of bevacizumab.[10] [20] Our study focuses on the extent of normal retinal vessel growth in the peripheral retina in cases where zone I and posterior zone II ROP had been deemed to have responded favourably to a single injection of IVB as sole treatment.[10] [14] [21] It is often difficult to accurately determine the vascular–avascular junction in the peripheral retina using indirect ophthalmoscopy or colour RetCam images. We therefore chose to use FA, which allows accurate visualisation of the outer borders of the vascular retina.[18] [19]

The birth weight and PMA of the neonates with zone I and posterior zone II disease in our series is higher than reports from similar series from developed countries. Carden et al[22] reported that 58 infants referred to the National Hospital of Paediatrics in Hanoi, Vietnam with ROP had birth weights ranging from 800–1900 g and gestational ages ranging from 28–35 weeks. Gu et al[23] reported birth weights of infants with ROP in China ranging from 1501–2000 g. Risk factors reported to cause ROP in more mature neonates are septicaemia and poorly controlled oxygen therapy.

Our study showed that 55% of eyes continued to have incomplete vascularisation at time of follow-up examination including up to 259 weeks after birth. In the eyes with the longest IVB-FA interval (case no. 10) there were also numerous areas of lattice degeneration, which may increase the future risk for development of retinal tears and complications after cataract surgery, as has been previously reported.[24 25] Although we did not see ridges or extraretinal fibrovascular proliferation in these 11 eyes, there was fluorescein leakage at the vascular–avascular border in 9 eyes. This may be important, as fluorescein leakage has previously been reported to be a sign of progression to severe ROP.[19]

In conclusion, our study demonstrates that although intravitreal bevacizumab can be very effective in causing resolution of zone I and posterior zone II ROP, ophthalmologists should remain cautious as infants may remain at risk due to avascular peripheral retinas even many years after treatment. Careful examination using FA allows accurate visualisation of risk factors such as the extent of avascular retina and the presence of dye leakage.

Contributors All work carried out for this study was performed by the listed authors. Review of medical records and fluorescein angiogram digital recordings by SGT and RH. Clinical science and editorial input by GCL (pediatric ophthalmologist) and SK. PGM went over the manuscript numerous times to provide editorial input.

Competing interests None.

Provenance and peer review Not commissioned; externally peer reviewed.

REFERENCES

1 Zin A, Gole GA. Retinopathy of prematurity-incidence today. Clin Perinatol 2013;40:185–200.
2 Katz X, Kychenthal A, Dorta P. Zone I retinopathy of prematurity. J Aapos 2000;4:373–6.
3 Drenser KA, Trese MT, Capone A Jr. Aggressive posterior retinopathy of prematurity. Retina 2010;30(4 Suppl):S37–40.
4 Good WV, Hardy RJ. The multicenter study of Early Treatment for Retinopathy of Prematurity (ETROP). Ophthalmology 2001;108:1013–14.
5 Azuma N, Ishikawa K, Hama Y, et al. Early vitreous surgery for aggressive posterior retinopathy of prematurity. Am J Ophthalmol 2006;142:636–43.
6 Vinekar A, Trese MT, Capone A Jr. Evolution of retinal detachment in posterior retinopathy of prematurity: impact on treatment approach. Am J Ophthalmol 2008;145:548–55.
7 Azad R, Chandra P. Intravitreal bevacizumab in aggressive posterior retinopathy of prematurity. Indian J Ophthalmol 2007;55:319; author reply 20.
8 Chung EJ, Kim JH, Ahn HS, et al. Combination of laser photocoagulation and intravitreal bevacizumab (Avastin) for aggressive zone I retinopathy of prematurity. Graefes Arch Clin Exp Ophthalmol 2007;245:1727–30.
9 Lalwani GA, Berrocal AM, Murray TG, et al. Off-label use of intravitreal bevacizumab (Avastin) for salvage treatment in progressive threshold retinopathy of prematurity. Retina 2008;28:S13–18.
10 Mintz-Hittner HA, Kuffel RR Jr. Intravitreal injection of bevacizumab (avastin) for treatment of stage 3 retinopathy of prematurity in zone I or posterior zone II. Retina 2008;28:831–8.
11 Quiroz-Mercado H, Martinez Castellanos M, Hernandez-Rojas M, et al. Antiangiogenic therapy with intravitreal bevacizumab for retinopathy of prematurity. Retina 2008;28:S19–25.
12 Travassos A, Teixeira S, Ferreira P, et al. Intravitreal bevacizumab in aggressive posterior retinopathy of prematurity. Ophthalmic Surg Lasers Imaging 2007;38:233–7.
13 Kusaka S, Shima C, Wada K, et al. Efficacy of intravitreal injection of bevacizumab for severe retinopathy of prematurity: a pilot study. Br J Ophthalmol 2008;92:1450–5.
14 Mintz-Hittner HA, Kennedy KA, Chuang AZ. Efficacy of intravitreal bevacizumab for stage 3+ retinopathy of prematurity. N Engl J Med 2011;364:603–15.
15 Blair MP, Shapiro MJ, Hartnett ME. Fluorescein angiography to estimate normal peripheral retinal nonperfusion in children. J Aapos 2012;16:234–7.
16 Ng EY, Lanigan B, O'Keefe M. Fundus fluorescein angiography in the screening for and management of retinopathy of prematurity. J Pediatr Ophthalmol Strabismus 2006;43:85–90.
17 Wagner RS. Fundus fluorescein angiography in retinopathy of prematurity. J Pediatr Ophthalmol Strabismus 2006;43:78.
18 Lepore D, Molle F, Pagliara MM, et al. Atlas of fluorescein angiographic findings in eyes undergoing laser for retinopathy of prematurity. Ophthalmology 2011;118:168–75.
19 Velia P, Antonio B, Patrizia P, et al. Fluorescein angiography and retinal vascular development in premature infants. J Matern Fetal Neonatal Med 2012;25(Suppl 3):53–6.
20 Dorta P, Kychenthal A. Treatment of type 1 retinopathy of prematurity with intravitreal bevacizumab (Avastin). Retina 2010;30(4 Suppl):S24–31.
21 Harder BC, von Baltz S, Jonas JB, et al. Intravitreal bevacizumab for retinopathy of prematurity. J Ocul Pharmacol Ther 2011;27:623–7.
22 Carden SM, Luu LN, Nguyen TX, et al. Retinopathy of prematurity: postmenstrual age at threshold in a transitional economy is similar to that in developed countries. Clin Experiment Ophthalmol 2008;36:159–61.
23 Gu MH, Jin J, Yuan TM, et al. Risk factors and outcomes for retinopathy of prematurity in neonatal infants with a birth weight of 1,501–2,000 g in a Chinese Neonatal Unit. Med Princ Pract 2011;20:244–7.
24 Kaiser RS, Fenton GL, Tasman W, et al. Adult retinopathy of prematurity: retinal complications from cataract surgery. Am J Ophthalmol 2008;145:729–35.
25 Kaiser RS, Trese MT, Williams GA, et al. Adult retinopathy of prematurity: outcomes of rhegmatogenous retinal detachments and retinal tears. Ophthalmology 2001;108:1647–53.

Fluorescein angiographic observations of peripheral retinal vessel growth in infants after intravitreal injection of bevacizumab as sole therapy for zone I and posterior zone II retinopathy of prematurity

Sjakon G Tahija, Rini Hersetyati, Geoffrey C Lam, et al.

Br J Ophthalmol 2014 98: 507-512 originally published online January 8, 2014
doi: 10.1136/bjophthalmol-2013-304109

Efficacy of Short-term Postoperative Perfluoro-n-octane Tamponade for Pediatric Complex Retinal Detachment

AYAKO IMAIZUMI, SHUNJI KUSAKA, HIROE NOGUCHI, YOSHIKAZU SHIMOMURA, AND
SHOICHI SAWAGUCHI

- PURPOSE: To evaluate the efficacy of perfluoro-n-octane as a postoperative short-term tamponade after vitrectomy in pediatric cases with complex retinal detachment (RD) and proliferative vitreoretinopathy (PVR).
- DESIGN: Prospective, noncomparative, interventional case series.
- METHODS: The medical records of 10 eyes of 9 children (6 boys and 3 girls), whose age ranged from 3 months to 11 years, with a median of 7.5 months, were reviewed. The cause of the PVR was retinopathy of prematurity (7 eyes of 6 patients); familial exudative vitreoretinopathy; or tractional RD associated with congenital optic nerve anomalies,[1] and persistent fetal vasculature. Perfluoro-n-octane was injected into the eyes at the primary surgery in 2 eyes and at the repeat surgeries in 8 eyes. The perfluoro-n-octane was removed after 1 to 4 postoperative weeks. The patients were followed for 5 to 43 months.
- RESULTS: At the last examination, the retinas were reattached in 8 eyes (80%). In the other two eyes, a retinal attachment was not obtained. Postoperatively, the best-corrected visual acuity improved from hand motion to 0.1 in 1 eye and could not be measured in the other 9 patients because of their ages. No apparent adverse events related to the use of perfluoro-n-octane were noted.
- CONCLUSIONS: Although cautions should be exercised regarding potential mechanical retinal injuries by heavy liquids in the eye, short-term perfluoro-n-octane tamponade was effective in pediatric cases with severe PVR in which retinal reattachment is considered to be difficult with conventional gas or silicone oil tamponade. (Am J Ophthalmol 2014;157:384–389. © 2014 by Elsevier Inc. All rights reserved.)

PEDIATRIC RETINAL DETACHMENTS (RDS) HAVE many characteristics that are distinct from adult RDs. One of these characteristics is that they are more often associated with congenital or developmental abnormalities, such as familial exudative vitreoretinopathy (FEVR), tractional RD associated with congenital optic nerve anomalies, persistent fetal vasculature, or retinopathy of prematurity (ROP), than are adult RDs. One other characteristic is late detection, which often means that the RDs are longstanding, have macular involvement and are associated with proliferative vitreoretinopathy (PVR).[1] These features make pediatric RDs complex and difficult to treat satisfactorily.

Long-acting gas and silicone oils are commonly used for postoperative tamponade to treat the severe rhegmatogenous retinal detachments (RRDs) associated with PVR. However, their effectiveness is limited when proliferative changes exist in the inferior retina because of their low specific gravity. Because of this, patients are requested to maintain a prone position for several days to weeks postoperatively. However, it is difficult to have an infant maintain this position for any length of time. For these cases, perfluoro-n-octane (C_8F_{18}), which has a specific gravity of 1.75, greater than that of water, theoretically should be more effective as a tamponade.

We report the surgical results of pediatric complex RRDs with PVR that underwent vitrectomy using perfluoro-n-octane as a short-term postoperative tamponade.

METHODS

THE MULTICENTER STUDY WAS PERFORMED IN ACCORDANCE with the tenets of the Declaration of Helsinki. The Institutional Review Board of the Naha City Hospital and Sakai Hospital Kinki University Faculty of Medicine approved this prospective study before the beginning of the study, and a written informed consent was obtained from the parents of all patients. The protocol of this study was in compliance with Health Insurance Portability and Accountability Act requirements.

A perfluoro-n-octane tamponade was used in 10 eyes of 9 young patients to treat various vitreoretinal disorders at the Naha City Hospital and the Sakai Hospital Kinki University Faculty of Medicine between August 2009 and January 2013. Of those patients, 1 eye of 1 patient had FEVR, 1 eye of 1 patient had an RD associated with congenital optic nerve anomalies,[2] 1 eye of 1 patient had persistent fetal vasculature, 6 eyes of 5 patients had stage 5 retinopathy of prematurity (ROP), and 1 eye of 1 patient had stage

Accepted for publication Oct 7, 2013.

From the Department of Ophthalmology, Naha City Hospital, Okinawa, Japan (A.I., H.N.); the Department of Ophthalmology, Sakai Hospital Kinki University Faculty of Medicine, Osaka, Japan (S.K., Y.S.); and the Department of Ophthalmology, Graduate School of Medicine, University of the Ryukyus, Okinawa, Japan (A.I., S.S.).

Inquiries to Shunji Kusaka, Department of Ophthalmology, Sakai Hospital Kinki University Faculty of Medicine, 2-7-1 Harayamadai, Minami-Ku, Sakai, 590-0132 Osaka, Japan; e-mail: kusaka-ns@umin.net

0002-9394/$36.00
http://dx.doi.org/10.1016/j.ajo.2013.10.002

TABLE. Characteristics of Patients and Results with Short-term Postoperative Perfluoro-n-octane Tamponade for Pediatric Proliferative Vitreoretinopathy

No.	Sex	Age	Disease	Number of vitrectomy before PFO tamponade	Period of PFO tamponade (weeks)	Anatomic results
1	Boy	11 Y	FEVR, PVR	5	3	RA
2	Girl	8 M	Stage 5 ROP	1	2	RA
		8 M	Stage 5 ROP	1	2	RA
3	Boy	3 M	Stage 5 ROP	1	2	RA
4	Boy	3 M	Stage 5 ROP	1	2	RA
5	Boy	1 Y	TRD associated with congenital optic nerve anomalies[1]	0	1	No RA (redetachment after 2 months of RA)
6	Boy	6 M	Stage 5 ROP	2	1	RA
7	Boy	16 M	PFV, PVR	1	3	RA
8	Girl	4 M	Stage 4 B ROP	0	4	RA
9	Girl	4 M	Stage 5 ROP	1	1	No RA

FEVR ¼ familial exudative vitreoretinopathy; M ¼ months-of-age; PFO ¼ perfluoro-n-octane; PFV ¼ persistent fetal vasculature; PVR ¼ proliferative vitreoretinopathy; RA ¼ retinal attachment; ROP ¼ retinopathy of prematurity; TRD ¼ tractional retinal detachment; Y ¼ years-of-age.

4B ROP. The ages of the patients ranged from 3 months to 11 years, with a median of 7.5 months (Table). Of the patients, 3 were female children and 6 were male children.

Perfluoro-n-octane was used in 2 eyes at the primary operation; 1 with RD associated with congenital optic nerve anomalies and 1 with stage 4B ROP. Perfluoro-n-octane was used in the 8 other eyes at the time of the reoperation. The follow-up-period ranged from 5 to 43 months, with a median of 19.5 months.

All surgeries were performed by one surgeon (S.K.). A standard 3-port pars plana vitrectomy using 23-gauge instruments was performed. Pars plana lensectomy, membrane segmentation, delamination, and peeling were performed, depending on the condition of the retina. If the retinal detachment had a closed funnel shape in the ROP cases, a vitreous scissors and/or forceps were used to cut the anterior vitreous fibers and proliferative membranes to gain access to the midvitreous cavity and the optic disc. An encircling #240 silicone band was placed at the equator in 3 eyes: 1 eye with FEVR, 1 eye with RD associated with congenital optic nerve anomalies, and 1 eye with persistent fetal vasculature. The crystalline lens was removed in all of the cases.

During the reoperations, fibrous membranes were removed as completely as possible to relieve the traction on the retina. Then, perfluoro-n-octane was injected slowly through a 25- or 27-gauge blunt needle to fill the vitreous cavity with a single bubble. This was followed by laser ablation around the retinal breaks. The perfluoro-n-octane was left in the eye, and the sclerotomy sites were securely sutured.

The parents of the patients were instructed to try to keep their children in a supine or sitting position as much as possible for 1 to 4 weeks. Postoperatively, fundus examinations, slit-lamp examinations, and intraocular pressure measurements using iCare (Tiolat, Helsinki, Finland) or Tono-Pen XL (Reichert, Depew, NY, USA) were performed periodically. Then vitrectomy, with an exchange of the perfluoro-n-octane by balanced salt solution (BSS plus) was performed with care being taken to ensure that all of the perfluoro-n-octane was removed. To remove as much of the perfluoro-n-octane as possible, we first aspirated the perfluoro-n-octane with BSS plus irrigation and then with air irrigation. A small amount of BSS plus was then injected onto the posterior retina. This then made the residual perfluoro-n-octane visible and easy to remove. If proliferative membranes were found, they were removed, and 10% to 20% sulfur hexafluoride (SF_6) or 10% perfluoropropane (C_3F_8) was used, according to the surgeon's decision.

In all patients, the perfluoro-n-octane tamponade duration was 1 to 2 weeks; however, it was delayed for 1 to 2 additional weeks in 3 eyes of 3 children because of their general medical conditions. One of these cases was an 11-year-old boy. The anatomic status of the retina, visual outcomes, and complications were assessed at the final follow-up examination.

RESULTS

- CASE REPORT 1: Case 1 was an 8-year-old boy who was referred to us for the treatment of a rhegmatogenous RD involving the macula of the right eye. Fundus examinations revealed a retinal break in the inferior temporal retina of the right eye and a peripheral avascular area with fibrovascular membranes in the temporal retina in both eyes. These findings suggested that the patient had FEVR in both eyes. The decimal best-corrected visual acuity (BCVA) was 0.04 in the right eye. The retina was reattached by scleral buckling; 6 months later, the BCVA had improved to 0.1 in the right eye.

Three years later, he developed a total retinal detachment with PVR in the right eye. A large tear of approximately

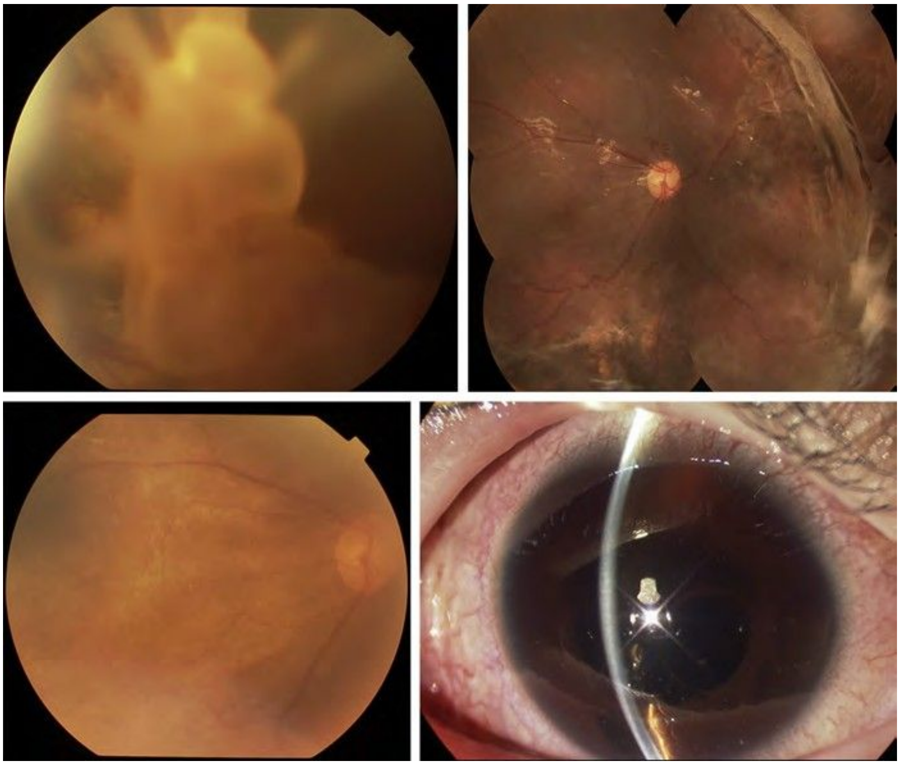

FIGURE 1. Case 1. Fundus photograph of the right eye of a patient with familial exudative vitreoretinopathy (FEVR). (Top left) fundus photograph of the right eye before the first vitrectomy, showing a total retinal detachment with PVR. (Top right) fundus photograph of the right eye before the sixth operation, showing a redetachment in the inferior retina due to reproliferations. (Bottom left) 3 months after the last vitrectomy. BCVA was 0.01 in the right eye. (Bottom right) slit-lamp photograph 2 weeks after PFO tamponade, showing PFO bubbles in the anterior chamber.

60 degrees was present in the upper nasal peripheral retina. The BCVA was hand motion in the right eye. Because of the repeated detachments, vitrectomy with silicone oil or C_3F_8 gas tamponade was performed 5 times. Because all of the redetachments were due to proliferation in the inferior retina, we decided to use perfluoro-n-octane as a postoperative tamponade. During the sixth vitrectomy, perfluoro-n-octane was injected into the eye. The patient was instructed to rest in a supine or sitting position after the perfluoro-n-octane tamponade. After 2 weeks, multiple perfluoro-n-octane bubbles were noted in the inferior anterior chamber. The perfluoro-n-octane was removed 3 weeks later and replaced with 10% C_3F_8 gas tamponade. The retina remained reattached during the 43-month follow-up. The BCVA at the last visit was 0.1 in the right eye (Fig. 1).

• CASE REPORT 2: Case 2 was a premature female infant with a birth weight of 758 grams and a gestational age of 23 weeks. She was referred to us with a diagnosis of bilateral severe ROP at a postconception age of 41-weeks. She had undergone photocoagulation to the avascular retina in both eyes at the postconception age of 31 weeks. Despite confluent photocoagulation in the avascular area, the ROP continued to progress, and she was referred to the Naha City Hospital.

At the initial examination, the patient was found to have stage 5 ROP in both eyes. At the postconception age of 45 weeks, vitrectomy and lensectomy was performed in both eyes. During the vitrectomy, fibrous membranes were removed as completely as possible, but an iatrogenic retinal break occurred in each eye. This was followed by C_3F_8 gas tamponade in both eyes. The retinas of both eyes were found to be detached when the C_3F_8 gas disappeared. At the age of 8 months, a second surgery, involving membrane peeling and retinotomy, was performed on both eyes, followed by injection of perfluoro-n-octane, which was retained in both eyes. After 2 weeks, the perfluoro-n-octane was removed and replaced with a 20% SF_6 gas tamponade. The retinas of the both eyes remained attached during the 22 months of follow-up, although the visual acuity at the last visit was limited to light perception (Fig. 2).

For all eyes, the total number of operations, including those that occurred when the perfluoro-n-octane was removed, ranged from 2 to 7, with a median of 3. The perfluoro-n-octane was retained in the eye after the first surgery in 2 eyes, after the second surgery in 6 eyes, after the third surgery in 1 eye, and after the sixth surgery in 1 eye for 1 to 4 weeks (median, 2.0 weeks). The postoperative perfluoro-n-octane tamponade was used at the primary vitrectomy in 2 eyes of 2 patients; 1 eye with a tractional RD

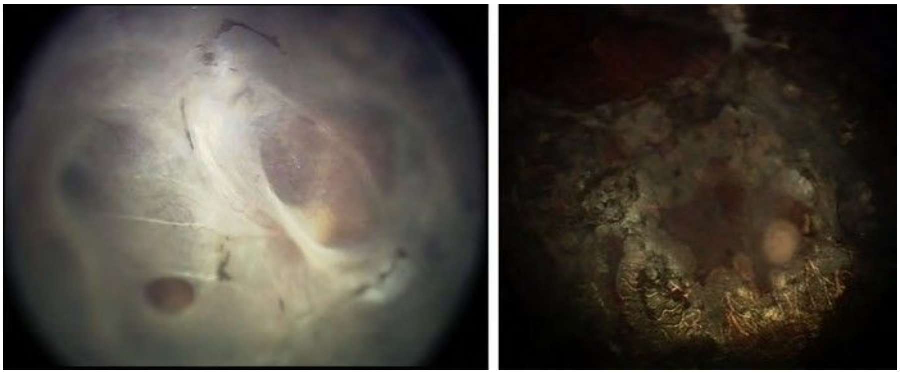

FIGURE 2. Case 2. Fundus photograph of the right eye of a patient with proliferative vitreoretinopathy (PVR). (Left) fundus photograph of the right eye after the first vitrectomy, showing total retinal detachment with PVR. (Right) fundus photograph of the right eye after PFO removal, showing reattachment of the retina.

associated with congenital optic nerve anomalies, and 1 eye with stage 4B ROP.

Because of the severe proliferation in the inferior retina, we believed it would be difficult to maintain the reattached retina by gas or silicone oil tamponade. In the other 8 eyes of 7 patients, perfluoro-n-octane tamponade was used at the time of reoperation after failure of retinal reattachment following a preceding vitrectomy using gas or silicone oil tamponade. Globule dispersion was noted in all of the eyes at the time of perfluoro-n-octane removal. During the perfluoro-n-octane tamponade, no eyes had intraocular pressures higher than 20 mm Hg or apparent intraocular inflammation.

At the latest examination, the retinas remained reattached in 8 of 10 eyes (80.0%). In 1 eye with tractional RD associated with congenital optic nerve anomalies (case 5), the perfluoro-n-octane was removed 1 week later, and the retina remained reattached for 1 month. However, 2 months after the perfluoro-n-octane was removed, a redetachment developed with severe PVR that was considered to be inoperable. In an eye with stage 5 ROP (case 9), a dense vitreous hemorrhage occurred after the primary vitrectomy. After 3 weeks, a reoperation was performed. At the second operation, extensive membrane removal was performed, followed by perfluoro-n-octane tamponade. After the second vitrectomy, vitreous hemorrhage occurred again despite the presence of perfluoro-n-octane in the eye. A third vitrectomy was performed 1 week later, and extensive membrane peeling was performed followed by C_3F_8 gas tamponade. However, 1 month later, the retina was totally detached, with severe PVR, which we considered inoperable.

DISCUSSION

POSTOPERATIVE PERFLUORO-N-OCTANE TAMPONADE WAS used for a short period in 10 eyes with pediatric complex RD, in which gas or silicone oil had been considered to be ineffective because the posterior proliferative changes were in the inferior retina. Perfluoro-n-octane tamponade was used because we believed that it would be difficult for children to maintain a prone position for any length of time. The perfluoro-n-octane was left in all of the eyes for 1 to 4 weeks, and the retinas remained reattached after removal of the perfluoro-n-octane in 8 of the 10 (80%) eyes. Given the complexity of the RD in the patients, we consider these results to be relatively good.

Silicone oil has been widely used as a postoperative tamponade in pediatric patients. Despite the proven long-term safety profile of silicone oil, it has been reported to release mitogenic factors, and thus may be a causative factor in PVR.[3] This would then lead to postoperative peri-silicone proliferation, which can cause redetachment. In addition, the lower specific gravity of gas and silicone oil as compared to water makes their tamponade effect unsatisfactory for detachments of the inferior retina, especially in pediatric patients whose compliance with maintaining the prone positioning is poor.

In contrast, perfluoro-n-octane has a high specific gravity of 1.75, which should have a better tamponade effect in inferior or posterior retinal detachments than gas or silicone oil. An earlier study showed that perfluoro-n-octane is biologically inert and does not contain protonated impurities measurable by nuclear magnetic resonance spectroscopy.[4] Also, perfluoro-n-octane appears to release fewer mitogenic factors than silicone oil.[3] It has been proposed that mediators of cellular proliferation, pigmented cells, chemoattractants, and serum components could diffuse into the vitreous chamber and become concentrated in the small amount of aqueous fluid that is still present.[5] Theoretically, heavy liquids should lift these mediators off the retinal surface, thereby preventing the development of PVRs.[5]

Another benefit of perfluoro-n-octane as a postoperative tamponade is the ease of its removal due to its lower viscosity of 0.58 mm^2/s compared to silicone oil, which has a viscosity of 1000 to 5000 mm^2/s.

Thus far, postoperative perfluoro-n-octane short-term tamponade has been used mainly for retinal detachments caused by giant tears.[5–7] Sirimaharaj and associates[6] reported that perfluoro-n-octane was effective for short-term postoperative tamponade to manage retinal detachments resulting from giant retinal tears. They elected to leave the perfluoro-n-octane in situ for 5 to 14 days because doing so provided sufficient time for chorioretinal adhesions to develop.[6] Rofail and associates[7] postulated that postoperative tamponade with perfluoro-n-octane decreases the rate of redetachments in eyes with giant retinal tears more than silicone oil or perfluorocarbon gas alone. To the best of our knowledge, there has been only 1 report on the use of perfluoro-n-octane for postoperative tamponade in eyes with a pediatric retinal detachment. Sick and associates[8] used this technique in an infant with X-linked retinoschisis and complex retinal detachment. The retina was successfully reattached after removal of perfluoro-n-octane, which had been retained in the eye for 25 days without significant inflammation. It has been suggested that the lower rate of redetachments when using perfluorocarbon liquids as postoperative tamponade is due to the extended apposition of the retinal tear to the underlying retinal pigment epithelium, resulting in more effective chorioretinal adhesion by retinopexy.[5,9] The incidence of inferior PVR was also lower after postoperative perfluorocarbon liquids tamponade, probably because of a lack of pooling of the retinal pigment epithelium cells, chemoattractants, and serum components over the inferior retina.[5,10]

Sirimaharaj and associates[6] reported that there were no serious adverse effects of perfluoro-n-octane as a postoperative tamponade. They also reported that the rate of cataract progression in their patients was 80.5%, which was comparable to the values in earlier reports of cataract progression (70% to 80%) after simple vitrectomy for an idiopathic epiretinal membrane.[11] Rofail and colleagues[7] reported that the rate of postoperative complications after perfluoro-n-octane postoperative tamponade was equivalent to that after intraoperative perfluoro-n-octane.[12,13] Thus, perfluoro-n-octane appears to be effective and safe as a postoperative tamponade as long as it is used for only a short period.

Animal studies have been conducted to determine the toxicity of perfluoro-n-octane as a tamponade substance. Chang and associates[14] reported that perfluoro-n-octane left for 1 week in rabbit eyes induced mild histologic changes, including thinning of the outer plexiform layer. After 2 weeks, focal areas of narrowing of the outer plexiform layer and ultrastructural distortions of the photoreceptor outer segments in the inferior retina were noted. These changes became more pronounced after 1 and 2 months. Because similar changes have been reported in the superior retina in silicone-filled eyes, these changes may represent mechanical rather than toxic effects.[14] Rabbit eyes injected with perfluoro-n-octane for 1 and 2 months had minimal lens changes, and they consisted of posterior subcapsular opacities in the portions of the lens capsule in contact with the perfluoro-n-octane liquid.[6] On the other hand, rabbit eyes in which the perfluoro-n-octane was left in the vitreous cavity for longer than 1 week had varying degrees of globule dispersion.[14] Similar findings were noted in all of the eyes in this study at the time of perfluoro-n-octane removal.

Taken together, the appropriate duration for postoperative perfluoro-n-octane tamponade seems to be approximately 1 to 2 weeks.

Although special caution should be exercised concerning the mechanical tamponade effects on the retina, it appears that short-term postoperative tamponade with perfluoro-n-octane is effective in pediatric cases with complex RD in which proliferations exist in the inferior or posterior retina.

THIS STUDY WAS SUPPORTED IN PART BY GRANT-IN-AID 23592597 FROM THE MINISTRY OF EDUCATION, CULTURE, SPORTS, Science and Technology, Japan. Design and conduct of study (A.I., S.K.); Collection of data (A.I., S.K., H.N.); Management, analysis, and interpretation of data (A.I., S.K.); Preparation of the manuscript (A.I., S.K.); and Review and approval of manuscript (S.K., Y.S., S.S.).

REFERENCES

1. Rumelt S, Sarrazin L, Averbukh E, Halpert M, Hemo I. Pediatric vs adult retinal detachment. Eye 2007;21(12):1473–1478.
2. Shapiro MJ, Chow CC, Blair MP, Kiernan DF, Kaufman LM. Peripheral nonperfusion and tractional retinal detachment associated with congenital optic nerve anomalies. Ophthalmology 2013;120(3):607–615.
3. Lambrou FH, Bourke JM, Aaberg TM. Effect of silicone oil on experimental traction retinal detachment. Arch Ophthalmol 1987;105(9):1269–1272.
4. Sparrow JR, Ortiz R, MacLeish PR, Chang S. Fibroblast behavior at aqueous interfaces with perfluorocarbon, silicone and fluorosilicone liquids. Invest Ophthalmol Vis Sci 1990;31(4):638–646.
5. Bottoni F, Bailo G, Arpa P, Prussiani A, Monticelli M, de Molfetta V. Management of giant retinal tears using perfluorodecaline as a postoperative short-term vitreoretinal tamponade: a long-term follow-up study. Ophthalmic Surg 1994;25(6):365–373.
6. Sirimaharaj M, Balachandran C, Chan WC, et al. Vitrectomy with short-term postoperative tamponade using perfluorocarbon liquid for giant retinal tears. Br J Ophthalmol 2005;89(9):1176–1179.
7. Rofail M, Lee LR. Perfluoro-n-octane as a postoperative vitreoretinal tamponade in the management of giant retinal tears. Retina 2005;25(7):897–901.

8. Sisk RA, Berrocal AM, Murray TG, Mavrofrides EC. Extended endotamponade with perfluoro-n-octane in pediatric retinal detachment. Ophthalmic Surg Lasers Imaging 2010; 3(9):1–3.
9. Chang S, Lincoff H, Zimmerman NJ, Fuchs W. Giant retinal tears: surgical techniques and results using perfluorocarbon liquid. Arch Ophthalmol 1989;107(5): 761–766.
10. Blinder KJ, Peyman GA, Desai UR, Nelson NC Jr, Alturki W, Paris CL. Vitreon, a short-term vitreoretinal tamponade. Br J Ophthalmol 1992;76(9):525–528.
11. Herfan GM, Michels RG, de Bustros S, Enger C, Glaser BM. Nuclear sclerotic cataract after vitrectomy for idiopathic epiretinal membranes causing macular pucker. Am J Ophthalmol 1991;111(4):434–438.
12. Scott IU, Murray TG, Flynn HW Jr, Feuer WJ, Schiffman JC, Perfluoron Study Group. Outcomes and complications associated with giant retinal tear management using perfluoro-n-octane. Ophthalmology 2002;109(10):1828–1833.
13. Ambresin A, Wolfensberger TJ, Bovey EH. Management of giant retinal tears with vitrectomy, internal tamponade, and peripheral 360 degrees retinal photocoagulation. Retina 2003;23(5):622–628.
14. Chang S, Sparrow JR, Iwamoto T, Gershbein A, Ross R, Ortiz R. Experimental studies of tolerance to intravitreal perfluoro-n-octane liquid. Retina 1991;11(4):367–374.

Biosketch

Ayako Imaizumi, MD, completed her residency in Ophthalmology at Osaka University Hospital. Currently she is the director of ophthalmology at Naha City Hospital and a postgraduate student at Graduate School of Medicine, University of the Ryukyus. Her field of interest includes surgical treatment of vitreoretinal disease such as diabetic retinopathy, retinal detachment, and retinopathy of prematurity.

Biosketch

Shunji Kusaka, MD is a Professor of Ophthalmology at Sakai Hospital Kinki University Faculty of Medicine, Sakai, Japan. Dr Kusaka completed his residency in Ophthalmology at Osaka University and his fellowship training in vitreoretinal surgery at Osaka National Hospital. After finishing research fellowship program at University of Michigan, he continues clinical research in vitreoretinal diseases in Japan. His research interests include treatment of various vitreoretinal disorders, especially pediatric retinal diseases.

Case Reports in Ophthalmology

Case Rep Ophthalmol 2014;5:318–324

DOI: 10.1159/000368298
Published online: October 2, 2014

Intravitreal Injection of Bevacizumab for Retinopathy of Prematurity in an Infant with Peters Anomaly

Tsuyoshi Minami[a] Kazuki Kuniyoshi[a] Shunji Kusaka[c] Koji Sugioka[a]
Hiroyuki Sakuramoto[a] Masuo Sakamoto[a] Akane Izu[b] Norihisa Wada[b]
Yoshikazu Shimomura[a]

Departments of [a]Ophthalmology and [b]Pediatrics, Kinki University Faculty of Medicine, and [c]Department of Ophthalmology, Sakai Hospital, Osaka, Japan

Key Words
Retinopathy of prematurity · Peters anomaly · Vascular endothelial growth factor · Anti-VEGF therapy · Bevacizumab

Abstract

Purpose: To report our findings in an infant with Peters anomaly type II whose retinopathy of prematurity (ROP) was treated with an anti-VEGF agent and surgeries. *Case Report:* A male infant weighing 548 g was born prematurely at 23 weeks and 1 day with corneal opacity and shallow anterior chambers in both eyes. At the postmenstrual age of 35 weeks and 3 days, the infant was tentatively diagnosed with stage 3 ROP because of a dilated tunica vasculosa lentis and ultrasonographic findings. The boy was treated with bilateral intravitreal injections of bevacizumab (IVB) because laser photocoagulation of the retina could not be performed due to the corneal opacity. The retina in the right eye detached 3 times, namely 5 days, 16 days, and 7 months after the IVB; encircling the scleral buckle and a vitrectomy with endolaser photocoagulation were therefore required. In his left eye, the retina was reattached after the initial IVB, and no additional treatment was required. ROP was not reactivated in both eyes until the last examination at the age of 2 years and 6 months. *Conclusions:* Our results showed that IVB is a useful treatment for ROP in patients with Peters anomaly. However, a retinal detachment can be a complication after IVB. The optimal timing of IVB for ROP in infants with hazy media needs to be determined.

Kazuki Kuniyoshi, MD
Department of Ophthalmology, Kinki University Faculty of Medicine
377-2 Ohno-Higashi, Osaka-Sayama 589-8511 (Japan)
E-Mail kuniyoshi-kazuki@umin.net

Introduction

Peters anomaly is characterized by congenital corneal opacities, defects of the Descemet's membrane, shallow anterior chambers, cataracts, and glaucoma [1, 2]. The corneal opacities in patients with Peters anomaly make the diagnosis and treatment of retinal disorders such as retinopathy of prematurity (ROP) difficult. Recently, the intravitreal injection of antivascular endothelial growth factors, including bevacizumab (IVB), was reported to be effective as a treatment for ROP [3, 4]. One advantage of IVB over traditional treatments for ROP, e.g., retinal photocoagulation, is that it can be performed on infants with hazy media.

We present our findings in an infant with Peters anomaly accompanied by ROP that was treated with IVB. The research protocol was approved by the Ethics Review Board of the Kinki University Faculty of Medicine in November 2011, and the procedures conformed to the tenets of the Declaration of Helsinki of the World Medical Association.

Case Report

Our patient, a male infant, was born prematurely at 23 weeks and 1 day and weighed 546 g. He was noted to have corneal opacities with shallow anterior chambers in both eyes soon after birth (fig. 1). He was diagnosed with Peters anomaly type II because he had corneal-lenticular adhesions in addition to a central corneal opacity with iridocorneal adhesions [1]. Details of the fundi could not be obtained because of the corneal opacity.

An ophthalmic examination performed at the postmenstrual age of 34 weeks and 2 days showed a dilated tunica vasculosa lentis, and ultrasonography showed an abnormal echo, which suggested ridge formation (white triangles in fig. 2). Although these findings suggested stage 3 ROP, which requires treatment [5], laser photocoagulation would have been difficult to perform because of the corneal opacity, dilated tunica vasculosa lentis, and the fixed pupils.

Thus, we selected to treat the eye with IVB [3, 4] (Avastin®; Genentech Inc., South San Francisco, Calif., USA). A detailed clinical information and treatment options, including cryotherapy and IVB, were given to the family, and the parents agreed and signed an informed consent to proceed with the IVB.

At the postmenstrual age of 35 weeks and 3 days, 0.25 mg/0.01 ml of bevacizumab were injected into the vitreous cavity of both eyes. Five days later, the dilatation of the tunica vasculosa lentis was reduced in both eyes, but a retinal detachment was detected by ultrasonography in the right eye (stage 4A ROP; black arrow in fig. 2). An encircling scleral buckle was placed on both eyes on the same day, and the retina of the right eye was detached again 11 days after the buckling surgery. We performed lens-sparing vitrectomy in the right eye because the tunica vasculosa lentis was reduced after the IVB and buckling surgery. The temporal area of the fundus, where the proliferation was most severe and the retina was partially detached, was barely observable, and vitrectomy with endolaser photocoagulation was performed. Since other areas of the fundus could not be observed due to the corneal opacity, we performed additional transscleral cryopexy in the right eye.

At 4 months after the IVB, a cataract with an increase of the intraocular pressure (IOP, 33 mm Hg) was detected in the right eye. The cataract was removed and the IOP was normalized. Seven months after the IVB, the corneal opacity was reduced in both eyes, allowing a better observation of the fundus (fig. 1, fig. 3). Ophthalmoscopy showed a third retinal detachment in the right eye (arrow in fig. 3), and fluorescein angiography showed an avascular zone in both eyes and some leakage of fluorescein in the right eye (fig. 3). The fovea of the right eye was displaced temporally (fig. 3).

A second vitrectomy was performed in the right eye, and no progression or reactivation of the ROP or retinal detachment was noticed at the last examination at the age of 2 years and 9 months. In his left eye, the IOP was normal and the retina was attached after the initial IVB, and no additional treatment was required. No apparent systemic side effects of the IVB were observed.

Discussion

The treatment for ROP in infants with corneal opacity is challenging. Although partial corneal opacity, which is occasionally observed in neonatal infants, allows clinicians to observe and treat ROP, dense and bilateral corneal opacities, which were present in our patient, obstructed the detection and treatment of the ROP.

We had several treatment options for our patient: IVB, combination of penetrating keratoplasty with laser photocoagulation, and endoscopic vitrectomy with laser photocoagulation. We selected IVB as the first treatment because it could be performed even in an eye with a corneal opacity. Penetrating keratoplasty was not considered before the treatment for ROP because we knew the results are not favorable in patients with Peters anomaly type II [2].

There are 3 problems in managing ROP in eyes with dense and bilateral corneal opacities: (1) how do we detect ROP, (2) when do we treat ROP, and (3) how do we treat ROP.

According to the results of the Early Treatment for Retinopathy of Prematurity (ETROP) study [5], the treatment for ROP should be performed within 72 h after a diagnosis of type 1 ROP. The most important finding required to make a decision on the treatment of the ROP is the ‘plus disease’ condition [5], which is difficult to recognize in infants with hazy media. Therefore, clinicians need to decide on the treatment for ROP in infants with hazy media without any information regarding the status of the fundus.

The ETROP Cooperative Group also reported that stage 3 ROP was present in 48.1% of infants whose birth weight was <750 g and in 43.3% of infants whose gestational age was ≤27 weeks [6]. In our institution, the first treatment is performed between the postmenstrual age of 30 and 35 weeks [7]. From the results of these treatments, the infants who had a high risk for ROP, mainly those with a gestational age of ≤27 weeks or a birth weight of <750 g, were recommended to be treated between the postmenstrual age of 30 and 35 weeks.

Our results indicated that IVB appeared to be effective and led to a regression of the ROP; however, additional surgeries were needed for the tractional retinal detachments. Although a retrospective analysis of our findings indicated that earlier IVB treatments may not lead to retinal detachments, the systemic condition of our patient did not allow an earlier treatment for the ROP.

A late reactivation of ROP [4, 8] as well as incomplete vascularization after IVB [4, 9] have recently been reported. The results of fluorescein angiography in our patient suggested that the ROP had not completely regressed even 7 months after the IVB (fig. 3). Longitudinal and careful observations are needed after IVB treatment for ROP.

In conclusion, IVB can be a treatment for ROP in infants with Peters anomaly. However, the diagnosis of ROP and the timing of the IVB in infants with hazy media need more investigation.

Acknowledgements

The authors express gratitude to Kyutaro Ito, MD, working at the Department of Ophthalmology, Tottori Prefectural Central Hospital, for referring the patient to our clinic. We also thank Masahiko Fukuda, MD, and Chota Matsumoto, MD, in the Department of Ophthalmology, Kinki University Faculty of Medicine, for their suggestions regarding this paper.

This research was supported by the research grants to S.K. and K.K. from the Japan Society for the Promotion of Science, Japan (23592597) and to Y.S. from the Ministry of Health, Labour and Welfare, Japan (82259921).

Disclosure Statement

The authors have no proprietary or commercial interests related to this research.

References

1 Zaidman GW, Flanagan JK, Furey CC: Long-term visual prognosis in children after corneal transplant surgery for Peters anomaly type I. Am J Ophthalmol 2007;144:104–108.
2 Bhandari R, Ferri S, Whittaker B, Liu M, Lazzaro DR: Peters anomaly: review of the literature. Cornea 2011;30:939–944.
3 Mintz-Hittner HA, Kennedy KA, Chuang AZ; the BEAT-ROP Cooperative Group: Efficacy of intravitreal bevacizumab for stage 3+ retinopathy of prematurity. N Engl J Med 2011;364:603–615.
4 Kuniyoshi K, Sugioka K, Sakuramoto H, Kusaka S, Wada N, Shimomura Y: Intravitreal injection of bevacizumab for retinopathy of prematurity. Jpn J Ophthalmol 2014;58:237–243.
5 Early Treatment for Retinopathy of Prematurity Cooperative Group: Revised indications for the treatment of retinopathy of prematurity. Arch Ophthalmol 2003;121:1684–1696.
6 Early Treatment for Retinopathy of Prematurity Cooperative Group: The incidence and course of retinopathy of prematurity: findings from the Early Treatment for Retinopathy of Prematurity study. Pediatrics 2005;116:15–23.
7 Kayazawa M, Kuniyoshi K, Sugioka K, Tsujioka D, Abe K, Matsumoto C, Wada N, Shimomura Y: Review of retinopathy of prematurity in very low birth weight infants and extremely low weight infants. Folia Jpn Ophthalmol Clin (Ganka Rinsho Kiyo) 2011;4:448–454.
8 Hu J, Blair MP, Shapiro MJ, Lichtenstein SJ, Galasso JM, Kapur R: Reactivation of retinopathy of prematurity after bevacizumab injection. Arch Ophthalmol 2012;130:1000–1006.
9 Tahija SG, Hersetyati R, Lam GC, Kusaka S, McMenamin PG: Fluorescein angiographic observations of peripheral retinal vessel growth in infants after intravitreal injection of bevacizumab as sole therapy for zone I and posterior zone II retinopathy of prematurity. Br J Ophthalmol 2014;98:507–512.

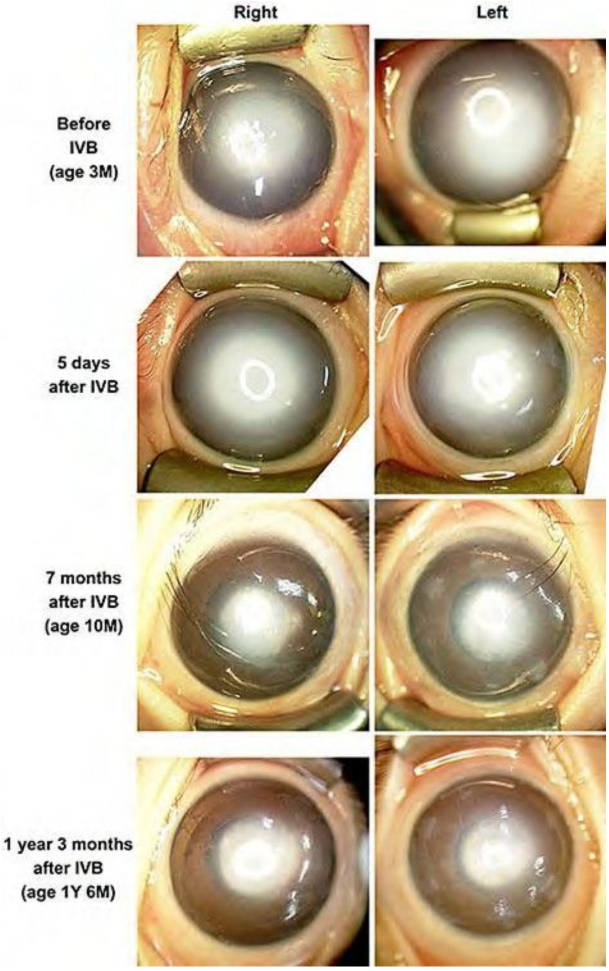

Fig. 1. Photographs of the anterior segment of eyes with Peters anomaly type II and ROP. The dense corneal opacities are gradually reduced. These photographs were taken with a RetCam® 3 (Clarity Medical Systems, Pleasanton, Calif., USA). Y=Year; M = month.

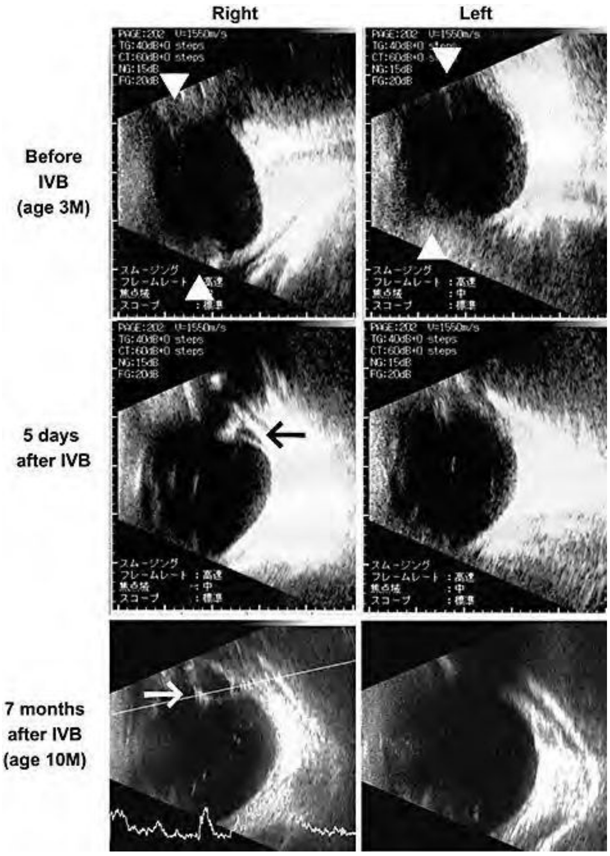

Fig. 2. Ultrasonographic findings of eyes with Peters anomaly and ROP. Before the IVB, abnormal echo was detected which suggested ridge formation (triangles in the upper row, stage 3 ROP). Five days after the IVB, a retinal detachment was suspected in the right eye (black arrow in the middle row, stage 4A ROP). Seven months after the IVB, a third retinal detachment is suspected in the right eye (white arrow in the lower row, stage 4A ROP).

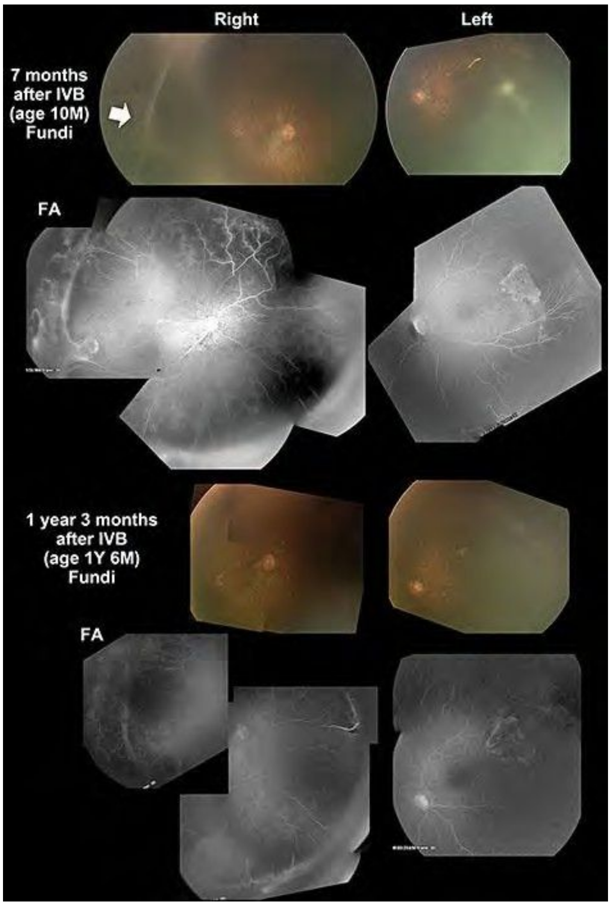

Fig. 3. Fundus photographs and fluorescein angiograms. A retinal detachment can be seen in the right eye 7 months after the IVB (arrow). An avascular zone and some leakage of fluorescein are still present in the periphery 1 year and 3 months after IVB. Photography was difficult because of the residual corneal opacity in both eyes. Fundus photography and fluorescein angiograms were performed using RetCam® 3.